To the Graduate Council:

I am submitting herewith a dissertation written by Paul D. Spence entitled "A Study of the Effective Electron Collision Frequency in a Weakly Ionized Turbulent Penning Discharge Plasma". I have examined the final copy of this dissertation for form and content and recommend that it be accepted in partial fulfillment of the requirements for the degree of Doctor of Philosophy, with a major in Engineering Science.

J. Reece Roth

Dr. J. Reece Roth, Major Professor

We have read this dissertation
and recommend its acceptance:

Henry C Simpson

A J Baker

Igor Alexeff

David Rosenberg

Accepted for the Council:

C W Minkel

Vice Provost
and Dean of The Graduate School

A STUDY OF THE EFFECTIVE ELECTRON COLLISION FREQUENCY IN A WEAKLY IONIZED TURBULENT PENNING DISCHARGE PLASMA

A Dissertation

Presented for the

Doctor of Philosophy

Degree

The University of Tennessee, Knoxville

PAUL D. SPENCE

AUGUST 1990

ACKNOWLEDGEMENT

The author would like to thank Professor J.R. Roth for training as an experimentalist and providing the well equipped laboratory used for this research.

The author thanks the remaining members of his committee: Professor A.J. Baker, Professor I. Alexeff, Professor H. Simpson, and Associate Professor D. Rosenberg. Special thanks go to Dr. D. Rosenberg for his assistance with many of the microwave related problems and his general patience and guidance.

The author extends his gratitude and appreciation to Research Associate Fred Dyer, who assisted in the testing and repairing of equipment on many occasions.

The author also thanks his typist, Christine Marks for the excellent job in preparing this manuscript.

Finally, the author wishes to express his appreciation to his parents for their support and encouragement throughout his academic career.

This work was supported by the Office of Naval Research under Contracts ONR N00014-80-C-0063, ONR N00014-88-K-0174, and by the Air Force Office of Scientific Research Contract AFOSR 81-0093-GRA. The network analyzers used in this research were provided by the University Research Instrumentation Program under Grant AFOSR 85-0152.

ABSTRACT

The effective electron collision frequency is studied on a weakly ionized, turbulent Penning discharge plasma. The magnetized plasma of this discharge is radially inhomogeneous and subject to a high level of low frequency electrostatic fluctuations due to drift wave turbulence. An effective electron collision frequency is determined from collision broadened absorption spectra of the extraordinary mode wave near the electron gyro frequency resonance. When the level of electrostatic turbulence is excited above the level of thermal fluctuations, the collision frequency is significantly greater than the electron-neutral collision frequency. The scaling of this collision frequency as a function of the absolute rms level of electrostatic fluctuations is investigated.

TABLE OF CONTENTS

LIST OF TABLES

Table **Page**

LIST OF FIGURES

Figure **Page**

LIST OF SYMBOLS

Unless indicated otherwise, the SI system of units is used in all formulas and symbols.

Latin Symbols:

A	Area m^2
A_x	Cross sectional area, m^2
a	Velocity exponent for velocity dependent collision frequency
B	Magnetic induction, Tesla
B_0	Static magnetic field, Tesla
C_{mn}	Coupling capacitance, farads
c	Speed of light, m/sec
D	Directivity
E	Electric field intensity, volts/m
$Erf(z)$	Error function
$\mathbf{e}$	Polarization vector
e	Electron charge, coulombs
F_t	Fraction of particles trapped due to magnetic mirroring
f	Frequency, Hz
G	Antenna gain, dB
g, h	Dielectric tensor correction factors for velocity dependent collision frequencies
$I_+(z)$	Function defined by $I_+(z) = -\frac{z}{\sqrt{2}}\, Z\left(\frac{z}{\sqrt{2}}\right)$
$I_n(z)$	Modified Bessel function of order n
$J_n(z)$	Bessel function of first kind of order n
K	Boltzmann constant
k	Wave number, m^{-1}
ℓ	Distance, m
m	Mode number
m_e	Electron mass, kg
m_i	Ion mass, kg

LIST OF SYMBOLS (continued)

N	Particle number density, $\#/\mathrm{m}^3$
$\nabla\Psi$	Scale function of potential and density gradients
n_0	Background neutral particle number density, $\#/\mathrm{m}^3$
n_e	Electron number density, $\#/\mathrm{m}^3$
n_i	Ion number density, $\#/\mathrm{m}^3$
p	Kinetic gas pressure, newtons$/m^2$
P	Radiated power, watts
P_{He}	Background gas pressure of helium, torr
Q	Total charge, coulombs
q	Species charge, coulombs
$\mathbf{R}, r$	Position vector, m
R, r	Position vector, m
R_{ie}	Frictional force due to ion-electron interaction
R_{in}	Frictional force due to ion-neutral interaction
T_e	Electron kinetic temperature, eV
T_i	Ion kinetic temperature, eV
u	Radiation Intensity, watts/solid angle
u	Particle speed, m/sec
$V_{\parallel}$	Particle drift velocity parallel to the static magnetic field, m/sec
$V_{\perp}$	Particle drift velocity perpendicular to static magnetic field, m/sec
$\mathbf{V}_{E\times B}$	$\mathbf{E}\times\mathbf{B}$ particle drift velocity m/sec
V_{di}, V_{de}	Ion and electron diamagnetic drift velocities m/sec
v_s	Ion sound speed m/sec
v_x, v_y, v_z	Discrete particle velocity components m/sec
v_{th}, v_{th}^i	Electron and ion thermal velocities m/sec
W	Radiated power density, watts$/m^2$
$Z(z)$	Plasma dispersion function

LIST OF SYMBOLS (continued)

Greek Symbols:

α	Attenuation coefficient
β	Correction factor for $\mathbf{E} \times \mathbf{B}$ drift velocity
β	Phase constant
β_p	Plasma stability index, ratio of the plasma kinetic pressure to the magnetic pressure
γ	Complex propagation coefficient
Γ	Particle flux
Γ	Reflection coefficient
δ	Ratio of electron to ion mass
δ	Ratio of the electron thermal velocity to the speed of light
ϵ_0	Permittivity of free space
ϵ_r	Relative permittivity
$\bar{\varepsilon}$	Plasma dielectric tensor
ε_{ij}	Plasma dielectric tensor component
ζ, ξ	Direction cosines
η_0	Impedance of free space, 377 ohms
η_1, η_2, η_3	Viscosity coefficients
η_e, η_i	Ratio of temperature to density scale lengths
θ	Angle; degrees, radians
θ_i	Incident angle, degrees
θ_s	Scattering angle, degrees
λ	Wavelength, m
λ_d	Debye shielding length, m
$\lambda_\perp$	Wavelength perpendicular to static magnetic field , m
$\lambda_{\|\|}$	Wavelength parallel to the static magnetic field, m
Λ	Argument of coulomb logarithm
μ_{ex}	Complex dielectric constant for extraordinary mode
μ_0	Permeability of free space, $4\pi \times 10^{-7}$ henry/m
ν	Collision frequency/particle
ν_{ei}	Electron-ion coulomb collision frequency, Hz

LIST OF SYMBOLS (continued)

ν_{eff}	Effective collision frequency, Hz
ν_{en}	Electron-neutral collision frequency, Hz
ν_{ii}	Ion-ion collision frequency, Hz
ν_{in}	Ion-neutral collision frequency, Hz
ν_t^e	Electron turbulent collision frequency, Hz
ν_{meas}^e	Measured electron collision frequency, Hz
π	Pi
Π_{ii}	Ion viscous stress tensor
Π_p	Electron plasma frequency, Hz
Π_{pi}	Ion plasma frequency, Hz
ρ	Charge density, coulomb/m^3
ρ	Particle gyro radius, m
ρ_e	Electron gyro radius, m
ρ_i	Ion gyro radius, m
σ	Scalar conductivity, Siemens (ohm-meter)$^{-1}$
$\overline{\sigma}$	Conductivity tensor
σ_{ij}	Conductivity tensor component
τ	Integration variable
ϕ	Potential, volts
Φ	Normalized potential
$\tilde{\phi}$	Fluctuating potential, volts
χ	Imaginary part of propagation constant
ω	Angular frequency, radians/sec
ω_{be}	Electron gyro frequency, radians/sec
ω_{bi}	Ion gyro frequency, radians/sec
ω_p	Plasma frequency, radians/sec
Ω	Solid angle, steradians
Ω_e	Electron gyro frequency, Hz
Ω_i	Ion gyro frequency, Hz
Ω_{UH}	Upper Hybrid Frequency, $\Omega_{UH}^2 = \Pi_p^2 + \Omega_e^2$, Hz

CHAPTER I

INTRODUCTION

A magnetically confined plasma is subject to radial gradients in plasma number density and temperature. These gradients act as free energy reservoirs for a variety of instabilities producing low frequency electrostatic and density fluctuations. When sufficiently strong gradients are present, the fluctuations may rise above the background level of thermal fluctuations until ultimately a highly turbulent plasma results. These fluctuations interact with the charged particles of the plasma through a variety of mechanisms to produce a plasma with enhanced collisionality (Galeev and Sagdeev 1966, Akhiezer et. al. 1975 and Sitenko 1980). An understanding of these mechanisms is essential for the steady state confinement of a magnetized plasma.

This work is concerned with the measurement of the effective electron collision frequency due to turbulent fluctuations and its relation to drift wave turbulence (Horton 1980) on a weakly ionized inhomogeneous plasma. Drift wave turbulence is characteristic of magnetized plasmas with strong radial gradients of plasma number density and temperature. For a collisional plasma, coherent resistive drift wave modes can emerge and enhance the background level of turbulent fluctuations. This produces a synergistic effect with a coherent mode enhancing the level of random small scale fluctuations. These fluctuations in turn enhance the collisionality of the plasma, which governs the growth rate and saturation level of the coherent mode. This results in a situation where coherent large scale structures are closely connected to the integrated effects of small scale random fluctuations.

For this study a Penning discharge (Roth, 1966) was used as the plasma source. The discharge was operated in the steady state to produce a magnetized and weakly ionized collisional plasma with $\omega_b > \omega_p \gg \nu$. This plasma had radial gradients of the background number density, temperature and floating potential making it susceptible to drift wave and other instabilities (Mikhailovsky 1983). The steady state operation of the plasma allowed the use of a variety of plasma diagnostics, and the application of an external forcing signal. This signal was used to modify the level of electrostatic turbulence of the discharge.

The effective collision frequency of electrons was determined by measuring the absorption spectra of an extraordinary mode wave propagated across the plasma column at a right angle to the static magnetic field. For the collisional plasma, this wave exhibits a strong absorption resonance near the upper hybrid frequency. The width of this absorption resonance is a function of the average effective electron collision frequency of the plasma.

CHAPTER II

EXPERIMENTAL APPARATUS

Introduction.

The Penning discharge was originally introduced as a neutron source and as a new type of vacuum gauge tube. The tube was constructed of a cylindrical anode, two cathode end plates, and a uniform axial magnetic field aligned along the axis of the anode (Penning et al. 1949). This geometry acts as an axial electrostatic trap for electrons, with the electrons oscillating back and forth between cathodes. Trapped electrons can suffer many collisions with neutral gas molecules before finally being collected by the anode. The increased number of collisions per electron gives the appearance of an elevated gas pressure, yielding a sensitive vacuum gauge and allowing the Penning discharge to operate at lower pressures than would otherwise be possible.

When scaled to produce a plasma for laboratory experiments, the Penning discharge relies primarily on two processes for the production of plasma. First, trapped electrons produce a cascading effect by colliding with neutrals or excited neutrals to yield ions and secondary electrons. These reactions are

$$A + e \longrightarrow A^{+} + 2e \ , \tag{2.1}$$

and

$$A^{*} + e \longrightarrow A^{+} + 2e \ . \tag{2.2}$$

Secondly, excited metastable neutrals will collide with other neutrals to produce an ion and electron (Eletsky et al. 1983),

$$A^* + B \longrightarrow A + B^+ + e \ . \tag{2.3}$$

This "Penning ionization" is essential for the production of free electrons in the weakly ionized Penning discharge plasma.

In order to improve ion containment in a Penning discharge for plasma physics experiments, a nonuniform magnetic field can be used (Roth 1966). By increasing the axial magnetic field near the cathodes, an axial magnetic "mirror" is produced. Ions (and electrons) tend to be reflected from the regions of high magnetic field to the central region of minimum magnetic field. For isotropic particle distributions, the fraction of particles trapped by this mirroring is given by the trapping fraction F_t, defined by (Roth 1986):

$$F_t = \left(1 - \frac{B_{\text{min}}}{B_{\text{max}}}\right)^{\frac{1}{2}} \ . \tag{2.4}$$

Experimental System Geometry.

Figures 2.1 through 2.4 show schematics of the various Penning discharge geometries used to generate turbulent plasmas in this study. These discharges consisted of one or more water cooled anode rings, two water cooled tungsten cathodes, a glass vacuum vessel, and a set of magnet coils used to produce an axial magnetic field. The center section of the glass vacuum vessel had a three way cross which allowed radial access to the plasma by various probes. The inside diameter of the glass vacuum vessel was 15.2 cm with a wall thickness of 0.95 cm. The maximum plasma diameter was determined by the anode rings which had 12.7 cm inside diameters

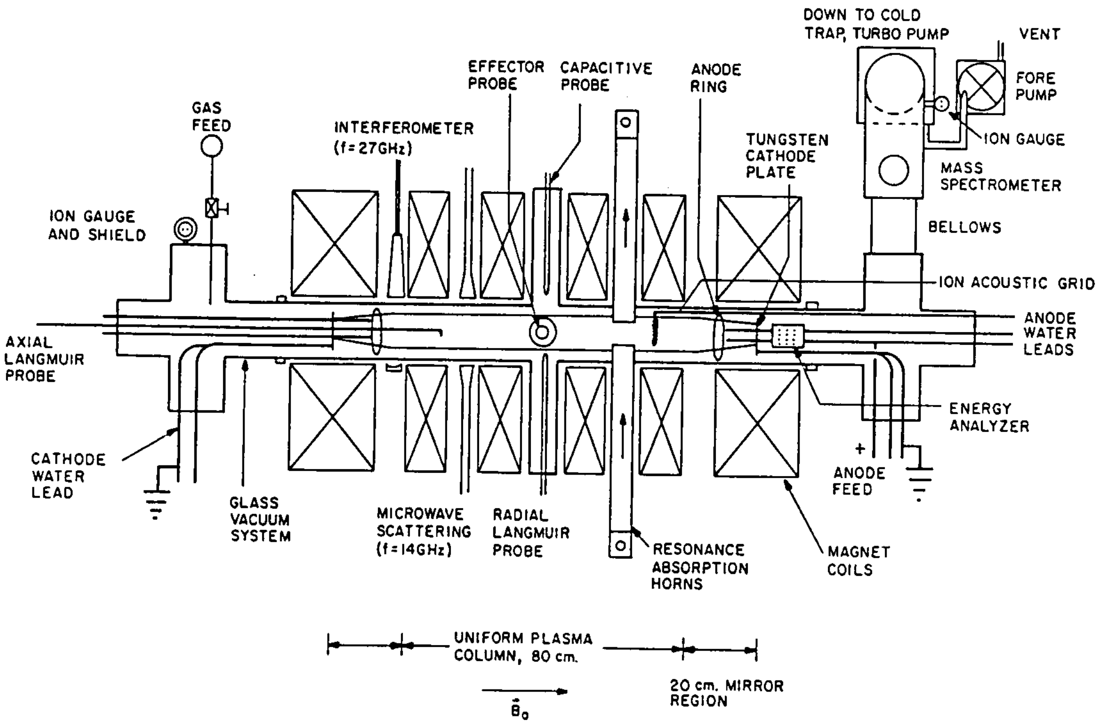

Figure 2.1. Penning discharge geometry using two anode rings and having a uniform magnetic field central cell region. This geometry was used primarily in the scaling study of ν_{eff}.

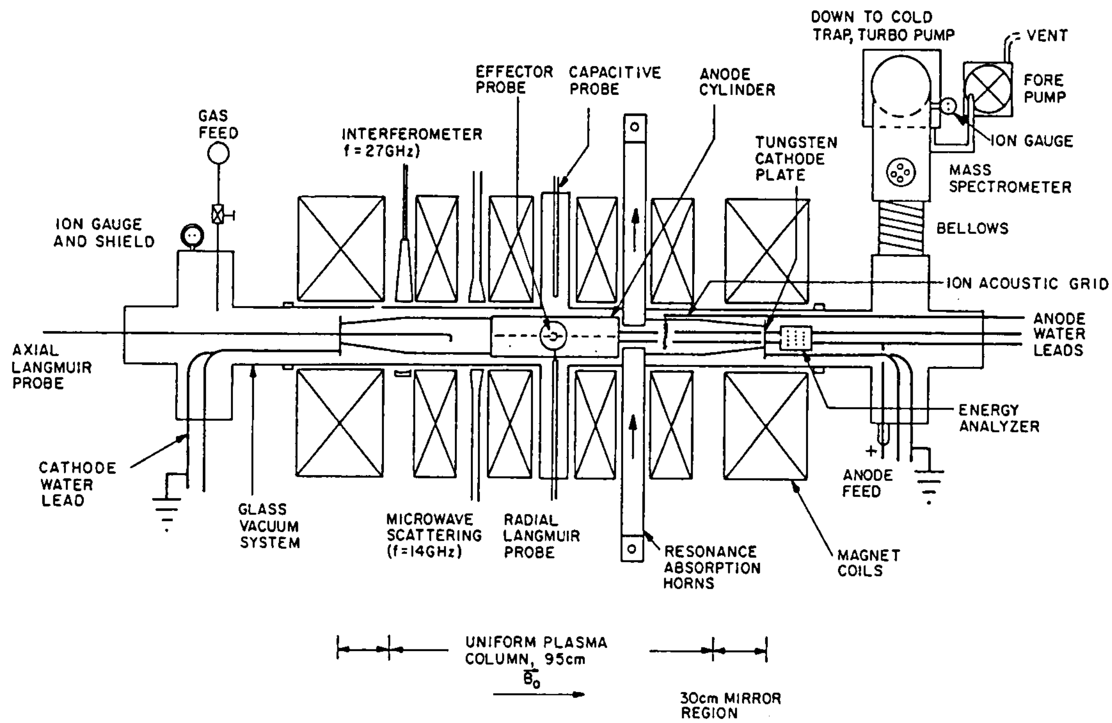

Figure 2.2. Penning discharge geometry using a 30cm. anode cylinder. This geometry was used to study drift waves under external forcing. This geometry was also configured with a central cathode rod in order to study a coaxial discharge.

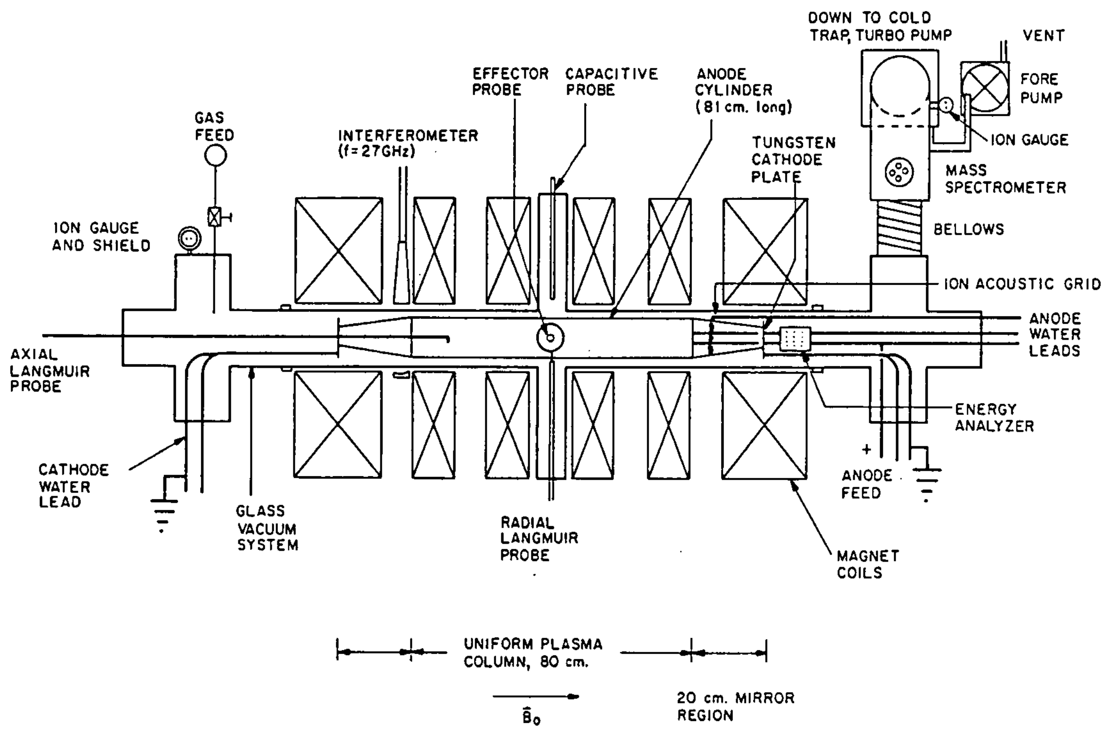

Figure 2.3. Penning discharge geometry using a 75cm. cylinder to produce coherent drift wave structures.

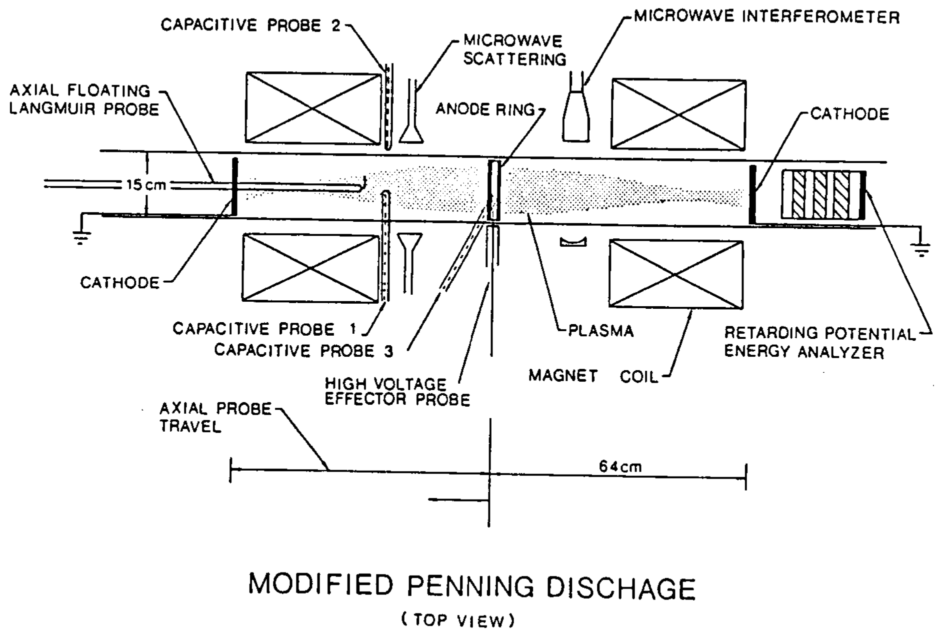

Figure 2.4. Modified Penning discharge geometry used in early drift wave studies and investigation of the geometric mean emission due to beam plasma interaction.

for all discharges. Vacuum sealing to the large crosses at either end of the system and to plexiglass cover plates was accomplished with Neoprene gaskets coated with vacuum grease. Feedthrus for water lines and probes were of the Veeco, or "O" ring type,with a vacuum grease coating.

The vacuum system was rough pumped by a mechanical forepump. A high vacuum was achieved by the combined use of a turbomolecular pump and a chevron cold trap. The cold trap had a dedicated refrigeration unit utilizing a special freon mixture and was capable of reaching temperatures of -130°C. The use of a cold trap greatly reduced the partial pressure of water vapor in the vacuum system. The vacuum pumping subsystem was mechanically isolated from the glass vacuum vessel by a stainless steel bellows. The system pressure was monitored by two ion vacuum gauges, one at each end of the system. Because Neoprene and "O" ring seals were used, a low base pressure of 5×10^{-6} torr was common. A two to one pressure differential was typically present between the two ion gauges.

In order to assist ion containment and reduce ion flux on the cathodes in the uniform Penning discharges, the magnetic field was increased slightly near the cathodes. Figure 2.5 shows the normalized axial magnetic field used in the configuration shown in Figures 2.1 through 2.3. Figure 2.6 shows the radial profile of the normalized axial magnetic field at the midplane. The mirror ratio of 1.3 to 1 for the profile of Figure 2.6 produced a trapping fraction of $F_t = 0.47$. Electric field effects aside, this allowed the ion containment time to be approximately twice what it would be without mirroring.

Figures 2.7 and 2.8 show the axial and radial magnetic field profiles used with the system geometry shown in Figure 2.4. This configuration had a mirror ratio of

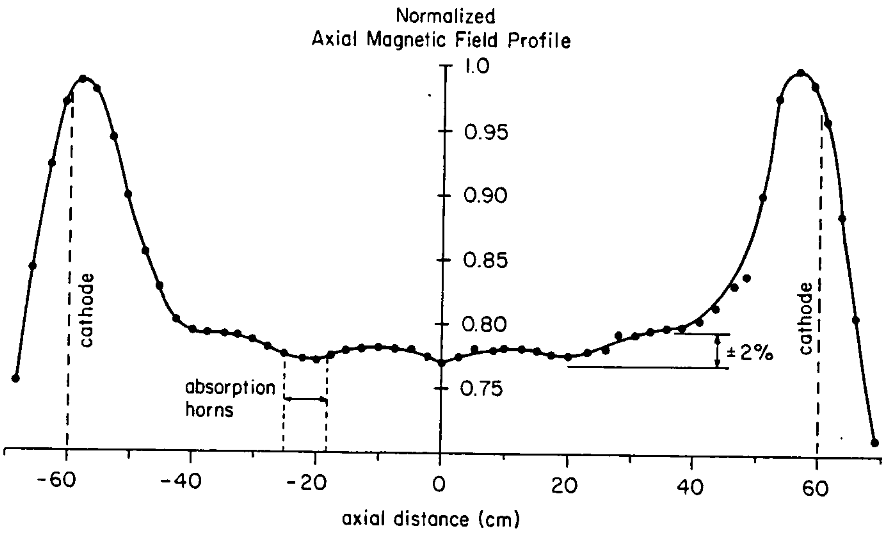

Figure 2.5. Normalized axial magnetic field profile for Penning discharge geometries in Figures 2.1, 2.2 and 2.3.

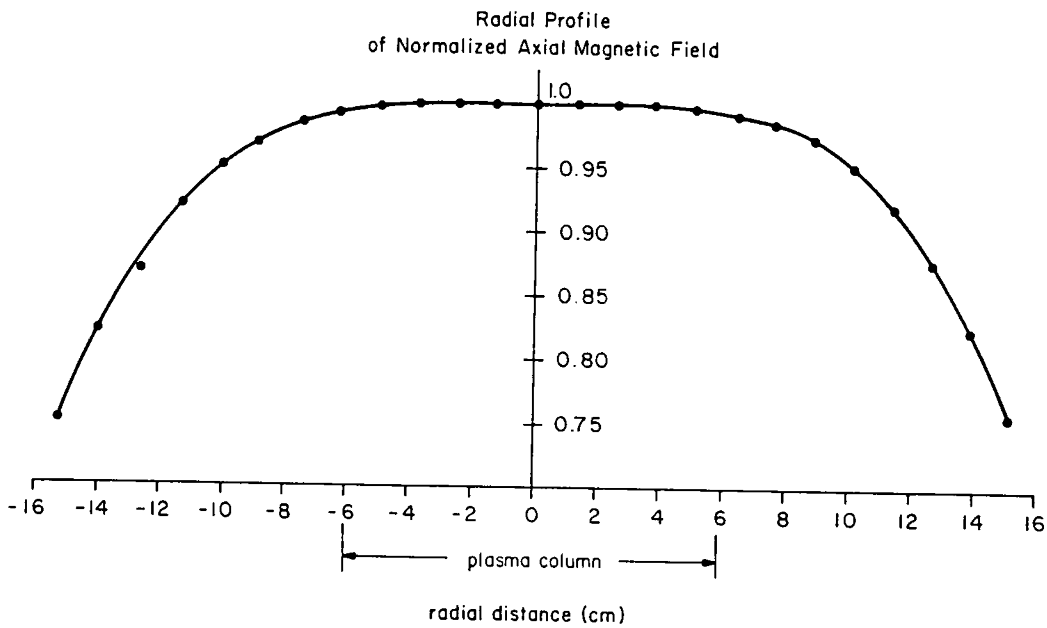

Figure 2.6. Normalized radial profile of the axial magnetic field in Figure 2.5 at the midplane.

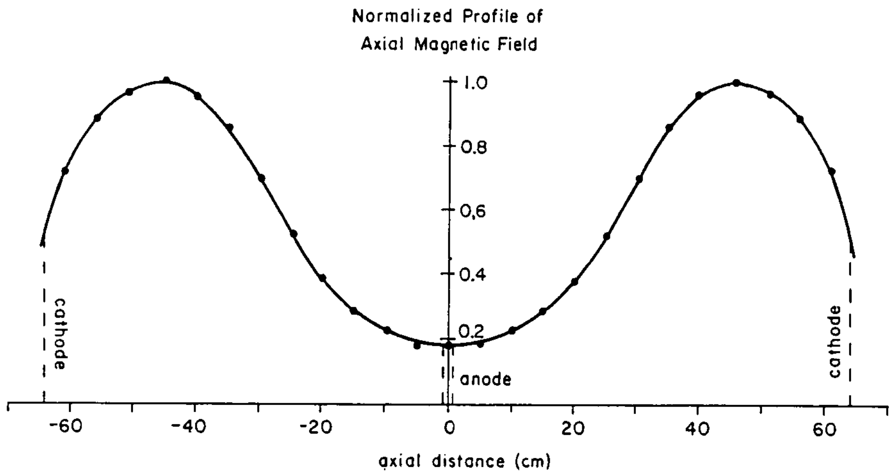

Figure 2.7. Normalized axial magnetic field profile for the Penning discharge geometry in Figure 2.4.

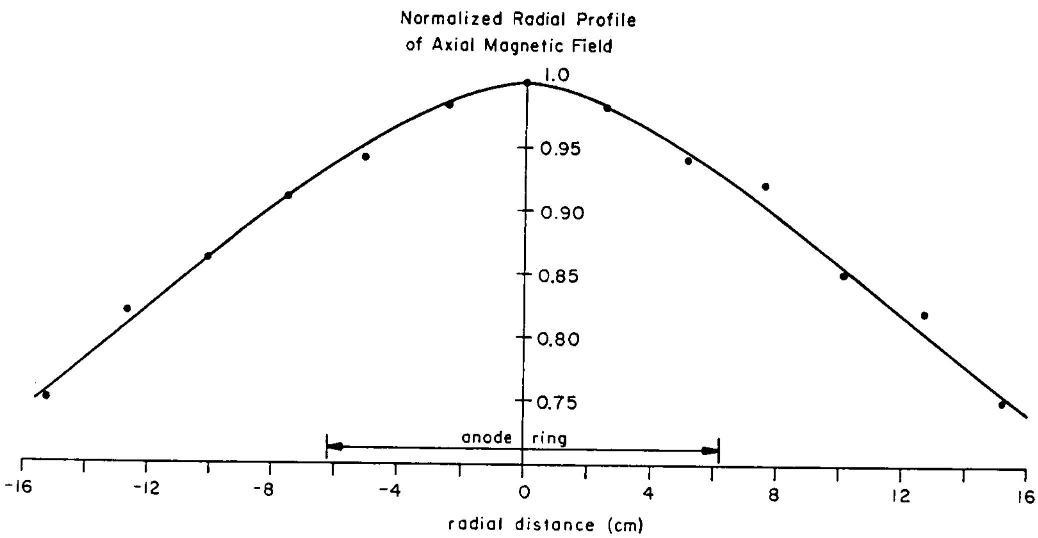

Figure 2.8. Normalized radial profile of the axial magnetic field in Figure 2.7 at the midplane.

5.7 to 1 and was used for some of the earlier studies of drift wave behavior. The large mirror ratio was chosen to enhance relevance to the earth's magnetosphere, where large mirror ratios are common.

The long term operating time of the system, on a time scale of tens of hours, was limited primarily by sputtering of metal from the tungsten cathodes and copper anodes. Sputtered metal would coat the inside of the glass, potentially reducing microwave access to the plasma and changing the boundary conditions of the plasma column. Excessive plating of the glass required dismantling the system and abrasive polishing of the interior surfaces.

Diagnostics.

In order to monitor various discharge and plasma parameters, a variety of test instruments and plasma diagnostics were used (see Figure 2.1). Ion gauges were located at both ends of the vacuum vessel to monitor the system's neutral gas pressure. System impurities such as water and nitrogen were detected by a 0-200 amu mass spectrometer. This unit was also used for leak detection of the system. The discharge current and anode voltage were monitored by a floating series current meter and a high voltage series volt meter connected to a 10 Megohm resistor string. The static magnetic field was determined by comparing the coil current from a 50-900 ampere DC power supply to a calibration curve giving axial magnetic field as a function of coil current. This curve was generated by measuring the magnetic field with a 1% rotating coil gaussmeter, as a function of the coil current.

Basic plasma parameters were monitored using Langmuir probes, a microwave interferometer, and a retarding potential energy analyzer. Both axial and radial Langmuir probes were used. These probes were used for electron number density, electron temperature, floating potential, and plasma potential measurements. Both axial and radial Langmuir probes used tungsten wire tips. These tips were typically 0.38mm in diameter, 6.4 mm in length, and were oriented perpendicular to the static magnetic field. The axial Langumir probe was constructed of semirigid coaxial transmission line and fitted with a quartz sheath. This probe had an outside diameter of 4 mm and a length of 56 cm. A small elliptical hole was cut in the cathode center to allow passage of the probe. The radial Langmuir probe located at the midplane of the discharge was constructed of a quartz capillary tube 1.5 mm in diameter and 6.5 cm in length. These probes were constructed as small as possible to minimize perturbations to the plasma. A 27 GHz polarization diplexing microwave interferometer originally designed and built by Perkins and Gardner [1968], was used for core averaged density measurements. This system was capable of a phase shift resolution of less than 0.5 degrees.

The integrated ion energy distribution function for ions escaping axially along the discharge was measured using a retarding potential energy analyzer (Roth, 1969). This analyzer consists of a series of electrostatic grids arranged perpendicular to the axial magnetic field. When the retarding grid is swept in voltage, the current on the collector disc varies, giving a current-voltage curve proportional to the integrated ion energy distribution. This curve is numerically fitted to a best-fitting Maxwellian or other distribution function (Roth et. al. 1968) to yield the ion temperature. A sample curve is given in Appendix C.

Turbulent potential and number density fluctuations were measured using capacitive probes and a 14 GHz microwave scattering system. The design and analysis of these systems are discussed in detail in Appendices A and B.

The effective electron collision frequency was determined by interpreting the absoption curves of a microwave signal launched and received by two "C" band microwave horns. These horns were expanded in the E plane of the waveguide only, due to limited space between the magnet coils. These horns have a useable bandwidth of 2.1 GHz to 6 GHz and are discussed in more detail in Chapter V.

In an attempt to measure the ion collision frequency, a fine mesh tungsten grid was installed in the plasma column. This grid was modudated with a high voltage signal in order to launch an ion acoustic wave. The spatial dispersion of these waves can be related to the ion collision frequency. This diagnostic is discussed in Appendix D along with a magneto-acoustic diagnostic which can also be used to determine the ion collision frequency.

Figure 2.9 shows the signal conditioning and detection system used for studying turbulent potential and density fluctuations. Fixed gain, variable attenuation Tektronix 1121 amplifiers were used for signal amplification. These amplifiers are quite robust and were placed in front of the high-low pass filter networks due to occassional probe failure and high voltage transients. The input impedance of these amplifiers is 1 Megohm with 31 picofarads shunt. The Langmuir probe was biased to either electron or ion saturation using a high voltage bias network. A signal proportional to either electron or ion density fluctuations was coupled from a Langmuir probe to the detection network using a capacitive coupling circuit. The frequency response of this network is given in Appendix C.

The amplified signals from the various diagnostics were band pass filtered using Kron-Hite model 3200 filters. These filters were typically set to a high pass of 2 KHz and a low pass of 1 MHz. By adjusting the high pass filter and using the

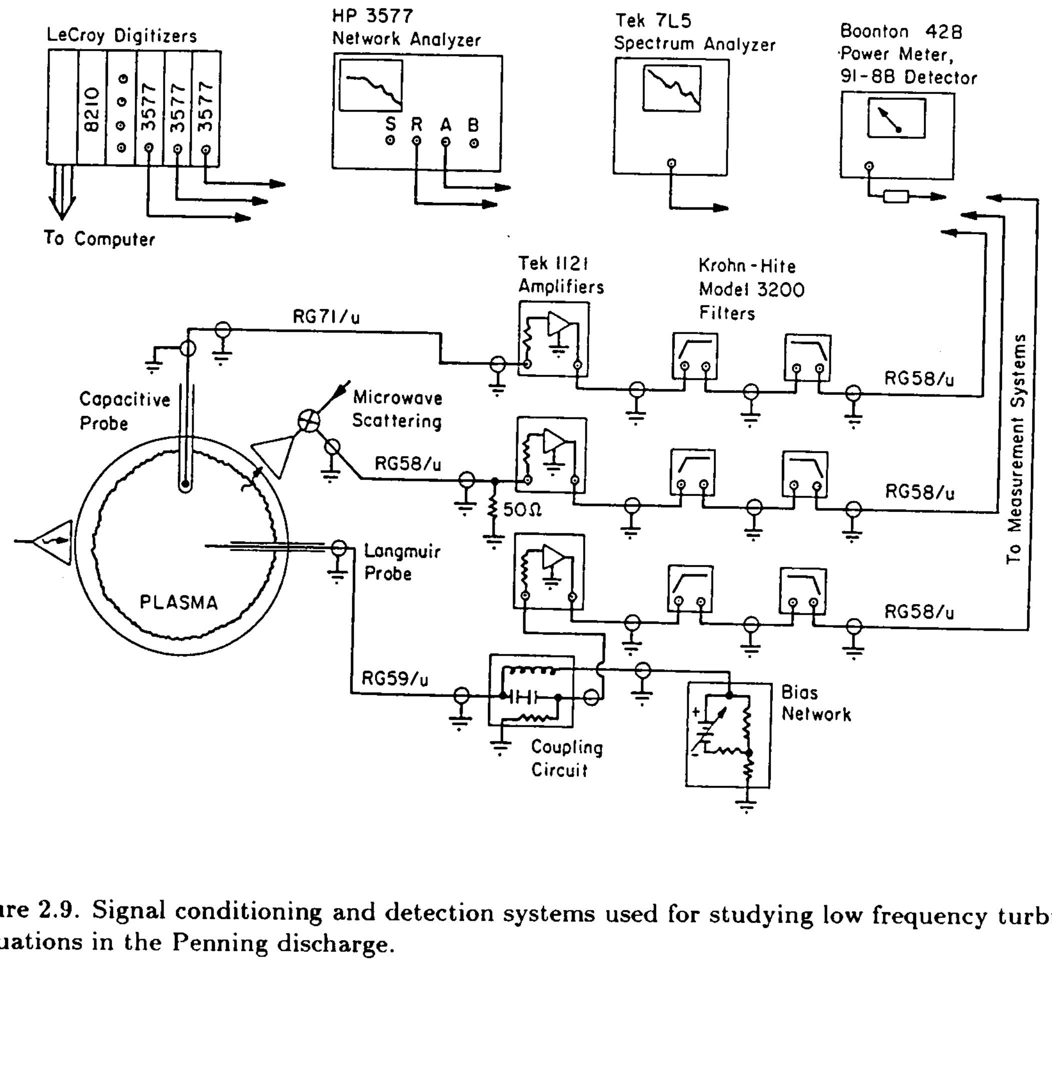

Figure 2.9. Signal conditioning and detection systems used for studying low frequency turbulent fluctuations in the Penning discharge.

broadband Boonton power meter, the integrated energy spectrum of a given signal could be measured as a function of the filter cut-off (see Appendix C).

The conditioned signals were studied in the frequency domain using one or more of the following: a Tektronix 7L5 spectrum analyzer, a Hewlett Packard 3577 network analyzer, or LeCroy model 8837 digitizers connected to a computer. The Tektronix 7L5 spectrum analyzer has a 0 to 4 MHz bandwidth with a linear frequency axis and either a linear or logarithmic amplitude response. For signals below 500 KHz, the Hewlett Packard 3577 network analyzer could be used as a spectrum analyzer or phase detector. When coupled to a frequency controlled filter network (Crowley 1987), the HP 3577 could be used as a spectrum analyzer to 10 MHz. This instrument has the convenient feature of allowing data to be displayed on a logarithmic frequency axis. The LeCroy digitizers were used in conjunction with a computer to produce power spectrum, squared coherency and phase spectra of the digitized data.

Plasma Column.

The Penning discharge has a number of features that contribute to the generation of a turbulent plasma. Consider the plasma column illustrated in Figure 2.10 and the model electrostatic potential well shown in Figure 2.11. When a high voltage is initially applied to the anode, electrons will be accelerated toward the anode. Some of these electrons will reach a sufficient energy to ionize the neutral gas and produce ions and secondary electrons. These ions and electrons will be accelerated and give rise to the cascading processes mentioned earlier. This process results in a plasma of increasing number density, until various losses balance the ionization process.

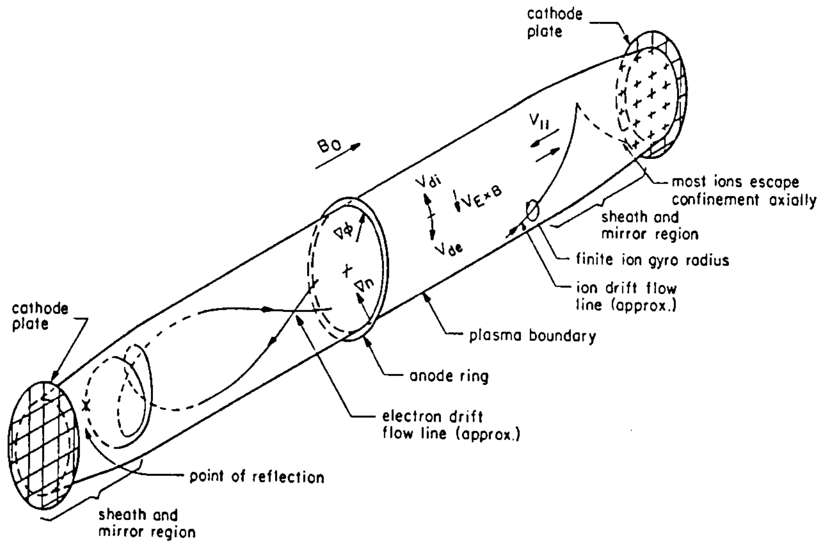

Figure 2.10. Plasma column used to illustrate various drift velocities in the inhomogeneous plasma.

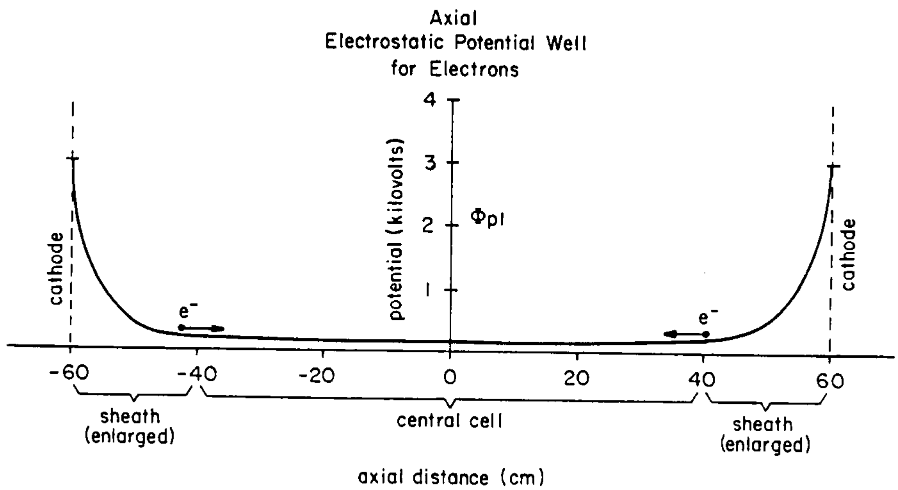

Figure 2.11. Model axial electrostatic potential well for electrons trapped between cathodes.

The axial magnetic field of the discharge tends to inhibit the radial motion of the ions and electrons. Electrons not collected by the anode ring will oscillate axially between cathode regions. These electrons are trapped by the electrostatic potential well and the mirroring of the magnetic field. Ions tend to be accelerated out of the plasma column by the axial potential, and can be trapped only by mirroring in the magnetic field. The ion flux to the cathodes results in sputtering of the cathode surface, and allows ions to recombine with electrons to form neutrals.

The axial drift motion of the electrons both as a current flux to the anode and as particles oscillating in a potential well, gives rise to a number of potential beam-plasma instabilities. If the drift velocity v_{de} is due to an axial current I, where

$$v_{de} = \frac{I}{n_e A_x e} \tag{2.5}$$

exceeds a critical velocity given approximately by the ion sound speed v_s, then low frequency electrostatic ion acoustic oscillations and turbulence will be excited (Kadomtsev (1965) and Sagdeev et al. (1969)). These oscillations can grow to some finite level for $T_e \gg T_i$, but are strongly Landau damped for $T_e \sim T_i$.

The symmetric form of the axial electrostatic potential well gives rise to the formation of two interpenetrating beams of electrons. These opposed beams can interact to generate high frequency oscillations (Alexeff et. al. 1981). For beams of equal density, the frequency of these oscillations is given by the geometric mean frequency

$$w_{gm} = \frac{\sqrt{w_{pe}^* w_{pi}}}{\sqrt{2}\ \sqrt[4]{3}}\ , \tag{2.6}$$

where w_{pe}^* is the electron plasma frequency based on beam density, and w_{pi} is the ion plasma frequency of the background plasma. The beam density in a Penning discharge is typically some fraction of the background plasma density. Appendix F discusses a method for estimating the electron beam density in a weakly ionized plasma due to an axial electric field.

Experimentally the two beam instability appears to interact parametrically with the instability of a single electron beam and background plasma (Alexandrov et. al. 1984). The single beam instability grows for $w \simeq w_{pe}$ where w_{pe} here is the electron plasma frequency of the background plasma. The electromagnetic emission spectra for the parametric interaction of these instabilities is an envelope centered at w_{pe} with harmonics at w_{gm},

$$S(w) \quad \alpha \quad A_n[w_{pe} \pm n w_{gm}] \quad n = 0, 1, 2, \dots \; , \tag{2.7}$$

and the amplitude function A_n is some decreasing function of the harmonic number n. These emissions are typically linearly polarized with the polarization along the axis of the static magnetic field. The net radiated power of this process is typically less than 0.1% of the input D.C. power to the discharge (Rosenberg et. al. 1985). At sufficiently high voltages, the Penning discharge has been observed by others to emit at the electron gyro frequency and its harmonics, but also with low efficiency (Waniek et. al. 1964).

The plasma column shown in Figure 2.10 has radial gradients of the plasma potential and pressure. These radial gradients are typically strongest near the region of the anode. Consider Figure 2.12, which illustrates the processes involved due to these radial gradients.

The radially inward electric field imposed by the anode ring gives rise to azimuthal

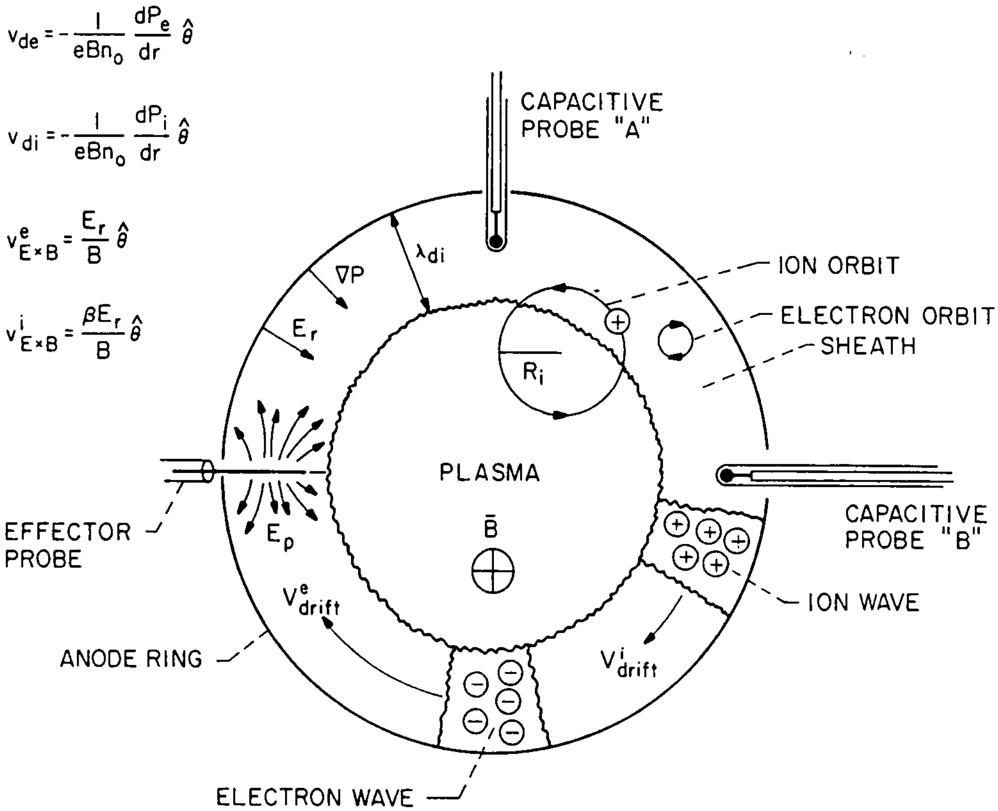

Figure 2.12. Cross section of the inhomogeneous plasma column.

particle drift velocities given by (Roth 1970),

$$V^e_{E\times B} = \frac{E_r}{B_0}\,\hat{\theta}\,, \tag{2.8}$$

and

$$V^i_{E\times B} = \frac{\beta E_r}{B_0}\,\hat{\theta} \tag{2.9}$$

for electrons and ions. Due to ion-neutral collisions and finite gyro radius effects, the ion $E \times B$ drift typically is smaller than the electron $E \times B$ drift by a factor β. The factor β is discussed in detail in Appendix G. This difference in electron and ion $E\times B$ drift velocities gives rise to charge bunching and the growth of unstable waves (Huh 1963). If the radial variation of E_r is not linear in r, shear flow instabilities of the Kelvin-Helmholtz type can also develop (Jassby 1972, Perkins et. al. 1971, Kent et. al. 1969). By using a radially increasing magnetic field (Dubovǐ et. al. 1966) the formation of $E \times B$ driven instabilities can be partially controlled.

The radial gradients of temperature or number density coupled with the finite gyro orbits of particles, gives rise to the diamagnetic drift velocities

$$V_{de} = \frac{1}{eB_0 n}\,\frac{dP_e}{dr}\,\hat{\theta}\,, \tag{2.10}$$

and

$$V_{di} = -\frac{1}{eB_0 n}\,\frac{dP_i}{dr}\,\hat{\theta}\,. \tag{2.11}$$

These velocities, unlike the $E \times B$ drift velocities, are not discrete particle drift velocities, but rather velocities associated with the azimuthal current flow due to the finite gyro orbits of particles, in temperature and density gradients (Alexandrov 1984).

The diamagnetic drift velocities give rise to a class of instabilities called drift instabilities (Chen, F.F. 1965, Motley 1975). The physical process responsible for this type of instability for a collisional plasma can be understood by considering Figure 2.12. If the plasma is subject to some perturbation so that it moves radially across field lines down the pressure gradient, a small charge separation will occur due to the mass difference of ions and electrons. This charge separation will give rise to radial electric fields. Since all laboratory plasmas have radial density gradients, this instability is often refered to as the "universal instability." If electrons are allowed to stream freely along field lines, a Boltzmann equilibrium will be maintained, and oscillations of the electron density n_e and electrostatic potential ϕ will occur, with n_e and ϕ in phase. If electrons are subject to collisions in moving along magnetic field lines, oscillations with n_e and ϕ out of phase will occur. In general this phase difference will cause a growth of the perturbation. The energy for this growth arises from the equilibrium drift motion due to the plasma inhomogenity.

Both forms of drift instability give rise to the growth of waves which are accompanied by charge bunching or rarefaction. The wave can occur either as a local bunching (or rarefaction) that propagates azimuthally, or as a discrete group of charge that travels azimuthally. In the first case the wave has a phase velocity which differs from the group velocity, while in the latter case the group and phase velocity of the wave are identical. If many waves are excited and propagate with the same group and phase velocities, a Taylor flow field (Tritton 1988) will develop with

$$\omega_i = k_i V \ . \tag{2.12}$$

This flow field has been observed on the edge of the Penning discharge. The potential fluctuations of these waves were experimentally detected using capacitive probes (see Figure 2.12). By displacing two or more of these probes azimuthally, the frequency spectra, phase spectra, and coherency spectra of the azimuthally propagating drift waves can be measured. A Langmuir probe biased in electron or ion saturation allows the density perturbations of the wave to the measured.

An effector probe was installed as shown in Figure 2.12 to allow coupling of an external oscillator to the potential fluctuations of drift waves. This probe was essentially a large Langmuir probe that could be D.C. biased to electron or ion saturation and then driven with a high voltage sine wave over the frequency range from 500Hz to 10MHz. This effector probe was used to enhance or damp the growth of drift waves.

Turbulent Plasma.

The Penning discharge plasma was considered turbulent when the spectrum of low frequency electrostatic potential fluctuations was excited well above the thermal noise level and consisted of a continuum of many excited modes. These fluctuations were typically below 1 MHz, with any distinct self-excited modes having a broad bandwidth. Drift modes which grow and interact nonlinearly will contribute to this turbulent spectrum (Horton 1984). A stationary turbulent plasma will occur when the spectrum of finite amplitude fluctuations coexists with the unstable velocity distribution function created by the radially inhomogeneous plasma. This spectrum will then change, but slowly in time, as the background plasma parameters are varied.

Figure 2.13 illustrates an idealized spectrum of low frequency fluctuations. This spectrum is broken into three distinct but overlapping regions; source, coupling, and dissipation (Tchen, C.M. 1976). Each region has a different spectral index indicating that different physical processes occur in each region.

The source region consists of "zero" frequency and low frequency oscillations which extract energy from the free energy reservoirs of the plasma such as radial inhomogenities. These oscillations typically have large coherence lengths, oscillate with $\tilde{n}_e$ and $\check{\phi}$ in phase, and have low dissipation. Drift vortices (Horton 1989 and Mikhailovskii et. al. 1984) are an example of low frequency coherent structures in the source region.

The coupling region consists primarily of wave-wave interaction in which waves mode couple or interact parametrically to produce modes of higher frequency. In Figure 2.13, a large amplitude drift mode is shown as a peak at ω_0. Here the drift mode acts as a source function to the turbulent spectrum and enhances the spectrum above ω_0.

The dissipation region is characterized by low amplitude waves which are strongly damped by viscous and Landau damping (Ishimaru 1973). Here wave energy is thermalized into random particle motion. Fluctuations in this region typically have coherence lengths on the order of a Debye length.

The three regions combine to produce a state in which large but finite amplitude oscillations exist to cascade energy upward in ω and k space. The initial growth rate of waves in the source and coupling regions is positive. As waves grow, non linear mechanisms cause the waves to saturate and couple energy to the dissipative

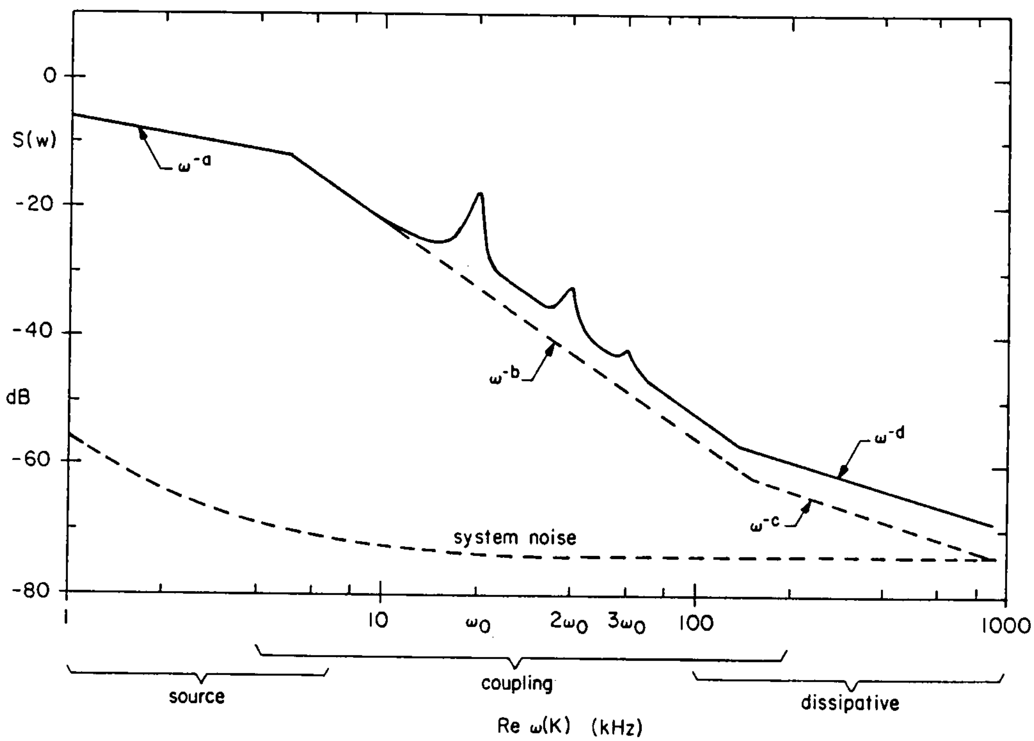

Figure 2.13. Idealized power spectrum of turbulent electrostatic potential fluctuations illustrating the three basic regions of low frequency turbulence.

region of the spectrum where waves are damped. These effects combine to result in a steady state continuim of turbulent fluctuations.

Experimental Data.

The Penning discharge was operated in a variety of configurations (see Figures 2.1 through 2.4) and under a broad range of operating parameters in order to investigate the behavior of a turbulent plasma. Table 2.1 lists the typical range of operating and plasma parameters for the steady-state uniform Penning discharge. The mirror field modified Penning discharge had a similar range in operating parameters except for slightly higher number densities.

The discharge had three parameters that could be set externally: static magnetic field B_0, helium gas pressure P_{He}, and anode voltage V_A. The magnetic field could be held very constant for levels below 0.1 Tesla but suffered drift due to ohmic heating of the current measuring shunt for larger fields. The helium gas pressure could be held constant for high pressures, but was subject to drift due to out-gassing of the walls at low pressure, high voltage operating conditions. The anode voltage was set by a voltage controlled power supply, but could drift as the result of changes in the load resistance. The anode current I_A to the plasma was a function primarily of the anode voltage and background gas pressure.

The discharge was not macroscopically stable under all operating conditions. In general, high discharge currents are stable for low voltage, high pressure conditions. High voltage, low current, low pressure discharges are the least stable. High plasma temperatures are associated with low current, high voltage discharges; and low temperatures result from low voltage, high current discharges.

Figure 2.14 shows the far field R.F. emission power spectrum and low frequency

TABLE 2.1

TYPICAL RANGE IN OPERATING AND PLASMA PARAMETERS
FOR THE STEADY-STATE PENNING DISCHARGE*

Parameter	Symbol	Range High	Range Low	Units
Anode Voltage	V_A	5000	500	volts
Anode Current	I_A	500	20	mA
He Gas Pressure	P_{He}	1000	150	microtorr
Magnetic Field (at midplane)	B_0	0.2	0.02	Tesla
Number Density	n_e	1×10^{10}	5×10^8	$\#/cm^3$
Electron Temperature	T_e	100	5	eV
Ion Temperature	T_i	300	20	eV
Plasma Frequency, e^-	Π_p	900	200	MHz
Ion Plasma Frequency	Π_{pi}	10.5	2.3	MHz
Gyro Frequency, e^-	Ω_e	6000	550	MHz
Ion Gyro Frequency	Ω_i	0.8	0.075	MHz
Perturbation Signal	f_p	10	0.005	MHz
Electron Debye Length	λ_{de}	0.34	0.02	cm
Electron Gyro Radius	ρ_e	0.12	0.003	cm
Ion Gyro Radius	ρ_i	12.5	0.32	cm
Thermal Velocity, e^-	v_{th}^e	4×10^8	9×10^7	cm/sec
Ion Thermal Velocity	v_{th}^i	2.4×10^7	6.3×10^6	cm/sec
Axial Electron Current Drift Velocity	v_{de}	1×10^7	1×10^6	cm/sec
Ion Sound Velocity	v_s	5×10^6	1×10^6	cm/sec
Kinetic to Magnetic Pressure Ratio	β_p	4×10^{-2}	5×10^{-4}	
Ionization Fraction	I^*	0.1	0.001	%

*For a helium plasma.

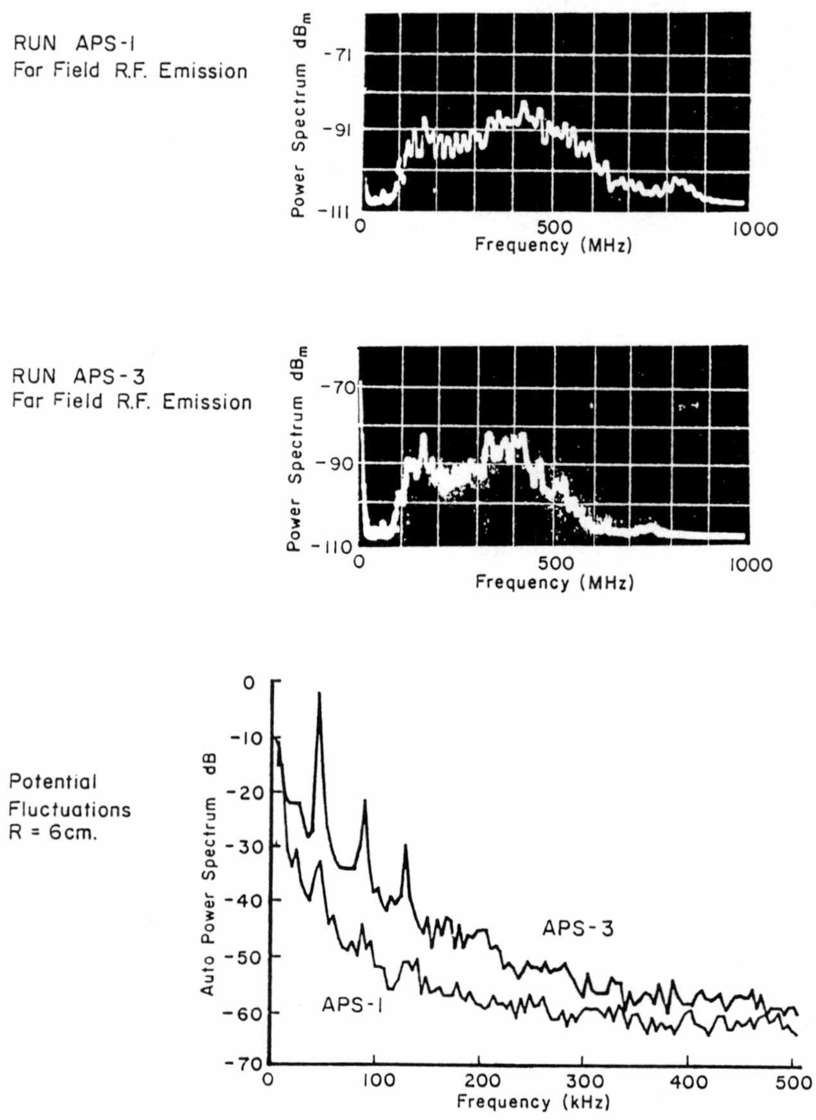

Figure 2.14. Power spectra of far field R.F. emission and low frequency electrostatic potential fluctuations for Runs APS-1 and APS-3.

electrostatic potential fluctuations for a self-excited turbulent plasma (Run APS-1) and the same plasma with external perturbation by the effector probe (Run APS-3). Figure 2.15 shows the phase and squared coherency spectra for the low frequency potential fluctuations of these plasmas, and Table 2.2 lists the operating and plasma parameters. These plasmas were generated by the modified Penning discharge shown in Figure 2.4.

The R.F. power spectra in Figure 2.14 where detected using a broadband conical spiral antenna calibrated for measurements below 1 GHz (Spence et al. 1984). This antenna had a flat frequency response from 100 MHz to 1.2 GHz which allowed quantitative measurement of the harmonic structure and net power of the emission.

The low frequency potential fluctuctions were detected by capacitive probes located just off the midplane of the discharge. The peak around 40 kHz on the power spectrum for Run APS-1 corresponds to an electron drift wave propagating azimuthally on the surface of the plasma column. Using two probes displaced azimuthally by 90° allowed the phase and coherency of this wave and others to be measured (Figure 2.15). When perturbed with the effector probe by a signal at 43 kHz, the drift wave was enhanced, along with the whole turbulent spectrum. Although energy was being supplied at a discrete frequency, it coupled to produce increased coherency over a broad frequency range and a well defined group velocity. Using the definition of group velocity

$$v_g = \frac{dw}{dk} , \tag{2.13}$$

or

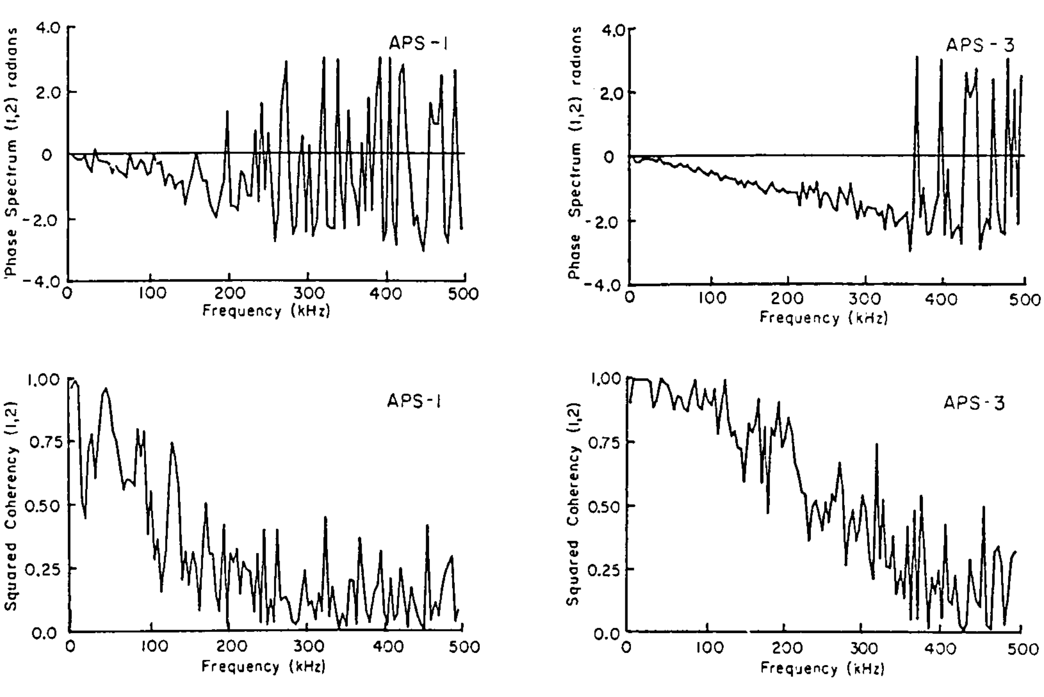

Figure 2.15. Phase and squared coherency spectra for Runs APS-1 and APS-2. Detecting capactive probes where displaced azimuthally 90° and located just off the midplane of the discharge in Figure 2.4.

TABLE 2.2

PLASMA PARAMETERS FOR EXPERIMENTAL RUNS APS-1 AND APS-3 ON THE MODIFIED PENNING DISCHARGE (FIGURE 2.4)

Parameter	Symbol	Run APS-1	Run APS-3	Units
Anode Voltage	V_A	3500	3550	volts
Anode Current	I_A	35	26	mA
He Gas Pressure	P_{He}	262	262	microtorr
Magnetic Field*(min)	B_0	0.021	0.021	Tesla
Number Density	n_e	1.6×10^9	0.7×10^9	$\#/cm^3$
Electron Temperature	T_e	19	60	eV
Plasma Frequency,	Π_p	350	230	MHz
Ion Plasma Frequency	Π_{pi}	4.1	2.7	MHz
Gyro Frequency,* e^-	Ω_e	588	588	MHz
Ion Gyro Frequency*	Ω_i	0.08	0.08	MHz
Geometric Mean:				
analytic, $n_b = 0.5n_e$	f_{gm}	17.2	8	MHz
experimental	f^*_{gm}	21	14	MHz
Effector Probe:		Off	On	
Signal:	43kHz, $0.8kV_p$, 8 mA			

*At the discharge midplane.

$$v_g \approx \frac{\Delta w}{\Delta k} \; . \tag{2.14}$$

Defining the wavenumber of an azimuthally propagating wave by

$$k(w) = \frac{\phi(w)}{\Delta s_1} \; , \tag{2.15}$$

where

$$\Delta s_1 = r_p \Delta \theta_{pr} \; . \tag{2.16}$$

For an $m = 1$ mode, with r_p the plasma radius and $\Delta\theta_{pr}$ the azimuthal displacement of the two probes, the group velocity for waves is given by

$$v_g = r_p \Delta\theta_{pr} \; \frac{\Delta w}{\Delta \phi_{12}} \; . \tag{2.17}$$

For the phase spectrum of Run APS-3 in Figure 2.14, the group velocity is $v_g = 6.4 \times 10^3$ m/sec.

The strong electric field of the effector probe not only enhances the drift wave, but results in heating of the plasma. The large amplitude, low frequency electric field of the probe accelerates electrons back and forth along magnetic field lines to heat the plasma (Kruer et al. 1972). The enhanced turbulence level of the plasma due to the strong coupling between drift wave and effector signal also produced turbulent heating of the plasma (Elagin et al. 1975 and Hamberger et al. 1972) with energy from the external oscillator cascading upward in k space. Although the effector signal is an effective method for heating a turbulent plasma, the enhanced turbulence level increases the radial transport in the discharge and lowers the plasma density. Even when accounting for the reduced discharge current in Run APS-3, the number density is decreased significantly from the number density in Run APS-1. The lower plasma density and reduced current in Run APS-3 not only indicate an increase in radial transport losses, but also an increase in the plasma resistivity, which is a function of the electron-ion and electron-neutral collision frequencies.

In addition to enhancing the drift wave, the application of the effector signal exhibits entrainment of the drift wave. The external oscillator could be detuned by as much as 20% in frequency from the self excited fundamental frequency, yet maintain coupling and pull the drift wave mode to the frequency of the oscillator. Excessive detuning decouples the external oscillator and returns the turbulent spectrum to its self-excited state unless an excessively large signal was used on the probe.

Figure 2.16 shows the power spectrum of potential fluctuations for a self-excited plasma (Run AQE-1) and the same plasma with a 1 kV_{pp}, 90 kHz signal on the effector probe (Run AQE-3). Table 2.3 lists the plasma conditions for the two cases. The spectrum of potential fluctuations for Run AQE-1 in Figure 2.16 has a well defined spectral index of 3.5 for a decade and a half in frequency. The power spectrum for Run AQE-3 illustrates the distinct step due to an energy input. The spectral index for Run AQE-1 and Run AQE-3 indicate little change in the dissipation and coupling process for the enhanced level of turbulence.

The previous examples illustrate some of the characteristics of a turbulent plasma in the Penning discharge and the effects of external perturbation of the plasma parameters that drive the self excited turbulence. This can be a serious problem for diagnostics when a radial or axial probe perturbs the plasma excessively. The plasma is often marginally macroscopically stable, and the introduction of a probe causes the plasma to change modes. The use of multiple anodes or a long anode

RUN AQE-1
Potential
Fluctuations
R = 6 cm.

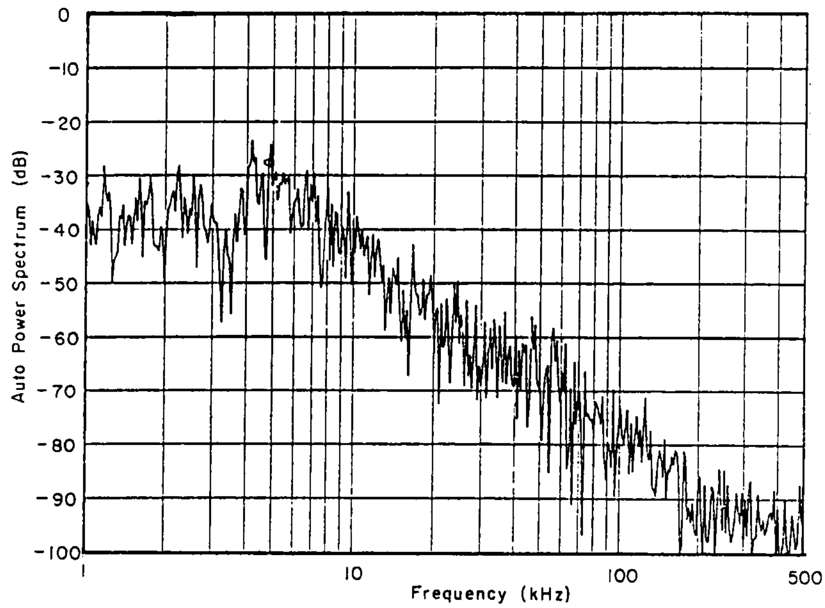

RUN AQE-3
Potential
Fluctuations
R = 6 cm.

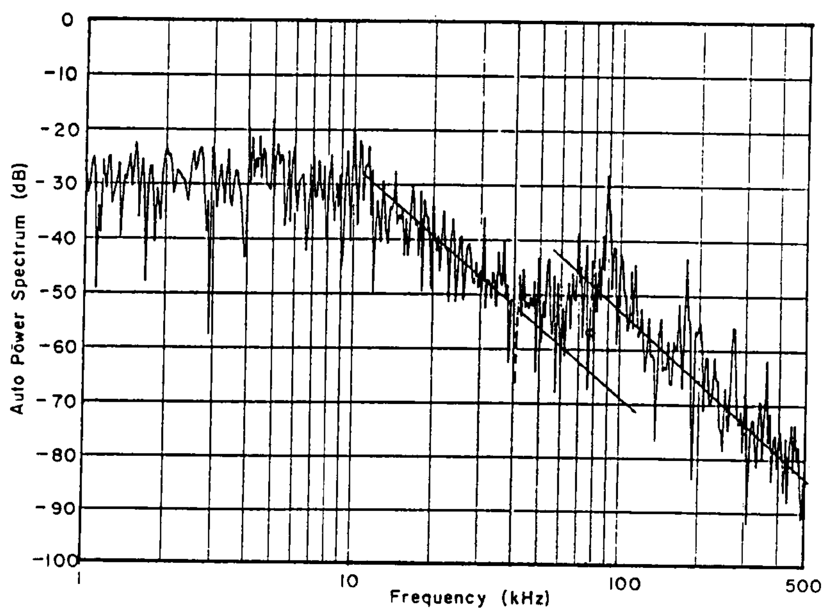

Figure 2.16. Potential fluctuations for a self excited plasma (Run AQE-1) and a plasma with external forcing (Run AQE-3) on the effector probe.

TABLE 2.3

PLASMA PARAMETERS FOR EXPERIMENTAL RUNS AQE-1 AND AQE-3 ON THE MODIFIED PENNING DISCHARGE (FIGURE 2.4)

Parameter	Symbol	Run AQE-1	Run AQE-3	Units
Anode Voltage	V_A	3000	3100	volts
Anode Current	I_A	30	28	mA
He Gas Pressure	P_{He}	300	286	microtorr
Magnetic Field (min)	B_0	0.026	0.026	Tesla
Number Density	$\overline{n}_e$	4.8×10^9	5.9×10^9	#/cm^3
Effector Probe:		Off	On	
Effector Signal	90kHz, 1kV$_{pl}$, 5 mA			
Spectral Index		3.5	4.3	$f < 90$ kHz
			4.5	$f > 90$ kHz

cylinder partially alleviates this problem. The most successful method of generating a plasma, that was insensitive to radial probes, was to use a coaxial geometry. The discharge shown in Figure 2.2 was fitted with a concentric coaxial cathode 1.3 cm in diameter. In this configuration the center cathode would draw approximately one half the discharge current.

Figure 2.17 illustrates the power spectra of electrostatic potential fluctuations of a plasma generated by the discharge described above for a self excited plasma (Run ASB-1) and the same plasma with symmetric forcing on the anode at 2.2 kHz (Run ASD-2). Table 2.4 lists the plasma parameters for these plasmas. In this case, a low frequency signal is used to damp part of the turbulent spectrum and increase the plasma density.

Figure 2.18 shows the phase spectra for Runs ASB-1 and ASD-2 from two probes displaced azimuthally 180°. The spectrum for Run ASB-1 has a well defined group velocity of $v_g = 3.2 \times 10^3$ m/sec for the self excited drift mode. The phase spectrum or Run ASD-2 shows the random phase of incoherent fluctuations except near the forcing frequency at 2.2 kHz. This spectrum also illustrates how two capacitive probes can have phase error between them.

Figures 2.19 and 2.20 illustrate the normalized radial profiles of electron number density, electron temperature and floating potential for the two plasmas. Clearly the drift wave corresponding to the frequency peak around 70 kHz in the power spectrum for Run ASB-1 in Figure 2.17 corresponds to a density driven drift wave. Using Equation (2.10) and the density gradient in Figure 2.19 yields an electron diamagnetic drift of $V_{de} = 2.5 \times 10^3$ m/sec. The discrepancy with the measured group velocity of $v_g = 3.2 \times 10^3$ m/sec from the phase spectrum can be partially

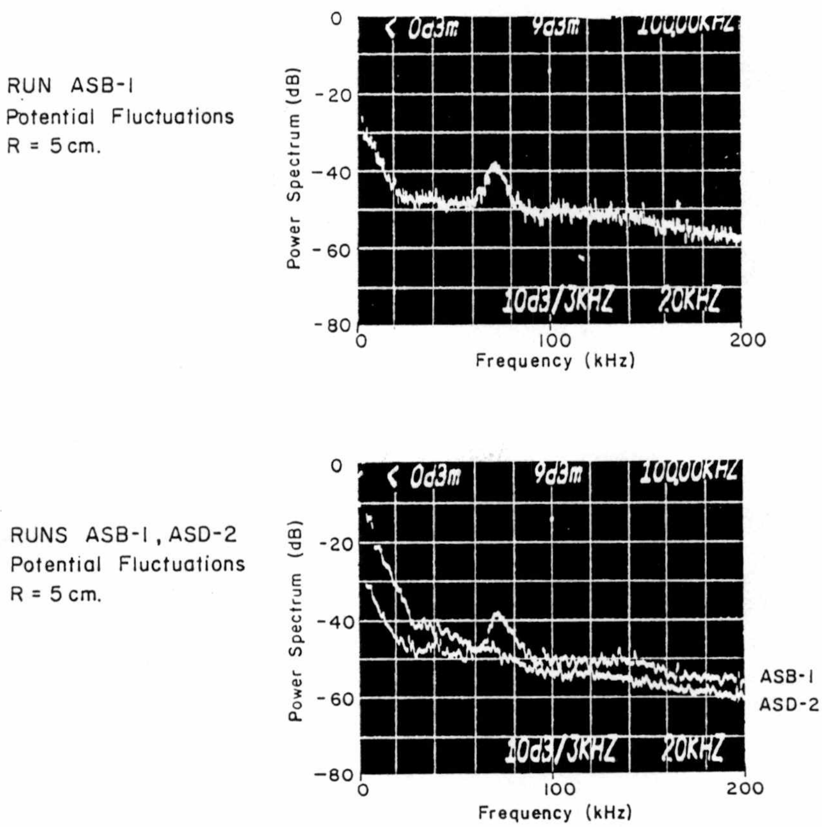

Figure 2.17. Power spectra for low frequency self excited potential fluctuations (Run ASB-1) and with external forcing on the anode cylinder (Run ASD-2).

TABLE 2.4

PLASMA PARAMETERS FOR EXPERIMENTAL RUNS ASB-1 AND ASD-2
FOR UNIFORM PENNING DISCHARGE FITTED WITH COAXIAL CATHODE (FIGURE 2.4)

Parameter	Symbol	Run ASB-1	Run ASD-2	Units
Anode Voltage	V_A	1750	1700	volts
Anode Current	I_A	70	73	mA
He Gas Pressure	P_{He}	1000	940	microtorr
Magnetic Field	B_0	0.14	0.14	Tesla
Number Density*	n_e	4.7×10^8	5.5×10^8	$\#/cm^3$
Electron Temperature*	T_e	23	230	eV
External Forcing (symmetrical)		Off	On	
Forcing Signal	2.2kHz, 1.6kV$_{pp}$, 20-30 mA			

*Radially averaged.

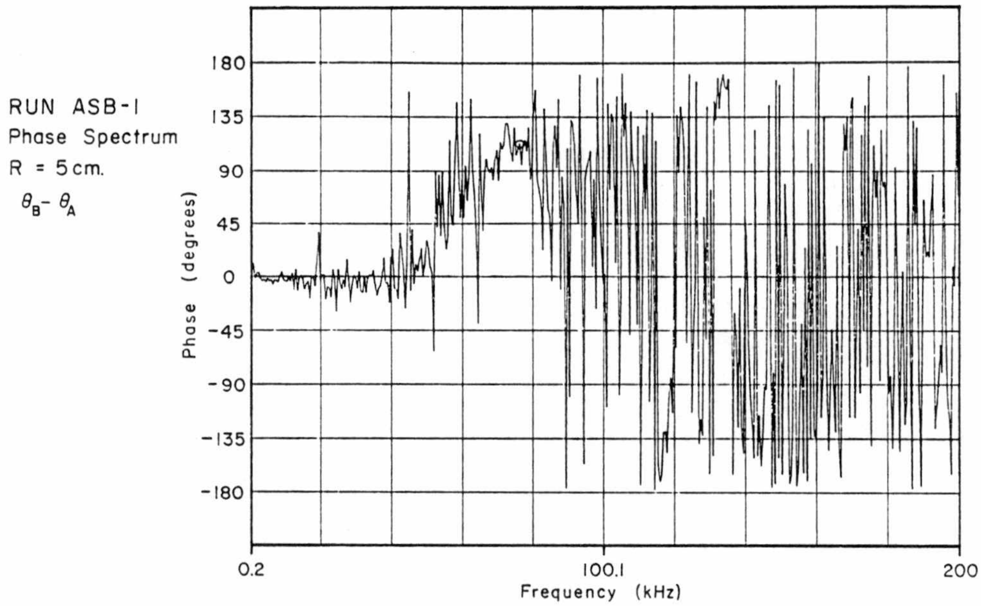

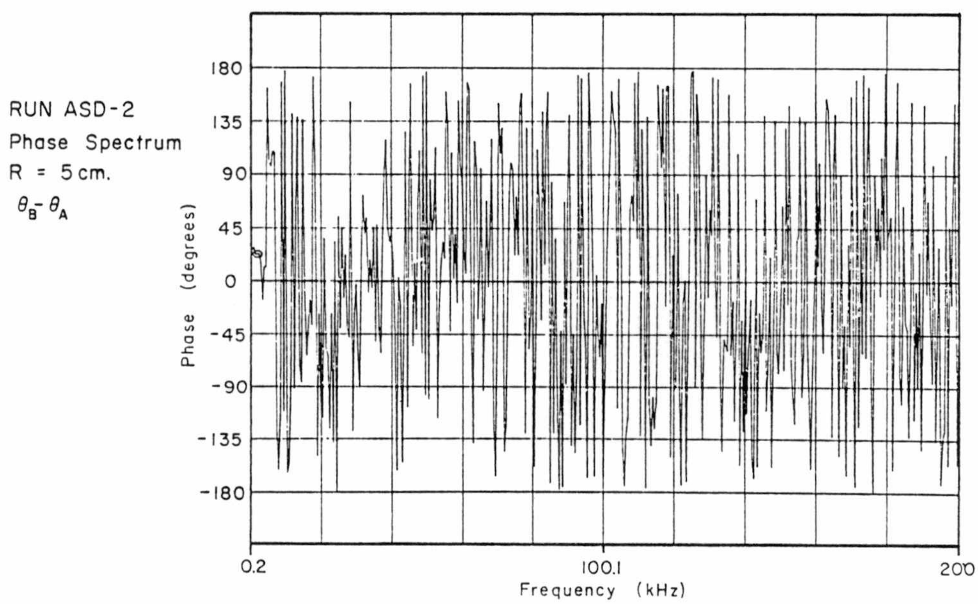

Figure 2.18. Phase spectrum for Runs ASB-1 and ASD-2.

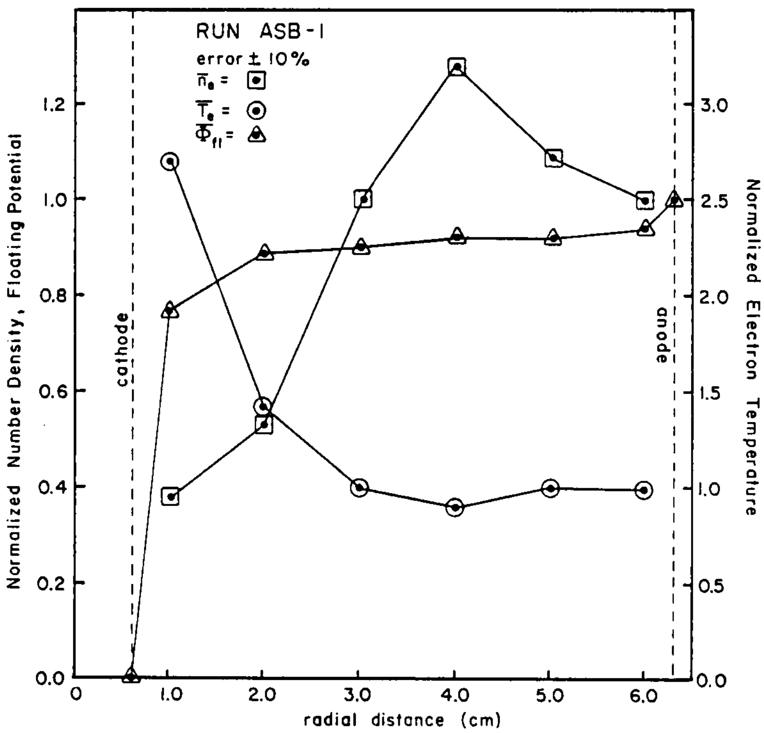

Figure 2.19. Radial profiles of normalized electron number density, electron temperature and plasma floating potential for Run ASB-1.

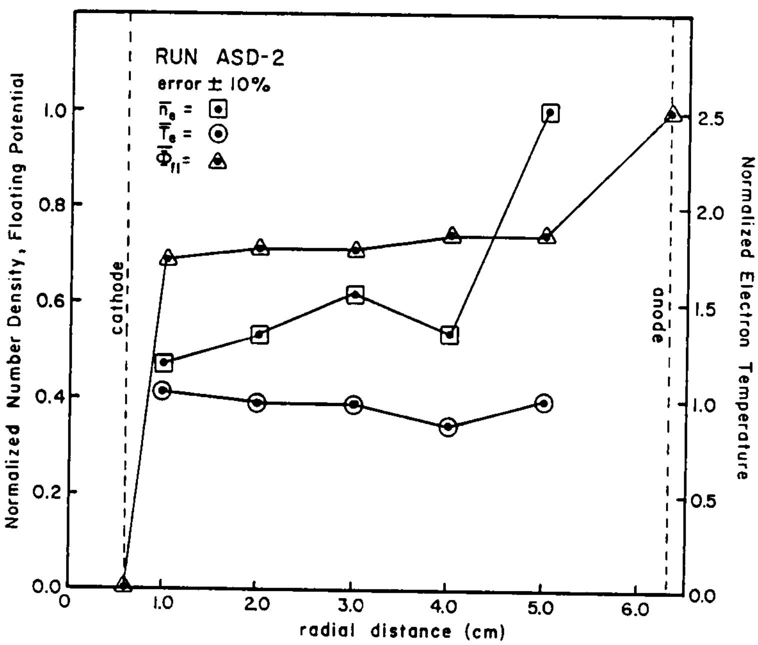

Figure 2.20. Radial profile of normalized electron number density, electron temperature and plasma floating potential for Run ASD-2.

accounted for by the addition of an $E \times B$ drift at $R = 5$ cm of $V_{E \times B} = 260$ m/sec. This mode is damped in Run ASD-2 primarily by a change in the radial profile of the electron number density and floating potential. Although data are missing for $R = 6$ cm in Figure 2.20 due to the strong fluctuations near the anode, the drift velocities due to number density and floating potential gradients tend to cancel each other for an electron drift wave.

Figure 2.21 illustrates a second example of damping of the turbulent spectrum of potential fluctuations in the coaxial discharge. Figure 2.21 shows the spectra of potential fluctuations of the self excited plasma (Run ASI-1) at various radial positions and for the plasma with external forcing (Run ASJ-1). Table 2.5 lists the plasma parameters for the two cases. Figure 2.22 shows the phase space plots of the potential fluctuations and its time derivative for the two plasmas, and the waveform of the external signal. The derivative of the potential fluctuation signal was generated by using a single pole high pass filter. The limit cycle behavior for Run ASI-1 is due primarily to the drift mode near 10 kHz.

Figure 2.23 illustrates the power spectra of potential fluctuations on a log frequency axis for Runs ASI-1 and ASJ-1. Figure 2.24 illustrates the phase spectra for the two plasmas. Figures 2.25 and 2.26 show the normalized radial profiles of electron number density, electron temperature and plasma floating potential for the two plasmas.

The previous examples indicate enhancement of electron collisionality, but were not performed on discharge geometries suitable for measurement of electron collisionality by electron cyclotron resonance absorption. The nonuniform magnetic field of the modified Penning discharge complicates the analysis of ECR absorption.

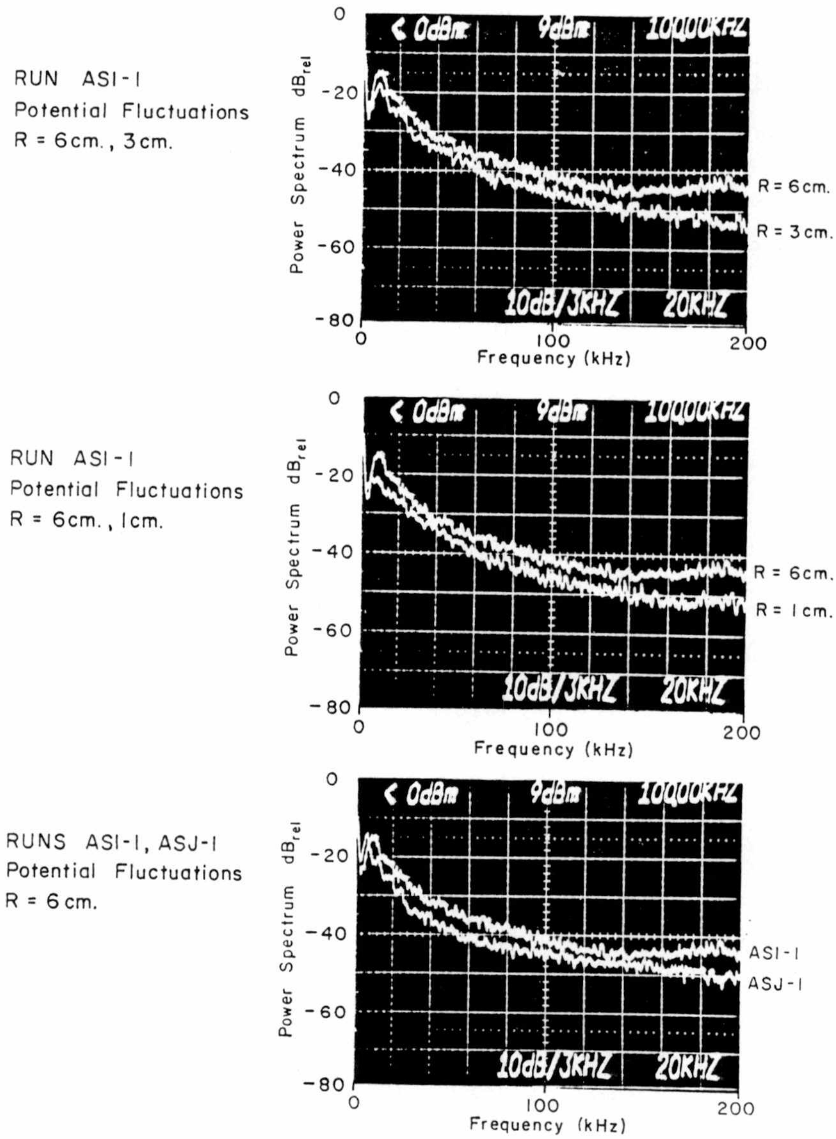

Figure 2.21. Power spectra of potential fluctuations at three radial positions for the self-excited plasma ASI-1 and at the edge for a plasma with external forcing, Run ASJ-1.

TABLE 2.5

PLASMA PARAMETERS FOR EXPERIMENTAL RUNS ASI-1 AND ASJ-1
FOR THE UNIFORM PENNING DISCHARGE WITH COAXIAL CATHODE (FIGURE 2.2)

Parameter	Symbol	Run		Units
		ASI-1	ASJ-1	
Anode Voltage	V_A	3150	3100	volts
Anode Current	I_A	67	79	mA
He Gas Pressure	P_{He}	222	225	microtorr
Magnetic Field	B_0	0.12	0.12	Tesla
Number Density*	n_e	8.5×10^8	8.7×10^8	#/cm^3
Electron Temperature*	T_e	160	225	ev
External Forcing (symmetrical)		Off	On	
Forcing Signal	6.2kHz, 1.5kV$_{pp}$, 20-30 mA			

*At $R = 6$ cm

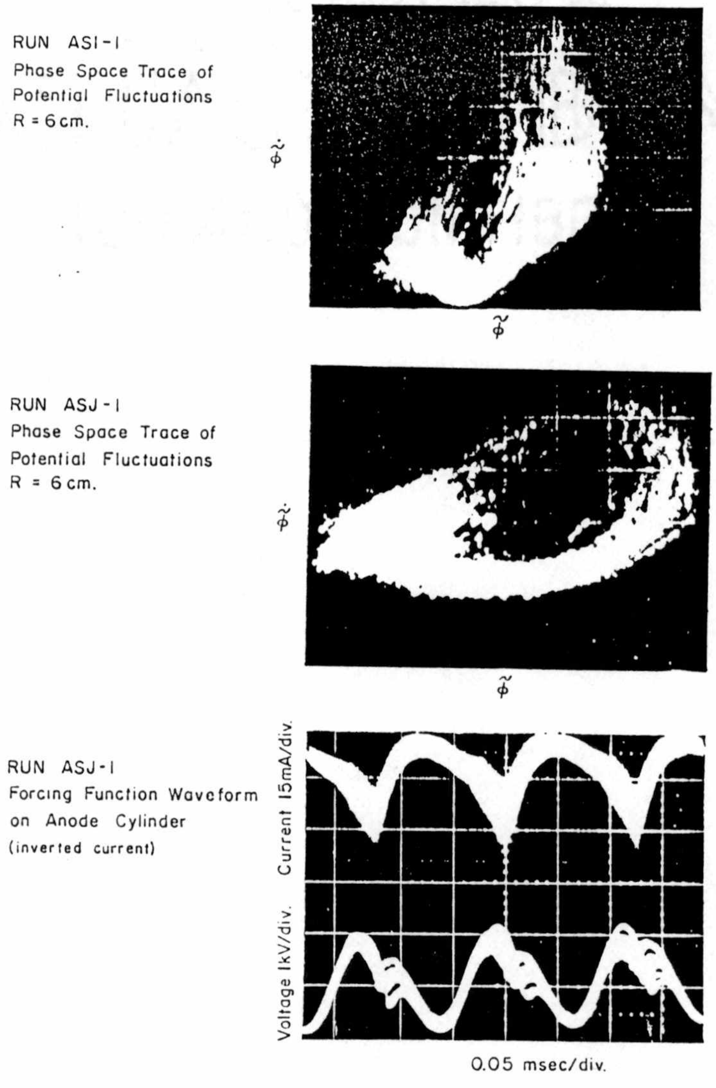

Figure 2.22. Phase space traces of electrostatic potential fluctuations for Runs ASI-1 and ASJ-1 and forcing function wave forms for Run ASJ-1.

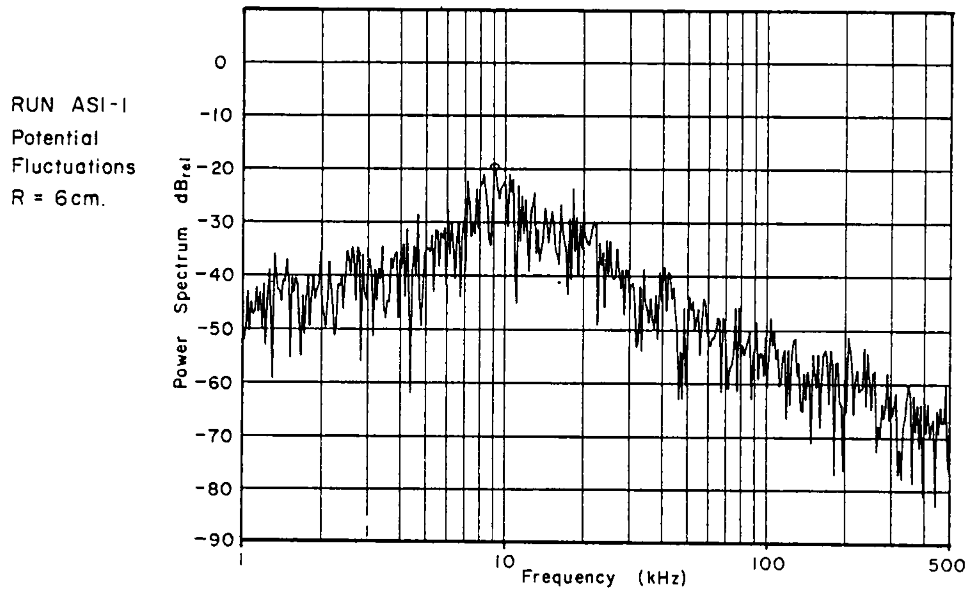

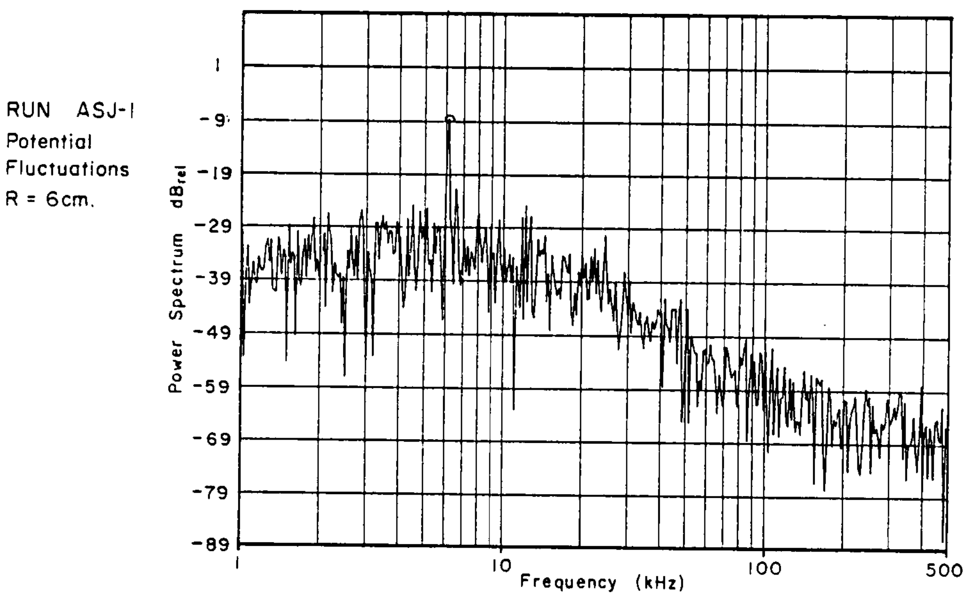

Figure 2.23. Power spectra of potential fluctuations on log frequency axis for Runs ASI-1 and ASJ-1.

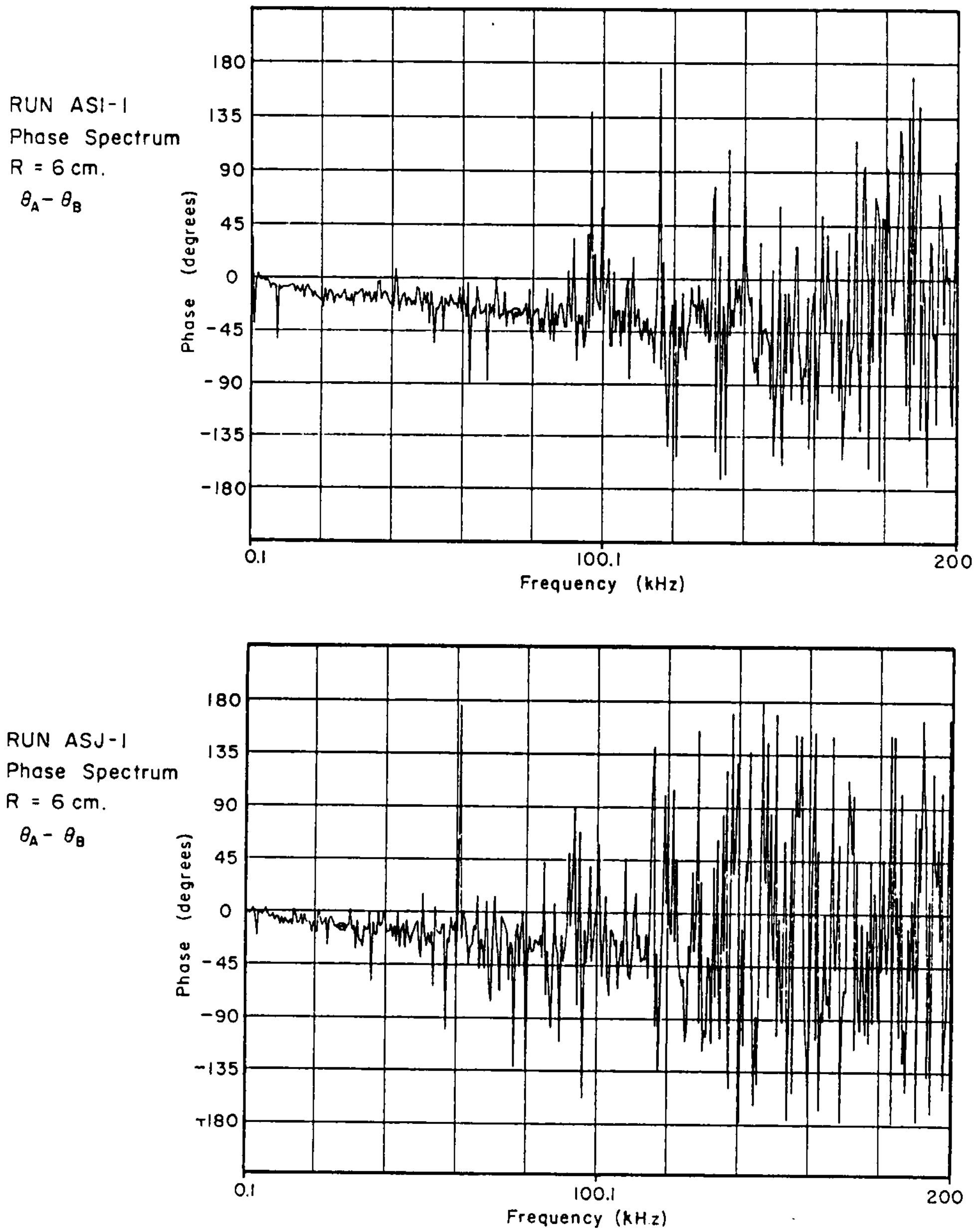

Figure 2.24. Phase spectra for Runs ASI-1 and ASJ-1 with capacitive probes displaced azimuthally 90°.

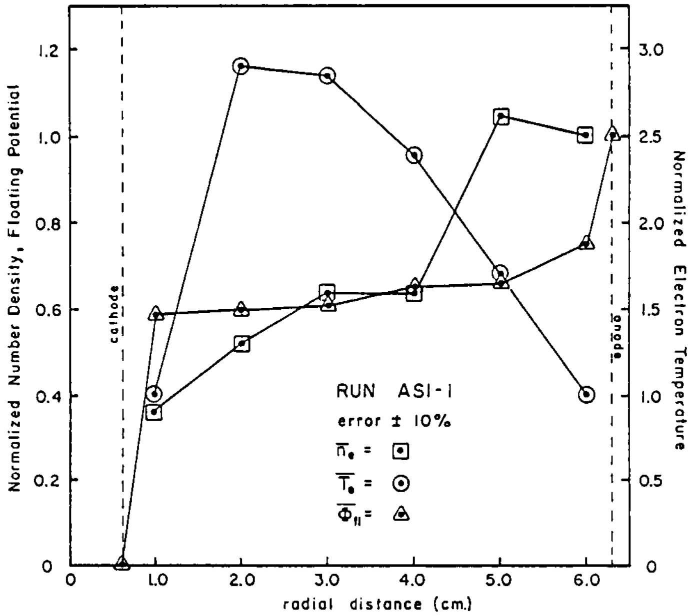

Figure 2.25. Normalized radial profilles of normalized electron number density, electron temperature and plasma floating potential for Run ASI-1.

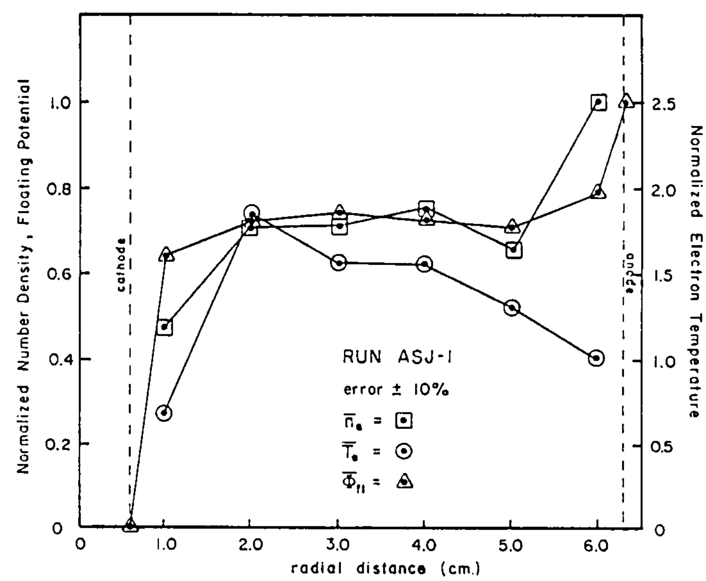

Figure 2.26. Normalized radial profiles of electron number density, electron temperature and plasma floating potential for Run ASJ-1.

The coaxial geometry used for Runs ASB-1, ASD-2, ASI-1 and ASJ-1 has unfavorable boundary conditions for launching a microwave beam across the plasma.

Using the geometry shown in Figure 2.2 without the coaxial cathode, microwave absorption near the electron gyrofrequency could be measured. Figure 2.27 illustrates the potential fluctuations and ECR absorption broadening for a self-excited turbulent plasma (Run AGE-1) and plasma with enhanced turbulence due to external forcing (Run AGE-2). Table 2.6 lists the plasma parameters for these plasmas. The ECR absorption curves are characterized by a frequency width $2\Delta f$ measured $3dB$ above maximum attenuation. This width will be shown in Chapter IV to be a function of the effective collision frequency of electrons.

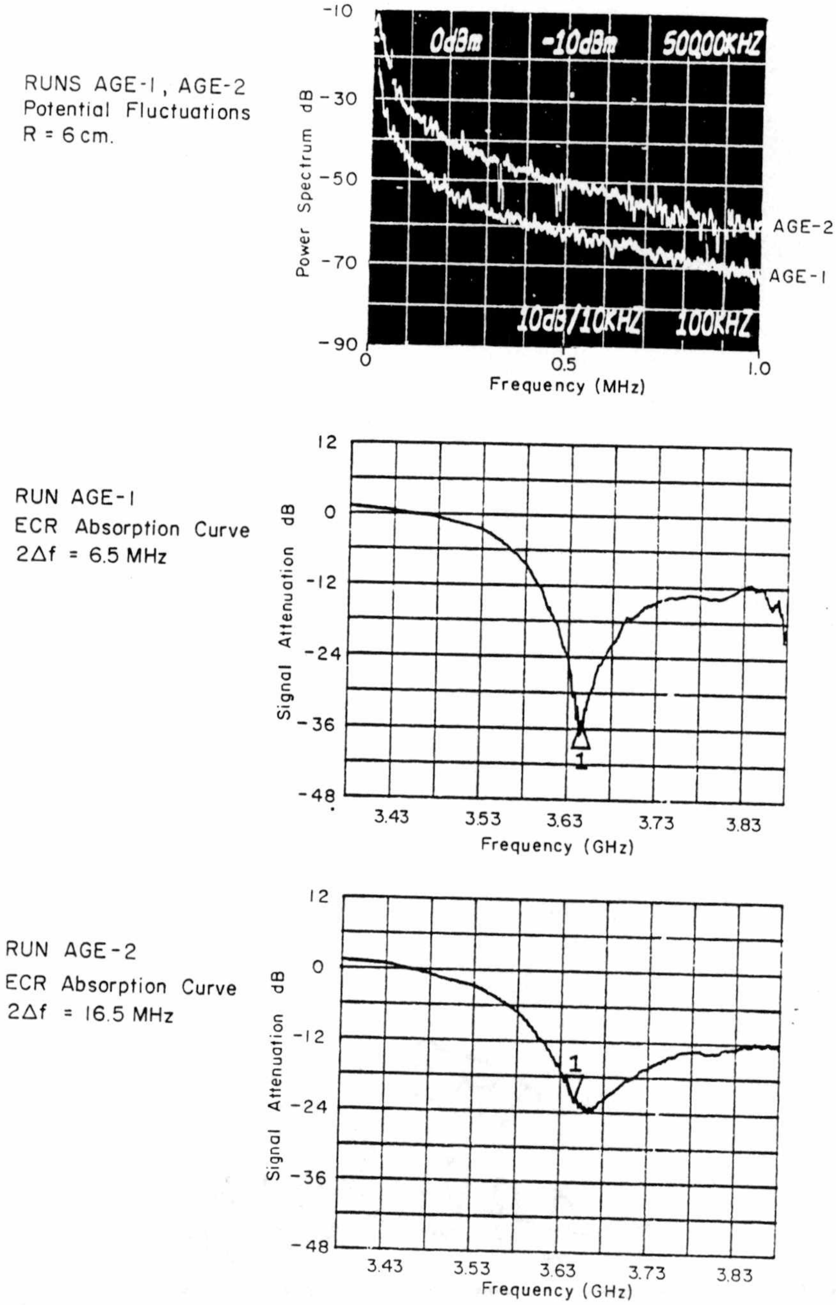

Figure 2.27. Power spectra of electrostatic potential fluctuations and electron cyclotron resonance absorption curves for a self excited turbulent plasma (Run AGE-1) and a plasma with enhanced turbulence (Run AGE-2).

TABLE 2.6

PLASMA PARAMETERS FOR EXPERIMENTAL RUNS AGE-1 AND AGE-2 FOR THE UNIFORM PENNING DISCHARGE (FIGURE 2.2)

Parameter	Symbol	Run		Units
		AGE-1	AGE-2	
Anode Voltage	V_A	2700	2650	volts
Anode Current	I_A	60	70	mA
He Gas Pressure	P_{He}	570	570	microtorr
Magnetic Field	B_0	0.18	0.18	Tesla
Number Density*	n_e	1.0×10^9	1.0×10^9	$\#/cm^3$
Electron Temperature*	T_e	73	230	ev
External Forcing (symmetrical)		Off	On	
Forcing Signal	500kHz, 2kV$_{pp}$, 5-10 mA			
ECR Broadening	$2\Delta f$	6.5	16.5	MHz

*At $R = 6$ cm

CHAPTER III

COLLISIONAL PROCESSES AND THE RESISTIVE DRIFT INSTABILITY IN THE WEAKLY IONIZED PENNING DISCHARGE PLASMA

Introduction.

The Penning discharge plasma presented in Chapter II is characterized as weakly ionized and inhomogeneous. The boundary conditions of the discharge and inhomogeneous nature of the plasma can produce non-Maxwellian particle distributions for both electrons and ions particularly at neutral gas pressures above 10^{-4} torr. These non-equilibrium distributions result in the onset of a variety of instabilities and ultimately a state of turbulent electrostatic fluctuations.

Several collisional and energy exchange mechanisms exist that can relax the non equilibrium plasma of the Penning discharge. For the weakly non-equilibrium plasma, such binary collision processes as electron-neutral, ion-neutral, and ionizing collisions dominate. It is probable that as the plasma becomes more non-Maxwellian, the amplitude of turbulent fluctuations grows and particles begin to interact strongly with the electrostatic fluctuations of the plasma. Relaxation mechanisms involving wave-particle, wave-wave and wave-particle-wave interactions will grow and add to the relaxation caused by binary collision processes. The interaction of particles with turbulent fluctuations and the resulting relaxation or thermalizing process leads to the introduction of a turbulent or effective collision frequency. The total collision frequency for a given species will be the sum of its binary collision frequencies with other particles and its turbulent collision frequency due to interaction with electromagnetic fluctuations within the plasma:

$$\nu_{tot} = \sum \nu_{bin} + \nu_{turb} \ . \tag{3.1}$$

Although shown as a scaler in Equation (2.1), the collision frequency for charged species in a magnetized plasma is a tensor quantity. Collisional processes parallel to the static background magnetic field in general differs from the collisional processes perpendicular to the static field.

Classical Collision Process.

Binary collisions will initially tend to relax the non-equilibrium distribution of a Penning discharge. For electrons these include electron-electron, electron-ion, electron-excited ion, electron-neutral and electron-excited neutral collisions. Only the last two may be significant in this plasma. Janev et. at. [1987] lists an excellent selection of cross section data for collision processes in hydrogen and helium plasma. Although some cross sections for electrons with excited helium ions are quite large, the dominant binary collision process for electrons in the weakly ionized Penning discharge plasma is the electron-neutral cross section.

Figure 3.1 shows the electron-neutral momentum collision frequency (Geller and Hosea 1968) as a function of background gas pressure and electron energy. For comparison with collisional broadening data in Chapter V, the curve in Figure 5.1 is averaged over a Maxwellian distribution. This is done by curve fitting Figure 5.1 (see Appendix F) and performing numerically the integral,

$$\langle \nu \rangle = 4\pi \left(\frac{m_e}{2\pi k T_e} \right)^{\frac{3}{2}} \int_0^\infty \nu(v) v^2 \ \exp\left(\frac{-v^2}{2v_{th}^2} \right) \ dv \ . \tag{3.2}$$

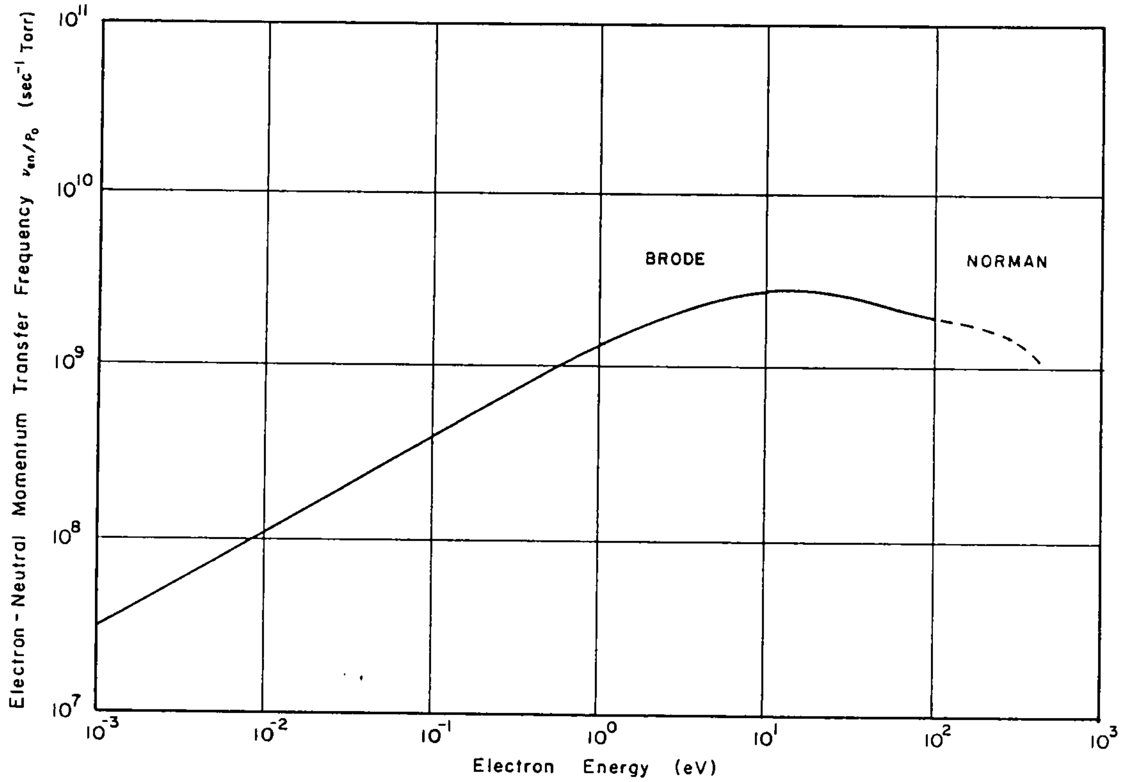

Figure 3.1. Electron-Neutral mometum transfer frequency as a function of electron energy and background gas pressure. Reproduced from Geller and Hosea [1977].

Turbulent Processes.

In a turbulent plasma, collisional and fluctuation processes are strongly related. Initially the presence of binary collisions, along with Landau damping, assist in saturating the exponential growth of linear instabilities. For stronger instabilities, such non-linear mechanisms as wave-wave interaction and wave-particle-wave interaction become important. In general these mechanisms tend to cascade wave energy upward in $\mathbf{k}$ and ω space to regions where energy is strongly dissipated by interparticle collisions and Landau damping. Hence the level of fluctuations in a turbulent plasma is ultimately determined by the mechanisms of electromagnetic energy coupling and dissipation in the plasma.

For the non equilibrium plasma dominated by drift wave instabilities and drift wave turbulence, at least three mechanisms will strongly contribute to the turbulent relaxation process.

1). The axial component of large amplitude coherent drift structures tends to accelerate electrons along the magnetic field. These accelerated electrons will exchange energy with the background plasma via three mechanisms.

A) Axially accelerated electrons will suffer binary collisions with other charged species and neutrals. For a weakly ionized plasma, electron-neutral collisions will dominate.

B) Electrons collectively accelerated will tend to excite beam-plasma instabilities. Accelerated electrons will lose energy in exciting electromagnetic waves. These waves can both radiate from the plasma and interact with other particles in the plasma. For electrons collectively accelerated to a velocity v_0 where $v_0 > c_s$ and c_s is the ion sound speed, ion-acoustic oscillations will be excited. Galeev and

Sagdeev [1969] derived an effective collision frequency for this process of the form

$$\nu_{eff} = w_{pe} \, \frac{W}{n_0 T_e} \; , \tag{3.3}$$

where W is the wave energy density of turbulent fluctuations. The derivation of this collision frequency is discussed later in this chapter and its scaling with experimental data from Penning discharge experiments is presented in Chapter V.

C) Electrons accelerated along field lines can be pitch angle or randomly scattered by the spectrum of background fluctuations. The collision frequency for this process was introduced by Horton and Choi [1974] in the form

$$\nu_{eff} = \frac{\pi}{4} \, v_e \int |\mathbf{k}| \, \frac{e^2 I(\mathbf{k})}{T_e^2} \, d\mathbf{k} \; , \tag{3.4}$$

where $I(\mathbf{k})$ is the spectrum of electrostatic fluctuations.

The electrons in process (B) are typically resonant particles in velocity space subject to the condition

$$\mathbf{k} \cdot \mathbf{v} = \omega_k \; , \tag{3.5}$$

which yields an irreversible process (Davidson 1976). The particles in process (C) suffer small changes and are non-resonant with the background fluctuations so that

$$(\mathbf{k} \cdot \mathbf{v} - \omega_k)^2 \gg \gamma_k^2 \; , \tag{3.6}$$

where γ_k is the wave's growth rate. This condition yields a reversible process.

2). A second relaxation mechanism due to dirft waves is produced by the transverse component of the electric field of a drift wave. This component induces $\mathbf{E} \times \mathbf{B}$ motion to both ions and electrons. Due to finite gyro radius effects (see Appendix G) the $\mathbf{E} \times \mathbf{B}$ motion of ions and electrons differs slightly.

Hence a polarization loss is produced as a fluid of electrons is swept through a fluid of ions.

3). A third mechanism which contributes to the relaxation of an inhomogeneous plasma with unstable dirft waves is the mode coupling of drift waves to cascade energy upward in ω and $\mathbf{k}$ space. Convective and $\mathbf{E} \times \mathbf{B}$ nonlinearities result in the formation of nonlinear waves (Horton 1984). These waves provide a mechanism for transporting energy from large scales. Coherent energy of large scale fluctuations is cascaded to small scale incoherent fluctuations which contribute to the pitch angle scattering collision process (C). This effect is investigated experimentally in Chapter V.

Beam Plasma Collision Frequency.

The effective electron-ion collision frequency for ion acoustic excitation (Equation (3.3)) was first derived by Galeev and Sagdeev [1969] in one of the original monographs on nonlinear plasma theory. Others have derived the same expression but relatively little work has been done to experimentally verify this result. Akama et. al. [1987] derived this result with corrections for a weakly inhomogeneous plasma using a variational approach. Shapiro and Sherchenko [1984] introduced the same expression with a small numerical factor for Langmuir turbulence, high frequency turbulence centered about w_{pe}.

Hamberger and Friedman [1968] performed some of the initial investigation into the scaling of plasma conductivity for a highly turbulent plasma. This work was performed on a non magnetized plasma and did not relate the spectrum or level of turbulent fluctuations to the observed conductivity. Manheimer and Flynn [1971] investigated the scaling of anomalous resistivity for a steady state turbulent plasma of unstable ion acoustic waves. Hamberg and Jancarik [1972] investigated the spectral distribution of weakly turbulent ion-sound waves and estimated the levels of fluctuation energy density from measured potential fluctuation spectra. Mase and Tsukishima [1975] were able to measure the level of turbulent ion-acoustic fluctuations with microwave scattering measurements and relate this to the effective collision frequency as measured by an RF probe method and a DC method. These authors were able to look at the scaling of ν_{eff} with the turbulent energy density W/n_eT_e.

Ion Acoustic Effective Collision Frequency.

The effective collision frequency for electrons which excite ion-acoustic turbulence was first derived by Galeev and Sagdeev [1969] using the conservation of momentum for the system of electron and wave. If electrons with a collective drift velocity V_d excite waves, these electrons will experience a mean momentum loss. This momentum loss can be expressed in terms of a frictional or viscous force F and an effective collision frequency ν_{eff} as

$$-F = \nu_{eff} m_e n_0 V_d \ . \tag{3.7}$$

If this momentum change is transfered to waves with wave energy density w, then the change in wave momentum is

$$\frac{\partial P_w}{\partial t} = \frac{1}{(2\pi)^3} \int_k \gamma_k^e \, W_k \, \frac{k}{w} \, d^3k \ . \tag{3.8}$$

The growth rate γ_k^e is the unstable wave's growth rate due to electrons. Equating the mean momentum loss of the drift motion of electrons to the momentum increase of the waves yields

$$\nu_{eff} = \frac{1}{2\pi^3 m_e n_0 V_d} \int_k \gamma_k^e \, W_k \, \frac{k}{w} \, d^3k \ . \tag{3.9}$$

For an electron drift velocity $V_d > V_s$ where V_s is the ion sound speed, the collective motion of electrons will excite ion-acoustic oscillations. These waves have a maximum growth rate of

$$\gamma_k^e \approx \frac{wV_d}{v_{th}} \tag{3.10}$$

in the region $k \sim \lambda_d^{-1}$. Making these substitutions in Equation (3.9) yields the relation

$$\nu_{eff} = \omega_{pe} \, \frac{W}{n_0 T_e K} \ . \tag{3.11}$$

The wave energy density W in Equation (3.11) is now the total wave energy density of excited waves in the region of k space with $k \approx \lambda_d^{-1}$. For the turbulent Penning discharge these waves are predominantly in the dissipative region of the spectrum. The scaling of ν_{eff} is Equation (3.9) is considered experimentally in Chapter V along with the measurement of W.

Simplified Resistive Drift Instability.

The two-fluid equations (Braginski 1965) are used to derive the dispersion relation for small amplitude waves of the resistive drift instability in the frequency range $\omega \ll \omega_{ci}$. This instability is characteristic of an inhomogeneous collisional plasma and for the cylindrical plasma, produces longitudinal waves which propagate essentially perpendicular to the static magnetic field. These waves have finite parallel wavelengths and are negative energy waves in that they tend to grow as they lose energy to the background plasma. In the linear fluid analysis, resistive drift waves have a growth rate proportional to the axial electron-ion collision frequency and a damping rate proportional to perpendicular ion viscosity.

The continuity and mometum equations of the two-fluid equations, neglecting particle source terms are given by

$$\frac{\partial n_j}{\partial t} + \nabla \cdot (n_j \mathbf{V}_j) = 0 \ , \tag{3.12}$$

and

$$m_j n_j \frac{d\mathbf{V}_j}{dt} = - \nabla \cdot \Pi_j - e_j n_j (\mathbf{E} + \mathbf{V}_j \times \mathbf{B}) - \nabla P_j + \mathbf{R}_j \ . \tag{3.13}$$

R_j is the frictional force and $j = e, i$ for electrons or ions. With thermal effects neglected, the frictional forces for electrons and ions are

$$\mathbf{R}_e = -m_e n_e \nu_{ei} \left(\frac{1}{2} \mathbf{U}_{||} + \mathbf{U}_{\perp} \right) - m_e n_e \nu_{en} \mathbf{V}_e \ , \tag{3.14}$$

and

$$\mathbf{R}_i = -m_i n_i \nu_{ie} \left(\frac{1}{2} \mathbf{U}_{||} + \mathbf{U}_{\perp} \right) - m_i n_i \nu_{in} \mathbf{V}_i \ , \tag{3.15}$$

where

$$\mathbf{U} = \mathbf{V}_e - \mathbf{V}_i \ . \tag{3.16}$$

For a constant magnetic field $\mathbf{B}$ in the $\hat{z}$ direction, the $\hat{z}$ component of the electron momentum equation with electron viscosity neglected, becomes

$$\frac{dV_{e||}}{dt} = \frac{-e}{m_e} E_{||} + \frac{1}{m_e n_e} \nabla_{||} P_e - \frac{\nu_{ei}}{2} \left(V_{e||} - V_{e||} \right) - \nu_{en} V_{e||} \ . \tag{3.17}$$

Taking $V_{e||} \gg V_{i||}$, expanding the convective derivative and neglecting temperature gradients, Equation (6.17) can be recast in the form of a wave equation

$$\frac{\partial V_{e_{||}}}{\partial t} + V_{e_{||}} \frac{\partial V_{e_{||}}}{\partial z} + \nu_e V_{e_{||}} + \frac{T_e}{m_e n_e} \frac{\partial n_e}{\partial z} - \frac{e}{m_e} \frac{\partial \phi}{\partial z} = 0 \; , \tag{3.18}$$

where

$$\nu_e = \nu_{ei} + \nu_{en} \tag{3.19}$$

and

$$E_{||} = -\frac{\partial \phi}{\partial z} \; . \tag{3.20}$$

If the last two terms of Equation (3.18) are considered small, a damped wave equation results,

$$\frac{\partial V_{e_{||}}}{\partial t} + V_{e_{||}} \frac{\partial V_{e_{||}}}{\partial z} + \nu_e \; V_{e_{||}} = 0 \; . \tag{3.21}$$

This equation can be solved in parametric form as an initial value problem by the method of characteristics (Whittam 1974). Although this section is concerned with the dispersion relation for small amplitude drift waves, the following illustrates why coherent drift modes with large axial wave numbers $k_{||}$ do not initially grow and attain large amplitudes.

In characteristic form Equation (3.20) becomes

$$\frac{dV_{e_{||}}}{dt} = -\nu_e \; V_{e_{||}} \; , \tag{3.22}$$

and

$$\frac{dz}{dt} = V_{e_{||}} \; . \tag{3.23}$$

The first characteristic can be integrated and combined with the second to yield

$$\frac{dz}{dt} = e^{-\nu_e t} f(\xi) \; , \tag{3.24}$$

where ξ is the characteristic variable. Using the initial condition $z = \xi$ at $t = 0$ allows Equation (3.24) to be integrated and yield the envelope,

$$z = \xi + \frac{1}{\nu_e} \left(1 - e^{-\nu_e t}\right) f(\xi) . \tag{3.25}$$

The condition for wave breaking, i.e. bunching of the axial flow of electrons, is given by setting the derivative of the envelope to zero at some finite time,

$$\frac{\partial z}{\partial \xi} = 1 + \frac{1}{\nu_e} \left(1 - e^{-\nu_e t}\right) \frac{\partial f}{\partial \xi} = 0 . \tag{3.26}$$

Since ν_e is always positive for electrons being accelerated above their thermal velocity, breaking can only occur for initial waves of sufficient negative slope,

$$\frac{\partial f}{\partial \xi} < -\nu_e . \tag{3.27}$$

Consider the $\hat{\mathbf{z}}$ component of the electron velocity as composed of a steady component and a fluctuating component of the form,

$$V_{e||} = V_{ez}^0 + \tilde{v}_z \, e^{i(k_{||} z - wt)} . \tag{3.28}$$

The breaking condition becomes

$$|k_{||} \tilde{v}_z| > \nu_e , \tag{3.29}$$

or

$$\lambda_{||} < \frac{2\pi \tilde{v}_z}{\nu_e} . \tag{3.30}$$

For $\nu_e \sim 2$ MHz and $\tilde{v} = (0.1)\ v_{th} = 2 \times 10^7$ cm/sec., Equation (3.30) yields wave breaking for

$$\lambda_{||} < 62 \text{ cm} ,$$

which is on the order of the length of the experimental device.

Equation (3.18) is essentially a damped wave equation with the forcing functions $\tilde{n}_e$ and $\tilde{\phi}$, with $\tilde{\phi}$ the potential fluctuation due to the drift wave. In general $\tilde{n}_e$ and $\tilde{\phi}$ will be out of phase due to ν_e. It is this phase difference that causes growth of the collisional drift wave and radial particle transport by the wave.

Now consider the drift motion of ions and electrons perpendicular to the static magnetic field. The ion and electron equations of motion with electron viscosity neglected are

$$m_e n_e \frac{d\mathbf{V}_{e\perp}}{dt} = -en_e \left(\mathbf{E}_\perp + \mathbf{V}_{e\perp} \times \mathbf{B}_0\right) - \nabla_\perp P_e + \mathbf{R}_\perp \ , \tag{3.31}$$

and

$$m_i n_i \frac{d\mathbf{V}_{i\perp}}{dt} = en_i \left(\mathbf{E}_\perp + \mathbf{V}_{i\perp} \times \mathbf{B}_0\right) - \nabla_\perp P_i - \nabla \cdot \overline{\overline{\Pi}}_i - \mathbf{R}_\perp \ . \tag{3.32}$$

Due to the large electron gyro frequency, the thermal effects in the frictional force $\mathbf{R}_\perp$ can be neglected so that

$$\mathbf{R}_\perp = -m_e n_e \nu_\perp \left(\mathbf{V}_{e\perp} - \mathbf{V}_{i\perp}\right) \ . \tag{3.33}$$

Here $\nu_\perp$ is the effective electron-ion collision frequency for motion perpendicular to the static magnetic field.

Adding Equations (3.31) and (3.32) and taking $\hat{z}\times$ the sum, yields the electron drift

$$\begin{aligned} V_{e\perp} = V_{i\perp} &- \frac{1}{eB_0}\ \hat{z} \times \left(\frac{\nabla_\perp P_e}{n_e} + \frac{\nabla_\perp P_i}{n_i}\right) + \frac{1}{en_iB_0}\ \hat{z} \times \nabla_\perp \cdot \overline{\overline{\Pi}} \\ &- \frac{1}{w_{bi}}\ \left(\delta\ \hat{z} \times \frac{dV_{e\perp}}{dt} + \hat{z} \times \frac{dV_{i\perp}}{dt}\right) \ , \end{aligned} \tag{3.34}$$

where $\delta = \frac{m_e}{m_i}$. By noting that the first two terms on the right hand side of Equation (3.34) dominate, and by using an iterative procedure (Hinton and Horton 1971), the electron drift velocity can be written as the sum of a zero order term and a smaller first order term,

$$\mathbf{V}_{e\perp} = \mathbf{V}^0_{e\perp} + \mathbf{V}^1_{e\perp} \ , \tag{3.35}$$

where

$$\mathbf{V}^0_{e\perp} = \mathbf{V}^0_{i\perp} - \frac{1}{eB_0} \ \hat{z} \times \left(\frac{\nabla_\perp P_e}{n_e} + \frac{\nabla_\perp P_i}{n_i} \right) \ , \tag{3.36}$$

and

$$\mathbf{V}^1_{e\perp} = \mathbf{V}^1_{i\perp} - \frac{1}{w_{bi}} \hat{z} \times \ \frac{d\mathbf{V}^0_{i\perp}}{dt} + \frac{1}{en_iB_0} \ \hat{z} \times \nabla_\perp \cdot \overline{\Pi}_i \ . \tag{3.37}$$

The convective derivative term for electron motion is of second order due to the small mass ratio δ and is neglected. The convective derivative and stress tensor in Equation (3.37) are defined using the zero order ion drift velocity.

Using the zero order electron drift velocity, the electrostatic approximation $\mathbf{E}_\perp = - \nabla_\perp \phi$, and taking $\hat{z}\times$ the ion momentum equation, allows the ion drift velocity to be written as

$$\mathbf{V}^0_{i\perp} = \frac{1}{B_0} \ \hat{z} \times \nabla_\perp \phi + \frac{1}{eB_0} \ \hat{z} \times \ \frac{\nabla_\perp P_i}{n_i} \ , \tag{3.38}$$

and

$$\begin{aligned} \mathbf{V}^1_{i\perp} = \frac{1}{w_i} \ \hat{z} \times \frac{d\mathbf{V}^0_{i\perp}}{dt} + \frac{1}{en_iB_0} \ \hat{z} \times \nabla_\perp \cdot \overline{\Pi}_0 \\ - \delta \ \frac{\nu_\perp}{w_{bi}} \ \hat{z} \times \left(\mathbf{V}^0_{e\perp} - \mathbf{V}^0_{i\perp} \right) \ . \end{aligned} \tag{3.39}$$

In order for the last term in Equation (3.39) to be of first order, the perpendicular collision frequency $\nu_\perp$ must be large enough so that

$$\frac{w}{\nu_\perp} \simeq \delta \ . \tag{3.40}$$

Using these results, the zero and first order electron drift velocity become

$$V_{e\perp}^0 = \frac{1}{B_0}\,\hat{z}\times\nabla_\perp\phi - \frac{1}{eB_0}\,\hat{z}\times\frac{\nabla P_e}{n_e}\,, \tag{3.41}$$

and

$$V_{e\perp}^1 = -\delta\,\frac{\nu_\perp}{w_{bi}}\,\hat{z}\times\left(V_{e\perp}^0 - V_{i\perp}^0\right)\,. \tag{3.42}$$

The zero order electron and ion drift velocities are composed of the $\mathbf{E}\times\mathbf{B}$ drift and the diamagnetic drift velocities discussed earlier in Chapter II. It is at this point that the effects of finite ion gyro radius are introduced. This effect is discussed in Appendix G and is not inherent to the two–fluid equations: however, it becomes important in the last term of Equation (3.39). Equation (3.38) becomes

$$V_{i\perp}^0 = \frac{\beta}{B_0}\,\hat{z}\times\nabla_\perp\phi + \frac{1}{eB_0}\,\hat{z}\times\frac{\nabla P_i}{n_i} \tag{3.43}$$

and β takes a different form depending on the form of $\nabla_\perp\phi$.

The effects of a temperature gradient on the pressure gradient of the diamagnetic drifts can be partially considered by introducing the following scale lengths defined for static variables;

$$\frac{1}{r_n} = \frac{1}{n}\,\frac{dn}{dr}\,, \quad \frac{1}{r_T} = \frac{1}{T}\,\frac{dT}{dr}\,. \tag{3.44}$$

The perpendicular gradient for the static pressure field becomes

$$\frac{\nabla_\perp P}{n} = (1+\eta)\,\frac{T}{n}\cdot\nabla_\perp n\,, \tag{3.45}$$

where $\eta = \frac{r_n}{r_T}$ and is defined for either electron or ion pressure.

By using the definitions of thermal velocity and ion gyro radius, and rescaling the potential as

$$\Phi = \frac{e\phi}{KT_e} \tag{3.46}$$

with T_e a constant, the zero order electron and ion drift velocities can be written

$$V_{i\perp}^0 = v_i\rho_i \; \hat{z} \times \nabla_\perp \Psi_i \; , \tag{3.47}$$

and

$$V_{e\perp}^0 = \alpha v_i\rho_i \; \hat{z} \times \nabla_\perp \Psi_e \; , \tag{3.48}$$

where

$$\nabla_\perp \Psi_i = \alpha\beta \, \nabla_\perp \, \Phi + (1+\eta_i) \, \nabla_\perp \, Ln(n_i) \; , \tag{3.49}$$

and

$$\nabla_\perp \Psi_e = \nabla_\perp \Phi - (1+\eta_e) \, \nabla_\perp \, Ln(n_e) \; , \tag{3.50}$$

with $\alpha = \frac{T_e}{T_i}$.

Using Equation (3.47) and neglecting pressure gradients in the viscous dominated stress tensor, the convective derivative and stress tensor terms of the first order ion drift velocity can be written,

$$\frac{1}{w_{bi}} \; \hat{z} \times \frac{dV_{i\perp}^0}{dt} = \rho_i^2 \left[- \nabla_\perp \, \dot{\Psi}_i + \rho_i \; v_i \hat{z} \times \nabla_\perp \Psi_i \cdot \nabla_\perp (\nabla_\perp \Psi_i) \right] \; , \tag{3.51}$$

and

$$\frac{1}{eB_0 n_i} \; \hat{z} \times \nabla_\perp \cdot \overline{\Pi}_0 \approx \frac{1}{4} \; \nu_{ii} \rho_i^4 \; \nabla_\perp^2 \left(\nabla_\perp \Psi_i \right) \; . \tag{3.52}$$

Using Equations (3.45) and (3.50) and the results in Equations (3.51) and (3.52), the ion and electron drift velocities can be written

$$\mathbf{V}_i = v_i\rho_i \ \hat{z} \times \nabla_\perp\Psi_i + \rho_i^2[- \nabla_\perp \dot{\Psi}_i + \rho_i v_i \ \hat{z} \times \nabla_\perp\Psi_i \cdot \nabla_\perp(\nabla_\perp\Psi_i)$$
$$+ \frac{1}{4} \ \nu_{ii}\rho_i^2 \ \nabla_\perp^2 \left(\nabla_\perp\Psi_i\right) - \delta\nu_\perp(\nabla_\perp\Psi_e - \nabla_\perp\Psi_i)] + \mathbf{V}_{iz} \ , \tag{3.53}$$

and

$$\mathbf{V}_e = \alpha v_i\rho_i \ \hat{z} \times \nabla_\perp\Psi_e - \rho_i^2\delta\nu_\perp(\nabla_\perp\Psi_e - \nabla_\perp\Psi_i)] + \mathbf{V}_{ez} \ . \tag{3.54}$$

The results in Equation (3.53) and (3.54) can be combined with the electron and ion continuity equations to determine the linear dispersion relation for initially unstable drift waves. Using a normal mode analysis for cartesian geometry and allowing density, potential, and $\hat{z}$ velocity to vary as

$$n(r,t) = n(x) + \tilde{n} \ \exp i(\mathbf{k} \cdot \mathbf{r} - \omega t) \ , \tag{3.55}$$

$$\Phi(r,t) = \tilde{\Phi} \ \exp i(\mathbf{k} \cdot \mathbf{r} - \omega t) \ , \tag{3.56}$$

and

$$v_z(r,t) = \tilde{v}_z \ \exp i(\mathbf{k} \cdot \mathbf{r} - \omega t) \ , \tag{3.57}$$

Equations (3.53) and (3.54) are inserted into the ion and electron continuity equations and linearized. Equating electron and ion density fluctuations then yields the dispersion relation for drift waves.

Using Equations (3.55) and (3.56) in the $\hat{z}$ momentum equations for electrons and ions yields

$$\tilde{v}_{ez} = -\frac{k_z v_{th}^2 \left(\tilde{\Phi} - \frac{\tilde{n}_e}{n}\right)}{\omega - i\nu_e} \ , \tag{3.58}$$

and

$$\tilde{v}_{iz} = -\frac{k_z v_s^2}{\omega}\ \frac{\tilde{n}_i}{n}\ . \tag{3.59}$$

Substituting Equation (3.58) into Equation (3.54) and substituting Equation (3.59) into Equation (3.53), neglecting the second order electron velocity, and then using the electron and ion continuity equations and linearizing, yields the density fluctuations

$$\frac{\tilde{n}_e}{n} = \tilde{\Phi}\ \frac{\omega_e^* - \frac{k_z^2 v_{th}^2}{\omega + i\nu_e}}{\omega - (1+\eta_e)\omega_e^* - \frac{k_z v_{th}^2}{\omega + i\nu_e}}\ , \tag{3.60}$$

and

$$\frac{\tilde{n}_i}{n} =$$

$$\beta\tilde{\Phi}\ \frac{\omega_e^* - \omega(\alpha c_2 + i\alpha c_1) - \frac{v_i}{r_n}\alpha c_3 - \nu_{ii}\left(i\alpha c_4 + \frac{1}{4}\ \frac{k_x^3\rho_i^4}{r_n}\right)}{\omega(1 + i(1+\eta_i)c_2) + (1+\eta_i)\nu_{ii}(c_3 + i\ c_4) + (1+\eta_i)^2\frac{\nu_i}{r_n}c_3 + \frac{k_z^2 v_s^2}{\omega}}\ , \tag{3.61}$$

where

$$\omega_e^* = -\frac{T_e}{eB_0}\ \frac{1}{n}\ \frac{\partial n}{\partial x}\ , \tag{3.62}$$

$$c_1 = \rho_i^2\ \frac{k_x}{r_n}\ , \tag{3.63}$$

$$c_2 = \rho_i^2(k_x^2 + k_y^2)\ , \tag{3.64}$$

$$c_3 = \rho_i^3(k_x^2 k_y + k_x k_y^2)\ , \tag{3.65}$$

$$c_4 = \frac{1}{4}\ \rho_i^4(k_x^4 + k_y^4)\ , \tag{3.66}$$

and

$$c_5 = \frac{1}{4}\ (1+\eta_i)\rho_i^4\ \frac{k_x^3}{r_n}\ . \tag{3.67}$$

In deriving Equations (3.60) and (3.61), only first order derivatives of the background density $n(x)$ are retained.

Equating Equations (3.60) and (3.61) for $\tilde{n}_e = \tilde{n}_i$, yields a quartic equation in ω. For low frequency oscillations of order $|\omega| \approx |\omega_e^*|$, where $\omega_e^* \ll \nu_e$, and of long wavelengths so that $k\rho_i \tilde{<} 1$, and driven by weak gradients with $\eta_e \approx \eta_i$, this quartic reduces to a cubic approximately given by,

$$
\begin{aligned}
&-\omega^3 \alpha\beta\rho_i^2 \left[k_i^2 + i\,\frac{k_x}{r_n}\right] \\
&+\omega^2 \Bigg[\alpha\beta\nu_e\rho_i^2\,\frac{k_x}{r_\perp} + \omega_e^*\left(1+\eta+\beta+2(1+\eta)\rho_i^2\,k_\perp^2\right) \\
&\qquad -i\left(\alpha\beta\nu_e\rho_i^2\,k_\perp^2 + \alpha\beta(1+\eta)\omega_e^*\,\rho_i^2\,\frac{k_x}{r_\perp}\right)\Bigg] \\
&-\omega\Bigg[\beta(1+\eta)\omega_e^* + \alpha\beta(1+\eta)\omega_e^*\,\nu_e\,\rho_i^2\,k_\perp^2 + \left(1+(1+\eta+\alpha\beta)\rho_i^2\,k_\perp^2\right)k_z^2\,v_{th}^2 \\
&\qquad +i\left(\frac{\alpha\beta}{4}\,\nu_e\nu_i\rho_i^4\,\frac{k_x^3}{r_n} + \alpha\beta k_z^2\,v_{th}^2\,\rho_i^2\,\frac{k_x}{r_n} - \frac{1}{4}\,(1+\eta+\alpha\beta)\omega_e^*\nu_i\rho_i^4(k_x^4+k_y^4)\right)\Bigg] \\
&+\Bigg[-\beta\omega_e^*\,k_z^2\,v_{th}^2 + (1+\eta)\omega_e^*\,k_z^2\,v_5^2 + 2\alpha\beta(1+\eta)k_z^2\,v_{th}^2\,\frac{v_i}{r_n}\,\rho_i^3\,k_{xy}^3 \\
&-i\left(\beta(1+\eta)\nu_e\omega_e^* + \nu_e\,k_z^2\,v_5^2 - 2\alpha\beta(1+\eta)\nu_e\omega_e^*\,\frac{v_i}{r_\perp}\,\rho_i^3\,k_{xy}^3\right)\Bigg] = 0\,, \qquad (3.68)
\end{aligned}
$$

where

$$k_\perp^2 = k_x^2 + k_y^2 \qquad (3.69)$$

and

$$k_{xy}^3 = k_x^2\,k_y + k_y^3\,. \qquad (3.70)$$

The solution of Equation (3.68) for unstable low frequency oscillation with $\omega \approx \omega_e^*$, can be obtained by considering the quadratic part of Equation (3.68). For

$\frac{k_x}{r_n} \approx k_\perp$, unstable oscillations are given approximately by

$$\omega \approx \frac{\beta(1+\eta)\omega_e^* - (1+\eta)\rho_i^2\ k_\perp^2 \frac{k_z^2 v_{th}^2}{\nu_e}}{1+(1+\eta)\rho_1^2\ k_\perp^2}$$

$$+ i\Bigg(1+\eta)\ \frac{\nu_e \nu_i}{\omega_e^*}\ \rho_i^4\ \frac{k_x^3}{r_n} - \frac{1}{4}\ (\alpha\beta + 1 + \eta)\nu_i\ \rho_i^4\ k_\perp^4\Bigg]\ . \tag{3.71}$$

Equation (3.70) shows the first order effect of finite ion gyro radius effects on the real part of the wave frequency. The term $(1+\eta)$ allows radially increasing temperature gradients to compensate for a radially decreasing density gradient and reduce the instability's onset.

CHAPTER IV

ELECTRON COLLISION FREQUENCY MEASUREMENT: THEORY

Introduction.

The electron collision frequency of the turbulent Penning discharge was determined by measuring the absorption spectrum of a microwave beam near the upper hybrid frequency. When propagated across the plasma column, a microwave signal with an electric field perpendicular to the static magnetic field exhibits strong absorption near the electron upper hybrid frequency for a plasma with strong to moderate collisions. For a weakly collisional plasma absorption will occur at both the upper hybrid frequency and the electron gyro frequency. The absorption spectrum of both of these processes tends to be broadened by the presence of collisions. For the strongly magnetized Penning discharge plasma, the upper hybrid and electron gyro frequencies are close together.

The propagation of a microwave signal near the electron cyclotron frequency is considered for a uniform plasma. The problems of mode conversion (Swanson 1989) with propagation in a nonuniform plasma are not considered, nor is the effect of wave diffraction by the cylindrical plasma column considered (Heald et. al. 1965). The plasma is considered underdense, but having finite collisions with $\omega_b > \omega_p \gg \nu_e$.

The propagation constants governing the attenuation and dispersion of a low power microwave signal propagating through a plasma are determined by solving the electromagnetic wave equation (Heald et. al. 1965 and Jackson 1975),

$$\nabla \times \nabla \times \mathbf{E} + \frac{1}{c^2}\,\frac{\partial^2 \mathbf{E}}{\partial t^2} + \mu_0 \frac{\partial}{\partial t}\,(\overline{\sigma} \cdot \mathbf{E}) = 0\ , \tag{4.1}$$

where $\overline{\sigma}$ is the conductivity tensor for the magnetized plasma. For the propagation of a plane wave of the form

$$\exp\ i(-\omega t + \mathbf{k} \cdot \mathbf{r}) \tag{4.2}$$

in a homogeneous medium, Equation (4.1) reduces to

$$\mathbf{k} \times (\mathbf{k} \times \mathbf{E}) + \frac{\omega^2}{c^2}\ \overline{\varepsilon} \cdot \mathbf{E} = 0\ . \tag{4.3}$$

The tensor $\overline{\varepsilon}$ is the plasma dielectric tensor and is related to the conductivity tensor $\overline{\sigma}$ by,

$$\overline{\varepsilon} = \mathbf{1} - i\ \frac{\overline{\sigma}}{\omega\varepsilon_0}\ . \tag{4.4}$$

Under experimental conditions, Equation (4.3) becomes a boundary value problem with a plasma of finite dimensions. This fixes ω to be real and $\mathbf{k}$ becomes complex. If propagation is restricted to the $\hat{x} - \hat{z}$ plane, and the static magnetic field is along the $\hat{z}$ axis, the vector $\mathbf{k}$ can be written as

$$\mathbf{k} = \breve{\mu}\ \frac{\omega}{c}\ (\xi, 0, \zeta)\ , \tag{4.5}$$

where $\breve{\mu}$ is the complex dielectric constant of the plasma. The direction cosines ξ and ζ are defined by

$$\xi = \sin\ \theta_i\ , \tag{4.6}$$

and

$$\zeta = \cos\ \theta_i\ , \tag{4.7}$$

where θ_i is the incident angle with respect to the static magnetic field. The dispersion relation defined by Equation (4.3) can be written in terms of $\breve{\mu}$ as,

$$\breve{\mu} \times (\breve{\mu} \times \mathbf{E}) + \overline{\varepsilon} \cdot \mathbf{E} = 0\ . \tag{4.8}$$

The solution for $\breve{\mu}$ from Equation (4.8) is given in the form of a quartic equation (Heald et. al. 1975)

$$A^* \ \breve{\mu}^4 - B^* \ \breve{\mu}^2 + C^* = 0 \ , \tag{4.9}$$

where

$$A^* = \varepsilon_{xx}\xi^2 + \varepsilon_{zz}\xi^2 + 2\varepsilon_{xz}\xi \ \zeta \ , \tag{4.10}$$

$$B^* = (\varepsilon_{xx}\varepsilon_{zz} - \varepsilon_{xz}^2) + (\varepsilon_{xx}\varepsilon_{yy} + \varepsilon_{xy}^2)\xi^2 + (\varepsilon_{yy}\varepsilon_{zz} + \varepsilon_{yz}^2)\zeta^2$$
$$+ 2(\varepsilon_{yy}\varepsilon_{xz} - \varepsilon_{xy}\varepsilon_{yz})\xi \ \zeta \ , \tag{4.11}$$

and

$$C^* = Det|\varepsilon_{ij}| \ . \tag{4.12}$$

For a specific form of the plasma dielectric tensor, the attenuation constant α and phase constant β are given by solving Equation (4.9) for $\breve{\mu}^2$ and then using (Heald et. al. 1965),

$$\breve{\mu} = \mu + i\chi \ , \tag{4.13}$$

with

$$\alpha = \chi \ \frac{\omega}{c} \ , \tag{4.14}$$

and

$$\beta = \mu \ \frac{\omega}{c} \ , \tag{4.15}$$

where μ is the real refractive index, and χ is the attenuation index. The propagation of the plane wave microwave beam takes the form

$$\mathbf{E}(x,t) = E_0 \ \exp\left[-i\omega t - (\alpha + i\beta)(\xi + \zeta)\ell\right] \ , \tag{4.16}$$

where ℓ is the distance the wave propagates through the plasma.

Homogeneous Dielectric Tensor With Constant Collision Frequency.

The plasma dielectric tensor for a homogeneous, quasi-equilibrium Maxwellian plasma was derived using the linearized Vlasov equation with a BGK collision term by Alexandrov et at. (1984). This dielectric tensor for electrons is given by

$$\varepsilon_{ij}(\omega, \mathbf{k}) = \delta_{ij} + \left[\delta_{i\mu} + i\, \frac{\nu G_i k_\mu}{\omega + i\nu^*}\right] \times \left(\frac{\omega + i\nu}{\omega}\right) \left[\varepsilon^{\alpha}_{\mu j}(\omega + i\nu, \mathbf{k}) - \delta_{\mu j}\right] \,, \tag{4.17}$$

where

$$\mathbf{G} = \begin{bmatrix} \frac{\omega_b}{k_\perp} \sum\limits_n \frac{n A_n(z)}{\omega + i\nu - n\omega_b}\, I_+(\beta_n) \\ -\, i\, \frac{\omega_b}{k_\perp} \sum\limits_n \frac{z A'_n(z)}{\omega + i\nu - n\omega_b}\, I_+(\beta_n) \\ -\, \frac{1}{k_z} \sum\limits_n A_n(z)[1 - I_+(\beta_n)] \end{bmatrix} . \tag{4.18}$$

The tensor $\varepsilon^{\alpha}_{\mu j}(\omega + i\nu, \mathbf{k})$ is the collisionless dielectric tensor at the shifted argument, $\omega \rightarrow \omega + i\nu$, and ν^* is given by

$$\nu^* = \nu(\mathbf{k} \cdot \mathbf{G}) \,, \tag{4.19}$$

where ν is the collision frequency of electrons.

The elements of the collisionless tensor $\varepsilon^{\alpha}_{\mu j}$ for equation (4.17) is given by

$$\varepsilon^{\alpha}_{xx} = 1 - \sum_n \frac{n^2\omega_p^2}{\omega(\omega - n\omega_b)} \frac{A_n(z)}{z} I(\beta_n) , \tag{4.20}$$

$$\varepsilon^{\alpha}_{yy} = \varepsilon^{\alpha}_{xx} + 2 \sum_n \frac{\omega_p^2 z}{\omega(\omega - n\omega_b)} A'_n(z)\, I_+(\beta_n) , \tag{4.21}$$

$$\varepsilon^{\alpha}_{xy} = -\varepsilon^{\alpha}_{yx} = -i \sum_n \frac{n\omega_p^2}{\omega(\omega - n\omega_b)} A'_n(z)\, I_+(\beta_n) , \tag{4.22}$$

$$\varepsilon^{\alpha}_{xz} = \varepsilon^{\alpha}_{zx} = -\sum_n \frac{\omega_p^2 n k_\perp}{\omega\omega_b k_z} \frac{A_n(z)}{z} (I_+(\beta_n) - 1) , \tag{4.23}$$

$$\varepsilon^{\alpha}_{yz} = -\varepsilon^{\alpha}_{zy} = i \sum_n \frac{\omega_p^2 k_\perp}{\omega\omega_b k_z} A'_n(z)\, (I_+(\beta_n) - 1) , \tag{4.24}$$

and

$$\varepsilon^{\alpha}_{zz} = 1 + \sum_n \frac{\omega_p^2}{k_z^2 v_{th}^2} \left[\left(\frac{\omega - n\omega_b}{\omega} \right) A_n(z)(I_+(\beta_n) - 1) \right] . \tag{4.25}$$

The summations in Equations (4.18) through (4.25) extend from $-\infty$ to $+\infty$. The arguments z and β_n are given for the collisional tensor by

$$z = \left(\frac{k_\perp v_{th}}{\omega_b} \right)^2 , \tag{4.26}$$

and

$$\beta_n = \left(\frac{\omega + i\nu - n\omega_b}{k_z v_{th}} \right) . \tag{4.27}$$

The function $A_n(z)$ is defined by

$$A_n(z) \equiv e^{-z} I_n(z) , \tag{4.28}$$

where $I_n(z)$ is the modified Bessel function of the first kind. The function $I_+(\beta_n)$ is related to the plasma dispersion function $Z(x)$ by

$$I_+(\beta_n) = -\frac{\beta_n}{\sqrt{2}}\, Z\left(\frac{\beta_n}{\sqrt{2}} \right) . \tag{4.29}$$

For wave propagation at $\omega \simeq \omega_b$ and with finite k_z, the dielectric tensor $\varepsilon_{ij}^{\alpha}$ and vector $\mathbf{G}$ can be somewhat simplified. By using the $n = -1, 0, 1$ terms and expanding the modified Bessel function for small argument, $z \to 0$, one may obtain

$$I_n(z) \sim \frac{\left(\frac{1}{2}\,z\right)^n}{\Gamma(n+1)} \,. \qquad n \neq -1, -2, \ldots \,. \tag{4.30}$$

The tensor

$$\bar{\varepsilon}_{ij} = \delta_{ij} + \left(\frac{\omega + i\nu}{\omega}\right) \left[\varepsilon_{ij}^{\alpha}(\omega + i\nu, \vec{\mathbf{k}}) - \delta_{ij}\right] \tag{4.31}$$

then has elements

$$\bar{\varepsilon}_{xx} = 1 - \frac{1}{2}\,\frac{\omega_p^2}{\omega}\,\left[\frac{I_+(\beta_{-1})}{\omega + i\nu + \omega_b} + \frac{I_+(\beta_1)}{\omega + i\nu - \omega_b}\right] \,, \tag{4.32}$$

$$\bar{\varepsilon}_{xy} = i\,\frac{1}{2}\,\frac{\omega_p^2}{\omega}\,\left[\frac{I_+(\beta_{-1})}{\omega + i\nu + \omega_b} - \frac{I_+(\beta_1)}{\omega + i\nu - \omega_b}\right] \,, \tag{4.33}$$

$$\bar{\varepsilon}_{xz} = -\frac{1}{2\xi}\,\frac{\omega_p^2}{\omega\omega_b}\,\left[I_+(\beta_1) - I_+(\beta_{-1})\right] \,, \tag{4.34}$$

$$\bar{\varepsilon}_{yz} = i\,\frac{1}{2\xi}\,\frac{\omega_p^2}{\omega\omega_b}\left[I_+(\beta_1) + I_+(\beta_{-1}) - 2\right] \,, \tag{4.35}$$

and

$$\begin{aligned} \varepsilon_{zz} = 1 - \frac{\omega_p^2}{\omega(\omega + i\nu)} + \frac{1}{2\xi^2}\,\frac{\omega_p^2}{\omega\omega_b^2}\,&\left[(\omega + i\nu + \omega_b)(I_+(\beta_{-1}) - 1)\right. \\ &\left. + (\omega + i\nu - \omega_b)(I_+(\beta_1) - 1)\right] \,, \end{aligned} \tag{4.36}$$

with $\bar{\varepsilon}_{yy} = \bar{\varepsilon}_{xx}, \bar{\varepsilon}_{zx} = \bar{\varepsilon}_{xz}, \bar{\varepsilon}_{zy} = -\bar{\varepsilon}_{yz}$, and $\bar{\varepsilon}_{yx} = -\bar{\varepsilon}_{xy}$.

The components of the vector $\mathbf{G}$ become

$$G_x = -\frac{1}{2}\,z\frac{\omega_b}{k_\perp}\,\left[\frac{I_+(\beta_{-1})}{\omega + i\nu + \omega_b} - \frac{I_+(\beta_1)}{\omega + i\nu - \omega_b}\right] \,, \tag{4.37}$$

$$G_y = -i\frac{1}{2}\,z\,\frac{\omega_b}{k_\perp}\,\left[\frac{I_+(\beta_{-1})}{\omega + i\nu + \omega_b} + \frac{I_+(\beta_1)}{\omega + i\nu - \omega_b}\right] \,, \tag{4.38}$$

and

$$G_z = \frac{1}{2}\,\frac{z}{k_z}\,\left[I_+(\beta_{-1}) + I_+(\beta_1) + I_+(\beta_0) - 3\right] \ . \tag{4.39}$$

Using the above results for $\bar{\varepsilon}_{ij}$ and $\mathbf{G}$ and fixing the wave vector to be in the $\hat{x}-\hat{z}$ plane, the elements of the collisional dielectric tensor ε_{ij} become, to first order in the small parameter z,

$$\varepsilon_{xx} = \bar{\varepsilon}_{xx} - i\ z\ \left(\frac{\nu}{\omega + i\nu^*}\right)\left(\frac{\omega\omega_b}{\omega_p^2}\right)(\bar{\varepsilon}_{yy} - 1)\ \left[\xi(\bar{\varepsilon}_{xx} - 2) + \zeta\ \bar{\varepsilon}_{zx}\right]\ , \tag{4.40}$$

$$\varepsilon_{yy} = \bar{\varepsilon}_{yy} - i\ z\ \left(\frac{\nu}{\omega + i\nu^*}\right)\left(\frac{\omega\omega_b}{\omega_p^2}\right)(\bar{\varepsilon}_{xx} - 1)\ \left[\xi\bar{\varepsilon}_{xy} + \zeta\ \bar{\varepsilon}_{zy}\right]\ , \tag{4.41}$$

$$\varepsilon_{xy} = \bar{\varepsilon}_{xy} - i\ z\ \left(\frac{\nu}{\omega + i\nu^*}\right)\left(\frac{\omega\omega_b}{\omega_p^2}\right)(\bar{\varepsilon}_{yy} - 1)\ \left[\xi\ \bar{\varepsilon}_{xy} + \zeta\bar{\varepsilon}_{zy}\right]\ , \tag{4.42}$$

$$\varepsilon_{xz} = \bar{\varepsilon}_{xz} - i\ z\ \left(\frac{\nu}{\omega + i\nu^*}\right)\left(\frac{\omega\omega_b}{\omega_p^2}\right)(\bar{\varepsilon}_{yy} - 1)\ \left[\xi\ \bar{\varepsilon}_{xz} + \zeta(\bar{\varepsilon}_{zz} - 1)\right]\ , \tag{4.43}$$

$$\varepsilon_{yz} = \bar{\varepsilon}_{yz} - i\ z\ \left(\frac{\nu}{\omega + i\nu^*}\right)\left(\frac{\omega\omega_b}{\omega_p^2}\right)(\bar{\varepsilon}_{xx} - 1)\ \left[\xi\bar{\varepsilon}_{xz} + \zeta(\bar{\varepsilon}_{zz} - 1)\right]\ , \tag{4.44}$$

and

$$\varepsilon_{zz} = \bar{\varepsilon}_{zz} - i\ z\ \left(\frac{\nu}{\omega + i\nu^*}\right)(I_+(\beta_1) + I_+(\beta_{-1}) + I_+(\beta_0) - 3)\left[\frac{1}{\xi}\ \bar{\varepsilon}_{xz} + \bar{\varepsilon}_{zz} - 1\right], \tag{4.45}$$

with $\varepsilon_{yx} = -\varepsilon_{xy}, \varepsilon_{zy} = -\varepsilon_{yz}$ and $\varepsilon_{zx} = \varepsilon_{xz}$.

The factors z and β_n defined by Equations (4.26) and (4.27) are functions of the wave vector components $k_\perp$ and k_z, which in turn are functions of the complex dielectric coefficient. Using Equation (4.5) the factors z and β_n can be written as

$$z = \breve{\mu}^2\left(\frac{\omega}{\omega_b}\right)^2\ \delta^2\ \xi^2\ , \tag{4.46}$$

and

$$\beta_n = \frac{1}{\breve{\mu}}\ \left(\frac{\omega + i\nu - \omega_b}{\delta\zeta\omega}\right)\ , \tag{4.47}$$

where $\delta = \frac{v_{th}}{c}$. This dependence on $\breve{\mu}$ of the factors z and β_n complicates the solution of Equation (4.9). The equation becomes transcendental with $\breve{\mu}$ contained in the argument of the plasma dispersion function $Z(\beta_n)$.

Appleton Equation.

In the limiting case of normal incidence, where $\theta_i = \frac{\pi}{2}$, and with thermal effects neglected, Equation (4.9) has two solutions given by

$$\breve{\mu}_{ex}^2 = \varepsilon_{yy} + \frac{\varepsilon_{xy}^2}{\varepsilon_{xx}} \ , \tag{4.48}$$

and

$$\breve{\mu}_{or}^2 = \varepsilon_{zz} \ , \tag{4.49}$$

where

$$\varepsilon_{xx} = \varepsilon_{yy} = 1 - \frac{\omega_p^2}{\omega} \frac{\omega + i\nu}{(\omega + i\nu)^2 - \omega_b^2} \ , \tag{4.50}$$

$$\varepsilon_{xy} = -i \frac{\omega_p^2}{\omega} \frac{\omega_b}{(\omega + i\nu)^2 - \omega_b^2} \ , \tag{4.51}$$

and

$$\varepsilon_{zz} = 1 - \frac{\omega_p^2}{\omega(\omega + i\nu)} \ . \tag{4.52}$$

Equation (4.48) defines the complex dielectric constant for propagation of the extraordinary wave; a wave with its electric field perpendicular to the static magnetic field. Equation (4.49) defines the complex dielectric constant for the ordinary wave; a wave with its electric field vector parallel to the static magnetic field.

Equation (4.48) has a resonance near the upper hybrid frequency (Ω_{UH}, where $\Omega_{UH}^2 = \Omega_b^2 + \Pi_p^2$). This equation is a special case of the Appleton Equation, which was originally derived to describe radio wave propagation in the ionosphere (Appleton 1932).

Figures 4.1 and 4.2 show the attenuation and phase spectra for an extraordinary mode wave propagating at $\theta_i = \frac{\pi}{2}$ through a 12 cm thick cold plasma with $\Omega_b = 4$ Hz, $\Pi_p = 1$ GHz and for $\nu_e = 20$ MHz and $\nu_e = 40$ MHz. Figure 4.1 illustrates the strong absorption near the electron gyro frequency, while Figure 4.2 illustrates the characteristic phase reversal due to resonance. The absorption curve broadening due to an increased collision frequency is clearly seen in the two curves in Figure 4.1. Although the curve for the larger collision frequency is broadened, the maximum attenuation is decreased, and the resonance frequency f_r is shifted slightly.

Figure 4.3 shows the attenuation at f_r for a fixed plasma frequency as a function of the gyro frequency for various collision frequencies. The maximum attenuation decreases for increasing collision frequency. Figure 4.4 shows the effect of increased plasma density as a function of collision frequency and a fixed gyro frequency. Here the maximum attenuation increases with increasing plasma frequency. Figures 4.3 and 4.4 both show decreasing wave attenuation as the electron collision frequency increases. This is due to the resonant interaction between particle and wave. As electrons suffer increasing collisions, the electrons gyrate over a smaller diameter, and pick up less energy per gyration in the wave's E field.

When the absorption curve is measured experimentally, it is convenient to measure the resonance frequency, the maximum attenuation and the width of the absorption curve 3dB above maximum attenuation. This 3dB width is not equal to the collision frequency, except for special conditions. Figure 4.5 compares the collision frequency with the 3dB width for various plasma frequencies. Only conditions

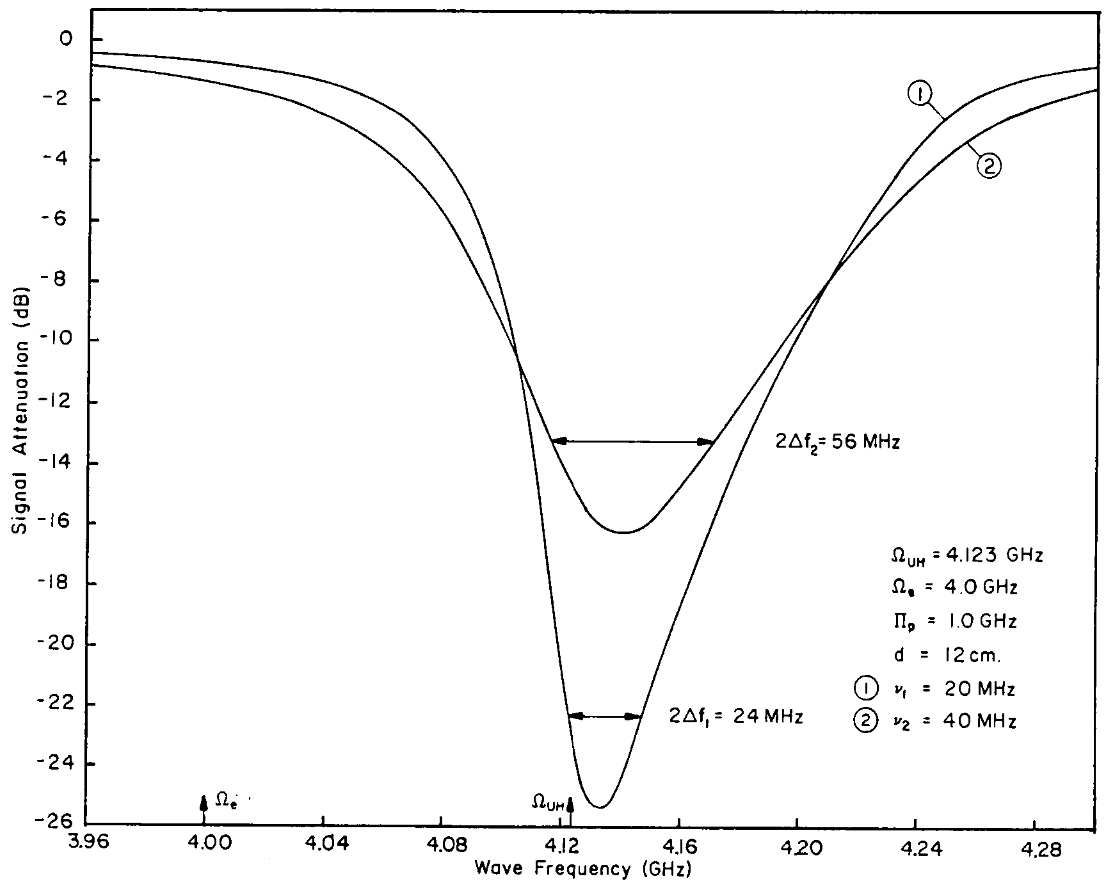

Figure 4.1. Signal attenuation for the extraordinary wave given by Appleton's Equation (Equation (4.48)) for a plasma 12cm thick with Ω_e = 4.0 GHz, Π_p = 1.0 GHz, and ν_e = 20 MHz and 40 MHz.

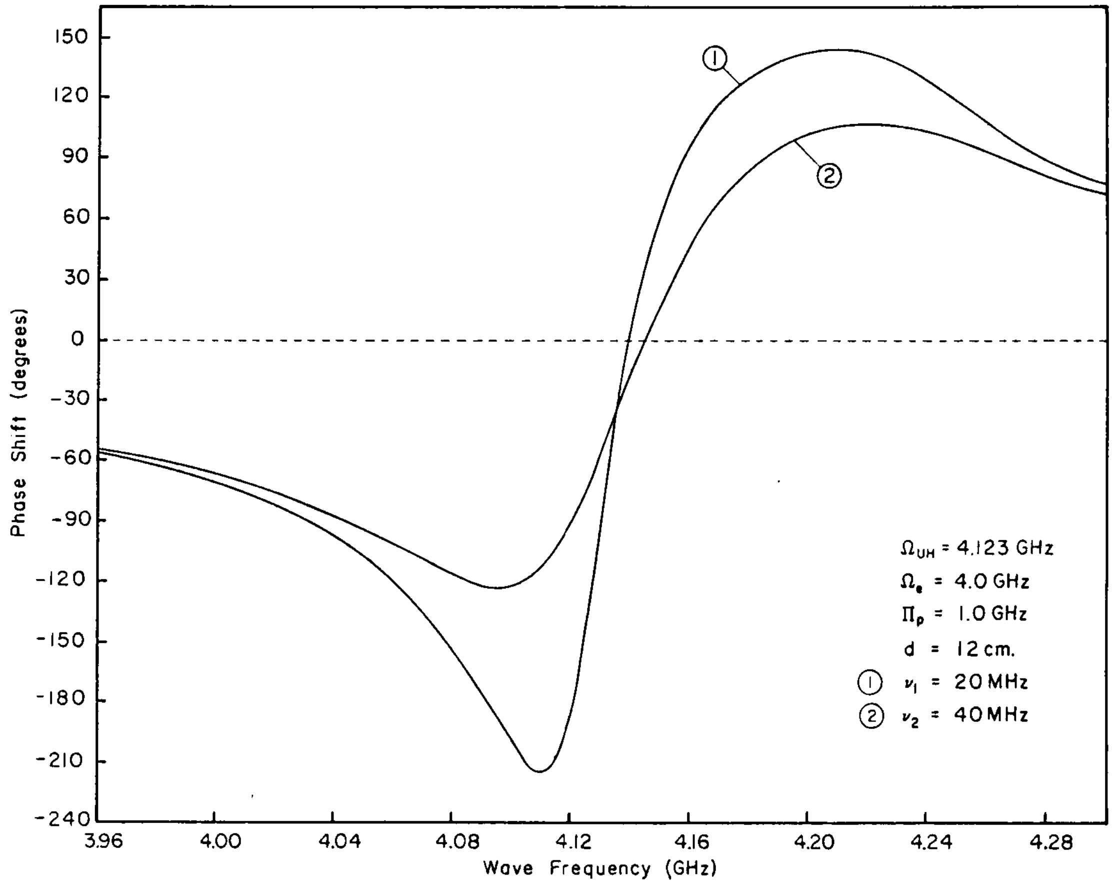

Figure 4.2. Signal phase shift for the extraordinary wave given by Appleton's Equation (Equation (4.48)) for a 12 cm thick plasma with Ω_e = 4.0 GHz, Π_p = 1.0 GHz, and ν_e = 20 MHz and 40 MHz.

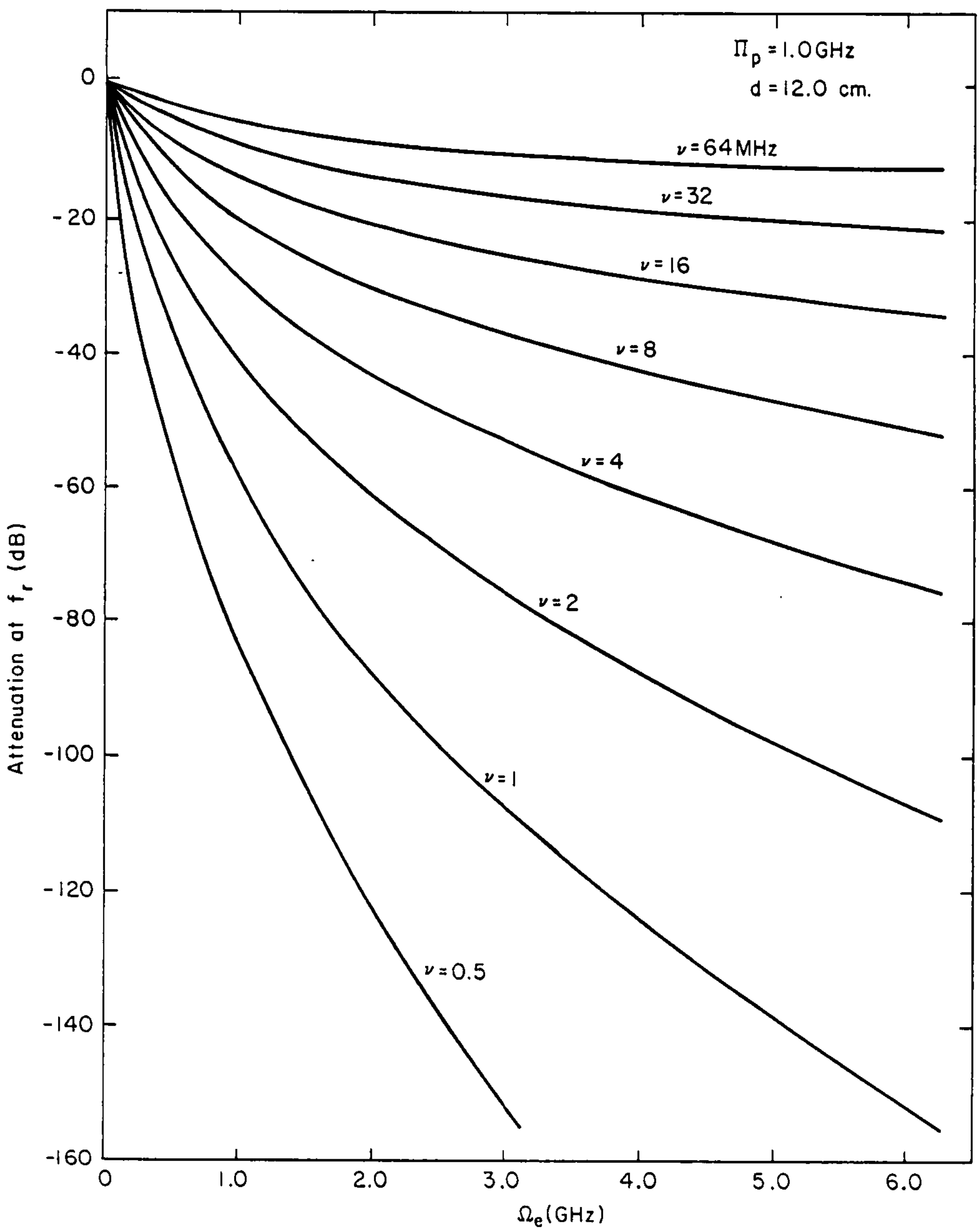

Figure 4.3. Attenuation at the resonance frequency f_r for solutions of Appleton's Equation (Equation (4.48)) as a function of the electron collision frequency ν_e and electron gyro frequency Ω_e for a fixed plasma frequency Π_p and thickness.

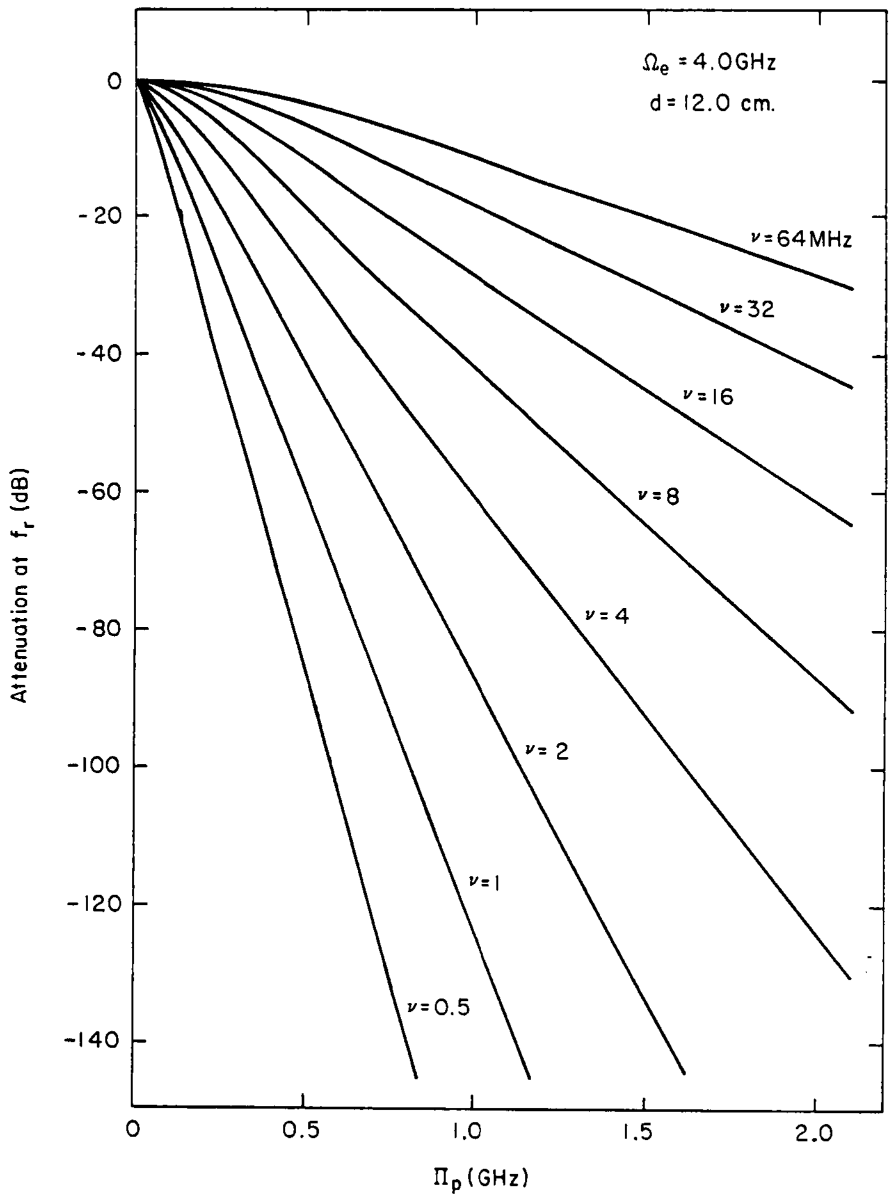

Figure 4.4. Attenuation at the resonance frequency f_r for solutions of Appleton's Equation (Equation (4.48)) as a function of the electron collision frequency ν_e and plasma frequency Π_p for fixed electron gyro frequency and thickness.

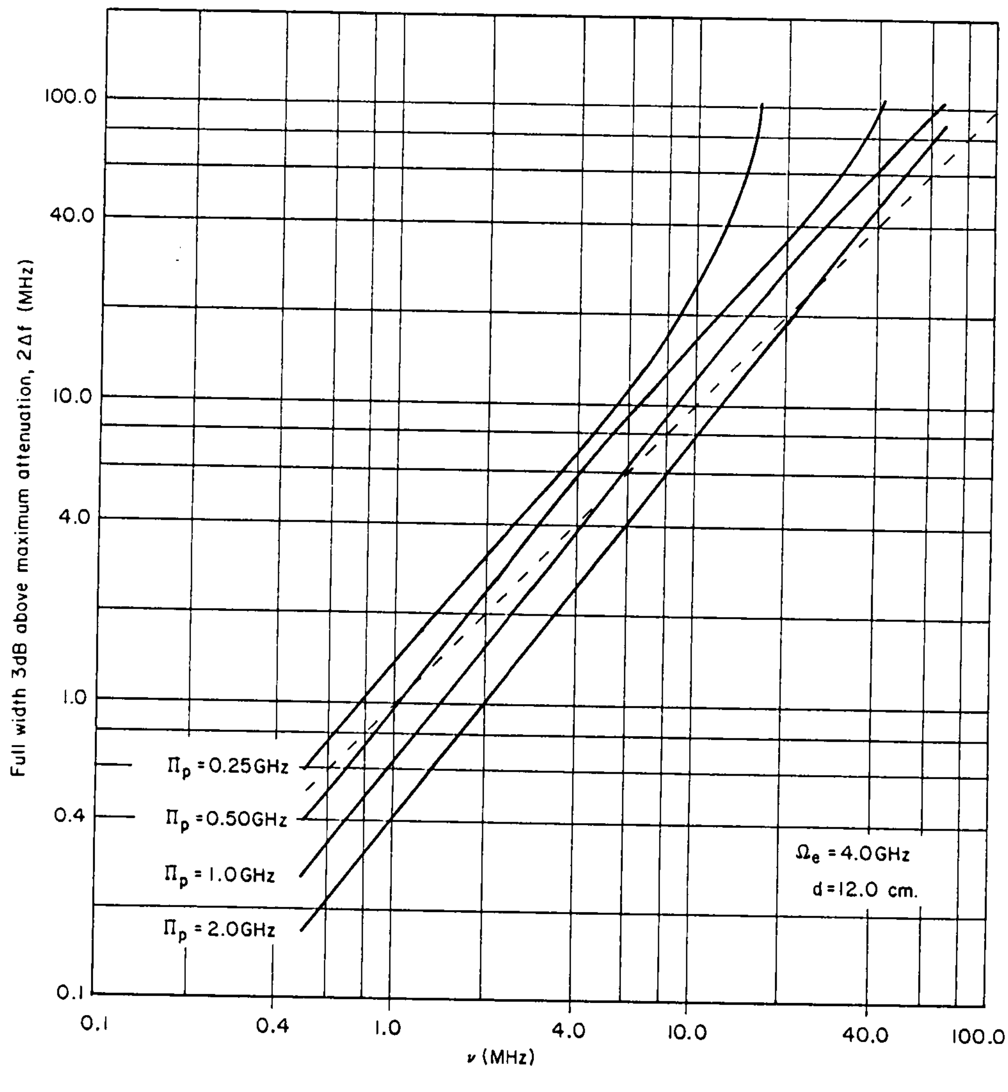

Figure 4.5. Curves of the full width of absorption curves 3dB above maximum attenuation ($2\Delta f$), versus the electron collision frequency ν_e from solutions of the Appleton Equation (Equation (4.48)).

along the dashed line have the 3dB width equal to the collision frequency. This increases the complexity of interpreting the absorption curve to determine the effective electron collision frequency.

Beam Geometry Effects.

Due to the finite geometry of the plasma and the method with which the microwave signal is launched across the plasma, the microwave beam has a slight divergence. Hence only a portion of the incident beam propagates exactly at $\theta_i = \frac{\pi}{2}$. The actual angle of propagation can be approximated as

$$\theta_i = \frac{\pi}{2} \pm \theta_0 \ . \tag{4.53}$$

where $\theta \ll \frac{\pi}{2}$. This beam divergence produces a nonzero k_z and through Equation (4.27), introduces quasi-thermal effects into the dispersion equation. For a finite temperature plasma, β_n becomes finite and z is nonzero. The dielectric tensor components are now given by the more general relations in Equations (4.40) through (4.45). In addition to the resonance close to the upper hybrid frequency, a resonance very close to the electron cyclotron frequency will occur for the extraordinary mode wave.

For the Penning discharge at moderate temperatures, $T_e \sim 20$ eV, the ratio of thermal velocity to the velocity of light δ is small, $\delta \simeq 0.01$. Hence the correction factors to the tensor ε_{ij} of order z or δ^2 given in Equations (4.40) through (4.45) can be negelected. The dielectric tensor is then given by Equations (4.32) through (4.36) with $\varepsilon_{yy} = \varepsilon_{xx}$. Under these conditions, the propagation constants of the extraordinary wave are given by the solution of

$$\breve{\mu}^2 = \frac{\xi^2\mu_x^2 + \bar{\varepsilon}_{zz}\left(1 + \zeta^2 - \frac{\mu_x^2}{\breve{\mu}^2}\right) + \overline{B} + \frac{\overline{C}}{\breve{\mu}^2}}{\xi^2 + \overline{A}} \ , \tag{4.54}$$

where

$$\overline{A} = \frac{1}{\overline{\varepsilon}_{xx}} \ \left[\zeta^2 \overline{\varepsilon}_{zz} + 2\zeta\xi\overline{\varepsilon}_{xz}\right] \ , \tag{4.56}$$

$$\overline{B} = \frac{1}{\overline{\varepsilon}_{xx}} \left[\zeta^2 \overline{\varepsilon}_{yz}^2 - \overline{\varepsilon}_{xz}^2 + 2\xi\zeta \left(\overline{\varepsilon}_{xz}\overline{\varepsilon}_{xx} - \overline{\varepsilon}_{xy}\overline{\varepsilon}_{yz}\right)\right] \ , \tag{4.55}$$

and

$$\overline{C} = \overline{\varepsilon}_{yz}^2 + \overline{\varepsilon}_{xz}^2 \ , \tag{4.57}$$

with μ_x^2 defined by Equation (4.48) using the finite temperature tensor components.

Equation (4.54) can be solved iteratively by using Newton's method (Henrici 1988), with

$$\breve{\mu}_{i+1}^2 = \breve{\mu}_i^2 - \frac{G\left(\breve{\mu}_i^2\right)}{G'\left(\breve{\mu}_i^2\right)} \ , \tag{4.58}$$

$$G\left(\breve{\mu}^2\right) = -\breve{\mu}^2 + \frac{\xi^2\mu_x^2 + \overline{\varepsilon}_{zz}\left(1 + \zeta^2 - \frac{\mu_x^2}{\breve{\mu}^2}\right) + \overline{B} + \frac{\overline{C}}{\breve{\mu}^2}}{\xi^2 + \overline{A}} \ , \tag{4.59}$$

and $G'\left(\breve{\mu}^2\right)$ given by

$$G'\left(\breve{\mu}^2\right) = \frac{\partial G(\mu^2)}{\partial \mu^2} \ . \tag{4.60}$$

Appendix D discusses the solution of Equation (4.58) along with the methods used to evaluate the plasma dispersion function $Z(\beta)$.

Table 4.1 lists solutions of Equation (4.58) near the electron cyclotron frequency for a range in ν_e at two beam divergence angles, $\theta_0 = 2.5°, 4.5°$. These angles were used with reference to the experimental beam geometry which is discussed in Chapter V.

The results in Table 4.1 show that significant attenuation at the electron gyro frequency occurs only for electron collision frequencies below the electron-neutral

TABLE 4.1

BEAM DIVERGENCE EFFECTS AT THE ELECTRON CYCLOTRON RESONANCE FREQUENCY FOR THE EXTRAORDINARY WAVE AT $\theta_e = \frac{\pi}{2} + \theta_0$

	ν_e (MHz)[1]	f_r (GHz)[2]	$P_0(f_r)$[3] (dB)[4]
Case 1	5	3.9960	-1.3
	1	4.0100	-5.6
	0.5	4.0150	-16.2
	0.1	3.9994	-22.0
	0.05	3.9994	-22.5
Case 2	5	4.0128	-0.2
	1	4.0100	-1.9
	0.5	3.9990	-14.9
	0.01	3.9991	-18.9
Case 1:	$\theta_0 = 2.5°, \delta = 0.01$[5],	$\Omega_e = 4.0$ GHz,	$\Pi_p = 1.0$ GHz
Case 2:	$\theta_0 = 4.5°, \delta = 0.01$[4],	$\Omega_e = 4.0$ GHz,	$\Pi_p = 1.0$ GHz

[1] ν_e; velocity independent electron collision frequency.
[2] f_r; resonance frequency.
[3] Attenuation for a 12 cm. thick plasma.
[4] $P_0(f_r)$; signal attenuation at f_r.
[5] δ; ratio of thermal velocity to speed of light.

collision frequency present in the weakly ionized Penning discharge, if the beam had a significant divergence.

For reference, Table 4.2 lists solutions of Equation (4.48) near the upper hybrid frequency. The attenuation at f_r is consistently much larger than the attenuation near the electron gyro frequency given in Table 4.1.

Homogeneous Dielectric Tensor with Speed Dependent Collision Frequency.

In general the collision frequency of electrons (and ions) is dependent on the particle's velocity and speed. This velocity dependence alters the components of the dielectric tensor and the form of the absorption curve. Using the linearized Boltzmann Equation with a Fokker-Planck term for electron-ion Coulomb collisions, and a Boltzmann term for speed dependent electron collisions with heavy neutrals, Shkarofsky (1961) derived the plasma conductivity for any degree of ionization. This work produced a set of correction factors g and h which turn out to be functions of a single argument;

$$g = g\left(\left|\frac{\omega - \omega_b}{\langle\nu_e\rangle}\right|\right) , \tag{4.61}$$

and

$$h = h\left(\left|\frac{\omega - \omega_b}{\langle\nu_e\rangle}\right|\right) , \tag{4.62}$$

where $\langle\nu_e\rangle$ is an average effective collision frequency of the velocity dependent collision frequencies,

$$\langle\nu_e\rangle = \langle\nu_{en}\rangle + \langle\nu_{ei}\rangle \ . \tag{4.63}$$

TABLE 4.2

ABSORPTION NEAR THE UPPER HYBRID RESONANCE FOR THE EXTRAORDINARY WAVE AT $\theta_i = \frac{\pi}{2}$, $\Omega_e = 4.0$ GHz, $\Pi_p = 1.0$ GHz, $\delta = 0$

ν_e (MHz)	F_r (GHz)	$P_0(f_r)$ (dB)
5	4.1260	-55
1	4.1237	-125
0.5	4.1234	-177
0.1	4.1232	-396
0.05	4.1232	-560

The conductivity tensor elements for electrons with the g and h correction factors take the following form in rotating coordinates (Shkarofsky, 1961)

$$\sigma_\ell = -i \frac{ne^2}{m} \frac{1}{ig\langle\nu_e\rangle + h(\omega + \omega_b)}, \tag{4.64}$$

$$\sigma_r = -i \frac{ne^2}{m} \frac{1}{ig\langle\nu_e\rangle + h(\omega - \omega_b)}, \tag{4.65}$$

and

$$\sigma_{||} = -i \frac{ne^2}{m} \frac{1}{h\omega + ig\langle\nu_e\rangle}, \tag{4.66}$$

where

$$\overline{\sigma} = \begin{bmatrix} \sigma_\ell & 0 & 0 \\ 0 & \sigma_r & 0 \\ 0 & 0 & \sigma_{||} \end{bmatrix}. \tag{4.67}$$

[1] ν_e; velocity independent collision frequency.
[2] f_r; resonance frequency.
[3] $P_0(f_r)$; signal attenuation at f_r.
[4] δ; ratio of thermal velocity to speed of light.

Using the relation between the plasma dielectric constants and the plasma conductivity, Equation (4.4), and changing from rotating to Cartesian coordinates using

$$\varepsilon_{xx} = \frac{1}{2}\,(\varepsilon_\ell + \varepsilon_r)\ , \tag{4.68}$$

$$\varepsilon_{xy} = \frac{1}{2}\,(\varepsilon_\ell - \varepsilon_r)\ , \tag{4.69}$$

and

$$\varepsilon_{zz} = \varepsilon_{||}\ , \tag{4.70}$$

the plasma dielectric tensor components become

$$\varepsilon_{xx} = 1 - \frac{\omega_p^2}{\omega}\,\frac{h\omega + ig\,\langle\nu_e\rangle}{(h\omega + ig\,\langle\nu_e\rangle)^2 - (h\omega_b)^2}\ , \tag{4.71}$$

$$\varepsilon_{xy} = -i\,\frac{\omega_p^2}{\omega}\,\frac{h\omega_b}{(h\omega + ig\,\langle\nu_e\rangle)^2 - (h\omega_b)^2}\ , \tag{4.72}$$

and

$$\varepsilon_{zz} = 1 + \frac{\omega_p^2}{\omega}\,\frac{1}{h\omega + ig\,\langle\nu_e\rangle}\ , \tag{4.73}$$

which are of the same form as the components in Equations (4.50) through (4.52).

The correction factors g and h are shown in Figure 4.6 for $\langle\nu_{en}\rangle \propto v^a$ with $a = 0, -1, -2, -3$ and in Figure 4.7 for $a = 0, 1, 2, 3$. These curves were reproduced from the tabular data given by Shkarofsky (1961) for the limiting case,

$$\frac{\langle\nu_{en}\rangle}{\langle\nu_{ei}\rangle} = 100\ . \tag{4.74}$$

These curves change slowly for decreasing ratios of the electron-neutral to electron-ion collision frequencies.

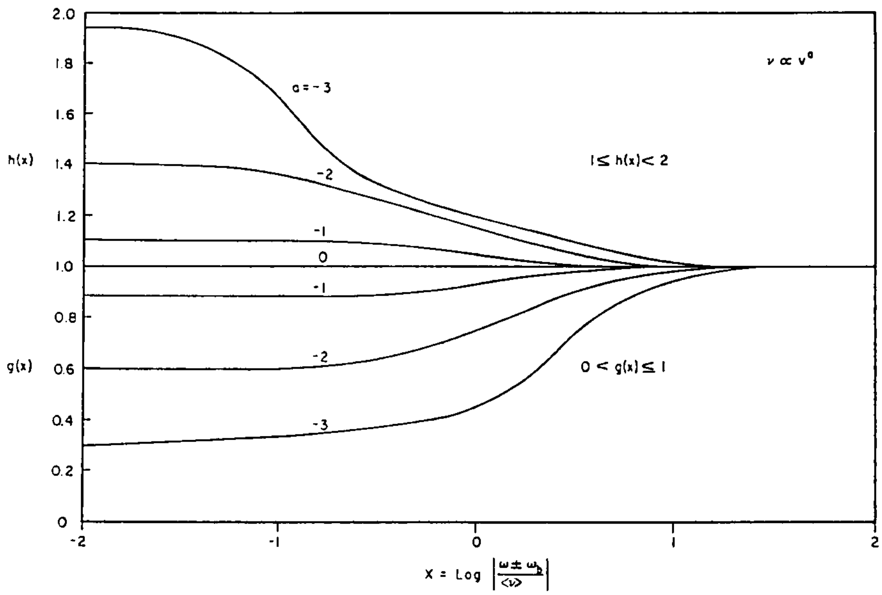

Figure 4.6. Dielectric tensor correction factors g and h for speed exponents $a = 0, -1, -2, -3$. Curves reproduced from tabular data due to Shkarofsky (1961).

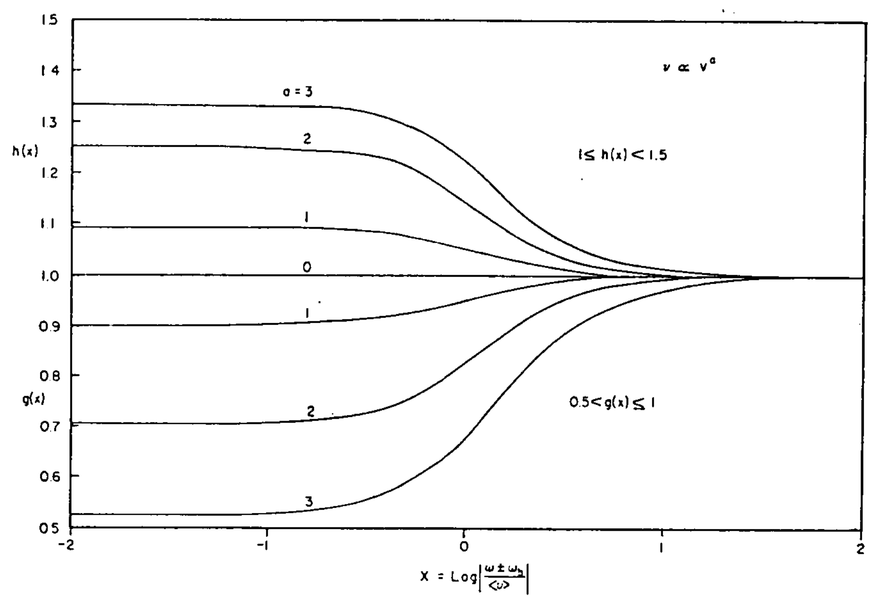

Figure 4.7. Dielectric tensor correction factors g and h for speed exponents $a = 0, 1, 2, 3$. Curves reproduced from tabular data due to Shkarofsky (1961).

For computational purposes in this work, the factors g and h in Figure 4.6 and Figure 4.7 were curve fitted to equations of the form

$$g(x) = 1 + A_g\left[1 + \tanh(a_g(x - x_g))\right] \ , \tag{4.75}$$

and

$$h(x) = 1 + A_h\left[1 - \tanh(a_h(x + x_n))\right] \ , \tag{4.76}$$

where

$$x = \mathrm{Log}\left|\frac{\omega - \omega_b}{\langle\nu_e\rangle}\right| \ . \tag{4.77}$$

The coefficients $A_g, a_g, x_g, A_h, a_h, x_h$ are shown in Table 4.3 for the various exponents a. These forms of g and h fit the data in Figure 4.6 to within $\pm$ 5% over most of the range in x shown. These results are used in the following chapter to account for a speed dependent turbulent collision frequency.

Using the forms of g and h defined by Equations (4.75) and (4.76), the dielectric tensor elements of Equations (4.71) and (4.72) and the Appleton Equation for $\theta_i = \frac{\pi}{2}$,

$$\breve{\mu}_{ex}^2 = \varepsilon_{xx} + \frac{\varepsilon_{xy}^2}{\varepsilon_{xx}} \tag{4.78}$$

the absorption curve as a function of a speed dependent electron collision frequency can be plotted. Figure 4.8 shows the absorption curve with $\Omega_e = 4.0$ GHz, $\Pi_p = 1$ GHz and $\langle\nu_e\rangle = 0.02$ GHz for $a = -3$ and $a = 0$. This illustrates how the correction factors have the effect of producing a decreased collision frequency, with the larger the magnitude of the exponent a, the greater the decrease.

TABLE 4.3

CURVE FITTING COEFFICIENTS FOR THE DIELECTRIC TENSOR

CORRECTION FACTORS g AND h*

Velocity exponent	Coefficients					
a	A_g	a_g	x_g	A_h	a_h	x_h
3	0.238	2.05	0.177	0.168	2.67	0.147
2	0.146	2.13	0.078	0.124	2.28	0.059
1	0.050	1.92	0	0.047	2.21	0.040
0	0	—	—	0	—	—
-1	0.058	1.97	0	0.055	2.00	0.050
-2	0.200	1.91	0.137	0.20	1.41	0.180
-3	0.350	2.20	0.39	0.49	0.90	0.810

*For Equations (4.75), (4.76) and (4.77) and the data in Figures 4.6 and 4.7.

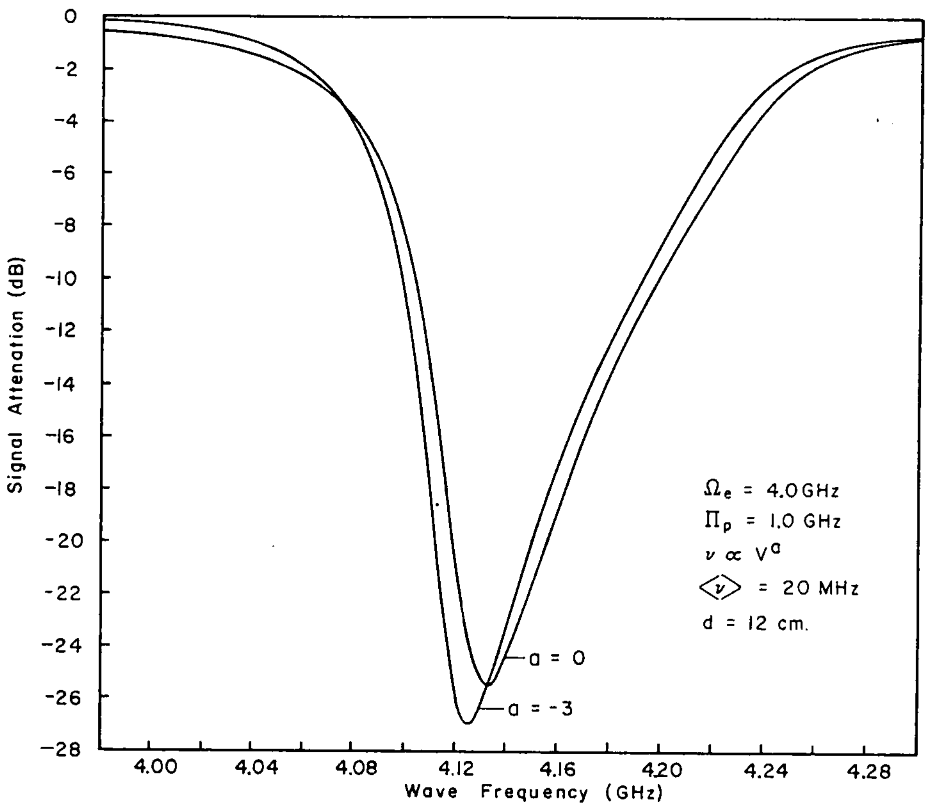

Figure 4.8. Signal absorption curves for the extraordinary wave using the g and h dielectric tensor correction factors with $a = 0, -3$.

CHAPTER V

EXPERIMENTAL MEASUREMENT OF ν_{eff} AND COMPARISON WITH THEORY

Introduction.

The effective electron collision frequency in the turbulent Penning discharge plasma was determined from microwave absorption data near the electron gyro frequency. This chapter discusses the experimental aspects of this measurement and summarizes the experimental data taken to illustrate the scaling of ν_{eff} with turbulent fluctuations. These data are then compared to the theory discussed in Chapter III.

Appendix H contains the experimental data considered in this chapter for the scaling of ν_{eff}. These data include: radial and axial profiles of electron temperature, electron number density, and plasma floating potential; the microwave absorption curves for each data run; calibrated power spectra of electrostatic potential fluctuations, microwave scattering data, and electron and ion density fluctuations.

Appendix I contains experimental data illustrating the enhancement of ν_{eff} by the application of external stimulus. These experiments were performed on the system configuration shown in Figure 2.3. A high voltage RF signal (70 to 75 V_{pp} at 12 MHz) was applied to the elongated anode to provide symmetric excitation of the plasma edge. This excitation enhanced the level of electrostatic fluctuations and broadened the resonance absorption curve.

Experimental Geometry.

Figure 5.1 illustrates the geometry and arrangement of the microwave horns used for absorption measurements, and Table 5.1 lists the relevant dimensions associated

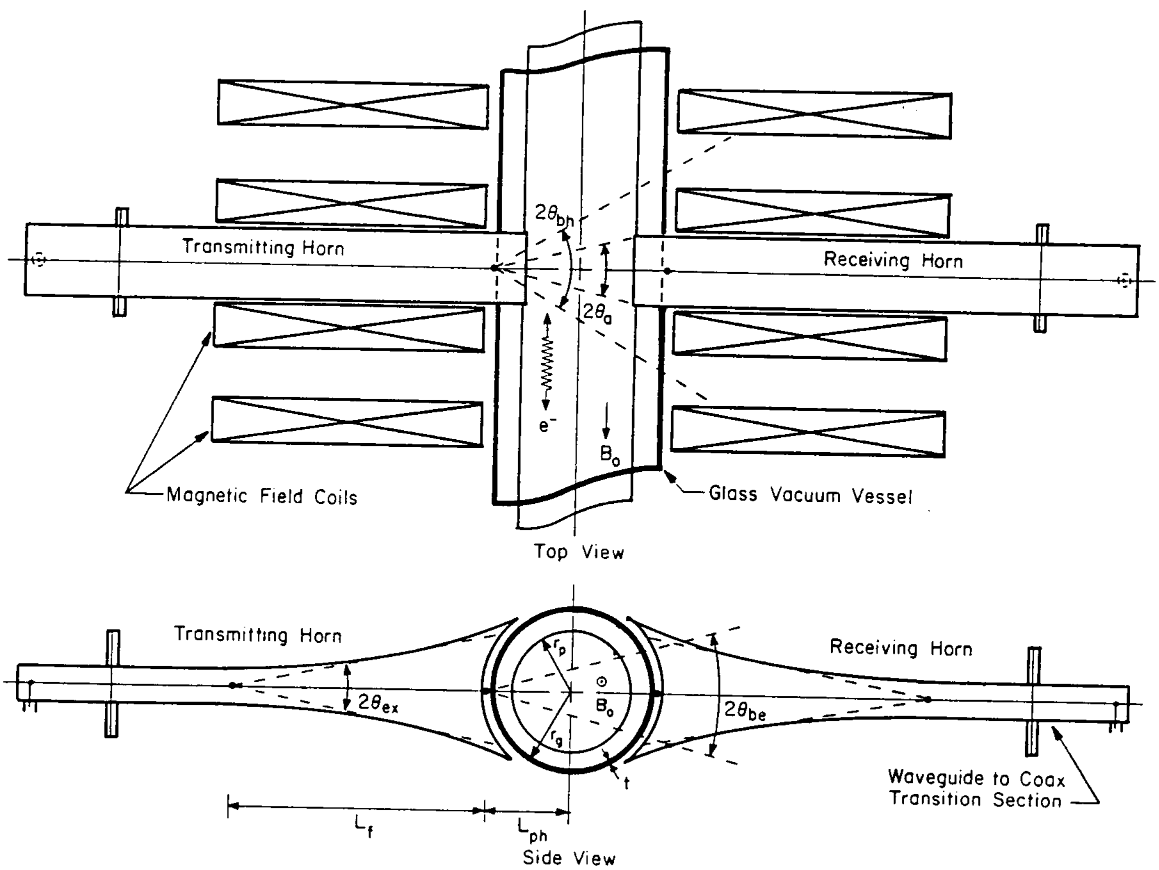

Figure 5.1. Microwave horn geometry for microwave absorption measurements near the electron gyro frequency.

TABLE 5.1

IMPORTANT PARAMETERS FOR THE MICROWAVE ABSORPTION HORN GEOMETRY*

Plasma Radius	r_p	6.3 cm
Glass Internal Radius	r_g	8.9 cm
Phase Center	L_{ph}	9.2 cm
Horn Focal Length	L_f	29 cm
Horn Expansion Angle	θ_{ex}	10.3 degrees
Horn Aperture Angle	θ_a	12.1 degrees

with this geometry. The horns were constructed using "C" band waveguide and copper sheet, and were oriented so that the **E** field of the launched wave was perpendicular to the static magnetic field. Due to the close spacing of the magnetic field coils, the horns were expanded in the **E** plane only. The side walls of the horns were curved so the horns could partially enclose the glass vacuum vessel and improve isolation between the horns.

The measured **E** and **H** plane power patterns for the horns are shown in Figures 5.2 and 5.3 for a 4.0 GHz wave frequency. Figure 5.4 plots the experimentally measured change in the 3dB, **H** plane divergence ($2\theta_{bh}$) as a function of wave frequency. This angle is important in considering the electron residence time in the microwave field. The **E** plane divergence, $2\theta_{be}$ always remained small enough for the wave to be contained within the plasma column. Despite this and the curved sides of the horns, an isolation of only 50dB could be expected between horns for a totally absorbing plasma.

*Refer to Figure 5.1.

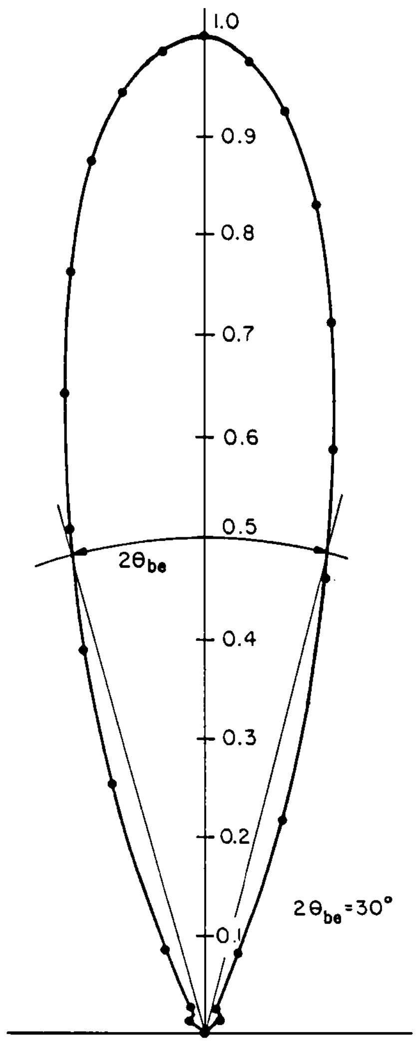

Figure 5.2. Linear polar plot of the experimentally measured **E** plane power pattern for the microwave absorption horns at 4.0 GHz.

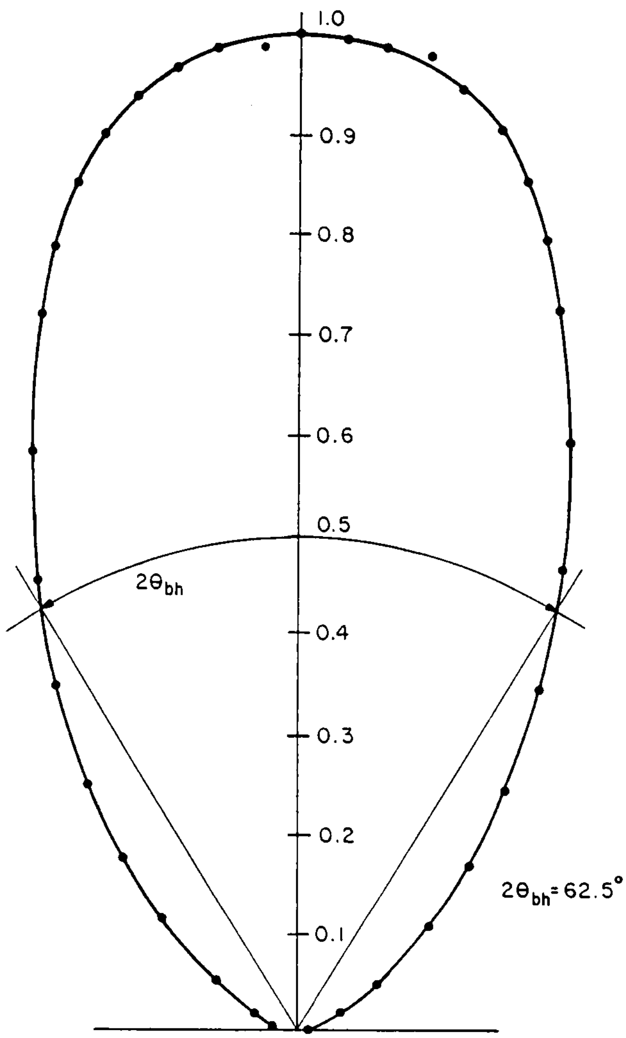

Figure 5.3. Linear polar plot of the experimentally measured **H** plane power pattern for the microwave absorption horns at 4.0 GHz.

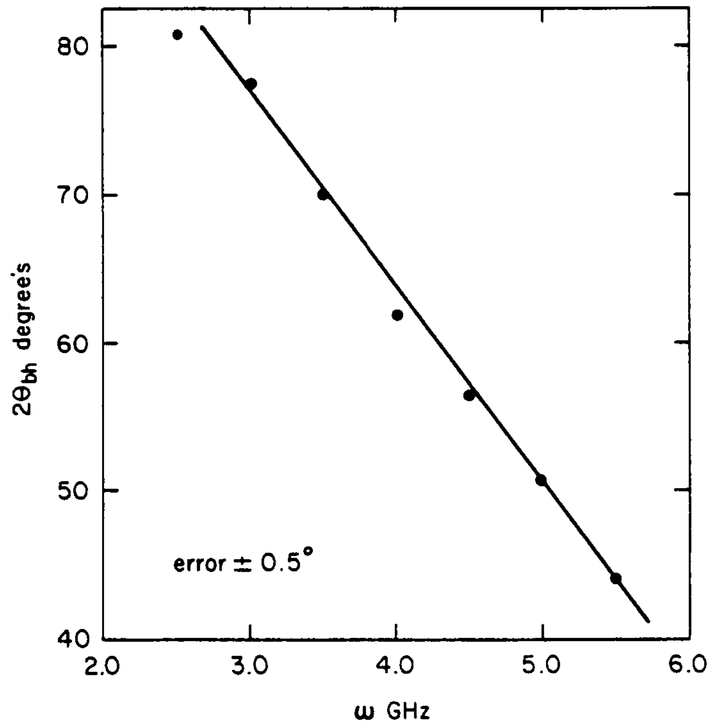

Figure 5.4. The 3dB **H** beam divergence, $2\theta_{bh}$, for the microwave absorption horns as a function of wave frequency.

Measurement of the microwave beam pattern was accomplished in the same manner as the procedure discussed in Appendix B for the microwave scattering horns. The phase center was estimated using graphical data (Balanis, 1982b), and due to the curved sides is essentially the same for both planes of the horn.

Measurement Technique.

Microwave absorption measurements were made as transmission measurements from the transmitting horn to the receiving horn using a Hewlett Packard 8510 Network Analyzer. This instrument has 80 dB of dynamic range and was capable of swept frequency measurements from 45 MHz to 18 GHz in the configuration used. This instrument can completely characterize the "**S**" parameters (see Lio, 1980) of a linear network. The analyzer used in this study was equipped with a YIG tuned oscillator. The specifications of this oscillator are given in Appendix C.

A transmission measurement of experimental data was first preceded by a transmission measurement with no plasma present. Figure 5.5 shows such a measurement, which includes cable and horn loss. This measurement was then stored and the display "normalized" for a 0 dB response. Next, a plasma was initiated and the absorption frequency located and verified by the characteristic phase reversal of a resonance. The center frequency of the analyzer was adjusted to be the resonance frequency and the sweep span reduced to allow improved resolution of the absorption curve. The normalization procedure was then repeated. Even using this normalization procedure, measurements near the system resonances of 4.74 GHz and 5.6 GHz shown in Figure 5.5 were avoided. These resonances were due primarily to the coaxial line to waveguide connection, and were subject to change with cable flexing.

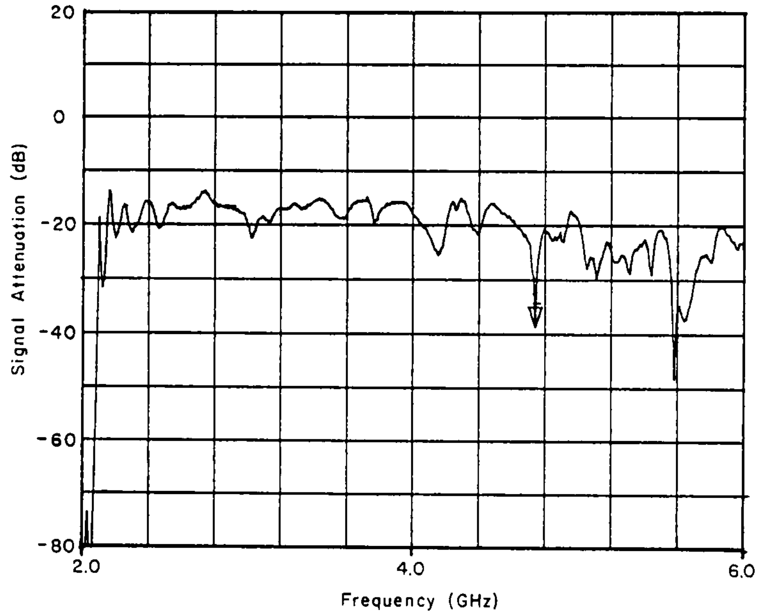

Figure 5.5. Transmission measurement across the glass vacuum vessel with no plasma present and including the 6 meter cable loss. Note the horn cut-off at 2.1 GHz.

In order to improve measurements, a slow frequency sweep of one to five seconds and instrument averaging were used. The analyzer was set up to average repeated sweeps with the number of sweeps, typically ten. Despite these measures, a frequency resolution of only 1 MHz could be obtained. This was due primarily to noise problems for measurements on a turbulent medium, the presence of short term drifts in the plasma characteristics, and drifts in the background static magnetic field. The root mean square, (rms) level of background magnetic field fluctuations was measured to be on the order of one gauss for a static field of two kilogauss. These fluctuations were below 50 kHz and were due to power supply current ripple.

Experimental Data.

The experimental data from the nine data runs presented in Appendix H is summarized in Tables 5.2 through Table 5.6. The runs are listed in terms of increasing collision frequency, with the exception of Run AGS-1, which had a double resonance curve.

Table 5.2 lists the plasma and discharge parameters. The electron temperature and number densities presented are radially averaged values. All of the experimental runs had nonuniform radial profiles of both electron temperature and number density. The ion temperature presented is that measured using the retarding potential energy analyzer (RPEA) and represents an average value. For these plasmas the average ion and electron kinetic temperatures differ by less than a factor of two. The values listed for plasma frequencies, Debye length, ion gyro radius, ion sound speed and ionization are all computed using the average plasma parameters.

Table 5.3 lists the microwave absorption data near the electron gyro frequency and the Maxwellian averaged electron-neutral collision frequency for each run.

TABLE 5.2

DISCHARGE AND RADIALLY AVERAGED PLASMA PARAMETERS FOR PLASMA RUNS USED IN ν_{eff} SCALING

PARAMETER	SYMBOL				RUN NUMBERS					UNITS
		AGS-1	AGR-1	AGO-1	AGN-1	AGP-3	AGP-2	AGO-2	AGP-1	AGQ-1	
Anode Voltage	V_A	900	700	800	1000	600	1070	930	1270	950	volts
Anode Current	I_A	160	78	138	63	46	128	98	30	40	mA
He Gas Pressure	P_{He}	952	1071	1214	833	1476	786	786	548	595	micro Torr
Magnetic Field[1]	B_0	1.8	1.4	1.4	1.1	1.1	1.1	1.14	1.1	0.9	KG
Number Density	$\hat{n}_e$	6.1	6.3	5.3	4.1	4.2	7.0	4.7	1.8	2.1	$10^9 \#/cm^3$
Electron Temperature	$\hat{T}_e$	28	16	21	24	11	32	15	29	58	eV
Ion Temperature	$\hat{T}_i$	15	17	15	19	13	28	19	20	58	eV
Plasma Frequency, e^-	Π_p	701	713	654	575	582	751	616	381	412	MHz
Ion Plasma Frequency	Π_{pi}	8.2	8.3	7.6	6.7	6.8	8.8	7.2	4.5	4.8	MHz
Gyro Frequency, e^-	Ω_e	5.0	3.8	4.0	3.2	3.2	3.2	3.8	3.2	2.5	GHz
Ion Gyro Frequency	Ω_i	0.68	0.52	0.54	0.43	0.43	0.43	0.52	0.43	0.34	MHz
Debye Length	λ_d	5.0	3.7	4.7	13.8	3.8	5.0	4.1	9.3	12.4	10^{-2} cm
Ion Gyro Radius	ρ_e	44.2	62.0	55.6	44.1	63.3	94.0	64.5	81.8	172.0	10^{-2} cm
Ion Sound Velocity	v_s	2.6	2.0	2.2	2.4	1.6	2.8	7.1	2.6	3.7	10^6 cm/sec
Ratio of Kinetic To Magnetic Pressure	β_p	2.1	2.2	2.2	3.1	1.4	6.8	1.5	1.6	6.1	10^{-6}
Ionization Fraction	I^*	1.9	1.7	1.3	1.4	0.8	2.6	1.7	1.0	1.0	10^{-4}

[1] Determined from $I_c vs. B_0$ calibration curve.

TABLE 5.3

ECR ABSORPTION CURVE DATA AND EFFECTIVE SPEED DEPENDENT COLLISION FREQUENCY COMPARISON

PARAMETER	SYMBOL	RUN NUMBERS									UNITS
		AGS-1	AGR-1	AGO-1	AGN-1	AGP-	AGP-2	AGO-2	AGP-1	AGQ-1	
Resonance Frequency[1]	f_r	4.940	3.662	3.708	3.093	3.108	3.151	3.860	3.060	2.540	GHz
Signal Attenuation @ f_r	P_m	-46/-36	-27	-41	-44	-29	-28	-23	-22	-11	dB
Full Width 3dB above f_r	$2\Delta f$	1/6	1.3	2.2	2.7	8.0	11.5	20.0	22	35.5	MHz
Electron-Neutral Coll. Freq.[2]	ν_{en}	2.7	3.1	3.5	2.4	4.1	2.2	2.2	1.6	1.5	MHz
	$\langle\nu\rangle^0$	1.1/5.5	1.4	2	2.2	5	8	13	11	15.5	MHz
Fitted Speed Dependent	$P(a = 0)$	-85/-39	-70	-54	-42	-27	-27.5	-18	-9.5	-8	dB
Effective Collision	$\langle\nu\rangle^{-1}$	1.1/5.1	1.4	2	2.1	5	8	13	11.5	16	MHz
Frequencies and Signal	$P_m(a=-1)$	-91/-40	-70	-54	-43	-27	27.6	-18	-9	-8	dB
Attenuations for Radially	$\langle\nu\rangle^{-2}$	1.1/5.0	1.4	1.96	1.8	5.2	7.7	13	12	17	MHz
Averaged Number Density	$P_m(a=-2)$	-91/-41	-70	-54.5	-46	-26.5	-28	-18.6	-10	-8.4	dB
	$\langle\nu\rangle^{-3}$	1.2/4.4	1.6	2.1	2.2	6	8.3	18	32	40	MHz
	$P_m(a=-3)$	-87/-41	-66	-53	-42	-25	-27.5	-18.5	-9	-8.3	dB
Gyro Frequency (fitted)	Ω_e	4.910	3.592	3.651	3.036	3.053	3.057	3.805	3.033	2.500	GHz

[1] Electron Cyclotron Upper Hybrid Resonance.
[2] From Figure 3.1 and using T_e radially averaged.

TABLE 5.4

TURBULENCE PARAMETERS FOR ELECTROSTATIC POTENTIAL FLUCTUATIONS

PARAMETER	LOCATION	RUN NUMBERS									UNITS
		AGS-1	AGR-1	AGO-1	AGN-1	AGP-3	AGP-2	AGO-2	AGP-1	AGQ-1	
Source-Coupling	R_1	6/30	5/30	6/30	5/40	5/100	6	5/40	5/100	6/60	KHz
Transition Frequency	R_2	6/60	5/50	5	5/70	5/60	6	5/70	5/50	5/70	KHz
Coupling-Dissipation	R_1	225	225	275	315	320	325	315	290	325	KHz
Transition frequency	R_2	225	265	250	235	260	315	200	255	250	KHz
Spectral Index	R_1	5.0/3.4	5.6/3.1	5.2/2.7	5.4/2.2	4.3/4.4	3.3	3.9/2.5	2.3/3.1	4.2/2.6	
Coupling Region	R_2	4.6/3.7	5.3/3.3	3.9	4.6/3.4	5.5/3.	3.4	4.7/2.3	2.4/3.0	4.2/2.4	
Spectral Index	R_1	2.0	2.3	5.3	1.5	2.0	4.0	5.2	3.5	1.6	
Dissipation Region	R_2	2.0	2.4	3.2	2.0	1.3	2.1	3.2	2.7	3.5	
Integrated Potential $20\mathrm{Log} \parallel \frac{e\phi}{T_e} \parallel_C$	R_1	5	8	7	-3	14	18	13	10	8	dB
Fluctuation Coupling	R_2	6	6	14	1	11	14	11	8	13	dB
Integrated Potential $20\mathrm{Log} \parallel \frac{e\phi}{T_e} \parallel_D$	R_1	-23	-25	-27	-32	-26	-20	-20	-16	-17	dB
Fluctuation Dissipation	R_2	-30	-40	-49	-34	-30	-23	-27	-15	-16	dB
Location Pair (R_1, R_2)		(4,2)	(3,0)	(5,2)	(6,2)	(4,2)	(5,3)	(5,2)	(3,0)	(4,0)	cm

TABLE 5.5

TURBULENCE PARAMETERS FOR DENSITY FLUCTUATION

DATA FROM MICROWAVE SCATTERING

PARAMETER	ANGLE					RUN	NUMBERS				UNITS
		AGS-1	AGR-1	AGO-1	AGN-1	AGP-3	AGP-2	AGO-2	AGP-1	AGQ-1	
Source-Coupling	75°	100	100	100	—	100	120	—	60	20	KHz
Transition Frequency	30°	85	100	75	100	40	50	—	40	30	KHz
Coupling-Dissipation	75°	225	280	350	—	250	330	—	200	215	KHz
Transition Frequency	30°	225	315	280	170	260	300	—	270	220	KHz
Spectral Index	75°	2.7	3.8	3.7	—	5.0	2.5	—	1.8	1.8	
Coupling Region	30°	3.7	5.0	4.3	4.3	3.5	3.0	—	2.6	3.2	
Spectral Index	75°	7.2	3.5	9.0	—	8.0	8.7	—	2.7	2.4	
Dissipation Region	30°	4.7	3.9	2.7	7.0	6.0	6.0	—	4.2	2.5	
Integrated Scattering	75°	-30	-32	-24	—	-26	-25	—	-20	-8	dB
Signal, Coupling $20\mathrm{Log}\ \Vert\langle\delta n_e\rangle\Vert_C$	30°	-31	-31	-22	-34	-32	-26	—	-24	-4	dB
Integrated Scattering	75°	-39	-44	-44	—	-42	-38	—	-26	-18	dB
Signal, Dissipation $20\mathrm{Log}\ \Vert\langle\delta n_e\rangle\Vert_D$	30°	-41	-53	-41	-43	-45	-45	—	-41	-23	dB

TABLE 5.6

TURBULENCE PARAMETERS FOR DENSITY FLUCTUATION

DATA FROM LANGMUIR PROBE

PARAMETER		RUN NUMBERS									UNITS
		AGS-1	AGR-1	AGO-1	AGN-1	AGP-3	AGP-2	AGO-2	AGP-1	AGQ-1	
Source-Coupling	e^-	70	70	80	—	80	70	—	60	90	KHz
Transition Frequency	e^+	70	50	50	—	50	30	—	40	30	KHz
Coupling-Dissipation	e^-	275	300	300	—	270	300	—	200	300	KHz
Transition Frequency	e^+	260	290	352	—	270	300	—	270	150	KHz
Spectral Index	e^-	4.4	4.3	3.8	—	5.0	3.1	—	3.8	5.0	
Coupling Region	e^+	3.6	4.4	3.7	—	4.6	2.8	—	3.8	4.0	
Spectral Index	e^-	5.4	4.4	9.5	—	6.0	4.5	—	6.0	5.0	
Dissipation Region	e^+	5.3	4.9	6.7	—	6.0	6.2	—	4.0	4.0	
Integrated Density $20\text{Log} \parallel \frac{\tilde{n}_e}{n_e} \parallel_C$	e^-	-4	-12	-23	—	-6	-0	—	-7	-13	dB
Fluctuations, Coupling	e^+	-7	-17	-14	—	-2	-9	—	-11	-4	dB
Integrated Density $20\text{Log} \parallel \frac{\tilde{n}_e}{n_e} \parallel_D$	e^-	-25	-33	-41	—	-26	-23	—	-23	-34	dB
Fluctuations, Dissipation	e^+	-27	-45	-39	—	-25	-20	—	-34	-25	dB
Radial Location		2	3	5	—	4	5	—	3.5	4	cm

Table 5.3 also lists the speed dependent collision frequency that yields the same collision broadened 3dB full width as measured experimentally. The attenuation at the resonance frequency f_r is also listed. These results follow from using Appleton's Equation in the form of Equation (4.78), with the dielectric tensor components in Equations (4.71) and (4.72). The radially averaged plasma frequencies were used. The electron gyro frequency was iterated from the values listed in Table 5.2 to yield a calculated resonance frequency that would match the measured resonance frequency. These data clearly indicate the problem of horn isolation in making measurements on a plasma with a low collision frequency. For an infinitely absorbing plasma, a leakage signal of at least 50 dB would be expected.

Tables 5.4 through 5.6 list data related to the level of electrostatic and density fluctuations in the plasmas. The absolute r.m.s. levels of fluctuating parameters are based on the analysis and calibration of the various diagnostics presented in Appendices A, B, and C. The total integrated fluctuation levels were computed graphically using Equation (C.28) and using $S(\omega) = S_0 \left(\frac{\omega}{\omega_0}\right)^{-m}$ for Equation (C.29). An error of $\pm$ 2dB was introduced for graphical interpreting.

Table 5.4 lists turbulence parameters for electrostatic potential fluctuations as detected by a radial capacitive probe at the midplane of the discharge. Parameters at two radial locations (R_1, R_2) are presented. Most data runs exhibited two transition frequencies in the inertial (source-coupling) region of the power spectra as well as two spectral indices. This was due primarily to the presence of a strong drift mode acting as an energy source.

Table 5.5 lists turbulence parameters for electron density fluctuations in the interior of the plasma. As discussed in Appendix B, the microwave diagnostic is sensitive to the scale size of fluctuations being detected. From Table B.1 the 30° scattering channel is most sensitive to fluctuations with perpendicular wavelengths of 4 cm. with a total spread of 5 cm. The 75° scattering channel is most sensitive to perpendicular wavelengths of 1.7 cm, with a total spread of 0.7 cm. Data for the integrated signals clearly show that the energy in the coupling region is fairly evenly distributed among scale sizes, whereas in the dissipative region more energy is present in the small scale sizes.

Table 5.6 lists turbulence parameters for electron and ion density fluctuations detected by a Langmuir probe. The Langmuir probe used had a tungsten tip 0.6 cm. in length. Fluctuation data were taken with a Langmuir probe, primarily for comparison with the electrostatic potential measurements of the capacitive probes and to qualitatively investigate the weak turbulence approximation (Horton 1984)

$$\tilde{n}_e \simeq \overline{n}_e \left[1 - i\delta_e\right] \frac{e\tilde{\phi}}{T_e} , \tag{5.1}$$

where δ_e is the dissipative contribution resulting in the phase shift between $\tilde{n}_e$ and $\tilde{\phi}$. By comparing Table 5.6 with Table 5.4 one can see that the integrated fluctuation levels in the dissipative region of the spectrum are comparable, except at the higher turbulence levels (Runs AGP-1 and AGQ-1). The integrated levels in the inertial regions differ significantly due to the scale size problem of a small Langmuir probe adequately sampling density fluctuations of large scale.

The data in Table 5.4 illustrates the increase in level of potential fluctuations in the dissipative region of the spectra with increasing collisional broadening $2\Delta f$. For comparison of the ν_{eff} theory of Galeev and Sagdeev [1965] with measured absorption data, the radial profile of absolute fluctuation amplitudes was required.

For runs AGO-1, AGP-3, AGP-2, AGO-2, AGP-1, and AGQ-1, radial profile data of the frequency integrated level of potential fluctuations in the dissipative region were taken. Using the approximation,

$$\frac{W}{n_0 T_e} \simeq \sum_{w} \mid \frac{e\hat{\phi}}{KT_e} \mid^2 \tag{5.2}$$

and the density profile data in Appendix H, the radial profile of ν_{eff} was determined for these runs. These results are shown in Figure 5.6.

Using the results in Figure 5.6 and the radial profiles of electron number density n_e, the absorption parameters for the extraordinary mode wave were calculated by evaluating the homogeneous dielectric tensor (Equations 4.50 and 4.51) in one centimeter increments and summing the contributions. This can be considered only as a weak approximation to the inhomogeneous plasma of the Penning discharge. Figure 5.7 shows the comparison between the $2\Delta f$ width calculated using the radial profile in Figure 5.6 and the experimentally measured $2\Delta f$ width.

Table 5.7 summarizes the comparison between measured absorption parameters and those calculated for an inhomogeneous plasma. For the calculated data, the average electron-neutral collision frequency was added to the ν_{eff} profiles in Figure 5.6. These results show a reasonable comparison between measured and calculated values. The results for AGO-1, however, indicate that the inhomogeneous density profile tends to broaden the calculated absorption curve. The contribution of ν_{eff} to ν_{tot} was small in this case so that the electron-neutral collision frequency was dominant. Here the measured broadening of 2.2 MHz was less than the electron-neutral collision frequency of 5.5 MHz. This put a lower bound on measurement resolution of approximately ± 1.5 MHz.

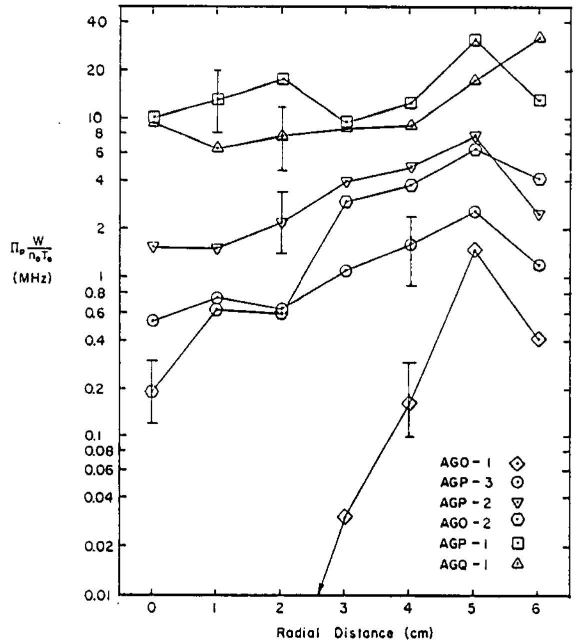

Figure 5.6. Radial profile of ν_{eff} calculated from integrated potential fluctuation data.

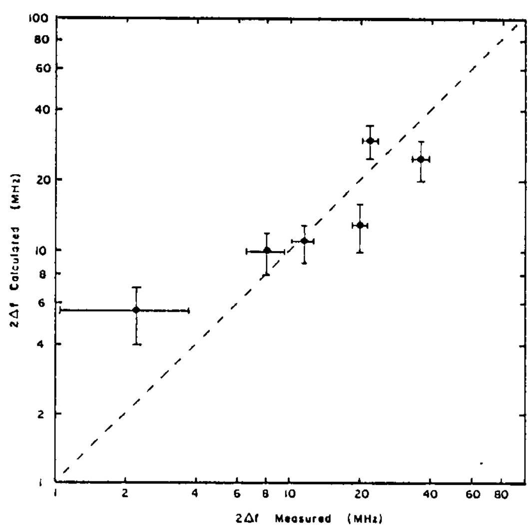

Figure 5.7. Comparison of $2\Delta f$ width calculated from radial profile of ν_{eff} with $2\Delta f$ width measured experimentally.

TABLE 5.7

COMPARISON OF MEASURED ABSORPTION PARAMETERS[1] WITH CALCULATED VALUES USING INHOMOGENEOUS ν_{eff} PROFILE*

PARAMATER	AGO-1	AGP-3	AGP-2	AGO-2	AGP-1	AGQ-1	UNITS
Electron-neutral Collision Frequency	3.5	4.1	2.2	2.2	1.6	1.5	MHz
Resonance Frequency							f_r
Measured	3.708	3.108	2.151	3.860	3.060	2.540	GHz
Calculated	3.718	3.118	3.160	3.859	3.060	2.540	GHz
Signal Attenuation							@f_r Pmin
Measured	-41	-29	28	-23	-22	-11	dB
Calculated	-29	-21	-25	-24	-8	-10	dB
Full Width 3dB above Pmin; $2\delta f$							
Measured	2.2	8	11.5	20	22	36	MHz
Calculated	5.5	10	11	13	30	25	MHz

[1] For extraordinary mode wave using the homogeneous Appleton Equation.
*See Figure 5.6. The average electron-neutral collision frequency was added to the ν_{eff} profile for calculated absorption data.

In order to test the effect of a turbulent electron collision frequency on coherent drift modes, the experimental configuration shown in Figure 2.3 was used. The elongated anode cylinder of the arrangement produced conditions favorable for coherent drift modes and allowed the application of an external forcing signal. The forcing signal was applied to the anode cylinder using the transformer network discussed in Appendix E and produced symmetric excitation of the plasma column. This signal was used to directly enhance the dissipative region of the turbulent spectrum and broaden the absorption spectrum of the extraordinary mode wave.

Appendix I lists radial profiles of plasma parameters and calibrated electrostatic potential fluctuation spectra for two pairs of data runs. Runs AGU-1 and AGV-2 were runs that produced coherent self-excited drift modes. Runs AGU-2 and AGV-2 had a 12 MHz high voltage RF signal applied to the anode cylinder. The change in the $2\Delta f$ collisional broadening from Run AGU-1 to Run AGU-2 was 1 MHz to 6 MHz. The change in the collisional broadening from Run AGV-1 to AGV-2 was 2 MHz to 6 MHz. Figure 5.8 shows the amplitude increase of the self-excited 5 kHz drift mode in Run AGU-1 to the larger amplitude mode in Run AGU-2 with extended forcing. The complete spectra are shown in Figures I.2 and I.3 for Run AGU-1 and Figures I.5 and I.6 for Run AGU-2. Figure 5.9 shows the amplitude change of the self-excited 15 kHz drift mode in Run AFV-1 to Run AGV-2 with external forcing. Here the mode's amplitude is increased in the outer region and damped in the plasma core. The total fluctuation spectra are shown in Figures I.10 and I.11 for Run AGV-1 and Figures I.13 and I.14 for Run AGV-2.

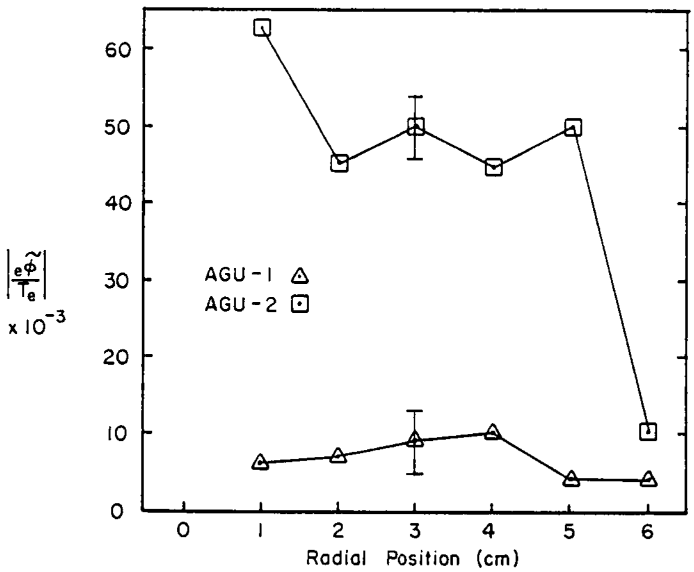

Figure 5.8. Radial profile of 5 kHz drift wave amplitude (1Hz bandwidth) for Runs AGU-1 and AGU-2.

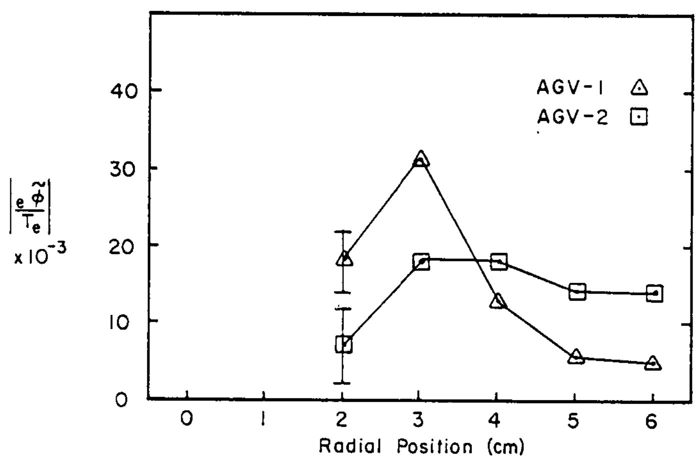

Figure 5.9. Radial profile of 15 kHz drift wave amplitude (1Hz bandwidth) for Runs AGV-1 and AGV-2.

CHAPTER VI

CONCLUSIONS

A weakly ionized Penning discharge has been operated in a turbulent steady state mode. The collisional broadening near the upper hybrid resonance of the extraordinary mode wave was measured on this plasma. Using the homogeneous Appletion Equation and measured electrostatic fluctuation data, the turbulent collision frequency introduced by Galeev and Sagdeev [1965]

$$\nu_{eff} = \omega_p \, \frac{W}{n_0 K T_e} \, , \tag{6.1}$$

was compared to measured values of collisional broadening of the upper hybrid resonance (Table 5.7). The total wave energy density W in Equation (6.1) was taken to be the integrated fluctuations in the dissipative region of the spectra and approximated by

$$\frac{W}{n_0 K T_e} \cong \sum_{\omega} \mid \frac{e\tilde{\phi}}{KT_e} \mid^2 \, . \tag{6.2}$$

For improved comparison between theory and experiment the inhomogeneous plasma was taken into account by incrementally evaluating the homogeneous dielectric tensor (Table 5.1).

Quasi-thermal effects due to finite beam geometry were determined not to be important for these measurements. By evaluating the warm plasma dielectric tensor for the extraordinary mode wave propagating at a small angle from normal, effects due to a finite temperature plasma were determined to be small for the collisional plasma studied (Table 3.5).

Using external forcing, the level of turbulent fluctuations was artifically enhanced and the resonance curve broadened. This produced a plasma with enhanced collisionality and increased the amplitude of coherent resistive drift modes within the plasma (Figures 5.8 and 5.9). This result demonstrates qualitatively the indirect but strong coupling between large scale structures and the integrated effects of small scale structures in a turbulent plasma.

LIST OF REFERENCES

LIST OF REFERENCES

[1]. Abramowitz, M. and I.A. Stegun, "Handbook of Mathematical Functions," Dover, New York, 1970.

[2]. Akama, H. and M. Nambu, *Anomalous resistivity in an inhomogeneous plasma*, Phys. Fluids **30** (1987), 275-277.

[3]. Akhiezer, A.I., I.A. Akhiezer, R.V. Polin, A.G. Sitenko and K.N. Stepanov, "Plasma Electrodynamics," Vol. 2, Pegamon Press, 1975.

[4]. Akhiezer, I.A., *On the interaction of charged particles and a turbulent plasma*, Sov. Phys. JETP **20** (1975), 445-451.

[5]. Alexandrov, A.F., L.S. Bogdankevich and A.A. Rukhadze, "Principles of Plasma Physics," Springer-Verlag, Berlin, Heidelberg, 1984.

[6]. Balanis, C.A., "Antenna Theory: Analysis and Design," Harper and Row, New York, 1982a.

[7]. Balanis, C.A., "Antenna Theory: Analysis and Design," p. 588, Harper and Row, New York, 1982b. (These data are originally due to: Hu.Y.Y., *A method of determining phase centers and its application to electromagnetic horns,* Journal of Franklin, Institute, Vol. 271, pp. 31-36, January 1961).

[8]. Bhatnagar, P.L., E.D. Gross and M. Krook, *A Model for collision processes in gases I. Small amplitude processes for charges and neutral one-component systems*, Phys. Rev. **94** (1954), 511-525.

[9]. D.L. Book, "NRL Plasma Formulary," Office of Naval Research, Washington D.C., 1983.

[10]. Braginski, S.I., *Transport phenomena in a completely ionized two-temperature plasma*, Soviet Phys. JETP **6** (1958), p. 358.

[11]. Braginski, S.I., "Reviews of Plasma Physics," Vol 1, M.A. Leontovich, ed., Consultants Bureau, New York, 1965.

[12]. Brennan, M.H., B.L. Jessup and I.R. Jones, *Determination of plasma density and temperature profiles using magneto-acoustic oscillations*, J. Plasma Physics **18** (1977), 33-44.

[13]. Chen, C.M., "Introduction to Plasma Physics and Controlled Fusion," Plenum Press,, 1988.

[14]. Chen, F.F., *Universal overstability of a resistive, inhomogeneous plasma*, Phys. Fluids **8** (1965), 1323-1333.

[15]. Choi, Duk-In and W. Horton Jr., *Modified Kadomtsev spectrum from renormalized plasma turbulence theory*, Phys. Fluids **17** (1974), 2048-2060.

[16]. Chu, T.K., B. Coppi, H.W. Hendel and F.W. Perkins, *Drift instabilities of a uniformly rotating cylinder*, Phys. Fluids **12** (1969), 203-208.

[17]. Cross, R.C., *Radio-frequency heating of a plasma*, Can. J. Phys. **48** (1970), 2888-.

[18]. Decker, J.F. and A.M. Levine, *Parametric suppression of large-amplitude plasma instability*, Phys. Rev. Lett. **28** (1972), 286-289.

[19]. Dubovĭ, L.V. and P.G. Popov, *Stabilization of a powerful Penning discharge by a radially increasing magnetic field*, Sov. Phys. JETP **22** (1966), 19-21.

[20]. Elagin, N.I. and S.D. Fanchenko, *Investigation of turbulent heating of a plasma as a function of ion mass*, Sov. Phys. JETP **40** (1975), 674-677.

[21]. Eletsky, A.V. and B.M. Smirnov, "Handbook of Plasma Physics," Chapter 1, Vol. 1, A.A. Galeev and R.N. Sudan, eds., North-Holland Pub., 1983.

[22]. Frommelt, J.J.B. and I.R. Jones, *The use of magneto-acoustic oscillations as a plasma diagnostic technique*, J. Plasma Phys. **14** (1970), 373-387.

[23]. Galeev, A.A. and Segdeev, R.Z., "Handbook of Plasma Physics," Chapter 4.3, vol. 1, M.N. Rosenbluth and R.Z. Sagdeev eds., North Holland, New York.

[24]. Galeev, A.A. and R.Z. Sagdeev, "Reviews of Plasma Physics," Vol. 7, M.A. Leontovich, ed., Consultants Bureau, New York, 1965.

[25]. Geller, R. and J. Hosea, *Electron collision frequencies*, Report EUR, CEA-FC-459 Association - Euratom - C.E.A. , Fontenay-aux-Roses (Seine) France.

[26]. Hamberger, S.M. and M. Friedman, *Electrical conductivity of a highly turbulent plasma*, Phys. Rev. Lett. **21** (1968), 674-676.

[27]. Hamberger, S.M. and J. Jancarik, *Experimental studies of electrostatic fluctuations in a turbulently heated plasma*, Phys. Fluids **15** (1972), 825-836.

[28]. Heald, M.A. and C.B. Wharton, "Plasma Diagnosicts with Microwaves," Krieger Pub., New York, 1978.

[29]. Hendel, H.W., T.K. Chu and P.A. Politzer, *Collisional drift waves-identification, stabalization and enhanced transport*, Phys. Fluids **11** (1968), 2426-2439.

[30]. Henrici, P., "Applied and computational complex analysis," Vol 1, Wiley Interscience, New York, 1985.

[31]. Hershcovitch, A. and P.A. Politzer, *Suppression of an instability by the introduction of external turbulence*, Phys. Fluids **22** (1979), 249-256.

[32]. Hewlett Packard, "Operating Information Booklet for 8510 Network Analyzer, part # 83592-90002," Hewlett Packard, Palo Alto, CA, 1983.

[33]. Hewlett Packard, "Spectrum Analysis: Noise Measurements, Applications Note 150-4," Hewlett Packard, Palo Alto, CA, 1974.

[34]. Hinton, F.L. and C.W. Horton Jr., *Amplitude limitation of a collisional drift wave instability*, Phys. Fluids **14** (1971), 116-123.

[35]. Hirshfield, J.L. and S.C. Brown, *Microwave method for measuring the probability of elastic collisions of electrons in a gas*, J. Appl. Phys. **29** (1958), 1749-1752.

[36]. Hoh, F.C., *Instability of Penning-type discharges*, Phys. Fluids **6** (1963), 1184-1191.

[37]. Horton, W., "Handbook of Plasma Physics," Chapter 6.4, Vol 2, M.N. Rosenbluth and R.Z. Sagdeev, eds., North Holland Pub., New York, 1984.

[38]. Horton, W., Duk-In Choi and R.A. Koch, *Scaling laws and asymptotic states for ion acoustic turbulence*, Phys. Fluids **22** (1979), 797-798.

[39]. Horton, W., *Spectral distribution of drift-wave fluctuations in Tokamaks*, Phys. Rev. Lett. **37** (1976), 1269-1272.

[40]. Ichimaru, S., "Basic Principles of Plasma Physics," W.A. Benjamin, Inc., Massachusetts, 1980.

[41]. Janev, R.K., W.D. Langer, K. Evans Jr. and D.E. Post Jr., "Elementary Processes in Hydrogen-Helium Plasma," Springer-Verlag, Berlin, Heidelberg, 1987.

[42]. Jassby, D.L., *Transverse velocity shear instabilities within a magnetically confined plasma*, Phys. Fluids **15** (1972), 1590-1604.

[43]. Jones, W.D., H.J. Doucet and J.M. Buzzi, "An Introduction to the Linear Theories and Methods of Electrostatic Waves in Plasmas," Plenum Press, New York, 1985.

[44]. Kawai, Y. and M. Gnyot, *Observation of anomalous resistivity caused by ion acoustic turbulence*, Phys Rev. Lett. **39** (1977), 1141-1144.

[45]. Kent, G.I., N.C. Jen and F.F. Chen, *Transverse Kelvin-Helm holtz instability in a rotating plasma*, Phys. Fluids **12** (1969), 2140-2151.

[46]. Koch, R.A. and W. Horton Jr., *Effects of angle scattering in plasma waves*, Phys. Fluids **18** (1975), 861-865.

[47]. Knorr, G., F.R. Hansen, J.P. Lynov, H.L. Pécseli and J.J. Rasmussen, *Finite Larmor radius effects to arbitrary order*, Phys. Scr. **38** (1988), 829-834.

[48]. Kruer, W.L., J. Katz, J. Byers and J. DeGroat, *Plasma heating by large-amplitude, low-frequency electric fields*, Phys. Fluids **15** (1972), 1613-1616.

[49]. Krawczonek, W.M., J.R. Roth, G.E. Boyd, J.Y. Hong and E.J. Powers, *A data acquisition and handling system for the measurement of radial plasma transport rates*, Proc. of the Seventh Symp. on Engineering Problems of Fusion Research **1** (1977), p. 392.

[50]. Legg, V.E., Bell system Tech J. **15** (1936), p. 39.

[51]. Liepmann, H.W. and D.M. Nosenchuck, *Active control of Laminar-turbulent transition*, J. Fluid Mech. **118** (1982), 201-204.

[52]. Lio, S.Y., *Microwave Devices and Circuits*, Prentice-Hall, Englewood Cliffs, New Jersey.

[53]. Manheimer, W.M. and R. Flynn, *Anomalous resistivity and ion-acousitc turbulence*, Phys. Rev. Lett. **27** (1971), 1175-1179.

[54]. Mase, A. and T. Tsukishima, *Measurements of ion wave turbulence by microwave scattering*, Phys of Fluids **18** (1975), 464-469.

[55]. Mazzucato, E., *Low-frequency microinstabilities in the PLT tokamak*, Phys Fluids **21** (1978), 1063-1068.

[56]. Mikhailovskii, A.B., V.D. Lakhin, L.A. Mikhailovskaya and O.G. Onishehenko, *On the theory of vortices in plasma*, Sov. Phys. JETP **59** (1985), 1198-1205.

[57]. Miyamoto, K., "Plasma Physics for Nuclear Fusion," MIT press, 1980.

[58]. Motley, R.M., "Q Machines," Academic Press, New York, 1975.

[59]. Penning, F.M. and K. Nienhuis, *Construction and design of a new design of the Philips vacuum gage*, Philips Tech Rev. **11 No. 4** (1957), 116-122.

[60]. Perkins, F.W. and D.L. Jassby, *Velocity shear and low-frequency plasma instabilities*, Phys. Fluids **14** (1971), 102-115.

[61]. Rosenberg, D., P. Spence, M. Laroussi and J.R. Roth, *Scaling for radiated RF power for classical and modified Penning discharge*, APS Bulletin **30** (1985).

[62]. Rosenbluth, M.N. and A. Simon, *Finite Larmor radius equations with nonuniform electric fields and velocities*, Phys. Fluids **8** (1965), 1300-1322.

[63]. Roth, J.R., "Introduction to Fusion Energy," Ibis Pub., Charlottesville, VA, 1986.

[64]. Roth, J.R., *Modification of Penning discharge useful in plasma physics experiments*, Rev. Sci. Inst. **37** (1966), 1100-1101.

[65]. Roth, J.R., *Spectral index and sense of energy cascading in a turbulent hot ion plasma*, APS Bulletin **15** (1970), p. 1427.

[66]. Roth, J.R. and M. Clark, *Analysis of integrated charged particle energy spectra from gridded electrostatic analyzers*, Plasma Phys. **11** (1969), 131-143.

[67]. Roth, J.R. and M. Clark, *Analysis of integrated charged particle energy spectra from gridded electrostatic analyzers,*, NASA TN D-4718 (1968).

[68]. Roth, J.R. and W.M. Krawczonek, *Paired comparison test of the relative signal detected by capacitive and floating Langmuir probes in turbulent plasma from 0.2 to 10 MHz*, Rev. Sci. Inst. **42** (1972), 589-594.

[69]. Roth, J.R., *Energy distribution functions of kilovolt ions in a modified Penning discharge*, Plasma Physics **15** (1973), 995-1005.

[70]. Ruthroff, C.L., *Some broadband transformers*, Proc. IRE (1959), 1337-1343.

[71]. Sagdeev, R.Z. and Z.A. Galeev, "Nonlinear Plasma Theory," Chapter 4, W.A. Benjamin, Inc., New York, 1969.

[72]. Schmidt, G., "Physics of High Temperature Plasma," Academic Press, New York, 1979.

[73]. Seshadri, S.R., "Fundamentals of Plasma Physics," Elsevier Pub., New York, 1973, pp. 76-83.

[74]. Sheffield, J., "Plasma Scattering of Electromagnetic Radiation," Academic Press, New York, 1975.

[75]. Shkarofsky, I.P., *Values of the transport coefficients in a plasma for any degree of ionizaiton based on a Maxwellian distribution*, Can. J. Phys. **39** (1961), 1619-1679.

[76]. Shkarofsky, I.P., I.B. Bernstein and B.B. Robinson, *Condensed presentation of transport coefficients in a fully ionized plasma*, Phys. Fluids **6** (1963), 40-47.

[77]. Simonen, T.C., T.K. Chu and H.W. Hendel, *Feedback control of collisional drift waves by modulated parallel electron-current sink experiments and interpertation*, Phys. Rev. Lett. **23** (1969), 568-571.

[78]. Sitenko, A.G. and K.N. Stepanov, *On the oscillations of an electron plasma in a magnetic field*, Sov. Phys. JETP **4** (1957), 512-520.

[79]. Sitenko, A.G., "Electromagnetic Fluctuations in Plasma," Academic Press, New York, 1967.

[80]. Soohoo, Ronald F., "Theory and Application of Ferrites," Prentice-Hall, New Jersey, 1960.

[81]. Stix, T.H., *Finite-Amplitude collisional drift waves*, Phys. Fluids **12** (1969), 627-639.

[82]. Swanson, D.G., "Plasma Waves," Academic Press, San Diego, CA., 1989.

[83]. Sy, W.N-C., *Magneto-acoustic oscillations in a current carrying plasma column*, Plasma Phys. **20** (1978), 33-44.

[84]. Tchen, F.F., "Introduction to Plasma Physics and Controlled Fusion," Plenum Press,, 1988.

[85]. Theimer, O. and R. Theimer, *Effects of collisions on the random density fluctuations in a plasma*, Plasma Phys. **15** (1973), 837-852.

[86]. D.J. Tritton, "Physical Fluid Dynamics," Oxford University Press, New York, 1988.

[87]. Waniek, R.W., R.T. Grannan and D.G. Sanson, *Anomalous cyclotron radiation from a plasma discharge*, Appl. Phys. Lett. **5** (1964), 89-90.

[88]. Whitham, G.B., "Linear and Nonlinear Waves," Wiley-Interscience, New York, 1974.

[89]. Wong, A.Y. and F. Hai, *Direct measurements of linear growth rates and nonlinear saturation coefficients of instabilities*, Phys. Rev. Lett. **23** (1969), 163-166.

APPENDICES

APPENDIX A

Capacitive Probes

Figure A.1 shows design details of the capacitive probes used to detect potential fluctuations in the turbulent plasma. These probes are constructed of semi-rigid coaxial cable and fitted with a copper tube body for use with a sliding "O" ring feedthrough. The probe couples to the plasma by having a portion of the center conductor exposed and fitted with a small spherical drop of soft solder. A quartz shield is then slid over the exposed center conductor and several centimeters of the semi-rigid coaxial cable. The opposite end of the probe is fitted with a commercial BNC connector to allow shielded connection to a detecting circuit. When in use, the copper tube housing is grounded to the experiment's framework with a stranded ground strap.

For quantitative measurements of the turbulent potential fluctuations, the amplitude and frequency response of the probe must be known. Figure A.2 shows a bench test arrangement for probe testing. By inserting a probe axially between the plates of a circular parallel plate capacitor (13 cm. dia., 1.9 cm. spacing), the probe tip couples capacitively to the ungrounded plate of the parallel plate capacitor.

The coupling capacitance between the probe tip and the flat plate is given approximately as the capacitance between a sphere and an infinite plate. In free space this capacitance is given by [Smythe 1968];

$$C = 4\pi\varepsilon_0 \; r_1 \sinh(\alpha) \sum_{n=1}^{\infty} \operatorname{csch}(n\alpha) \ , \tag{A.1}$$

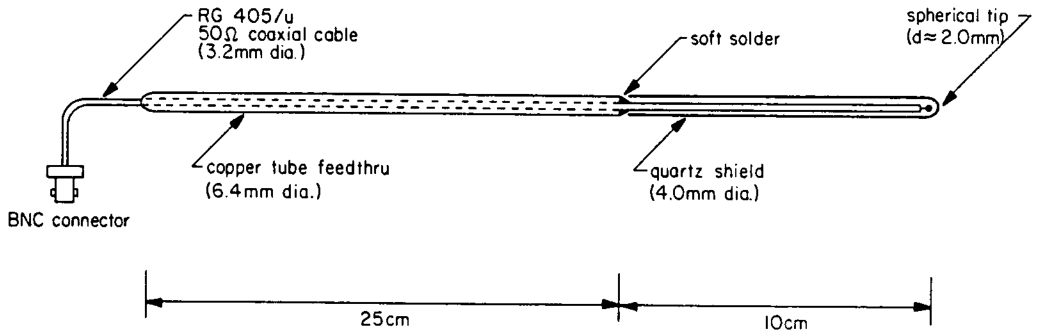

Figure A.1. Capacitive probe design detail.

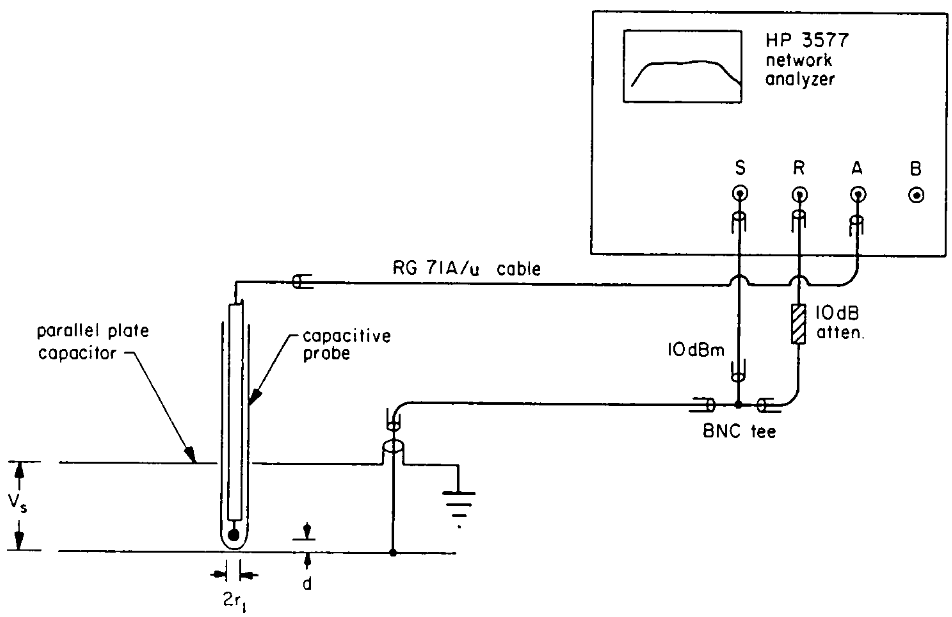

Figure A.2. Capacitive probe bench test set up.

where $d = r_1 \cosh(\alpha)$. This capacitance is shown graphically in Figure A.3 for the range in size and spacing relavant to this work. The summation has been carried out to $n = 20$. Due to the quartz shield and close spacing, the spherical tip of the probe is effectively embedded in a dielectric of quartz. Hence, the value of a coupling capacitance given by Figure A.3 must be multipled by the relative dielectric constant of quartz where $\varepsilon_r = 3.8$.

With the coupling capacitance of the probe determined, an equivalent circuit for the probe and detecting circuit can be modeled. Figure A.4 shows such a circuit for low frequency operation (i.e. with no transmission line effects). The shunt capacitances C_{pr}, C_c and C_d are due to the probe itself, the connecting cable and the detection circuit respectively. This network acts as a voltage divider with the ratio of the source voltage and detector voltage given by

$$\frac{V_d}{V_S} = \frac{C_{11}}{C_S + C_{11} - j\left(\frac{1}{\omega R}\right)}, \tag{A.2}$$

where $C_S = C_{pr} + C_c + C_d$. For $C_S \gg C_1$ and $C_S \gg 1/\omega R$, the network behaves as a capacitive voltage divider with both voltages in phase and related by,

$$\frac{V_d}{V_S} \simeq \frac{C_{11}}{C_S}. \tag{A.3}$$

Figure A.5 shows the frequency response of probe A. This response compares well with the probes built and tested by Roth and Krawczonek [1971]. The network analyzer has been set up so that the source signal is $-10\ dB_m$ and the input impedance on Channel A is $R_d = 1M\Omega$, $C_d = 30\ pf$. The probe response is normalized by dividing the probe's response with the shield in place to its response with the probe tip shorted to the ungrounded plate of the test capacitor. The

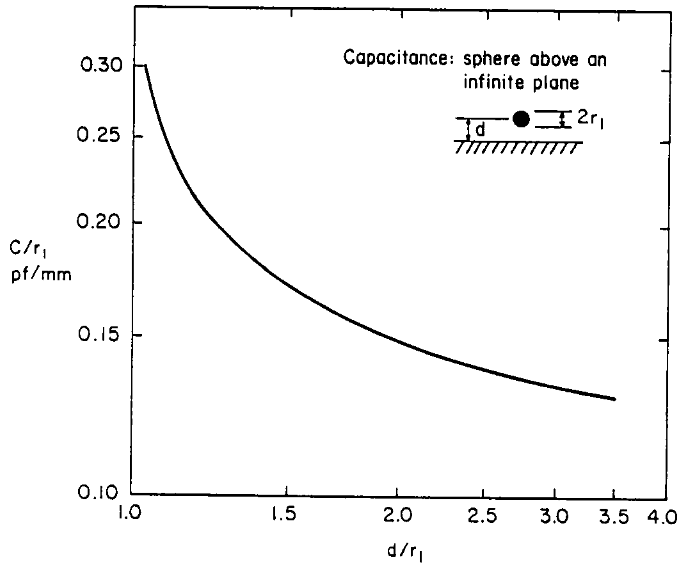

Figure A.3. Coupling capacitance for a sphere above an infinite plane in free space.

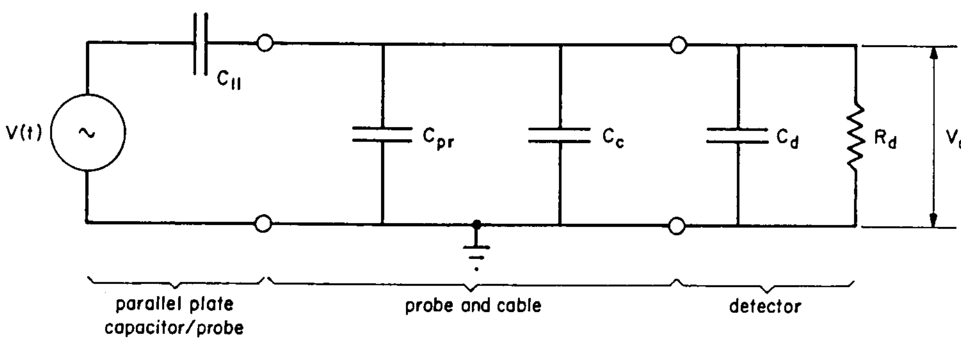

Figure A.4. Low frequency equivalent circuit for capacitive probe in bench test setup (Figure A.2).

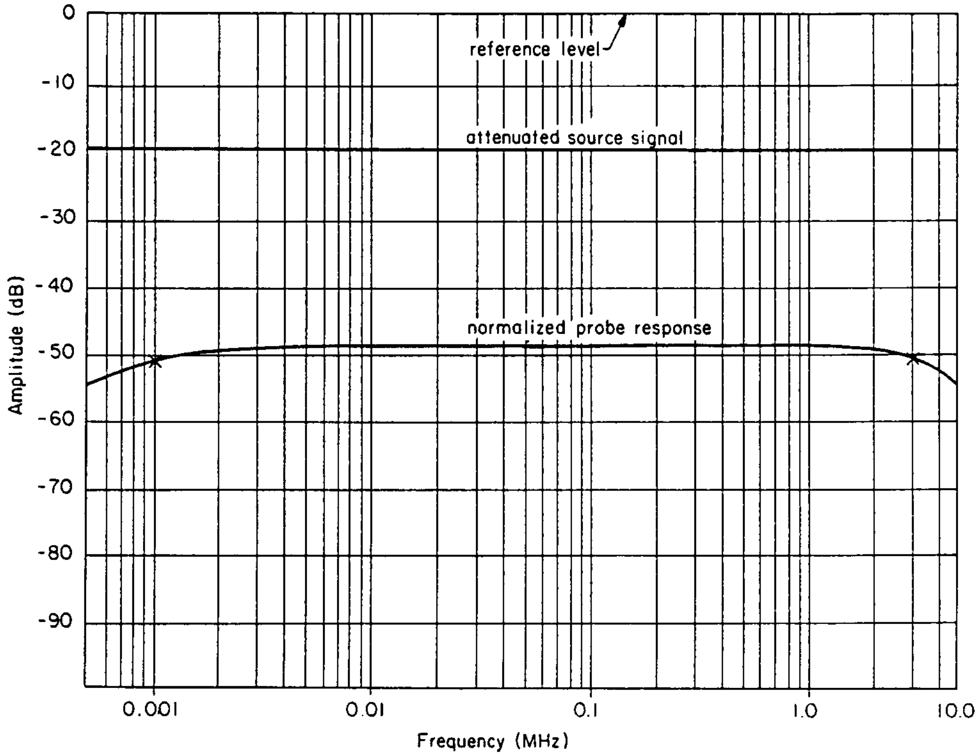

Figure A.5. Capacitive probe frequency response for bench test setup (Figure A.2).

probe's coupling in the passband is shown as $-49dB$ in power, or $-24.5dB$ in voltage. For $d/r_1 \simeq 3.5$ Figure A.3 gives $C'_{11} = .13\ pf$, and with $C_{pr} + C_c = 145\ pf$ the voltage gain in dB is given by

$$\frac{V_d}{V_S} \simeq 10 \log \frac{\varepsilon_r C_{11}}{C_S} , \tag{A.4}$$

$$\frac{V_d}{V_S} = -25.5\ dB , \tag{A.5}$$

yielding only a 1 dB diffrence from the measured value.

For a capacitive probe immersed in a plasma, the situation is somewhat more complicated and the coupling coefficient determined by a bench test is inadequate. Consider Figure A.6 with a probe surrounded by a plasma. A plasma sheath [Seshadri 1973] will form about the surface of the quartz shield. In this region a slight departure of charge neutrality will exist so that $n_e \neq n_i$. Any potential fluctuations existing in the plasma must couple through this sheath and the capacitance determined by the probe tip to the surface of the quartz shield.

The capacitance between the probe tip and the surface of the quartz tube can be measured by immersing the probe tip in a mercury bath. By measuring the capacitance between the probe tip and the mercury bath the coupling capacitance between tip and shield (C_{12}) is known. This measurement is best facilitated by letting the probe tip be at high potential and adequately grounding the probe housing. For probe A, $C_{12} = 0.35\ pf$ and for probe B, $C_{12} = 0.40\ pf$.

Since the plasma has a complex relative dielectric permittivity ε_p, the equivalent circuit for a probe in a plasma becomes slightly more complicated than the circuit in Figure A.4. Figure A.7 shows a low frequency equivalent circuit for the capacitive probe in a plasma. The parameters C_{12}, C_{pr}, C_c, C_d and R_d are all known or

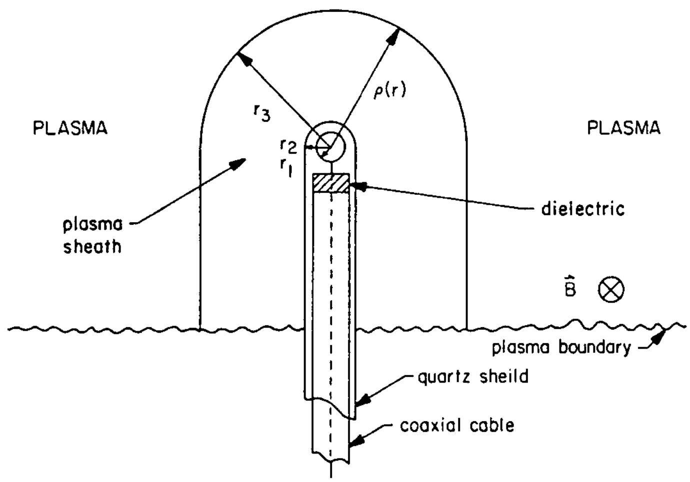

Figure A.6. Capacitive probe immersed in a plasma.

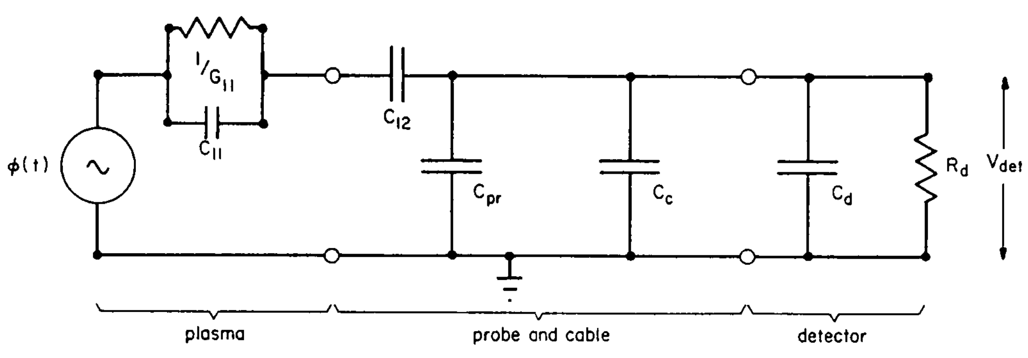

Figure A.7. Low frequency equivalent circuit for a capacitive probe in a plasma (Figure A.6).

measured. The parameters C_{11} and G_{11} must be calculated with G_{11} a conductance due to the imaginary part of ε_p.

In order to determine C_{11} and G_{11} the probe sheath must be analyzed. For spherical symmetry and with magnetic field effects neglected, Poisson's equation relates the charge distribution to the static potential $\Phi(r)$,

$$\frac{1}{r^2}\frac{d}{dr}\left(r^2\,\frac{d\Phi(r)}{dr}\right) = \frac{\rho(r)}{\varepsilon_0\varepsilon_\rho}\ , \tag{A.6}$$

where $\rho(r) = e(n_e(r) - n_i(r))$. Taking the electron density to be related to the electrostatic potential $\Phi(r)$ by a Boltzmann distribution (adequate for a plasma close to equilibrium)

$$n_e(r) = n_0 \exp\left(\frac{e\Phi(r)}{T_e}\right)\ . \tag{A.7}$$

Letting $e\Phi/T_e$ be small and n_0 a constant, the electron density is given by

$$n_e(r) \approx n_0\left(1 + \frac{e\Phi(r)}{T_e}\right)\ . \tag{A.8}$$

Taking the ion density to be constant, $n_i = n_0$, the charge density may be written

$$\rho(r) \simeq \left(\frac{\varepsilon_0\varepsilon_\rho}{\lambda_d^2}\right)\ \Phi(r)\ , \tag{A.9}$$

where

$$\lambda_d = \left|\ \frac{\varepsilon T_\varepsilon}{e^2 n_0}\ \right|^{\frac{1}{2}} \tag{A.10}$$

is the electron Debye length with $\varepsilon = \varepsilon_0|\varepsilon_p|$.

The spherical Poisson equation now becomes

$$\frac{1}{r^2}\frac{d}{dr}\left(r^2\,\frac{d\Phi(r)}{dr}\right) = \frac{1}{\lambda_d^2}\ \Phi(r)\ , \tag{A.11}$$

with boundary conditions

$$\Phi = \Phi_{f\ell} \qquad\qquad r = r_2 \ ,$$

and

$$\Phi = 0 \qquad\qquad r = \infty \ .$$

The solution for $\Phi(r)$ with the given boundary condition is

$$\Phi(r) = A \ \frac{\exp\left(-r/\lambda_d\right)}{r} \ , \tag{A.12}$$

with

$$A = \Phi_{f\ell} r_2 \exp\left(\frac{r_2}{\lambda_d}\right) \ . \tag{A.13}$$

With $\Phi(r)$ known, the capacitive coupling between the surface of the quartz shield and the plasma sheath can be computed using the definition of capacitance,

$$C = \frac{Q}{\Delta\Phi} \ , \tag{A.14}$$

where Q is the total charge in the sheath and $\Delta\Phi$ is the change in potential across the sheath. The total charge Q is given by,

$$Q = \int_{\text{vol}} \rho(r) d \text{ vol} \tag{A.15}$$

$$= A \ \frac{\varepsilon_0 \varepsilon_\rho}{\lambda_d^2} \int_0^{2\pi} \int_{-\frac{\pi}{2}}^{\frac{\pi}{2}} \int_{r_2}^{\infty} \frac{\exp\left(\frac{-r}{\lambda_d}\right)}{r} \ r^2 \ \sin \ \Theta \ d \ \Theta \ d\Phi' dr \tag{A.16}$$

$$\approx 4\pi\varepsilon_0\varepsilon_\rho \ \frac{A}{\lambda_d^2} \int_{r_2}^{r_2+n\lambda_d} \exp\left(\frac{-r}{\lambda_d}\right) \ dr \tag{A.17}$$

$$\approx 4\pi\varepsilon_0\varepsilon_\rho A \left(\frac{r}{\lambda_d} + 1\right) \ \exp\left(\frac{-r}{\lambda_d}\right) \Bigg|_{r_2}^{r_2+n\lambda_d} \ . \tag{A.18}$$

The radial integration has been terminated at an integer number of Debye lengths because it is a characteristic self-shielding length of a plasma.

The potential difference across this charge volume is,

$$\Delta\Phi = A \left. \frac{\exp\left(\frac{-r}{\lambda_d}\right)}{r} \right|_{r_2}^{r_2+n\lambda_d} . \tag{A.19}$$

The coupling capacitance C_{11} is then given by

$$C_{11} = 4\pi\varepsilon_0\varepsilon_\rho r_2 \, \frac{(\alpha+1)\exp(-\alpha) - (\alpha+n+1)\exp(-\alpha-n)}{\frac{\exp(-\alpha-n)}{1+n/\alpha} - \exp(-\alpha)} , \tag{A.20}$$

for $\alpha = \frac{r_2}{\lambda_d}$.

The value of $C'_{11} = C_{11}/\varepsilon_\rho$ as a function of r_2/λ_d for $n = 1, 2, 3$ is plotted in Figure A.8.

The conductance G_{11} is given by

$$G_{11} = \omega C'_{11} Im[\varepsilon_\rho] . \tag{A.21}$$

and the ratio of the detected voltage to the source voltage for the circuit in Figure A.7 becomes

$$\frac{V_d}{\Phi} = \frac{C_{12}\overline{C}_{11}}{\left(C_S - i\frac{1}{wR_d}\right)\left(C_{12} + \overline{C}_{11}\right) + C_{12}\,\overline{C}_{11}} , \tag{A.22}$$

where $\overline{C}_{11} = C'_{11}(Re[\varepsilon_\rho] - i\ Im[\varepsilon_\rho])$.

For the weakly ionized plasma of the Penning discharge, the charge Q is considered as free and $\varepsilon_p \approx \varepsilon_0$. A correction using the drift approximation $\mathbf{V}_\perp = \mathbf{E} \times \mathbf{B}/B^2$ yields a correction factor (Book 1983)

$$\frac{\varepsilon_p}{\varepsilon_0} = 1 + 36\pi \times 10^9 \, \frac{\rho_m}{B^2} , \tag{A.23}$$

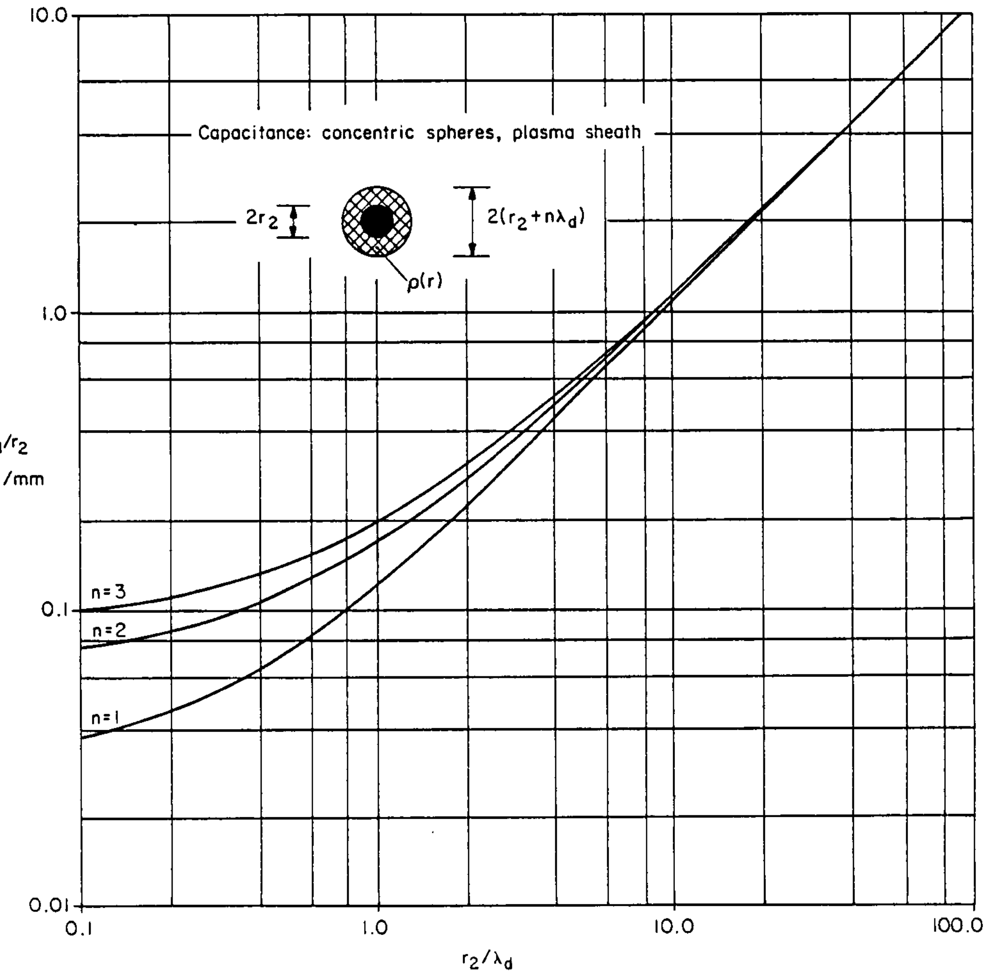

Figure A.8. Coupling capacitance for quartz shield to plasma sheath in spherical model.

where ρ_m is the mass density.

For experimental data reduction the capacitance value for $n = 3$ was used from Figure A.8. This value was multiplied by $\frac{2}{3}$ to account for the probe geometry being hemispherical - cylindrical rather than purely spherical. The factor $\frac{2}{3}$ was based on measurements of the capacitance C_{12} and its relation to calculated values of C_{12} based on the probe geometry.

APPENDIX B

MICROWAVE SCATTERING SYSTEM

A two channel microwave scattering system has been used to study the random electron density fluctuations of the plasma interior. Figure B.1 shows a schematic of the system used. An input L.O. (local oscillator) signal at $\omega_i = 14$ GHz is coupled through a 10 dB coupler to a microwave horn and launched into the plasma column. The linearly polarized wave is launched in the ordinary mode with the wave's electric field vector parallel to the static magnetic field, $\mathbf{B_0}$. The incident wave is weakly scattered primarily by electrons [Sheffield 1975], with some of the scattered wave collected by receiving horns A and B. The scattered R.F. (radio frequency) signal at ω_S will be a signal centered at ω_i with side bands of the spectrum of electron density fluctuations. By down converting the scattered R.F. signals in mixers A and B, a low frequency I.F. (intermediate frequency) signal is produced. This I.F. signal is proportional to the amplitude spectrum of electron density fluctuations. For a properly calibrated scattering system with known scattering volume and scattering cross section, the total power of the scattered signal can be directly related to the level of electron density fluctuations in the plasma.

The important parameters to be measured for a calibrated scattering system are the characteristics of the various microwave components used and the overall system noise level. The microwave horns and mixers are the most important components of the system in Figure B.1. For the microwave horns, the radiation patterns, gains, and reflection coefficients must be measured. For mixers A and B, the conversion efficiency of the R.F. signal to the I.F. signal and the frequency response must be

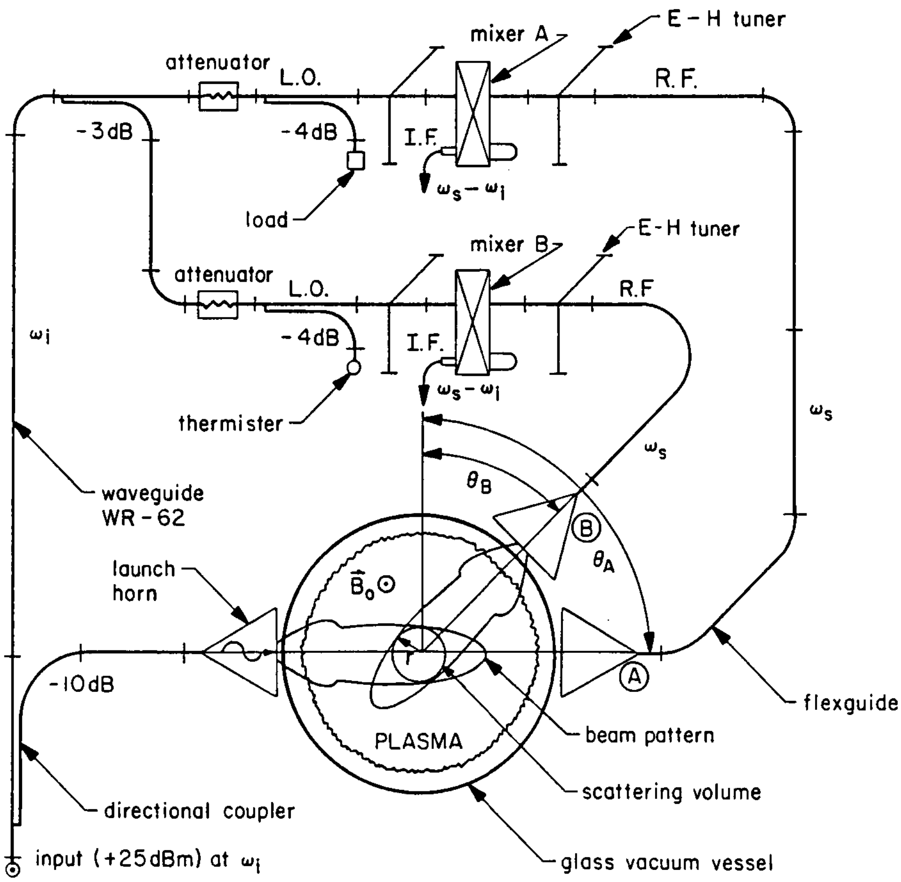

Figure B.1. Two channel microwave scattering system used for electron density fluctuation measurements.

measured. The system's noise level is determined primarily by the high gain amplifier used to generate the local oscillator signal and the quality of the diodes used in mixers A and B.

Three identical horns were constructed for the scattering system. The measured reflection coefficient for these horns was $\Gamma = -18\ dB \pm 0.5\ dB$ at 14 GHz. The gain of the horns was measured by aligning two horns for maximum reception with matched polarity and using the Friis transmission equation [Balanis 1982a] is

$$\frac{P_r}{P_t} = \left(\frac{\lambda}{4\pi R}\right)^2 G_r G_t \ , \tag{B1}$$

where P_r is the power delivered to the receiving load, P_t is the input power to the transmitting horn, G_r and G_t are the directive gain of the receiving and transmitting horns respectively, and $(\lambda/4\pi R)^2$ is the free space loss factor due to the spherical spread of the radiated energy. The distance R is the separation distance of the phase centers of the horns and λ is the free space wavelength of the radiation. Using graphical data [Balanis 1975b], the phase center for a horn was determined to be located approximately at the center of the horn's aperture.

Using a Hewlett Packard 8510 Network Analyzer to measure P_r/P_t and normalize cable responses, a horn gain of $G_0 = 17.2\ dB$ or 53 was measured at 14 GHz for $R = 35$ cm and with $G_0 = G_r = G_t$. If a 180° section of glass identical to the glass of the vacuum system was placed in front of the transmitting horn a 1.1 dB reflection-transmission loss was observed. The horn gain under these condition was measured to be 16.6 dB or 46.

The radiation pattern of the horns was measured by orienting the horns as in the gain measurement, and then normalizing so that $P_r/P_t = 0\ dB$. The receiving horn was then held at constant R and rotated about an axis thrrough the phase center of the transmitting horn. The ratio P_t/P_t was then measured in 2.5 and 5.0 degree increments. Figures B.2 and B.3 show the radiated power pattern in the plane of the **E** field, and Figures B.4 and B.5 show the power pattern in the plane of the **H** field. Both sets of curves include the effects of a curved section of glass placed in front of the transmitting horn.

For use in determining the scattering volume, the radiation patterns are characterized in terms of a 3 dB beam width; the angle at which the radiated power is one half its maximum value. For the **E** plane, $2\Theta_{be} = 22° \pm 1°$ and for the H plane, $2\Theta_{bh} = 27° \pm 1°$. Since the beam pattern is not symmetric an average beam angle of $2\Theta_b = 24.5° \pm 1°$ is used.

Using the measured radiation patterns and the horn's directivity, the percentage of the total radiated power which is radiated into the 3 dB beam width can be determined. Introducing the radiated power density [Balanis, 1975a]

$$\text{watts} = W_r r \qquad watts/m^2 , \tag{B.2}$$

or

$$W = \frac{A_0 F(\Theta)}{r^2} , \tag{B.3}$$

where $F(\Theta)$ is the pattern factor shown in Figures B.2 and B.3 for the **E** plane and in Figures B.4 and B.5 for the **H** plane, and A_0 is the peak power. The radiation intensity is given by

$$U = r^2 W_r \qquad \text{watts/steradian} , \tag{B.4}$$

and the total radiated power by;

$$P_{\text{rad}} = \int_o^{2\pi} \int_0^{\frac{\pi}{2}} U \ \sin\,\Theta \ d\Theta \ d\Phi \qquad \text{watts} . \tag{B.5}$$

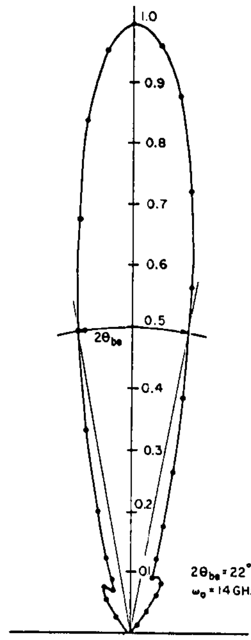

Figure B.2. Linear polar plot of E plane power pattern including glass effects.

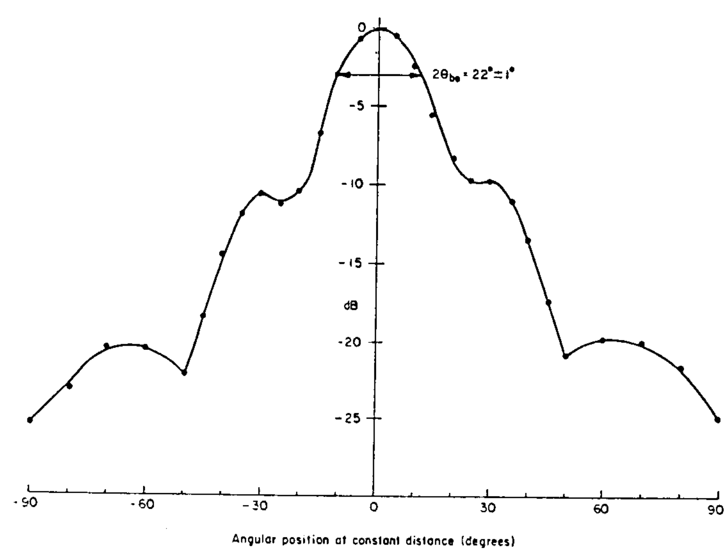

Figure B.3. E plane power pattern including glass effects.

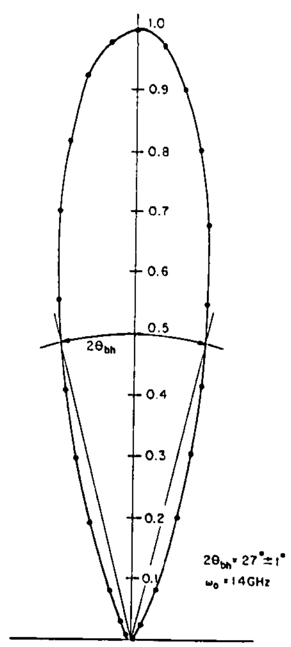

Figure B.4. Linear polar plot of H plane power pattern including glass effects.

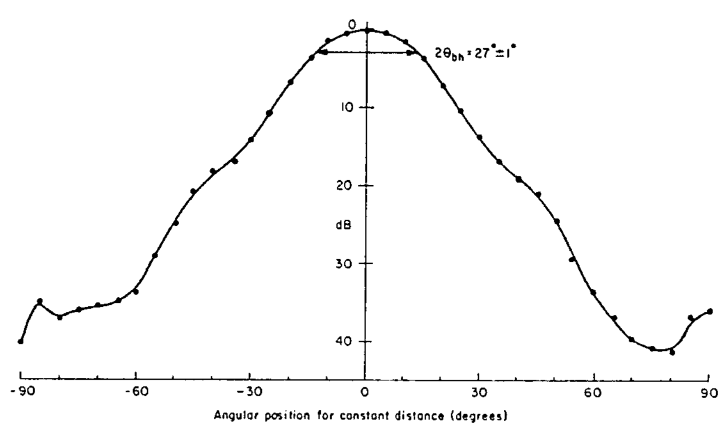

Figure B.5. H plane power pattern including glass effects.

The horn's directivity D_0 is defined as

$$D_0 = \frac{4\pi U_{\mathbf{max}}}{P_{\mathbf{rad}}} \,, \tag{B.6}$$

where $U_{\mathbf{max}} = A_0$. The directivity D_0 is related to the gain G_0 used in the Friis transmission equation by

$$G_0 = \varepsilon_{re} \left[1 - |\Gamma|^2\right] \, D_0 \,, \tag{B.7}$$

where ε_{re} is the radiating efficiency of the horn.

Rewriting Equation (B.5) and neglecting any back lobes in the radiation pattern, the total radiation power is given by

$$P_{\mathbf{rad}} = A_0 \int_0^{2\pi} \int_0^{\pi/2} F(\Theta) \sin \, \Theta \, d\Theta \, d\Phi \,, \tag{B.8}$$

and the power radiated into the 3 dB beam width is

$$P_{\Theta_b} = A_0 \int_0^{2\pi} \int_0^{\Theta_b} F(\Theta) \, \sin \, \Theta \, d\Theta \, d\Phi \,. \tag{B.9}$$

Taking $F(\Theta)$ to be given by Figure B.3 for the **E** plane and by Figure B.5 for the **H** plane, and performing the integrals in Equations (B.8) and (B.9) numerically using Simpsons rule, yields

$$\left.\begin{aligned} D_0 &= 46 \qquad &\text{(B.10)} \\ \frac{P_{\Theta_b}}{P_{\mathbf{rad}}} &= 34.1\% \qquad &\text{(B.11)} \end{aligned}\right\} \mathbf{E}\text{ plane}$$

and

$$\left.\begin{aligned} D_0 &= 49 \qquad &\text{(B.12)} \\ \frac{P_{\Theta_b}}{P_{\text{rad}}} &= 48.0\% \qquad &\text{(B.13)} \end{aligned}\right\} \textbf{H} \text{ plane.}$$

Averaging the **E** plane and **H** plane directivities and power ratios for use as a symmetric beam yields,

$$\overline{D}_0 = 47 \; , \tag{B.14}$$

and

$$\frac{P_{\Theta_b}}{Prad} = 41\% \; . \tag{B.15}$$

Relating D_0 to the value of G_0, measured with the effects of the glass section, through Equation (B.7) gives a radiating efficiency of $\varepsilon_{re} = 97.7\%$.

The calibration of mixers A and B is performed with the test arrangement shown in Figure B.6. The double balanced mixers A and B are both Microwave Associates model 1119A hybrid orthotee balanced mixers with MA 4901 ER diodes. They are supplied with local oscillator signals at $\omega_0 = 14$ GHz of known amplitude. For testing mixer B, the diodes of mixer A are pumped with an I.F. signal of frequency ω_m. The output R.F. signal of mixer A at $\omega_0 \pm \omega_m$ is fed to mixer B and coupled to an HP 8555A spectrum analyzer. The R.F. signal sent to mixer B is then down converted to an I.F. signal at ω_m which is measured on channel B of the HP 3577 network analyzer ($z_0 = 50\ \Omega$). By ramping the amplitude of the I.F. signal to mixer A with ω_m held constant, the down conversion loss of mixer B is measured. In order to eliminate the up conversion loss of mixer A, the power in the sidebands

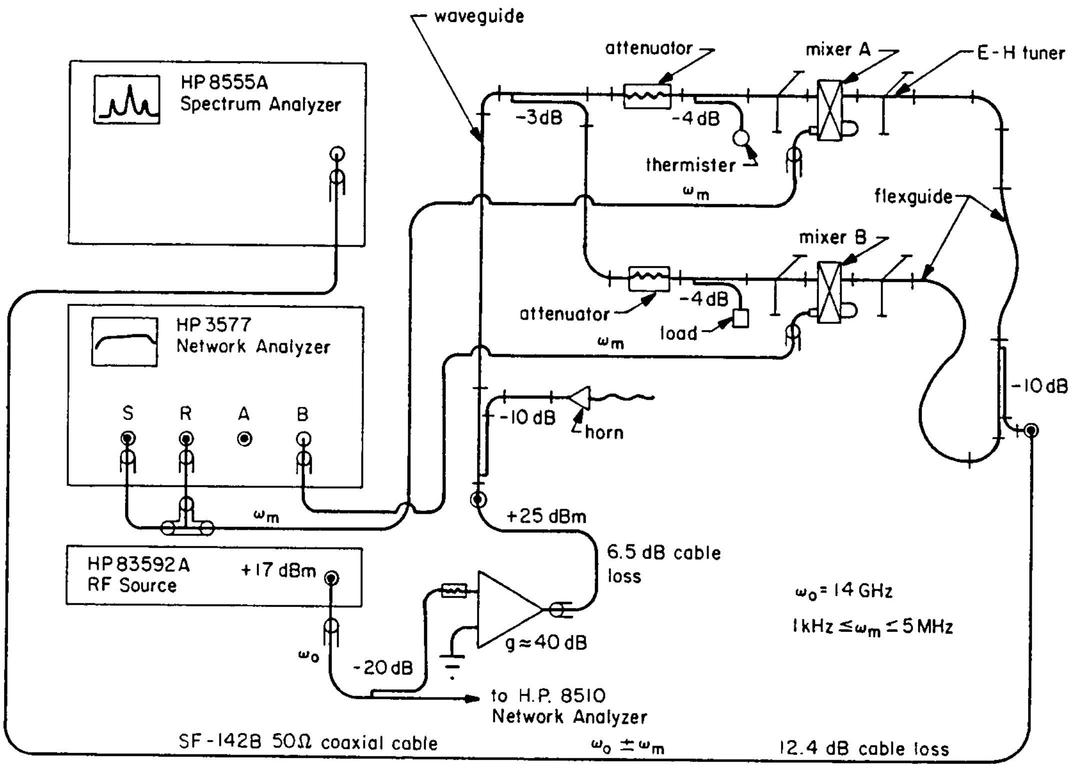

Figure B.6. Test arrangement for measuring mixer frequency response and conversion efficiency.

of the R.F. signal is measured on the HP 8555A spectrum analyzer. Reversing the roles of the I.F. signals of mixers A and B and reversing the 10 dB coupler for the spectrum analyzer allows the down conversion loss of mixer A to be measured. The mixer's I.F. frequency response is measured with the same set-up as that used for the amplitude response measurement, except with the I.F. amplitude held constant and ω_m swept over the frequency range of interest. Both measurements should be done with the E-H tuners properly adjusted for maximum response. These tuners acts as impedence matching transformers to allow maximum power transfer to or from the mixers.

Figures B.7 and B.8 show the swept amplitude responses of mixers A and B. The calibration points are where the power in the sidebands of the R.F. signal is measured on the HP 8555A spectrum analyzer. The measured down conversion losses of 9.6 ± 0.2 dB for mixer A and 12.4 ± 0.2 dB for mixer B are valid only for the L.O. signal level of $+5.0$ dBm. The conversion efficiency of the diodes is typically a strong function of the L.O. amplitude and frequency.

Figures B.9 and B.10 show the frequency response of mixers A and B for different R.F. signal levels. The change above 2 MHz is due to an improved match between the I.F. port of the mixer and the 50 Ω port of the network analyzer. The I.F. port impedance is typically 400 Ω, but tends to decrease with higher frequency due to the contact capacitance in the diode holders of the mixer.

The noise level of the I.F. signal was measured by using a wide band power meter. A 10 dB difference between an I.F. signal for no plasma and an I.F. with a plasma was required for acceptable data. Redundant grounding of the scattering system hardware aids in reducing stray electrostatic pick-up.

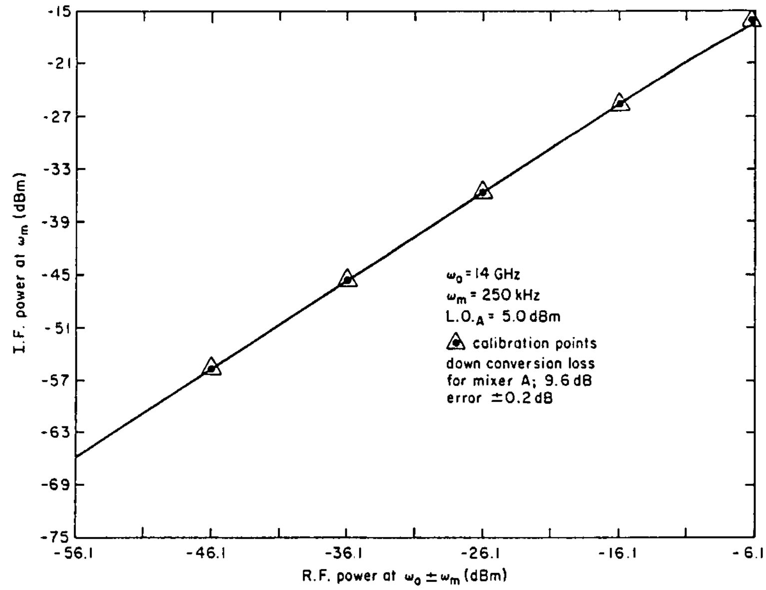

Figure B.7. Amplitude sweep of R.F. power versus I.F. power for mixer A.

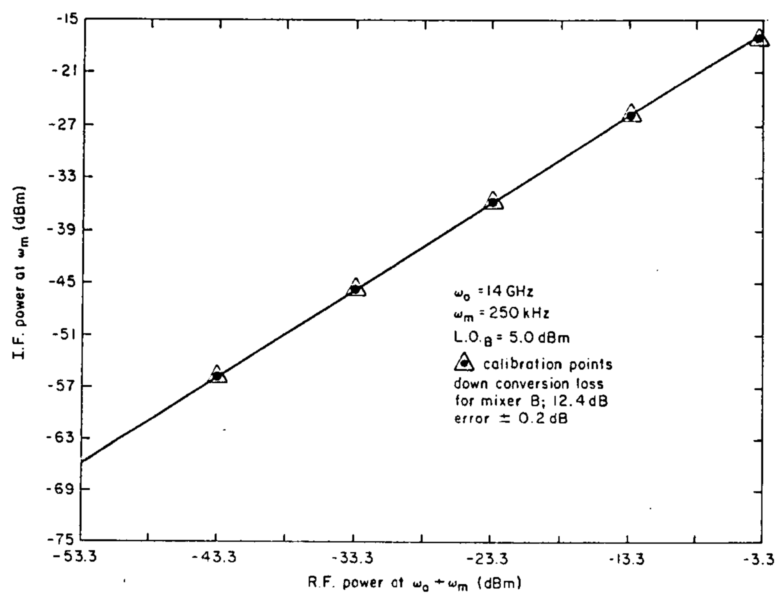

Figure B.8. Amplitude sweep of R.F. power versus I.F. power for mixer B.

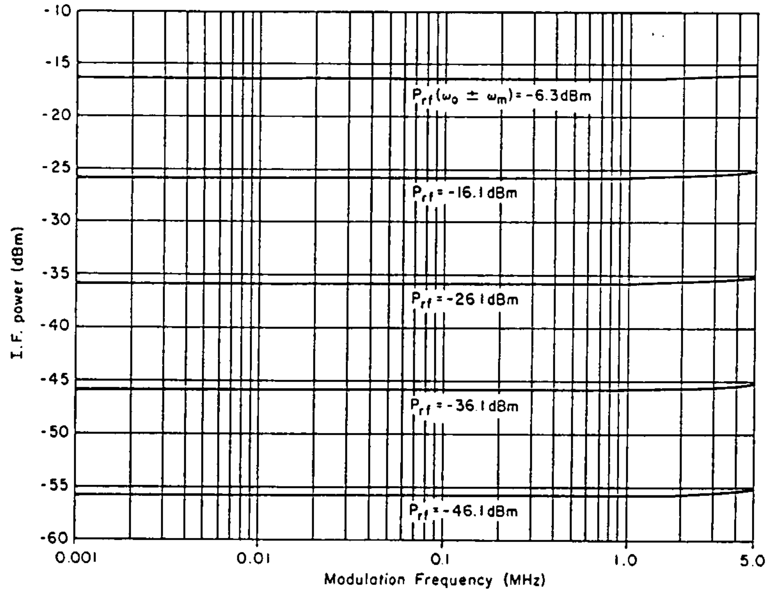

Figure B.9. Mixer A linearity for various R.F. signal levels.

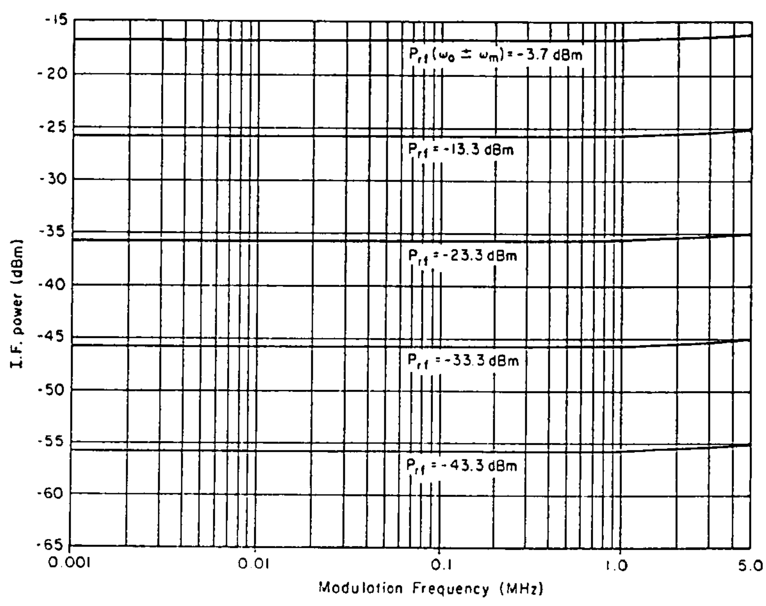

Figure B.10. Mixer B linearity for various R.F. signal levels.

The process of incoherent scattering of an incident microwave beam by random electron density fluctuations for the system shown in Figure B.1 can be described by the first order Born approximation [Heald and Wharton 1975]. In this approximation the scattering is considered sufficiently weak that the incident wave is ot significantly altered. This implies that $\omega_i \gg \omega_{co}$, where ω_{co} is the cutoff frequency ($\omega_{co} \simeq \omega_p$), and that the incident electric field is small enough that it does not perturb the plasma. The perturbed velocity of the electrons due to the incident electric field E_i, should therefore be much smaller than the electron thermal velocity,

$$\frac{eE_i}{n_e \omega_i} \ll u_{th} \ . \tag{B.16}$$

The incident electric field is related to the incident power density P_i by

$$P_i = \frac{E_i^2}{2Z_0} \ , \tag{B.17}$$

where $Z_0 = \sqrt{\varepsilon/\mu}$ is the wave impedence. The incident power density in terms of the total radiated beam power P_{rad} is

$$P_i = P_{\text{rad}} \ \frac{G_0 F(\Theta)}{4\pi R^2} \ , \tag{B.18}$$

where G_0 is the directive gain of the antenna as before and $F(\Theta)$ is the power pattern factor. Combining Equations (B.16), (B.17) and (B.18) yields the following criteria for the total radiated beam power,

$$P_{\text{rad}} \ll 2\pi R^2 \ \frac{\omega_i^2 u_{th}^2 m_e^2}{Z_0 G_0 e^2} \ \text{watts} \tag{B.19}$$

with R the distance from the horn's phase center to the region of interest. For $P_{\text{rad}} \simeq 30$ milliwatts, $R = 9$ cm, $T_e = 30\ eV, G_0 = 46, Z_0 \simeq 377$ ohms and $\omega_i =$ 14GHz, Equation (B.19) yields;

$$3 \times 10^{-2} \ll 9.8 \times 10^4 \ \text{watts}. \tag{B.20}$$

Within the above limits and with no mode conversion of the incident wave [Sitenko 1965], the incident and scattered waves will satisfy energy and momentum conservation. Referring to Figure B.11, the incident and scattered wave vectors and corresponding frequencies will satisfy,

$$\mathbf{k} = \mathbf{k}_S - \mathbf{k}_i \ , \tag{B.21}$$

and

$$\omega = \omega_S - \omega_i \ . \tag{B.22}$$

Using the law of cosines, the magnitude of the wave vector $\mathbf{k}$ will be related to the scattering angle Θ_S,

$$k^2 = (k_i^2 + k_S^2 - 2k_S k_i \ \cos \ \Theta_S) \ . \tag{B.23}$$

In the limit $v \ll c$ for $\omega = \mathbf{k} \cdot \mathbf{v}$, where $\mathbf{v}$ is the velocity associated with density fluctuations, then $k_i \sim k_S$ and

$$||\mathbf{k}|| = 2||\mathbf{k}_i|| \ \sin\left(\frac{\Theta_S}{2}\right) \ . \tag{B.24}$$

Since $\mathbf{k}$ is predominantly perpendicular to the static magnetic field $\mathbf{B}_0$, let $\mathbf{k} \rightarrow k_\perp$. The spectrum of fluctuations given by ω in Equation (B.22) will therefore be due to density fluctuations of wavelength,

$$\lambda_\perp = \left(\frac{\lambda_i}{2 \ \sin(\Theta_S/2)}\right) \ , \tag{B.25}$$

where λ_i is the wavelength of the incident radiation. The spectrum of fluctuations measured at a given scattering angle Θ_S will result from a spread in $\lambda_\perp$ due to the

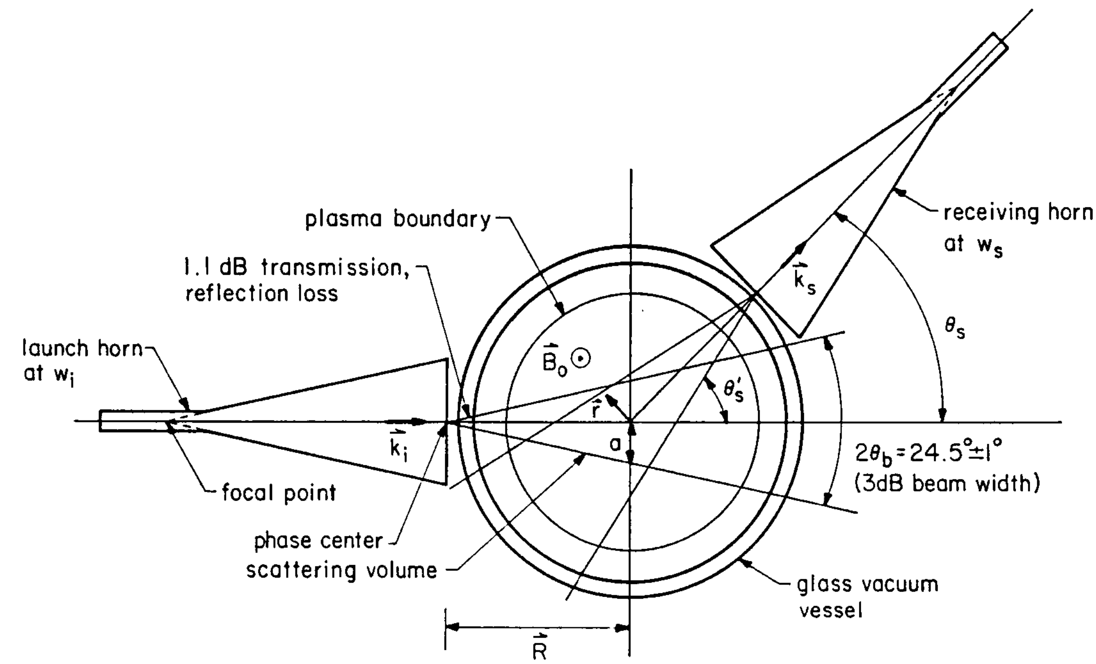

Figure B.11. Beam geometry used for determining the scattering volume and wave vector resolution.

finite beam geometry. This spread in $\lambda_\perp$ is determined by the spread in Θ_S of $\pm\Theta_b$, where $2\Theta_b$ is the averaged 3 dB beam width of the receiving horn.

The differential power density dP_S at frequency ω_S scattered into a receiving horn is related to an average scattering cross section σ of the scattering volume given by [Muzzucato 1977],

$$dP_s = \overline{\sigma}\; P_i \Omega_S \; dV \;, \tag{B.26}$$

where $P_i(\mathbf{r})$ is the incident power density, $\Omega_S(\mathbf{r})$ is the effective solid angle of reception, and dV is the differential scattering volume. The quantities $P_i(\mathbf{r})$ and $\Omega_S(\mathbf{r})$ are related to the radiation pattern factor and horn gain G_0 by

$$P_i(\mathbf{r}) = \frac{P_{\text{rad}} G_0 F(\Theta_\ell)}{4\pi |\mathbf{R}_\ell - \mathbf{r}|^2} \;, \tag{B.27}$$

and

$$\Omega_S(\mathbf{r}) = \frac{\lambda_i^2 G_0 F(\Theta_\ell)}{4\pi |\mathbf{R}_r - \mathbf{r}|^2} \;, \tag{B.28}$$

where the vectors $\mathbf{R}_\ell$ and $\mathbf{R}_r$ locate the phase centers of the launch and receiving horns with respect to the center of the scattering volume, and $\mathbf{r}$ spans the scattering volume. Integrating Equation B.26 over the total scattering volume, yields the total power scattered into a receiving horn as a function of the power radiated into the scattering volume and an average scattering cross section

$$P_S = P_{\text{rad}}\; \overline{\sigma} \left(\frac{G_0 \lambda_i}{4\pi} \right)^2 \int_V \frac{F(\Theta_\ell) F(\Theta_r)}{|\mathbf{R}_\ell - \mathbf{r}|^2 |\mathbf{R}_r - \mathbf{r}|^2} \; dV \;. \tag{B.29}$$

The scattered power will contain the spectrum of electron density fluctuations through the fluctuations of the cross section σ. For a magnetized plasma, the differential scattering cross section of electrons for waves scattered into an element of solid angle due to electron density fluctuations is given by [Sitenko 1965],

$$d\sigma = \frac{n_0}{2\pi}\left(\frac{e^2}{m_e c}\right)^2 \frac{\omega_i^2 \omega_S^2}{\omega_p^4}\,\mathbf{R}|\zeta|^2 < \delta n_e^2 >_{k,\Delta\omega} d\omega d\Omega \ , \tag{B.30}$$

where $< \delta n_e^2 >_{k,\Delta\omega}$ is the density-normalized spectral density of low frequency electron density fluctuations expressed as a correlation function over the frequency interval $\Delta\omega$. The factors R and ζ are coefficients related to the complex polarization vector $\mathbf{e}$, the plasma dielectric premittivity tensor ε_{ij} and the refractive index η of the plasma. For a uniform plasma with thermal motion and collisions neglected,

$$R = \frac{\eta^3}{\eta_0\left(|\mathbf{e}_0|^2 - \frac{|\mathbf{e}_0 \cdot \mathbf{k}|}{k_0^2}\right) e_i^* \varepsilon_{ij} e_j} \ , \tag{B.31}$$

and

$$\zeta = e_i^* \left(\varepsilon_{ij}^0 - \delta_{ij}\right) e_j^0 \ , \tag{B.32}$$

where

$$\mathbf{e}_0 = \left[\ 1; \frac{i\varepsilon_2^0}{\eta_0^2 - \varepsilon_1^0}\ ;\ \frac{\eta_0^2 \sin\ \Phi_0 \cos\ \Phi_0}{\eta_0^2\ \sin^2\ \Phi_0 - \varepsilon_3^0}\ \right] \ , \tag{B.33}$$

and

$$\mathbf{e} = \left[\cos\ \Theta_S - \frac{i\varepsilon_2}{\eta^2 - \varepsilon_1}\ \sin\ \Theta_S;\ \sin\ \Theta_S + \frac{i\varepsilon_2}{\eta^2 - \varepsilon_1}\ ;\ \frac{\eta^2 \sin\ \Phi\ \cos\ \Phi}{\eta^2 \sin^2\ \Phi - \varepsilon_3}\right], \tag{B.34}$$

with

$$\varepsilon_{ij} = \begin{vmatrix} \varepsilon_1 & -i\varepsilon_2 & 0 \\ i\varepsilon_2 & \varepsilon_1 & 0 \\ 0 & 0 & \varepsilon_3 \end{vmatrix} \tag{B.35}$$

for

$$\varepsilon_1 = 1 - \frac{\omega_p^2}{\omega_S^2 - \omega_b^2} \ , \tag{B.36}$$

$$\varepsilon_2 = \frac{\omega_b}{\omega_S}\ \frac{\omega_p^2}{\omega_S^2 - \omega_b^2} \ , \tag{B.37}$$

and

$$\varepsilon_3 = 1 - \frac{\omega_p^2}{\omega_S^2} \ . \tag{B.38}$$

The superscript and subscript o refer to the incident beam and $*$ denotes the complex conjugate. The angle Φ is the angle between the incident or scattered wave vector and the static magnetic field $\mathbf{B}_0$. The factor

$$r_0^2 = \left(\frac{e^2}{m_e^2 c^2}\right) \tag{B.39}$$

is the square of the classical electron radius.

For the scattering of an ordinary wave incident at a right angle to $\mathbf{B}_0$, the refractive index η is given by

$$\eta^2 = \varepsilon_3 \ . \tag{B.40}$$

Neglecting the spread in ϕ due to finite beam geometry, the incident and scattered complex polarization vectors become ($\phi = \pi/2$)

$$e_0 = (1 \ ; \ ib \ ; \ 0) \ , \tag{B.41}$$

and

$$\mathbf{e} = (\cos \ \Theta_S - ib \ \sin \ \Theta_S; \ \sin \ \Theta_S + ib \ \cos \ \Theta_S; \ 0) \ , \tag{B.42}$$

where

$$b = \frac{\varepsilon_2}{\varepsilon_3 - \varepsilon_1} \ . \tag{B.43}$$

Using Equations (B.40), (B.41), (B.42) and (B.35) through (B.38) and noting $\omega_i \simeq \omega_S$, the factors R and $|\zeta|^2$ become

$$R = \frac{\varepsilon_3^2}{(\varepsilon_1(1+b^2) + 2\varepsilon_2 b)(b^2+1)} \ , \tag{B.44}$$

and

$$|\zeta|^2 = [2\varepsilon_2 b + (\varepsilon_1 - 1)(1 + b^2)]^2 + [2b(\varepsilon_1 - 1) + \varepsilon_2(b^2 + 1)]^2 \; . \tag{B.45}$$

These can be combined with the factor $(\omega_i/\omega_p)^4$ to yield a net polarization-dielectric factor F_p, which is a function of ω_p, ω_b, and ω_i,

$$F_p = \frac{\omega_i^4}{\omega_p^4}\; R|\zeta|^2 \; . \tag{B.46}$$

The factor F_p is plotted in Figure B.12 as a function of ω with $\omega_i = 14$ GHz and for $\omega_p = 0.5, 3.0$ and 5.0 GHz. The factor F_p turns out to be weakly dependent on ω_p for the experimental conditions encountered but increases the differential cross section by 10% to 60% for the relavant range in ω_b.

For scattering of a beam oriented in the extraordinary mode with propagation perpendicular to the static magnetic field, the refractive index η and polarization vectors $\mathbf{e}_0$ and $\mathbf{e}$ become,

$$\eta^2 = \varepsilon_1 - \frac{\varepsilon_2^2}{\varepsilon_1} \; , \tag{B.47}$$

and

$$\mathbf{e}_0 = \left(1 \; ; \; -i\, \frac{\varepsilon_1}{\varepsilon_2} \; ; \; 0\right) \; , \tag{B.48}$$

and

$$\mathbf{e} = \left(\cos\, \Theta_S - i\, \frac{\varepsilon_1}{\varepsilon_2}\; \sin\, \Theta_S \; ; \; \sin\, \Theta_S + i\, \frac{\varepsilon_1}{\varepsilon_2}\; \cos\, \Theta_S \; ; \; 0\right) \; . \tag{B.49}$$

The factors R and $|\zeta|^2$ then become

$$R_x = \frac{\varepsilon_1^2 \varepsilon_2^4 - \varepsilon_2^6}{\varepsilon_1^6 - \varepsilon_1^2 \varepsilon_2^4} \tag{B.50}$$

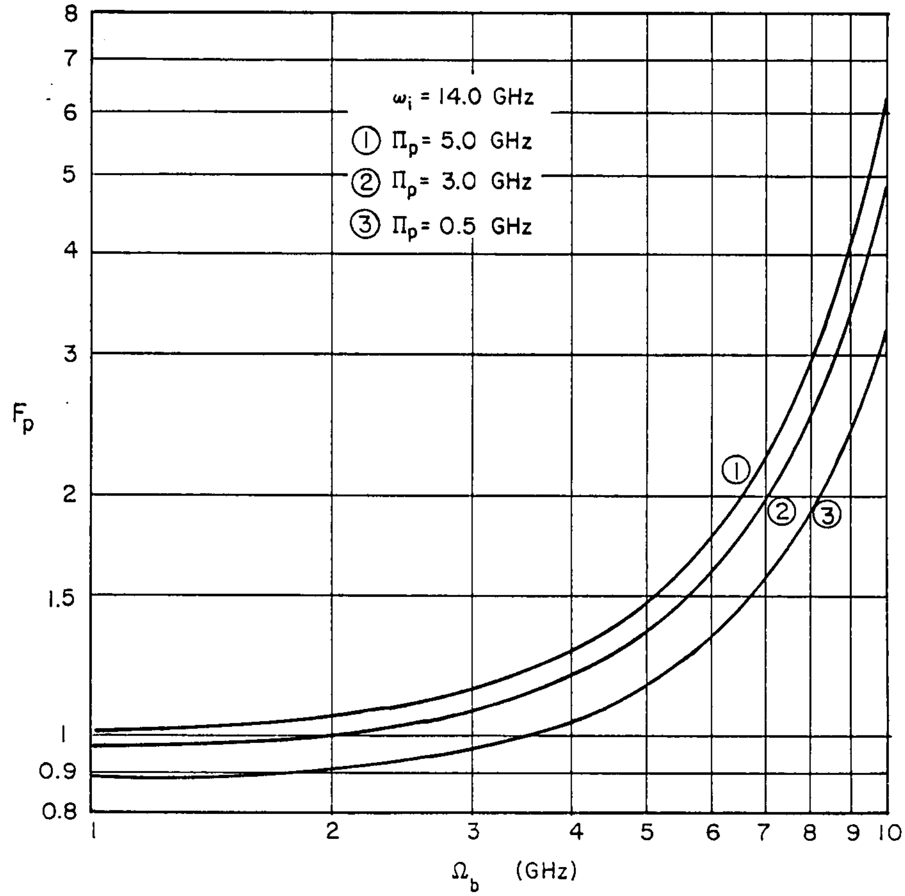

Figure B.12. Polarization-dielectric factor F_p for the ordinary wave propagating perpendicular to the static magnetic field.

and

$$|\zeta|_x^2 = 2 + \varepsilon_2^2 - \varepsilon_1^2 + 2\varepsilon_1 + \left(\frac{\varepsilon_1}{\varepsilon_2}\right)^2 \left[2 - 4\varepsilon_1 + 3\varepsilon_1^2 + \left(\frac{\varepsilon_1}{\varepsilon_2}\right)^2 (1-\varepsilon_1)^2\right] . \qquad \text{(B.51)}$$

The polarization-dielectric factor for the extraordinary wave F_{px} becomes

$$F_{px} = \left(\frac{\omega_i}{\omega_p}\right)^4 R_x \, |\zeta|_x^2 \, . \qquad \text{(B.52)}$$

The factor F_{px} is shown graphically in Figure B.13.

The differential scattering cross section can now be written as,

$$d\sigma = n_e r_0^2 \, F_p \, \frac{1}{2\pi} < \delta \, n_e^2 >_{k\Delta\omega} \, d\omega \, d\Omega \, . \qquad \text{(B.53)}$$

The total averaged scattering cross section is determined by integrating Equation (B.46) over the frequency range $\Delta\omega = \omega_S - \omega_i$ and the spread in k, where $k = k_\perp$

$$\sigma = n_e r_0^2 F_p \, \frac{1}{2\pi} \int_\Omega \int_{\Delta\omega} < \delta n_e(k_\perp, \Delta\omega)^2 > d\omega \, d\Omega \, . \qquad \text{(B.54)}$$

The integration over ω is performed experimentally by passing a detected signal proportional to P_S through a bandpass filter and then summing in a wide band detector.

In order to complete the expression for the total scattered power in Equation (B.29), the volume integral over the scattering volume must be computed. Let $I(\Theta_S)$ be given by

$$I(\Theta_S) = \int_V \frac{F(\Theta_\ell) F(\Theta_r)}{|\mathbf{R}_\ell - \mathbf{r}|^2 \, |\mathbf{R}_r - \mathbf{r}|^2} \, dV \, . \qquad \text{(B.55)}$$

For sufficiently narrow beam patterns, the scattering volume shown in Figure B.11 as the intersection of two cones, can be approximated as the volume of intersection

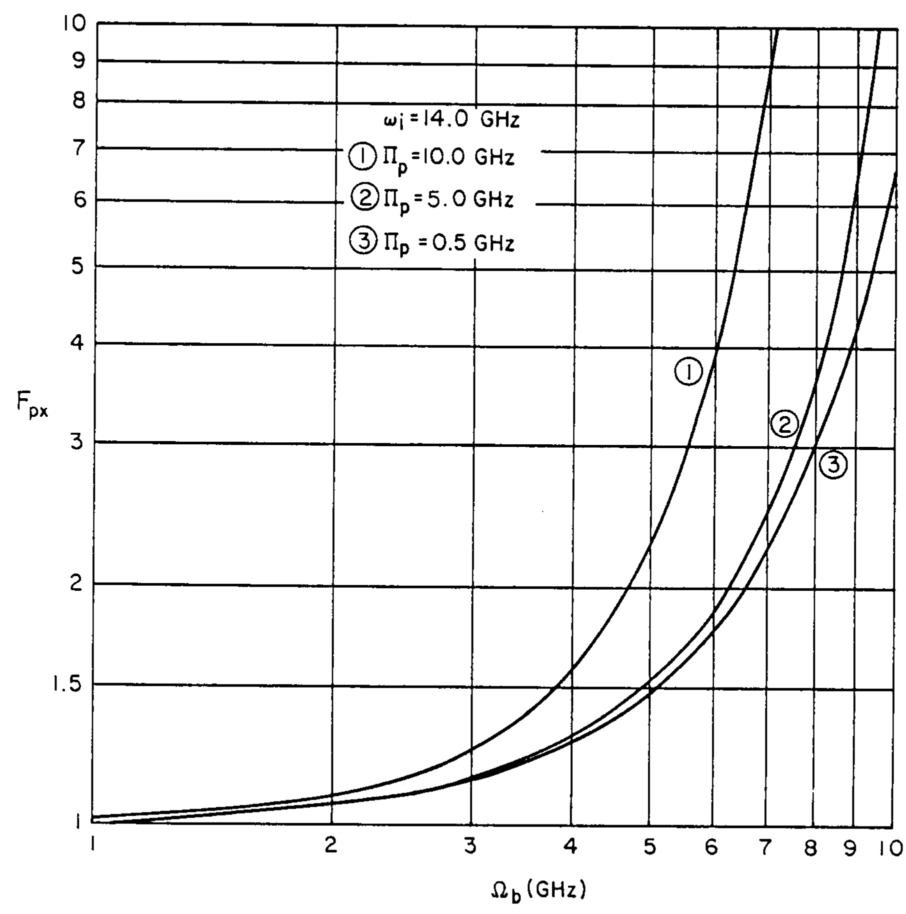

Figure B.13. The polarization-dielectric factor F_{px} of the scattering cross section as a function of ω_b.

for two cylinders of radius a at angle Θ_S. Figure B.14 shows the intersection of two cylinders of radius a at angle Θ_S. The vectors $\mathbf{R}_t$ and $\mathbf{R}_r$ locate the phase centers of the transmitting (launch) horn and the receiving horn respectively. With $\mathbf{R}_r$ located in the $x-y$ plane, $\mathbf{R}_t$ along the z axis and $\mathbf{r}$ expressed in spherical coordinates. For the receiving horn's phase center,

$$\mathbf{R}_r - \mathbf{r} = -(r \sin\Theta \cos\Phi)\,\hat{\mathbf{x}} - (r \sin\Theta \sin\Phi)\,\hat{\mathbf{y}} - (R_0 + r\, cos\,\Theta)\hat{\mathbf{z}}, \quad \text{(B.56)}$$

or

$$|\mathbf{R}_r - \mathbf{r}|^2 = R_0^2 + r^2 + 2\,R_0 r \cos\Theta. \quad \text{(B.57)}$$

For the transmitting horn's phase center,

$$\mathbf{R}_t - \mathbf{r} = (R_0 \sin\Theta_S - r \sin\Theta \cos\Phi)\hat{\mathbf{x}} - (r \sin\Theta \sin\Phi)\,\hat{\mathbf{y}}$$
$$+(R_0 \cos\Theta_S - r \cos\Theta)\,\hat{\mathbf{z}} \quad \text{(B.58)}$$

or

$$|\mathbf{R}_t - \mathbf{r}|^2 = R_0^2 + r^2 - 2R_0 r(\sin\Theta_S \sin\Theta \cos\Phi + \cos\Theta_S \cos\Phi)\,, \quad \text{(B.59)}$$

where $R_0 = |\mathbf{R}_t| = |\mathbf{R}_r|$. Combining Equations (B.57) and (B.59) yields

$$\begin{aligned}|\mathbf{R}_t - \mathbf{r}|^2\,|\mathbf{R}_r - \mathbf{r}|^2 = R_0^4\Big[\,1 &- 2\,\frac{r^2}{R_0^2}\,(\sin\Theta_S \sin\Theta \cos\Phi + (\cos\Theta_S - 1)\cos\Theta)\\ &- 4\,\frac{r^2}{R_0^2}\left(\sin\Theta_S \sin\Theta \cos\Theta_s \cos\Phi - \cos\Theta_S \cos^2\Theta - \frac{1}{2}\right)\\ &- 2\frac{r^2}{R_0^2}(\sin\Theta_S \sin\Theta \cos\Phi + (\cos\Theta_S - 1)\cos\Theta)\\ &+ \frac{r^4}{R_0^4}\,\Big]\,. \end{aligned} \quad \text{(B.60)}$$

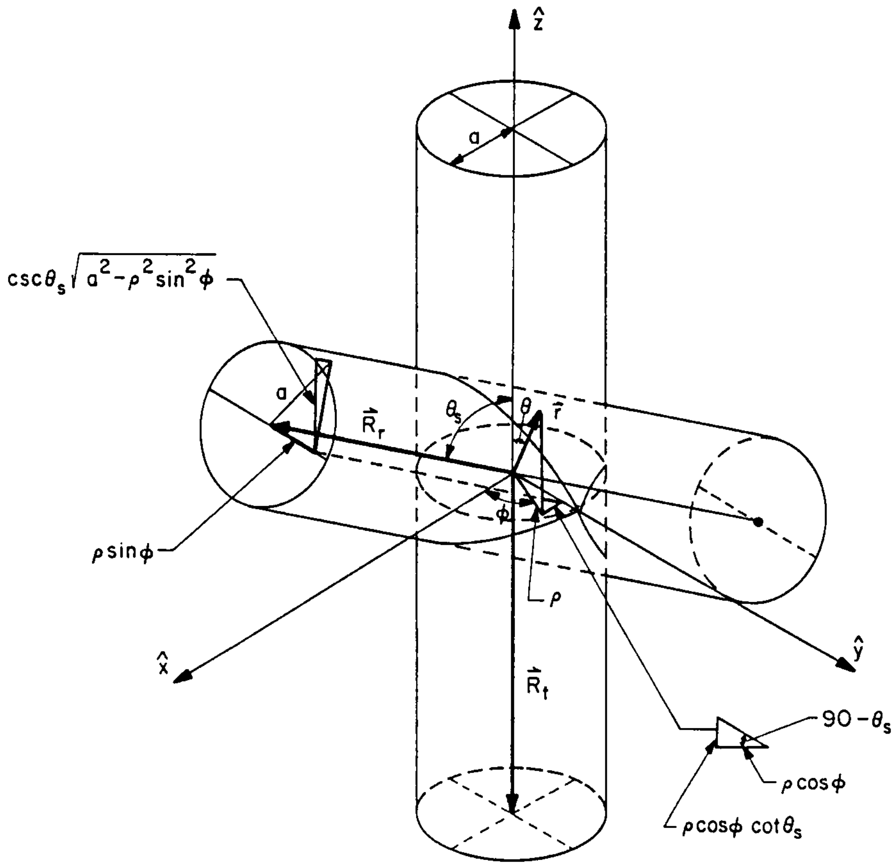

Figure B.14. Geometry used for the scattering volume integration.

Expanding $\left[|\mathbf{R}_t - \mathbf{r}|^2 \; |\mathbf{R}_r - \mathbf{r}|^2\right]^{-1}$ as

$$\frac{1}{1-x} = 1 + x + x^2 + \cdots |x| < 1 \; , \tag{B.61}$$

for $r/R_0 < 1$, keeping terms of order $(r/R_0)^2$ and then converting from spherical coordinates to cylindrical coordinates yields

$$\frac{1}{|\mathbf{R}_t - \mathbf{r}|^2 |\mathbf{R}_r - \mathbf{r}|^2} = \frac{1}{R_0^4}\left[1 + \frac{2\rho}{R_0} \sin\,\Theta_S \cos\,\Phi + \frac{2}{R_0}(\cos\,\Theta_S - 1)z \right.$$
$$+ \frac{4}{R_0^2}\,\rho^2\left(\sin^2\,\Theta_S \cos\,\Phi - \frac{1}{2}\right) + \frac{4}{R_0^2} \sin\,\Theta_S(2\cos\,\Theta_S - 1)z\rho\cos\,\Phi$$
$$\left. + \frac{4}{R_0^2}\left(\cos\,\Theta_S \cos^2\,\Theta_S - \cos\,\Theta_S + \frac{1}{2}\right)z^2\right] \; . \tag{B.62}$$

Keeping only the first three terms of Equation (B.62) and referring to Figure B.12, the volume integral $I(\Theta_S)$ becomes

$$I(\Theta_S) = \frac{2}{R_0^4}\int_0^{\pi}\int_0^{a}\int_{z_1}^{z_2}\left[1 + \frac{2\rho}{R_0}\sin\,\Theta_S\cos\,\Phi + \frac{2z}{R_0}(\cos\,\Theta_S - 1)\right]dz\rho d\rho d\Phi, \tag{B.63}$$

with

$$z_1 = \rho\cos\,\Phi\cot\,\Theta_S - \csc\,\Theta_S\left[a^2 - \rho^2\sin^2\Phi\right]^{\frac{1}{2}} \tag{B.64}$$

and

$$z_2 = \rho\cos\,\Phi\cot\,\Theta_S + \csc\,\Theta_S\left[a^2 - \rho^2\sin^2\Phi\right]^{\frac{1}{2}} \; . \tag{B.65}$$

under the restriction that $z \leq \mathbf{r}_p, \rho \leq \mathbf{r}_p$ and $\Theta_S < \pi/2$, where $\mathbf{r}_p$ is the radius of the plasma column.

Performing the integration of Equation (B.63), yields

$$I(\Theta_S) = \frac{a^3}{R^4}\left[\frac{16}{3}\csc\,\Theta_S + \frac{a}{R_0}\left[2\pi(1 - \cos\,\Theta_S)\cot\,\Theta_S - \frac{\pi}{8}\right]\right] \; . \tag{B.66}$$

Noting that $\tan\ \Theta_b = a/R_0$, Equation (B.66) becomes

$$I(\Theta_S) = \frac{1}{R_0}\ \tan^3\Theta_b \left[\frac{16}{3}\ \csc\ \Theta_S + \tan\ \Theta_b \left(2\pi(1-\cos\ \Theta_S)\ \cot\ \Theta_S - \frac{\pi}{8}\right)\right] . \tag{B.67}$$

The expression for the total power scattered into a receiving horn given by Equation (B.29) can be written as

$$P_S = P_{\Theta_b}\hat{n}_e r_0^2 F_p N_S I(\Theta_S)\left(\frac{G_0\lambda_i}{4\pi}\right)^2 \left\{\frac{\Omega_r}{2\pi}\int_{\Delta\omega} < \delta n_e(k_\perp,\Delta\omega)^2 > d\omega\right\}\ , \tag{B.68}$$

where P_{Θ_b} is the power radiated into the scattering volume, $\hat{n}_e$ is the average electron number density of the scattering volume, F_p is the polarization-dielectric factor given in Figure B.12 or B.13, and $I(\Theta_S)$ is given by Equation (B.67). The effective solid angle of reception for the receiving horn, Ω_r, is related to the effective aperture A_e of the recieving horn as

$$\Omega_r \simeq \frac{A_e}{R_0^2}\ . \tag{B.69}$$

The area A_e is determined by using the average horn directivity $\overline{D}_0$ and

$$A_e = \frac{\lambda_i^2}{4\pi}\ \overline{D}_0\ , \tag{B.70}$$

to yield $A_e = 17.3\ \mathrm{cm}^2$. When ratioed to the physical aperture of the horn, this yields an aperture efficiency of $\varepsilon_{ap} = 45\%$. An optimum gain horn with a uniform flare typically has an aperture efficiency of $\varepsilon_{ap} = 50\%$.

In conclusion, Table B.1 lists the important parameters of the two channel microwave scattering system needed for calibrated measurements of the spectrum of electron density fluctuations.

TABLE B.1

IMPORTANT PARAMETERS FOR TWO CHANNEL MICROWAVE SCATTERING SYSTEM

Parameter	Symbol	Channel A	Channel B	Units
Signal Frequency[1]	ω_i	14.0	14.0	GHz
Scattering Angle	Θ_S	30°	75°	degrees
Scattered Wavelength	$\lambda_\perp$	4.14	1.67	cm
Spread in $\lambda_\perp$	$\Delta\lambda_\perp$	3.97	0.68	cm
3dB Beam Angle	$2\Theta_b$	$24.5° \pm 1°$	$24.5° \pm 1°$	degrees
Phase Center Location	R_0	9.4	9.4	cm
Scattering Volume[2]	Vol_S	21.3	11.0	cm^3
Pattern Integral	$I(\Theta_S)$	1.12×10^{-2}	6.60×10^{-3}	cm^{-1}
Horn Gain (no glass)	G_0	53	53	
Mixer Loss (+5dBm L.O.)		9.6±.2	12.4 ± .2	dB
Polarization Factor	F_p	$0.9 < F_p < 1.6$ (Figure B.12)		
Input Power[3]	P_i	+25.0 dBm		
Radiated Power	P_{rad}	+15.0 dBm		
Scattering Volume Power	P_{Θ_b}	+10.0 dBm		

[1] $\lambda_i = 2.14$ cm.
[2] Calculated for the 3dB beam angle.
[3] Used for Runs AGP through AGS.
[4] Classical electron radius $r_0 = 2.818 \times 10^{-13}$ cm.

APPENDIX C

MISCELLANEOUS DIAGNOSTICS

In addition to the capactive probes and microwave scattering system, a number of other diagnosties were used that require further explanation. These diagnostics include the ion acoustic grid and magneto-acoustic diagnostics, the retarding potential energy analyzer, and the method for determining the integrated power in the dissipative region of the turbulent energy spectra. The frequency and phase response of the low frequency coupling network used with the Langmuir probe and the specifications of the sweeper used with the high frequency network analyzer are included in this appendix.

Ion Acoustic Grid.

Because of its importance in the stability of drift waves, a concerted effort was made to measure the ion-ion collision frequency. The ion-ion collision frequency contributes to viscous damping of ion movement which aids in the damping of drift waves.

The first attempt to measure the ion-ion collision frequency was to place a grid in the plasma column in order to launch ion-acoustic waves along the magnetic field. The spatial dispersion and frequency response of these waves can be used to determine the collision frequency of ions (Doucet et. al. 1984).

A grid 12 cm. in diameter with 2mm. mesh and 0.5 mm. wire was placed on a moveable support in the plasma column perpendicular to the static magnetic field (see Figure 2.1). The grid was biased into ion saturation and then modulated by a high voltage signal over the frequency range of .5 to 100 kHz. By using either a radial or axial Langmuir probe biased in ion saturation, ion acoustic waves launched by the grid could be detected. This experiment was performed using the Hewlett Packard 3577 network analyzer and a high voltage amplifier as a transfer function measurement. A swept measurement was made with the grid close to a sensing Langmuir probe and then normalized. The grid was then moved axially in one centimeter increments, and successive amplitude and phase response measurements were made. Any spatial dispersion of the waves launched, could be detected by the network analyzer.

Despite the direct measurement procedure of this diagnostic, no consistent data could be obtained from its use on the Penning discharge. Any waves launched were damped within 2 cm. of the launch grid. Since the spatial resolution of the detecting probe was on the order of a centimeter, acceptable data could not be obtained in the 2 cm. region of the wave. Attempts to produce stronger waves, by modulating the grid with higher voltage resulted in destablizing the entire plasma column. Excessive high voltage modulation caused the grid to become alternately a cathode and an anode. As an anode, the grid becomes a sink to electrons, and limits the cascading process necessary for plasma production.

These results, although disappointing for the measurement of the ion collision frequency, confirmed the presence of strong damping of ion acoustic waves in the Penning discharge plasma.

Magneto-Acoustic Diagnostic.

The second method used in an attempt to measure the ion collision frequency was the magneto-acoustic diagnostic. This diagnostic uses an external solenoid wrapped around the plasma column to excite low frequency oscillations of the axial magnetic field. By measuring the radial variation of this field, the radial profile of electron temperature and ion-neutral cross section have been deduced (Frommelt et. al. 1970), as well as electron density and electron temperature profiles (Brennan et. al. 1977). The diagnostic can also be extended to current carrying plasmas (Sy 1978), and with sufficient collisionality, used as a heating method (Cross 1970).

Figure C.1 shows the initial design of a coil used to excite magneto-acoustic oscillations. The anode cylinder used in the configuration shown in Figure 2.2 was slit along its length. Two copper tubes were soldered along each side of the slit and a section of 50Ω cable with its outer insulation removed was slid into each tube. The center leads of the coaxial cable were joined to complete the circuit. One of the coaxial cables was connected to a 100 watt R.F. amplifier through an isolation network. The other cable was connected to a high power 25Ω load that could be placed outside the vacuum vessel for the required cooling. A 25Ω load was used to increase the current in the coil. In this configuration a 10 to 250 MHz bandwidth was obtained and a magnetic field of up to 3 gauss produced with no plasma present.

With the broad bandwidth of the single turn coil shown in Figure C.1, the magneto-acoustic resonance near the ion gyro frequency could be investigated as well as the MHD resonance for $\omega \sim \sqrt{\omega_{bi}\omega_{be}}$ (Alexandrov et. al. 1984). The low frequency resonance effects for $\omega \sim \omega_{bi}$ will be dominated by ion collisions, with the

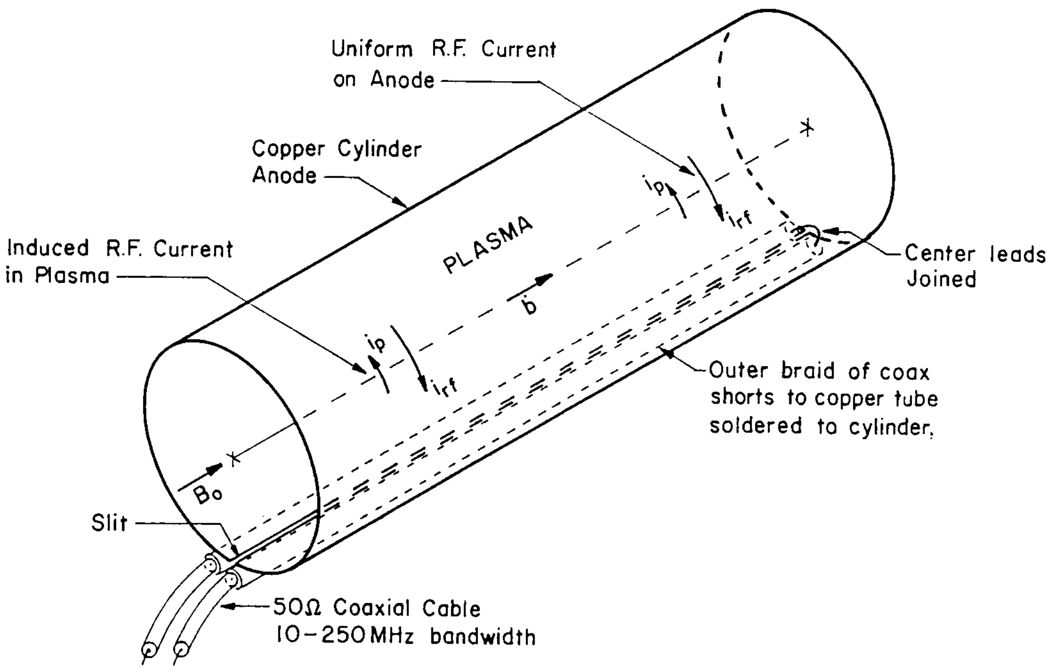

Figure C.1 Anode design for magneto-acoustic diagnostic.

higher frequency resonance affected by both ion and electron collisions. Experimentally, both resonances were observed on the Penning discharge by monitoring the impedance of the coil. For the configuration shown in Figure C.1, the resonances were not independent of the direction in which the source oscillator was swept in frequency. Near resonance, the impedance of the network would increase significantly to produce a strong electric field across the slit in the anode. This field would heat the plasma enough to produce an asymmetric plasma.

In order to shield the plasma from the electric field across the coil gap, a Faraday shield was constructed. Figure C.2 shows the initial design of a Faraday shield. This shield was constructed of an anode cylinder with a series of axial slits almost the length of cylinder that alternately start at opposite ends. This design shielded the plasma from the stray fields of the coil, but because a closed current path existed in the shield, the magnetic field induced in the plasma was reduced and the inductance of the R.F. current loop was increased due to the mutual inductance of the shield. The bandwidth of the R.F. coil was significantly reduced so that the higher frequency, MHD resonance could not be detected.

Figure C.3 shows an improved Faraday shield design using an elongated anode cylinder. By placing the continuous section of the shield far from the current loop, a minimun R.F. current is induced in the shield. This design was not implemented due to time and funding limitations.

For the low frequency resonance, the magneto-acoustic diagnostic can be analyzed using Maxwell's equation and the plasma dielectric tensor. Maxwell's equations can be written

$$\nabla \times \mathbf{B} = \mu_0 \varepsilon_0 \frac{\partial \mathbf{E}}{\partial t} + \mu (\mathbf{j}_p + \mathbf{j}_0) \ , \tag{C.1}$$

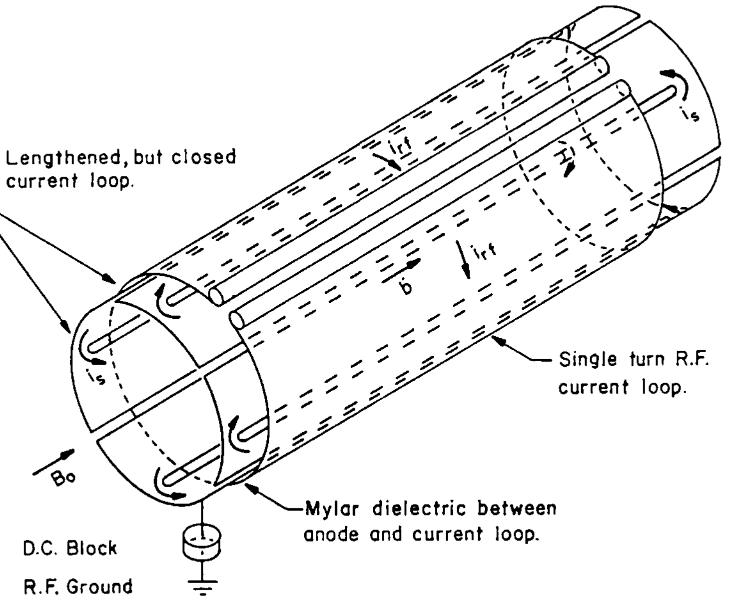

Figure C.2. Slit anode design using as Faraday shield for R.F. current loop.

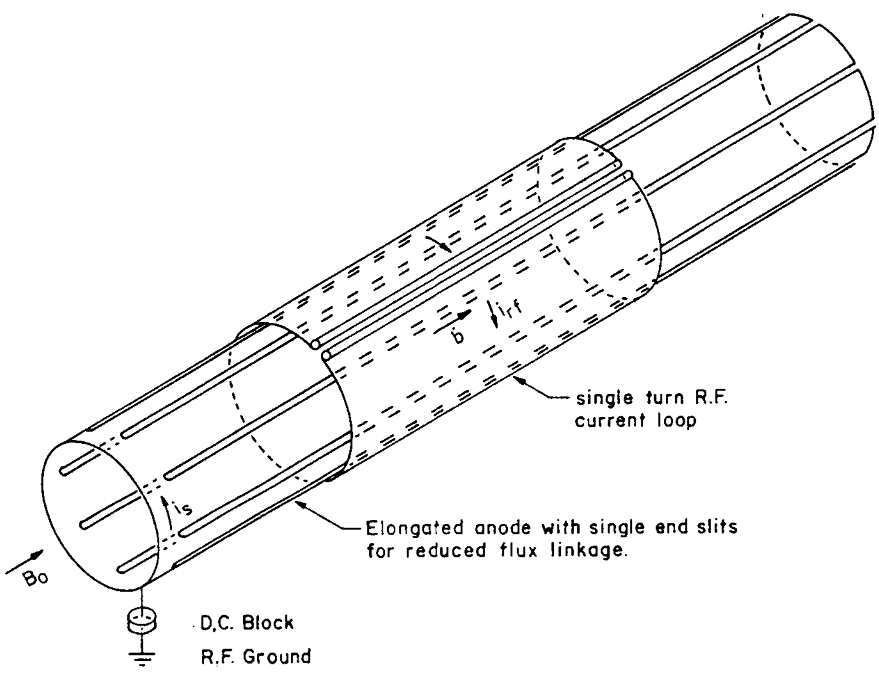

Figure C.3. Elongated anode cylinder for improved Faraday shield.

$$\nabla \times \mathbf{E} = -\frac{\partial \mathbf{B}}{\partial t} , \tag{C.2}$$

$$\nabla \cdot \mathbf{D} = \rho_0 , \tag{C.3}$$

and

$$\nabla \cdot \mathbf{B} = 0 , \tag{C.4}$$

where $\mathbf{j}_0$ is the external current density, $\mathbf{j}_p$ is the current density induced in the plasma, and ρ_0 is the external charge density. The electric displacement $\mathbf{D}$ is related to the electric field $\mathbf{E}$ through the dielectric tensor,

$$D_i = \varepsilon_{ij} E_j . \tag{C.5}$$

Using Equation (C.5), Ampere's Law (Equation (C.1)) can be written in the plasma as

$$\nabla \times \mathbf{B} = \frac{1}{c^2} \frac{\partial \mathbf{D}}{\partial t} , \tag{C.6}$$

and Equation (C.3) becomes

$$\nabla \cdot \mathbf{D} = 0 , \tag{C.7}$$

since the external charge is shielded from the plasma. For low frequency excitation $\omega \sim \omega_{bi}$, allowing

$$\frac{\partial}{\partial z} \simeq \frac{\partial}{\partial \theta} \simeq 0 , \tag{C.8}$$

and neglecting oscillations of the plasma dielectric, Equations (C.2), (C.4), (C.6), and (C.7) form a closed set of equations. The authors mentioned previously, use the MHD equations (Cross 1970) or the two fluid equations (Frommelt et. al. 1970 and Brennan et. al. 1977) to eliminate the current density j_p in Equation (C.1) by solving for the drift velocities and using

$$j_p = en_e(V_e - V_i) \ . \tag{C.9}$$

Letting the quantities **E** and **B** vary in time,

$$\mathbf{B} = B_0 + b_z(r)e^{-i\omega t} \qquad \hat{z} \ , \tag{C.10}$$

and

$$\mathbf{E} = E(r)e^{-i\omega t} \qquad \hat{\phi} \ , \tag{C.11}$$

where $b_z \ll B_0$, Equations (C.2) and (C.6) yield a single equation for b_z as

$$\frac{d}{dr}\left(\frac{re^2}{\omega\varepsilon_{\phi\phi}}\frac{db_z}{dr}\right) + rb_z = 0 \ . \tag{C.12}$$

The dielectric tensor component $\varepsilon_{\phi\phi}$ can be obtained from the cartesian tensor by

$$\varepsilon_{\phi\phi} = \hat{\phi}^T \cdot [\varepsilon_{ij}] \cdot \hat{\phi} \ , \tag{C.13}$$

where $\hat{\phi}$ is given by

$$\hat{\phi} = -\sin\,\phi\hat{\mathbf{x}} + \cos\,\hat{\phi}\hat{\mathbf{y}} \ , \tag{C.14}$$

so that

$$\varepsilon_{\phi\phi} = \varepsilon_{\perp} = \varepsilon_{xx} \ , \tag{C.15}$$

provided $\varepsilon_{xx} = \varepsilon_{yy}$. Adding the ion component to Equation (4.50) allows $\varepsilon_{\perp}$ to be written as

$$\varepsilon_{\perp} = 1 - \frac{1}{\omega}\left[\frac{\omega_{pe}^2(\omega + i\nu_e)}{(\omega + i\nu_e)^2 - \omega^2 - \omega_{be}} - \frac{\omega^2 - \omega_{pi}^2(\omega + i\nu_i)}{(\omega + i\nu_i)^2 - \omega_{bi}^2}\right] \ . \tag{C.16}$$

For $\omega \sim \omega_b$ and $\omega_{bi} < \omega_{pe} < \omega_{be}$, Equation (C.16) can be approximated as

$$\varepsilon_\perp \simeq \frac{C^2}{V_A} \left[\frac{1 + i\frac{\nu_i}{\omega}}{\frac{\omega^2}{\omega^2-\omega_{bi}^2} - 1 + 4\nu_e\nu_i\left(\frac{\omega^2-\nu_e\nu_i}{\omega_{be}^2\omega_{bi}^2}\right) + i2\frac{\nu_i}{\omega_{bi}}} \right] , \tag{C.17}$$

where V_A is the Alfvén velocity given by

$$V_A^2 = \frac{B^2}{\mu_0 n_i m_i} . \tag{C.18}$$

For the low density Penning discharge, the Alfvén velocity is quite high; $V_A \simeq 3\times10^9$ cm/sec.

If the plasma is radially homogeneous, Equation (C.12) becomes a Bessel equation;

$$\frac{d}{dr}\, r\, \frac{db_z}{dr} + rk^2 b_z = 0 , \tag{C.19}$$

subject to the boundary conditions

$$b_z(r=a) = b_0 , \tag{C.20}$$

$$\frac{\partial b_z}{\partial r}|_{r=0} = 0 , \tag{C.21}$$

where

$$k^2 = \frac{\omega^2}{V_A^2} \left[\frac{1 + i\frac{\nu_i}{\omega}}{\frac{\omega^2}{\omega^2-\omega_{bi}^2} - 1 + 4\nu_e\nu_i\left(\frac{\omega^2-\nu_e\nu_i}{\omega_{be}^2\omega_{bi}^2}\right) + i2\frac{\nu_i}{\omega_{bi}}} \right] . \tag{C.22}$$

The solution to Equation (C.19) is the zero order Bessel function of the first kind,

$$b_z(r) \sim J_0(kr) , \tag{C.23}$$

and the induced magnetic field is given as

$$b_z(r,t) = Re\Big|\ |b_z(a)|\frac{J_0(kr)}{J_0(ka)}\ \exp(-i\omega t)\ \Big| . \tag{C.24}$$

Hence $b_z(r,t)$ will have a maximum for a minimum in $J_0(ka)$. Since k is complex, and there are no complex zeros to $J_0(ka), b_z$ will remain finite. If the imaginary part of k is small, a minimum of $J_0(ka)$ occurs for

$$|ka| \approx \alpha_1, \alpha_2, \alpha_3 \ldots \ , \tag{C.25}$$

where α_i is the i'th real zero of the zero order Bessel function. By considering the form of k^2 in Equation (C.22), ka can be close to a root only for $\omega \sim \omega_{bi}$.

Finally the impedance of the R.F. circuit will change as $\omega \rightarrow \omega_{bi}$ by an increase in the inductance of the single turn coil L_S,

$$L_S = \frac{\Phi}{I_0} \ , \tag{C.26}$$

where I_0 is the drive current, and Φ is the induced flux in the coil given by

$$\Phi = 2\pi \int_0^a r b_z(r) \, dr \ . \tag{C.27}$$

In order to complete the integral of Equation (C.27), the radial profile of $b_z(r)$ is usually measured experimentally and the integral done numerically.

Ion Temperature Measurement.

The ion temperature of the plasma was determined by analyzing the integrated ion energy distribution curve produced by a retarding potential energy analyzer (Roth 1969). This analyzer consists of a series of grids that can be swept in voltage, resulting in a decreasing current flux on a collector electrode. Experimentally, the analyzer is positioned behind one of the discharge cathodes and allowed to capture ions that stream along magnetic field lines through a small hole in the cathode.

Figure C.4 shows a sample current–voltage curve produced by the retarding potential energy analyzer (RPEA). This curve should always be monotone decreasing or flat. The flat portion in Figure C.4 arises because the Penning discharge floats at a high positive potential. Escaping ions fall out of this potential to produce a constant current to the analyzer. The retarder voltage at which the collector current begins decreasing is typically near the discharge anode voltage.

The information containing the ion temperature is actually in the tail of the curve. Figure C.5 shows the data points sampled graphically from the curve in Figure C.4 to be used for analysis. Here the voltage axis has been shifted. Using these data points, a software program (Roth et al. 1968) is used to fit to a Maxwellian velocity distribution. Figure C.6 shows the resulting integrated ion energy distribution for the best fitting Maxwellian distribution and its temperature.

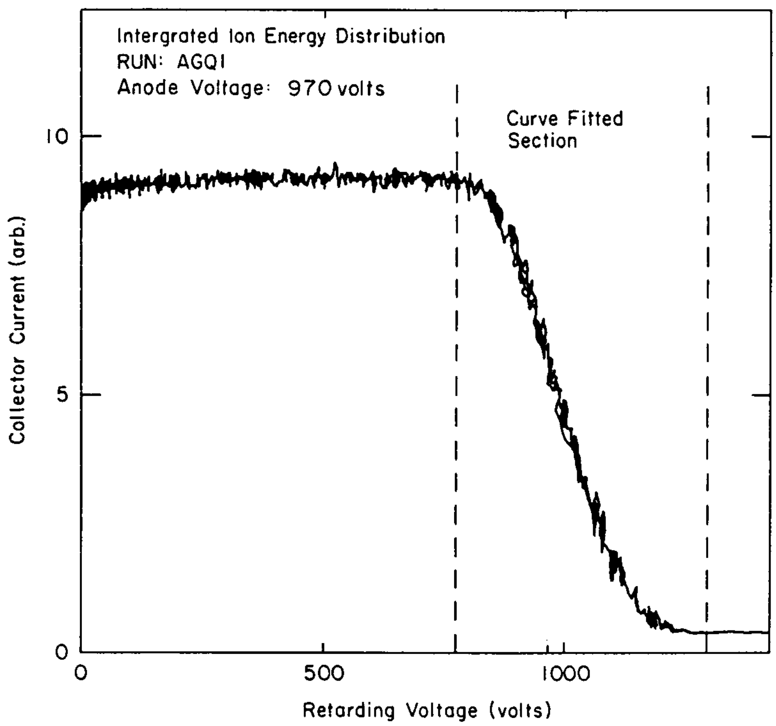

Figure C.4. Current-voltage experimental data curve for retarding potential energy analyzer (RPEA).

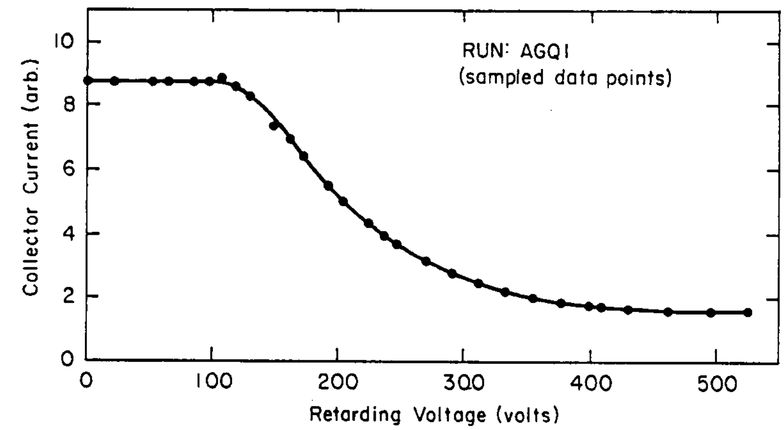

Figure C.5. Sampled data points points from experimental current-voltage (RPEA) curve.

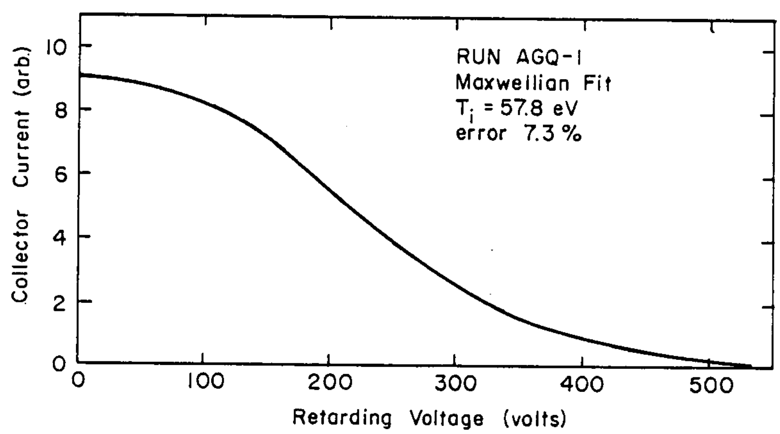

Figure C.6. Best Maxwellian fit for sampled data points in Figure C.5.

Spectral Energy Density Measurement.

The calibrated power spectra illustrated in Appendices H and I were measured using a Hewlett Packard 3577 Network Anaylzer or Tektronix 7L5 spectrum analyzer. The amplitude calibration of these spectra is based on an analysis of the particular diagnostic used as discussed in Appendices A, B, and C, and a correction based on the instruments being used for a noise measurement.

The spectral density displayed on a spectrum analyzer is typically in units of watts per hertz. When used for broadband noise measurements the analyzer's amplitude response must be normalized for the resolution bandwidth used when making a given measurement (Hewlett Packard 1974). For signal levels expressed as power in dB, this correction takes the form,

$$S'(w) = S(w) - 10\log\left[\frac{\text{resolution bandwidth}}{\text{normalized bandwidth}}\right] .$$

Hence when using a 1 kHz resolution bandwidth, a factor of 30 dB must be subtracted from the analyzer's amplitude response to normalize to a one hertz bandwidth.

In addition to the correction due to the instrument's resolution bandwidth, a factor of 2.5 dB must be added to a power spectra when making noise measurements (Engleson 1984). Since the analyzer is equipped with envelope detectors rather than true r.m.s detectors, a voltage error of $\frac{2}{\sqrt{\pi}}$ or 1.05 dB is produced for measurements of a narrow band gaussian process. When a logarithmic display is used, an error of 1.45dB is introduced, since the log of the mean is not the same as the mean of the log.

With the power spectra corrected using the above factors and calibrated for a given diagnostic, the total power over a particular frequency range can be obtained from

$$P_{tot} = \frac{1}{2\pi} \int_{w_1}^{w_2} S(w) dw \ , \tag{C.29}$$

where $S(w)$ is the displayed spectral density in watts per hertz. When displayed on a log amplitude versus log frequency format with a straight line power law (see Figure 2.13), the spectral density has the power law form

$$S(w) = S_1 \left(\frac{w}{w_1} \right)^{-m} \ . \tag{C.30}$$

The frequency w_1 and amplitude S_1 are the reference levels for the power law region with spectral index m, with m defined as

$$m = \frac{S(w_1) - S(w_2)}{10 \log \left(\frac{w_2}{w_1} \right)} \ ,$$

and $S(w)$ expressed in dB.

The total energy in the dissipative region of the turbulent spectrum (see Figure 2.13) contributes to the turbulent electron collision frequency. Because the transition frequency from the coupling region to the dissipation region is often difficult to observe from power spectra, an alternative method was used to determine this frequency. The detected signal from a given diagnostic was band pass filtered and then measured using a broadband detector. By moving the high pass filter cut–off frequency and measuring the integrated power spectra as a function of this cut–off frequency, the transition frequency could be determined.

Figures C.7 and C.8 show the uncalibrated integrated power spectra of various diagnostic signals as functions of the high pass filter cut–off frequency. The tran-

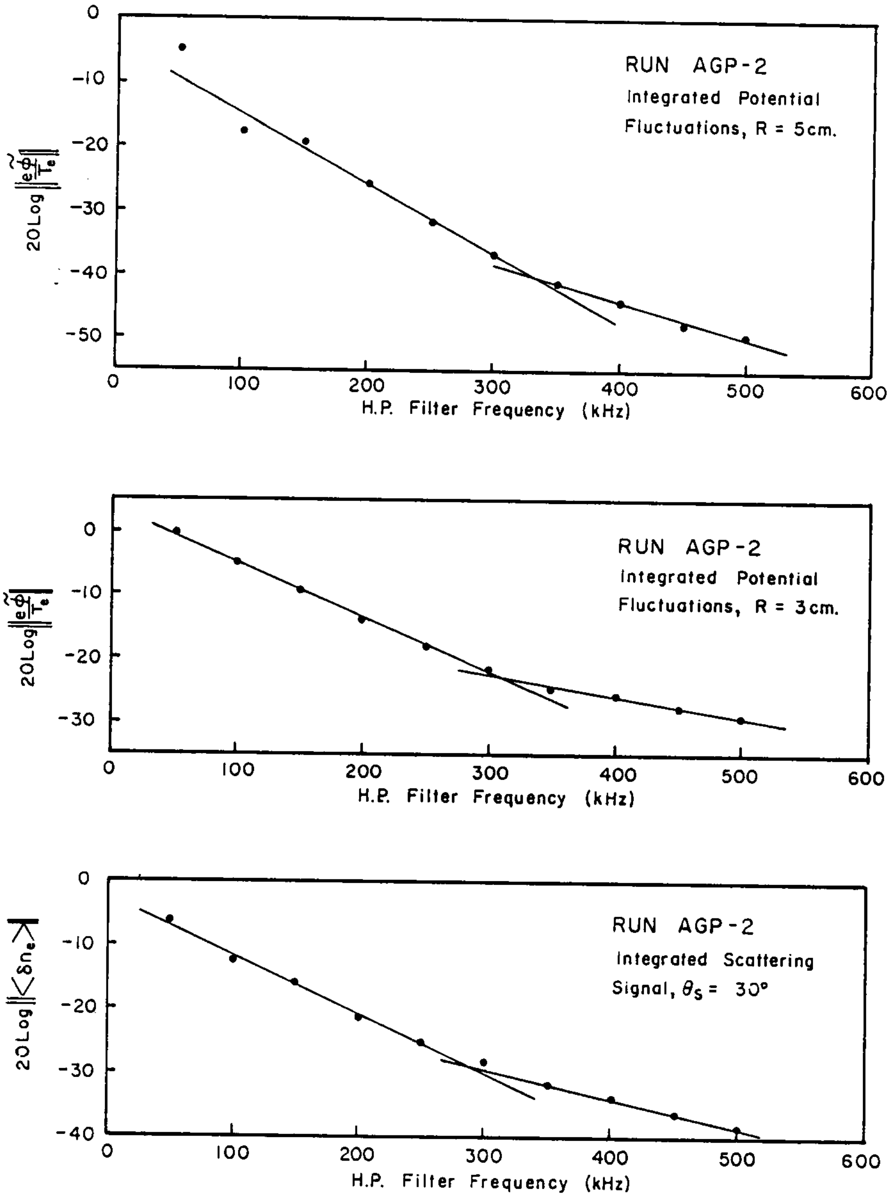

Figure C.7. Integrated potential fluctuation and microwave scattering signal versus high pass filter frequency for Run AGP2.

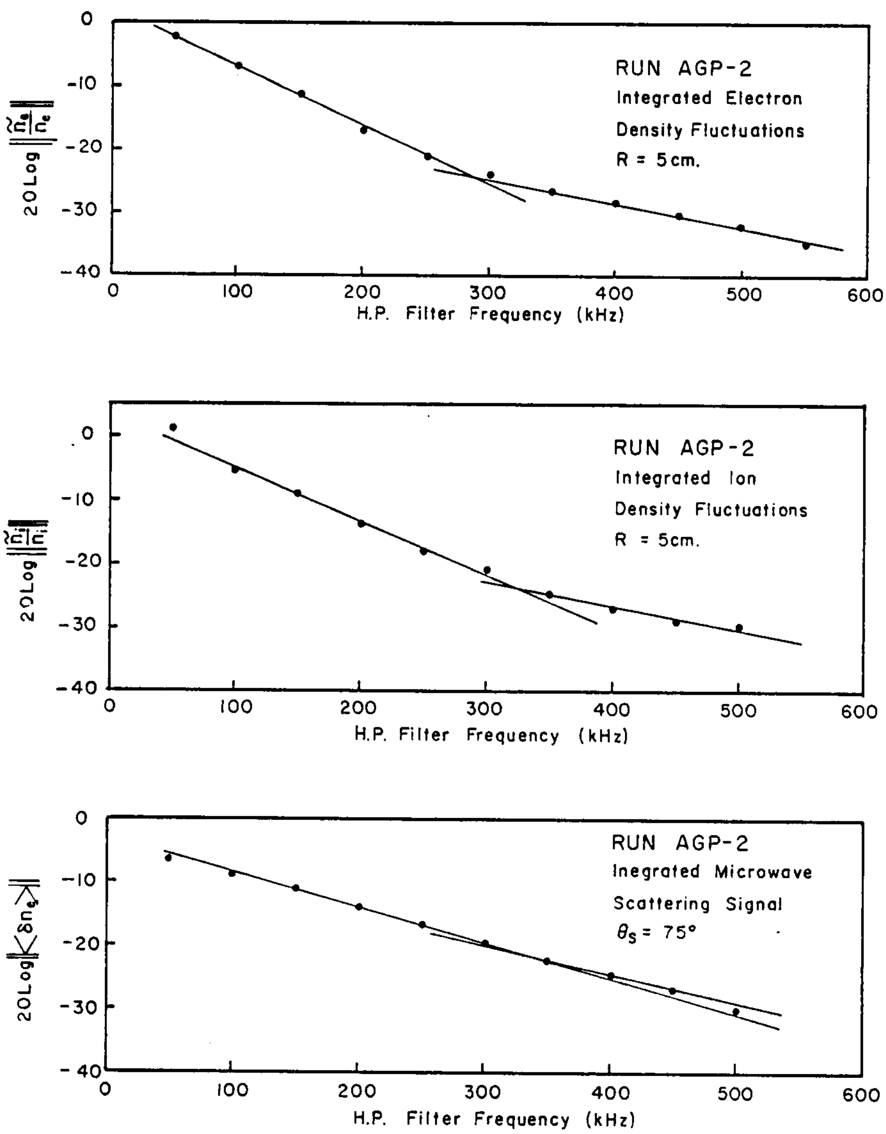

Figure C.8. Integrated density fluctuation signals and microwave scattering signal versus high pass filter frequency for Run AGP2.

sition frequency becomes quite evident by the difference in slope of the integrated power in the two regions of the spectrum. Although tedious, this procedure proved necessary for adequate measurement of the low level power in the dissipative region of the turbulent sepctra and in locating the transition frequency from the coupling region to the dissipative region.

Langmuir Probe Coupling Circuit.

The coupling circuit shown in Figure 2.9 was used to allow D.C. biasing of a Langmuir probe and detection of density fluctuations. A large inductor (7.2 henrys) was used to isolate the bias network, while two high voltage ceramic capacitors (0.1 microfarads) were used to couple to the fluctuating signal. A 1k-ohm load was provided for the fluctuating signal. The network had a usable bandwidth of 5kHz to 1MHz. Figure C.9 shows the amplitude and phase response for this network.

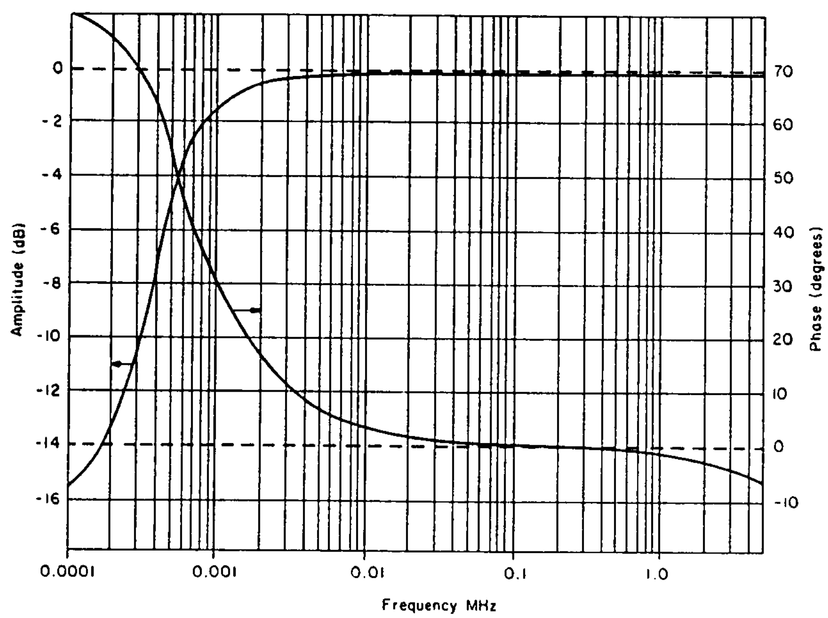

Figure C.9. Amplitude and phase response for Langmuir probe coupling network.

Oscillator Specificaions.

The Hewlett Packard 8510 network analyzer used for electron cyclotron absorption measurements was used with the HP model 8350A sweeper installed with a HP 83592A module. This sweeper is of the YIG tuned type with a usable bandwidth of 45 MHz to 21 GHz, and a maximum output power of $+13dB_m$. Table C.1 lists the stability and accuracy of this unit when installed with the HP 8510 network analyzer (Hewlett Packard 1984). The frequency accuracy of this unit was verified using a cavity frequency meter, type 5814 of PRD Electronics Inc. having a Q of 10,000.

TABLE C.1

ACCURACY AND STABILITY CHARACTERISTICS OF HP 83592A SWEEPER

Accuracy		
CW mode	± 5 MHz	2.4-7.0 GHz range
Sweep mode	± 20 MHz	
Stability	± 50 kHz	with 10% line voltage change
	± 100 kHz	for 3:1 load SWR
	± 100 kHz	with time/1hr warm up
	≤ 8 kHz	residual FM peak, 10 kHz bandwidth

APPENDIX D

Finite Temperature Dielectric Constant and Plasma Dispersion Function

This appendix deals with the solution of Equation (4.58) for the finite temperature dielectric constant of the extraordinary mode wave. Additional terms not given in Chapter IV are presented here along with the methods used to evaluate the plasma dispersion function.

The programs FTDF and VDCF are listed for reference. These programs were run on an HP41CX calculator. Program FTDF calculates the signal attenuation and phase change for the wave with non zero k_z. Program VDCF calculates the wave's attenuation and phase change from Appleton's Equation with a speed dependent collision frequency.

Dielectric Constant.

The complex dielectric constant $\breve{\mu}$ for the extraordinary mode wave moving through a finite temperature plasma with a velocity independent electron collision frequency is given by the solution of Equation (4.54). For a solution of the extraordinary mode wave, it is solved iteratively using Newton's method as Equation (4.58) with the initial guess for $\breve{\mu}^2$ given by $\breve{\mu}_x^2$ for the zero temperature plasma. For very small collision frequencies, and when ω is close to ω_b, the solution of Equation (4.58) begins to deviate from the zero temperature plasma. Under these conditions the initial guess of $\breve{\mu}_x^2(T = 0)$ is insufficient, and Equation (4.58) is solved by starting ω far from ω_b, and then making small steps in ω and using the previous solution of Equation (4.58) as an initial guess.

Equation (4.58) is defined using the tensor components in Equations (4.32) through (4.36) and written here for reference

$$\breve{\mu}_{i+1}^2 = \breve{\mu}_i^2 - \frac{G(\breve{\mu}_i^2)}{G'(\mu_i^2)} , \tag{4.58}$$

where

$$G(\breve{\mu}^2) = -\breve{\mu}^2 + \frac{\xi^2\mu_x^2 + \bar{\varepsilon}_{zz}(1 + \zeta^2 - \frac{\mu_x^2}{\breve{\mu}^2}) + \overline{B} + \frac{\overline{C}}{\breve{\mu}^2}}{\xi^2 + \overline{A}} , \tag{4.59}$$

and $\overline{B}, \overline{A}$ and $\overline{C}$ are given by Equations (4.55), (4.56) and (4.57), and $G'(\breve{\mu}^2)$ is given by

$$G'(\mu^2) = \frac{\partial G(\breve{\mu}^2)}{\partial \mu^2} . \tag{4.60}$$

For proper convergence of Equation (4.58) the derivative of Equation (4.59) should not be approximated. Due to the behavior of the plasma dispersion function $Z(\beta)$ it is easy for an approximation to Equation (4.60) to become very large and incorrectly yield convergence of Equation (4.58). For the results listed in Table 4.1, acceptable convergence occurs when the signal attenuation computed from a given $\breve{\mu}_i$ changes by 5% or less. Convergence usually occurs within two to six iterations.

Using Equation (4.59) and Equations (4.55) through (4.57), Equation (4.60) can be written as,

$$
\begin{aligned}
&(\xi^2+\overline{A})\ G'(\mu^2) = -(\xi^2+\overline{A}) \\
&+\frac{\partial\varepsilon_{xx}}{\partial\mu^2}\ \left[\left(\xi^2-\frac{\varepsilon_{zz}}{\mu^2}\right)\left(1-\frac{\varepsilon_{xy}^2}{\varepsilon_{xx}^2}\right)+\frac{1}{\varepsilon_{xx}}\ \left(2\xi\zeta\varepsilon_{xz}-\overline{B}\ \right)+\overline{A}\left(\frac{G(\mu^2)+\mu^2}{\varepsilon_{xx}}\right)\right] \\
&+2\ \frac{\partial\varepsilon_{xy}}{\partial\mu^2}\left[\left(\xi^2-\frac{\varepsilon_{zz}}{\mu^2}\right)\ \frac{\varepsilon_{xy}}{\varepsilon_{xx}}-\xi\zeta\ \frac{\varepsilon_{yz}}{\varepsilon_{xx}}\ \right] \\
&-2\ \frac{\partial\varepsilon_{xz}}{\partial\mu^2}\left[\xi\zeta\left(\frac{G(\mu^2)+\mu^2}{\varepsilon_{xx}}-1\right)+\frac{\varepsilon_{xz}}{\varepsilon_{xx}}-\frac{\varepsilon_{xz}}{\mu^2}\right] \\
&+2\ \frac{\partial\varepsilon_{yz}}{\partial\mu^2}\left[\xi^2\ \frac{\varepsilon_{yz}}{\varepsilon_{xx}}+\xi\zeta\ \frac{\varepsilon_{xy}}{\varepsilon_{xx}}+\frac{\varepsilon_{yz}}{\mu^2}\right] \\
&+\frac{\partial\varepsilon_{zz}}{\partial\mu^2}\left[1+\zeta^2-\frac{\mu_x^2}{\mu^2}-\zeta^2\left(\frac{G(\mu^2)+\mu^2}{\varepsilon_{xx}}\right)\right] \\
&+\frac{1}{\mu^4}\ \left(\varepsilon_{zz}\ \mu_x^2-\overline{C}\ \right)\ .
\end{aligned}
\tag{D.1}
$$

The bar over the tensor components has been dropped here. The derivatives of these tensor components are given by

$$\frac{\partial\varepsilon_{xx}}{\partial\mu^2} = -\ \frac{1}{2}\ \frac{\omega_p^2}{\omega}\ \left[\frac{I'_+(\beta_{-1})}{\omega+i\nu+\omega_b}+\frac{I'_+(\beta_1)}{\omega+i\nu-\omega_b}\ \right]\ , \tag{D.2}$$

$$\frac{\partial\varepsilon_{xy}}{\partial\mu^2} = i\ \frac{1}{2}\ \frac{\omega_p^2}{\omega}\ \left[\frac{I'_+(\beta_{-1})}{\omega+i\nu-\omega_b}+\frac{I'(\beta_1)}{\omega+i\nu-\omega_b}\ \right]\ , \tag{D.3}$$

$$\frac{\partial\varepsilon_{zz}}{\partial\mu^2} = i\ \frac{1}{2\omega}\ \frac{\omega_p^2}{\zeta^2\omega_b^2}\ \left[(\omega+i\nu+\omega_b)I'_+(\beta_{-1})+(\omega+i\nu-\omega_b)I'_+(\beta_1)\right]\ , \tag{D.4}$$

$$\frac{\partial\varepsilon_{xz}}{\partial\mu^2} = -\ \frac{1}{2\omega}\ \frac{\omega_p^2}{\zeta^2\omega_b}\ \left[I'_+(\beta_{-1})-I'_+(\beta_1)\right]\ , \tag{D.5}$$

and

$$\frac{\partial\varepsilon_{yz}}{\partial\mu^2} = \frac{i}{2\omega}\ \frac{\omega_p^2}{\zeta^2\omega_b}\ \left[I'_+(\beta_{-1})+I'_+(\beta_1)\right]\ , \tag{D.6}$$

where

$$I'_+(\beta) = \frac{\partial}{\partial\beta}\ I_+(\beta)\ \frac{\partial\beta}{\partial\mu^2}\ . \tag{D.7}$$

Using the relations in Equations (4.29) and (4.47), and the differential equation in Equation (D.10), Equation (D.7) becomes

$$I'_+(\beta) = \frac{\hat{\beta}}{2\mu^2} \left[Z(\hat{\beta})\,(1 - 2\hat{\beta}^2) - 2\hat{\beta} \right] , \tag{D.8}$$

where $\hat{\beta} = \sqrt{2}\,\beta$.

Plasma Dispersion Function.

The plasma dispersion function is defined by the integral (Fried and Conte 1961)

$$Z(\beta) = \frac{1}{\sqrt{\pi}} \int_{-\infty}^{\infty} \frac{e^{-\xi^2}}{\xi - \beta}\, d\xi \qquad Im(\beta) > 0 , \tag{D.9}$$

and satisfies the differential equation

$$Z'(\beta) = -2[1 + \beta Z(\beta)] . \tag{D.10}$$

For $Im(\beta) < 0$, $Z(\beta)$ is given by

$$Z(\beta) = 2i\sqrt{\pi}\, \exp(-\beta^2) + Z(\beta^*) \qquad Im(\beta) < 0 , \tag{D.11}$$

where β^* is the complex conjugate. Equation (D.11) shows that $Z(\beta)$ becomes large for large negative imaginary components of β.

For $Re(\beta) < 0$, $Z(\beta)$ satisfies the following,

$$Re\ Z(-\beta r, \beta_i) = Re\ Z(\beta_r, \beta_i) , \tag{D.12}$$

and

$$Im\ Z(-\beta_r, \beta_i) = Im\ Z(\beta_r, \beta_i) , \tag{D.13}$$

where β_r and β_i are positive and are the real and imaginary components of the argument β.

In the solution of Equation (4.50), the plasma dispersion function $Z(\beta)$ is computed for large arguments using an asymptotic expansion (Swanson 1984) and for small arguments using a continued fraction (Fried and Conte 1961).

For $|\beta| \geq 10$

$$
\begin{aligned}
Z(\beta) \simeq & -\frac{1}{\beta}\left(1+\frac{1}{2\beta^2}+\frac{3}{2\cdot 2\cdot \beta^2}+\frac{3\cdot 5}{2\cdot 2\cdot 2\cdot \beta^6}+\cdots\right) \\
& + i\sigma\sqrt{\pi}\ \exp(-\beta^2)\ ,
\end{aligned}
\tag{D.14}
$$

with

$$
\sigma = \begin{cases} 0 & \beta_i > 0,\ \ |\beta_i| > |\beta_r| \\ 1 & \beta_i = 0,\ \ |\beta_i| < |\beta_r| \\ 2 & \beta_i < 0,\ \ |\beta_i| > |\beta_r|\ . \end{cases}
\tag{D.15}
$$

For $|\beta| < 10$,

$$
Z(\beta) \simeq \cfrac{a_1}{b_1 - \cfrac{a_2}{b_2 - \cfrac{a_3}{b_3 - \cfrac{a_4}{\cdots}}}}\ ,
\tag{D.16}
$$

with

$$
a_1 = \beta \qquad ,
\tag{D.17}
$$

$$
a_{n+1} = n\left(n-\frac{1}{2}\right) \qquad n = 1, 2, 3, \cdots\ ,
\tag{D.18}
$$

and

$$
b_{n+1} = -\beta^2 + \frac{1}{2} + 2n \qquad n = 0, 1, 2, \cdots\ .
\tag{D.19}
$$

By noting that

$$\lim_{n\to\infty} \frac{a_n}{a_{n+1}} = 1 \tag{D.20}$$

the partial fraction in Equation (D.16) is started by letting the last denominator be $b_{n+1} - 1$. Using a value of $n = 5$ for $1 < |\beta| < 10$ and a value of $n = 10$ for $|\beta| \leq 1$ yields excellent agreement with the tabulated values of $Z(\beta)$ given by Fried and Conte [1961].

Program FTDF.

The following data registers must be initiallized for program FTDF. This program requires a total of 65 registers. Frequencies are in GHz and distance in meters. Register 04 is the error in χ for stepping in ω and register 05 is the error in χ for iterative calculations in determining the plasma dispersion funcition. The normalized attenuation and phase shift are in registers 34 and 35.

Register

04	$\Delta\chi_1$	28	$\Delta\omega$	(step)
05	$\Delta\chi_2$			
06	ω	39	d	
07	ω_p			
08	ω_b			
09	ν			
10	ξ			
11	ζ			
12	δ			

```
 01▶LBL "FTDF"
SF 04  SCI 5  PRTON
6.012  PRREGX  PRTOFF

 08▶LBL 05
SF 10  XEQ 01  RCL 38
ST+ 06  RCL 06  RCL 37
X>Y?  GTO 05  STOP
GTO "FTDF"

 19▶LBL 01
1  STO 52  STO 56  0
STO 53  STO 57
XEQ "EXXYX"  XEQ "MUX"
XEQ "POW"  FS? 09
GTO 06  PRTON  ADV
34.035  PRREGX  PRTOFF

 36▶LBL 06
FC? 10  GTO 02

 39▶LBL 03
RCL 16  STO 14  RCL 17
STO 15  RCL 36  STO 13

 46▶LBL 02
XEQ "BETA"  XEQ "PDF"
50.054004  REGMOVE
XEQ "BETA1"  XEQ "PDF"
XEQ "EXXYX"  XEQ "EXZYZ"
XEQ "EZZ"  XEQ "MUX"
CF 10  "PDF"  PCLPS
"GPMU"  GETP  XEQ "GMU"
XEQ "GPMU"  "GPMU"
PCLPS  "PDF"  GETP
RCL 43  RCL 42  RCL 45
RCL 44  XROM "C/"
ST- 14  X<>Y  ST- 15
RCL 14  STO 16  RCL 15
STO 17  XEQ "POW"
RCL 36  RCL 13  -
RCL 36  STO 13  /  ABS
RCL 05  X<=Y?  GTO 02
PRTON  ADV  RCL 06  PRX
RCL 34  PRX  PRTOFF  RTN

 99▶LBL "EXXYX"
RCL 57  RCL 56  RCL 06
RCL 08  +  RCL 09  X<>Y
XROM "C/"  STO 18
STO 20  X<>Y  STO 19
STO 21  RCL 53  RCL 52
RCL 06  RCL 08  -
RCL 09  X<>Y  XROM "C/"
ST+ 18  ST- 20  X<>Y
ST+ 19  ST- 21  RCL 07
X^2  RCL 06  /  2  /
STO 00  CHS  0  X<>Y
RCL 19  RCL 18
XROM "C*"  1  +  STO 18
X<>Y  STO 19  RCL 00  0
RCL 21  RCL 20
XROM "C*"  STO 20  X<>Y
STO 21  RTN

153▶LBL "EXZYZ"
RCL 52  STO 22  STO 24
RCL 53  STO 23  STO 25
RCL 56  ST- 22  ST+ 24
RCL 57  ST- 23  ST+ 25
-2  ST+ 24  RCL 60
RCL 08  /  RCL 11  /
STO 00  CHS  0  X<>Y
RCL 23  RCL 22
XROM "C*"  STO 22  X<>Y
STO 23  RCL 00  0
RCL 25  RCL 24
XROM "C*"  STO 24  X<>Y
STO 25  RTN

192▶LBL "EZZ"
RCL 09  RCL 06  RCL 08
+  RCL 56  1  -  RCL 57
X<>Y  XROM "C*"  STO 26
X<>Y  STO 27  RCL 09
RCL 06  RCL 08  -
RCL 52  1  -  RCL 53
X<>Y  XROM "C*"  ST+ 26
X<>Y  ST+ 27  RCL 60
RCL 08  /  RCL 11  /  0
X<>Y  RCL 27  RCL 26
XROM "C*"  STO 26  X<>Y
STO 27  RCL 07  X^2
RCL 06  /  0  X<>Y
RCL 09  RCL 06
XROM "C/"  ST- 26  X<>Y
ST- 27  1  ST+ 26  RTN

247▶LBL "BETA"
RCL 15  RCL 14  2
XROM "Z^1/N"
XROM "CINV"  RCL 06
RCL 08  +  RCL 09  X<>Y
XROM "C*"  RCL 06
RCL 11  *  RCL 12  *  2
SQRT  *  0  X<>Y
XROM "C/"  STO 40
STO 58  X<>Y  STO 41
STO 59  RTN

276▶LBL "BETA1"
RCL 09  RCL 06  RCL 08
-  RCL 06  RCL 08  +
RCL 09  X<>Y  XROM "C/"
RCL 41  RCL 40
XROM "C*"  STO 40  X<>Y
STO 41  RTN

294▶LBL "MUX"
RCL 21  RCL 20  2
XROM "Z^N"  RCL 19
RCL 18  XROM "C/"
RCL 19  RCL 18
XROM "C+"  STO 16  X<>Y
STO 17  RTN

309▶LBL "POW"
RCL 17  RCL 16  2
XROM "Z^1/N"  X<>Y  ABS
CHS  STO 36  RCL 06  *
6.6667  *  RCL 39  *
RCL 10  /  E^X  LOG  10
*  STO 34  X<>Y  1  +
RCL 39  *  RCL 10  /
RCL 06  *  382  *
STO 35  RTN  END
```

```
 01▶LBL "GMU"
RCL 21  RCL 20  RCL 19
RCL 18  XROM "C/"
RCL 25  RCL 24
XROM "C*"  RCL 19
RCL 18  XROM "C-"
RCL 10  RCL 11  *  -2  *
0  X<>Y  XROM "C*"
STO 42  X<>Y  STO 43
RCL 23  RCL 22  RCL 19
RCL 18  XROM "C/"
RCL 23  RCL 22
XROM "C*"  ST- 42  X<>Y
ST- 43  RCL 25  RCL 24
RCL 19  RCL 18
XROM "C/"  RCL 25
RCL 24  XROM "C*"
RCL 11  X^2  0  X<>Y
XROM "C*"  ST+ 42  X<>Y
ST+ 43  RCL 47  STO 35
RCL 46  STO 34  RCL 17
RCL 16  RCL 15  CHS
RCL 14  CHS  XROM "C/"
RCL 11  X^2  1  +  +
RCL 27  RCL 26
XROM "C*"  ST+ 42  X<>Y
ST+ 43  RCL 10  X^2  0
X<>Y  RCL 17  RCL 16
XROM "C*"  ST+ 42  X<>Y
ST+ 43  RCL 25  RCL 26
RCL 15  RCL 14
XROM "C/"  RCL 25
RCL 24  XROM "C*"
STO 60  X<>Y  STO 61
RCL 23  RCL 22  RCL 15
RCL 14  XROM "C/"
RCL 23  RCL 22
XROM "C*"  ST+ 60  X<>Y
ST+ 61  RCL 60  ST+ 42
RCL 61  ST+ 43  RCL 10
RCL 11  *  2  *  0  X<>Y
RCL 23  RCL 22
XROM "C*"  STO 32  X<>Y
STO 33  RCL 27  RCL 26
RCL 11  X^2  0  X<>Y
XROM "C*"  RCL 33
RCL 32  XROM "C+"
RCL 19  RCL 18
XROM "C/"  RCL 10  X^2
+  STO 44  X<>Y  STO 45
X<>Y  XROM "CINV"
RCL 43  RCL 42
XROM "C*"  RCL 19
RCL 18  XROM "C/"
STO 32  X<>Y  STO 33
RCL 45  RCL 44  RCL 15
RCL 14  XROM "C*"
ST- 42  X<>Y  ST- 43  -1
ST* 44  ST* 45  RTN  END
```

```
 01▶LBL "GPMU"
RCL 59  RCL 58  2
XROM "Z^N"  0  ENTER^
-2  XROM "C*"  1  +
RCL 55  RCL 54
XROM "C*"  STO 28  X<>Y
STO 29  RCL 59  RCL 58
0  ENTER^  2  XROM "C*"
ST- 28  X<>Y  ST- 29
RCL 59  RCL 58  RCL 15
RCL 14  XROM "C/"  0
ENTER^  .5  XROM "C*"
RCL 29  RCL 28
XROM "C*"  STO 28  X<>Y
STO 29  RCL 41  RCL 40
2  XROM "Z^N"  0  ENTER^
-2  XROM "C*"  1  +
RCL 51  RCL 50
XROM "C*"  STO 30  X<>Y
STO 31  RCL 41  RCL 40
0  ENTER^  2  XROM "C*"
ST- 30  X<>Y  ST- 31
RCL 41  RCL 40  RCL 15
RCL 14  XROM "C/"  0
ENTER^  .5  XROM "C*"
RCL 31  RCL 30
XROM "C*"  STO 30  X<>Y
STO 31

 82▶LBL "PEXX"
RCL 29  RCL 28  RCL 06
RCL 08  +  RCL 09  X<>Y
XROM "C/"  STO 46
STO 48  X<>Y  STO 47
STO 49  RCL 31  RCL 30
RCL 06  RCL 08  -
RCL 09  X<>Y  XROM "C/"
ST+ 46  ST- 48  X<>Y
ST+ 47  ST- 49  RCL 07
X^2  RCL 06  /  2  /
STO 00  CHS  ST* 47
ST* 46  RCL 00  0
RCL 49  RCL 48
XROM "C*"  STO 48  X<>Y
STO 49

127▶LBL "PEXZ"
RCL 31  RCL 30  RCL 29
RCL 28  XROM "C-"
RCL 60  RCL 08  /
RCL 11  /  STO 00  CHS
0  X<>Y  XROM "C*"
STO 50  X<>Y  STO 51

146▶LBL "PEYZ"
RCL 29  RCL 28  RCL 31
RCL 30  XROM "C+"
RCL 00  0  XROM "C*"
STO 52  X<>Y  STO 53

158▶LBL "PEZZ"
RCL 09  RCL 06  RCL 08
-  RCL 30  1  -  RCL 31
X<>Y  XROM "C*"  STO 54
X<>Y  STO 55  RCL 09
RCL 06  RCL 08  +
RCL 28  1  -  RCL 29
X<>Y  XROM "C*"  ST+ 54
X<>Y  ST+ 55  RCL 00
RCL 11  /  RCL 08  /
ST* 54  ST* 55
```

```
192▶LBL "GPXX"
RCL 33  RCL 32  RCL 45
RCL 44  XROM "C*"
STO 00  X<>Y  STO 01
RCL 23  RCL 22  RCL 10
RCL 11  *  2  *  0  X<>Y
XROM "C*"  RCL 35
RCL 34  XROM "C-"
RCL 19  RCL 18
XROM "C/"  ST+ 00  X<>Y
ST+ 01  RCL 27  RCL 26
RCL 15  RCL 14
XROM "C/"  CHS  RCL 10
X^2  +  STO 02  X<>Y
CHS  STO 03  RCL 21
RCL 20  RCL 19  RCL 18
XROM "C/"  2  XROM "Z^N"
CHS  1  +  X<>Y  CHS
X<>Y  RCL 03  RCL 02
XROM "C*"  RCL 01
RCL 00  XROM "C+"
RCL 47  RCL 46
XROM "C*"  ST+ 44  X<>Y
ST+ 45

258▶LBL "GPXY"
RCL 21  RCL 20  RCL 19
RCL 18  XROM "C/"
RCL 03  RCL 02
XROM "C*"  STO 00  X<>Y
STO 01  RCL 25  RCL 24
RCL 19  RCL 18
XROM "C/"  RCL 10
RCL 11  *  CHS  0  X<>Y
XROM "C*"  RCL 01
RCL 00  XROM "C+"
RCL 49  RCL 48
XROM "C*"  0  ENTER^  2
XROM "C*"  ST+ 44  X<>Y
ST+ 45

295▶LBL "GPXZ"
RCL 33  RCL 32  1  -
RCL 10  RCL 11  *  0
X<>Y  XROM "C*"  STO 00
X<>Y  STO 01  RCL 23
RCL 22  RCL 15  RCL 14
XROM "C/"  ST- 00  X<>Y
ST- 01  RCL 23  RCL 22
RCL 19  RCL 18
XROM "C/"  RCL 01
RCL 00  XROM "C+"
RCL 51  RCL 50
XROM "C*"  0  ENTER^  2
XROM "C*"  ST- 44  X<>Y
ST- 45
```

```
335▶LBL "GPYZ"
RCL 25  RCL 24  RCL 10
X^2  0  X<>Y  XROM "C*"
STO 00  X<>Y  STO 01
RCL 25  RCL 24  RCL 15
RCL 14  XROM "C/"
ST+ 00  X<>Y  ST+ 01
RCL 21  RCL 20  RCL 10
RCL 11  *  0  X<>Y
XROM "C*"  RCL 01
RCL 00  XROM "C+"
RCL 19  RCL 18
XROM "C/"  RCL 53
RCL 52  XROM "C*"  0
ENTER^  2  XROM "C*"
ST+ 44  X<>Y  ST+ 45

378▶LBL "GPZZ"
RCL 33  RCL 32  RCL 11
X^2  CHS  0  X<>Y
XROM "C*"  STO 00  X<>Y
STO 01  RCL 17  CHS
RCL 16  CHS  RCL 15
RCL 14  XROM "C/"
STO 02  X<>Y  STO 03
X<>Y  RCL 01  RCL 00
XROM "C+"  1  +  RCL 11
X^2  +  RCL 55  RCL 54
XROM "C*"  ST+ 44  X<>Y
ST+ 45  RCL 03  RCL 02
RCL 15  RCL 14
XROM "C/"  RCL 27
RCL 26  XROM "C*"
ST- 44  X<>Y  ST- 45
RCL 61  RCL 60  RCL 15
RCL 14  XROM "C/"
RCL 15  RCL 14
XROM "C/"  ST- 44  X<>Y
ST- 45  RTN  .END.
```

Program VDCF.

The following data registers must be initialized for program VDCF. This program requires a total of 38 data registers. Frequencies are in GHz and distance is in meters. The waves normalized attenuation and phase shift are in registers 34 and 35. The zero speed exponent case is run by setting register 11 to zero. Register 38 is the frequency step in GHz.

Register

06	ω	31	d
07	ω_p		
08	ω_b	38	$\Delta\omega$
09	$\langle\nu\rangle$		
11	A_h		
12	a_h		
13	x_h		
14	A_g		
15	a_g		

```
 01▶LBL "VDCF"
PRTON  7.016  PRREGX
RCL 36  STO 06

 07▶LBL 01
RCL 06  RCL 08  -
RCL 09  /  ABS  X=0?
GTO 04  LOG  STO 17
XEQ "GHX"  GTO 05

 20▶LBL 04
1.0 E-05  STO 17
XEQ "GHX"

 24▶LBL 05
RCL 22  CHS  RCL 20  2
XROM "Z^N"  RCL 21  X^2
-  XROM "CINV"  STO 24
X<>Y  STO 25  X<>Y
RCL 22  CHS  RCL 20
XROM "C*"  RCL 07  X^2
RCL 06  /  0  X<>Y
XROM "C*"  CHS  1  +
STO 26  X<>Y  CHS
STO 27

 56▶LBL 02
RCL 25  RCL 24  RCL 21
RCL 06  /  RCL 07  X^2
*  0  X<>Y  XROM "C*"  2
XROM "Z^N"  CHS  X<>Y
CHS  X<>Y  RCL 27
RCL 26  XROM "C/"
RCL 27  RCL 26
XROM "C+"  2
XROM "Z^1/N"  STO 33
X<>Y  ABS  CHS  STO 32
RCL 06  0.3  /  RCL 32
*  2  *  RCL 31  *  E^X
LOG  10  *  STO 34  1.0
RCL 33  +  RCL 31  *
RCL 06  *  382  *
STO 35

111▶LBL 03
PRTON  6.006  PRREGX
34.035  PRREGX  PRTOFF
RCL 37  RCL 06  X>Y?
STOP  RCL 38  ST+ 06
GTO 01

125▶LBL "GHX"
RCL 11  X=0?  GTO "GHND"
RCL 17  RCL 13  +
RCL 12  *  XEQ "TANH"
CHS  1  +  RCL 11  *  1
+  STO 18  RCL 06  *
STO 20  RCL 18  RCL 08
*  STO 21  RCL 17
RCL 16  -  RCL 15  *
XEQ "TANH"  1  -  RCL 14
*  1  +  STO 19  RCL 09
*  STO 22  RTN

167▶LBL "TANH"
STO 30  E^X  RCL 30  CHS
E^X  -  RCL 30  E^X
RCL 30  CHS  E^X  +  /
RTN

182▶LBL "GHND"
RCL 06  STO 20  RCL 08
STO 21  RCL 09  STO 22
RTN  .END.
```

APPENDIX E

HIGH VOLTAGE R.F. TRANSFORMER

A two stage R.F. transformer circuit was constructed to provide a high voltage R.F. signal for plasma heating and perturbation experiments. Two 1 to 4 impedance ratio transformers were cascaded to yield a 1 to 16 impedance step-up network with a 1 to 4 voltage gain. Using a 100 watt wide band amplifier (Amplifier Research 100AL) with a swept oscillator for the voltage source, R.F. voltages of up to 300 volts over the frequency range of 10 kHz to 20 MHz could be produced.

Figure E.1 shows the construction layout of the R.F. transformer circuit and load. The basic winding design was taken from Ruthroff [1959]. The first stage transformer was constructed using two J4613 toroids (Magnetics Inc.) and seven turns of a 22 gauge bifilar winding. The second stage transformer was constructed of one J4613 toroid, one P4613 toroid and seven turns of a 22 gauge bifilar winding. All toroids had dimensions of 61 mm 0.D., 44 mm I.D. and 13 mm in height. The J material toroids have a measured relative permeability of $\mu_r \simeq 5000$ for frequencies below 300 KHz. The P material toroid has a slightly larger relative permeability. Both transformers were flush mounted to a copper plate with a heat sink grease to improve thermal contact. The copper plate served as both a ground and heat sink. The transformers and input connector were mounted as close together as possible in order to reduce stray capacitance and inductive effects.

The output of the second stage transformer was connected to a load constructed of 6 each 100Ω and 2 each 50Ω low inductance carbon resistors. The plasma, which is a high impedance, was coupled off in shunt to the 700Ω resistor bank through

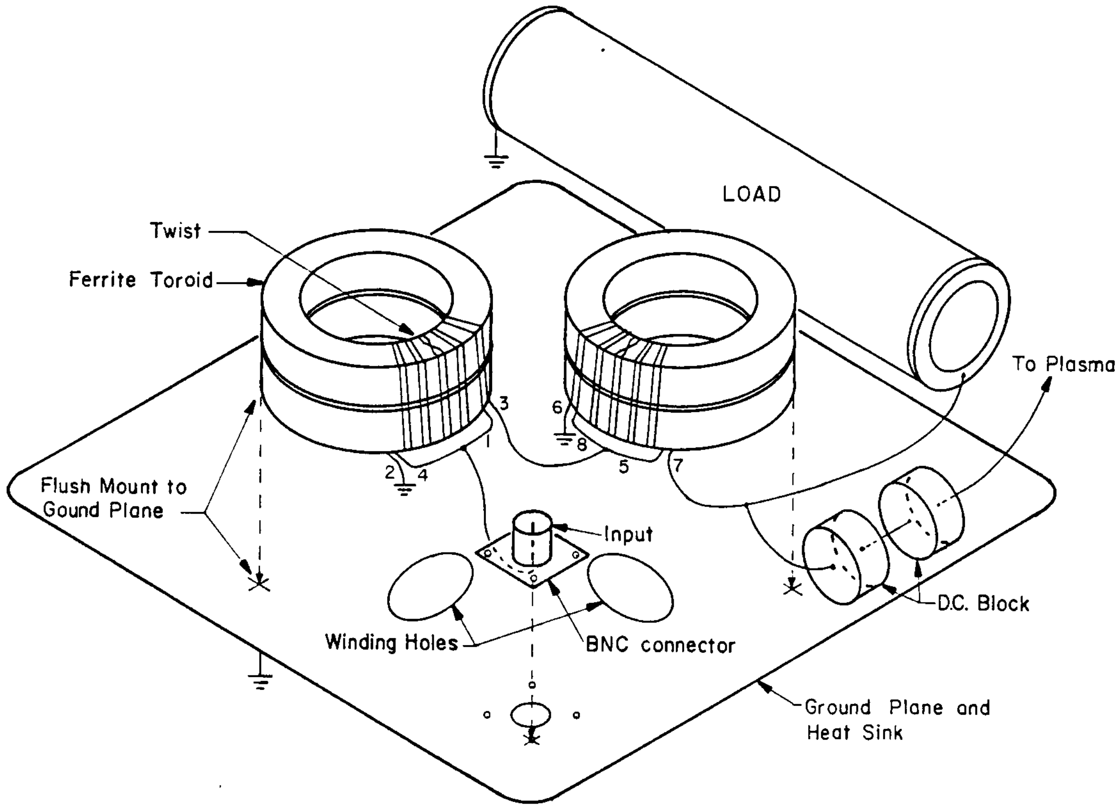

Figure E.1. High voltage R.F. transformer and load.

two high voltage ceramic capacitors which served as a D.C. voltage block.

Figure E.2 shows a transmission line circuit model for the two stage transformer network. The bifilar windings on the toroids form transmission line sections of approximately 53 cm. in length. The swept oscillator and power amplifier are represented by the voltage source V_g with impedance $R_g = 50\Omega$.

For the circuit in Figure E.2, maximum power will be transmitted to the load Z_L when the impedances of the successive stages match, or $R_g = Z_{il}, Z_{t1} = Z_{i2}$, and $Z_{t2} = Z_L$. In order to determine the input and output impedances of a given transformer stage the transmission line equations must be analyzed.

The equations for the first stage transformer can be written as:

$$V_g - (I_1 + I_2)R_g - V_1 = 0 \ , \tag{E.1}$$

$$V_g - (I_1 + I_2)R_g + V_2 - I_2 Z_{i2} = 0 \ , \tag{E.2}$$

$$V_1 - V_2 \cosh \Upsilon\ell - I_2 Z_{01} \sinh \Upsilon\ell = 0 \ , \tag{E.3}$$

and

$$I_1 - I_2 \cosh \ \Upsilon\ell - V_2/Z_{01} \sinh \Upsilon\ell = 0 \ , \tag{E.4}$$

where Z_{01} is the characteristic impedance of the bifilar transmission line of length ℓ and propagation constant Υ. The propagation constant Υ can be expressed in terms of a series resistance R, series inductance L, shunt conductance G, and shunt capacitance C of the transmission line [Lio 1980],

$$\Upsilon = \sqrt{(R + j\omega L) \ / \ (G + j\omega C)} \ . \tag{E.5}$$

In Equation (E.5) ω is the radian frequency where $\omega = 2\pi \ f$.

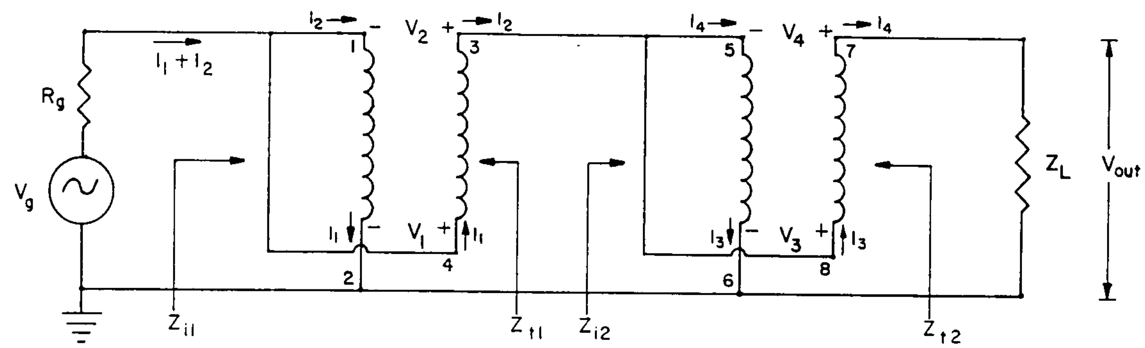

Figure E.2. Transmission line circuit model for two stage transformer.

In the limit

$$R \ll \omega L \qquad \text{and} \qquad G \ll \omega C\ . \tag{E.6}$$

The propagation constant Υ becomes

$$\Upsilon \simeq \frac{1}{2}\left(R\sqrt{\frac{C}{L}} + G\sqrt{\frac{L}{C}}\right) + j\omega\sqrt{LC}\ , \tag{E.7}$$

which can be expressed in terms of the attenuation constant α and phase constant β as

$$\Upsilon = \alpha + j\beta\ , \tag{E.8}$$

where

$$\alpha = \frac{1}{2}\left(R\sqrt{\frac{C}{L}} + G\sqrt{\frac{L}{C}}\right)\ , \tag{E.9}$$

and

$$\beta = \omega\sqrt{CL}\ . \tag{E.10}$$

The characteristic impedance of a transmission line can also be expressed in terms of the line's circuit parameters as

$$Z_0 = \sqrt{\frac{R + j\omega L}{G + j\omega C}}\ , \tag{E.11}$$

which can be approximated as

$$Z_0 \simeq \sqrt{\frac{L}{C}}\left[1 + \frac{1}{2}\left(\frac{R}{j\omega L} - \frac{G}{j\omega C}\right)\right]\ , \tag{E.12}$$

or

$$Z_0 \simeq \sqrt{\frac{L}{C}} \, . \tag{E.13}$$

The inductance L used above is the series inductance due to the turns on the toroid of large μ_r. The capacitance C will be the capacitance of adjacent wires of the bifilar windings and the series resistance R will be principally due to losses in the ferromagnetic material of the toroid. This resistance can be expressed as the sum of three parts as given by the Legg equation [Soohoo 1960],

$$R_f = \mu_r L[ef^2 + afB_{\mathbf{max}} + cf] \, , \tag{E.14}$$

where μ_r is the relative permeability of the toroid, L is the self inductance of the windings and the toroid core, $B_{\mathbf{max}}$ is the maximum flux density in the core at frequency f and e, a, and c are constants. If the copper losses of the winding are small, the terms on the right of Equation (E.14) represent respectively the eddy current, the hysteresis, and the residual losses of the core.

Returning now to the circuit Equations (E.1) through (E.4), the input and output impedance of the first stage transformer can be written as

$$Z_{i1} = Z_{o1} \left[\frac{Z_{i2} \cosh \Upsilon \ell_1 + Z_{o1} \sinh \Upsilon \ell_1}{2Z_{o1}(1 + \cosh \Upsilon \ell_1) + Z_{i2} \sinh \Upsilon \ell_1} \right] \, , \tag{E.15}$$

and

$$Z_{t1} = Z_{o1} \left[\frac{2Z_{i2}(1 + \cosh \Upsilon \ell_1) + Z_{o1} \sinh \Upsilon \ell_1}{Z_{o1} \cosh \Upsilon \ell_1 + Z_{i2} \sinh \Upsilon \ell_1} \right] \, . \tag{E.16}$$

The input and output impedances of the second stage transformer can be written by letting $Z_{o1} \rightarrow Z_{o2}, Z_{i2} \rightarrow R_L$ and $\Upsilon \ell_1 \rightarrow \Upsilon \ell_2$ in Equations (E.15) and (E.16).

The output power of the first stage, is given by

$$P_{o1} = |I_2|^2 Z_{i2} \, , \tag{E.17}$$

or

$$P_{o1} = \frac{V_g^2(1+\cosh\Upsilon\ell_1)^2 Z_{i2}}{[2R_g(1+\cosh\Upsilon\ell_1)+Z_{i2}\cosh\Upsilon\ell_1]^2+\left[\frac{R_g Z_{i2}+Z_{o1}^2}{Z_{o1}}\right]^2\sinh^2\Upsilon\ell} . \tag{E.18}$$

In considering the lossless network where $\alpha = 0$, [Ruthroff 1959] shows that by setting

$$\left.\frac{dP_o}{dR_L}\right|_{L=o} = 0 ,$$

where R_L is Z_{i2} above, the transformer is matched when $R_L = 4R_g$ for the single stage network. The optimum value of Z_{o1} is then determined by minimizing the coefficient of $\sinh^2\Upsilon\ell$ in Equation (E.18), which yields $Z_{o1} = 2R_g$.

Extending the above to the second stage, it follows that maximum power is transferred for the lossless two stage transformer when

$$Z_{o1} = 2R_g , \tag{E.19}$$

$$Z_{o2} = 8R_g , \tag{E.20}$$

and

$$Z_L = 16R_g . \tag{E.21}$$

Hence for a 50Ω generator impedance, the two stage transformer should be terminated in an 800Ω load with the characteristic impedances of the successive stage being $Z_{o1} = 100\Omega$, and $Z_{o2} = 400\Omega$.

By using a Hewlett Packard 3577 Network Analyzer the small signal voltage gain and phase of the two stage transformer was measured with an 8 resistor 700Ω load. This measurement is shown in Figure E.3. A voltage gain of 4 is shown for much of

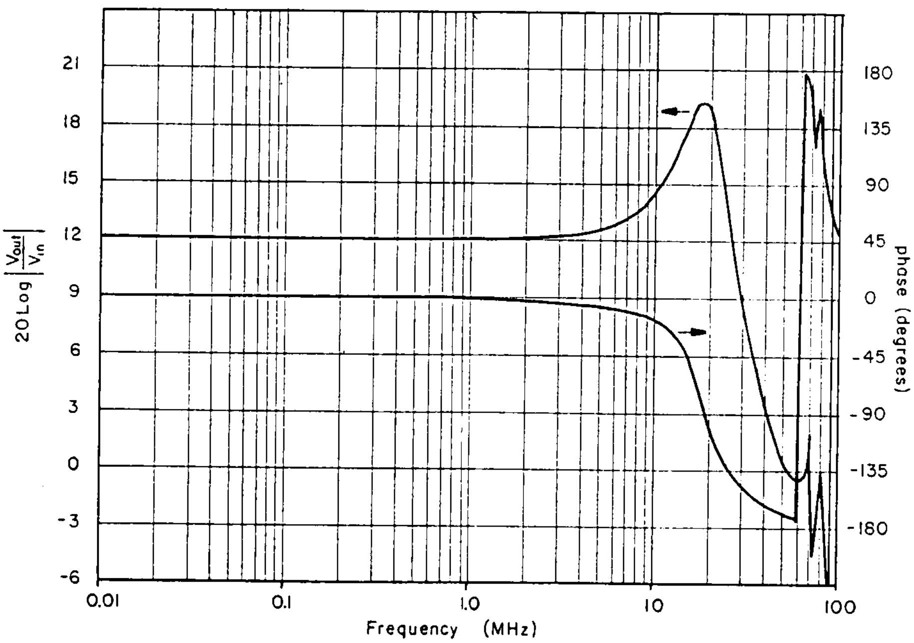

Figure E.3. Voltage gain and phase for two stage transformer.

the bandwidth with a resonance occuring near 10 MHz. The large bandwidth and 1 to 4 voltage gain shown in Figure E.3 are encouraging but are accompanied by a large reflection coefficient Γ over much of the bandwidth. This is shown in Figure E.4, which is the measured reflection coefficient of the two stage transformer. The large reflection coefficient is due in part to a change in Z_L with frequency and the values of Z_{o1} and Z_{o2}. Figure E.5 shows the measured load impedance Z_L used for the two stage network.

The characteristic impedances Z_{o1} and Z_{o2} and the propagation factors $\Upsilon\ell_1$ and $\Upsilon\ell_2$ of the two transformers cannot be measured directly. However, referring to Equation (E.15), the open circuit impedance of the first stage transformer is determined by letting $Z_{i2} \to \infty$ and is given by

$$Z_{oc1} = Z_{o1} coth \Upsilon\ell_1 \ . \tag{E.22}$$

The short circuit impedance for the first stage transformer is similarly determined by letting $Z_{i2} \to 0$ and is given by

$$Z_{oc1} = Z_{o1} \frac{\sinh \Upsilon\ell_1}{2(1+\cosh \Upsilon\ell)} \ . \tag{E.23}$$

Taking the ratio,

$$\frac{Z_{oc1}}{Z_{sc1}} = \frac{2\cosh \Upsilon\ell_1(1+\cosh \Upsilon\ell_1)}{\sinh^2 \Upsilon\ell_1} \ , \tag{E.24}$$

and using identities for the hyperbolic functions, $\Upsilon\ell_1$ is given by,

$$\Upsilon\ell_1 = 2 \text{ arc } \sinh \left[\frac{\sqrt{2}}{2} \left(\frac{1}{2} \frac{Z_{oc1}}{Z_{sc1}} - 1 \right) \right]^{-\frac{1}{2}} \ . \tag{E.25}$$

Taking the product,

$$Z_{oc1} Z_{sc1} = Z_o^2 \frac{\cosh \Upsilon\ell_1}{2(1+\cosh \Upsilon\ell_1)} \ , \tag{E.26}$$

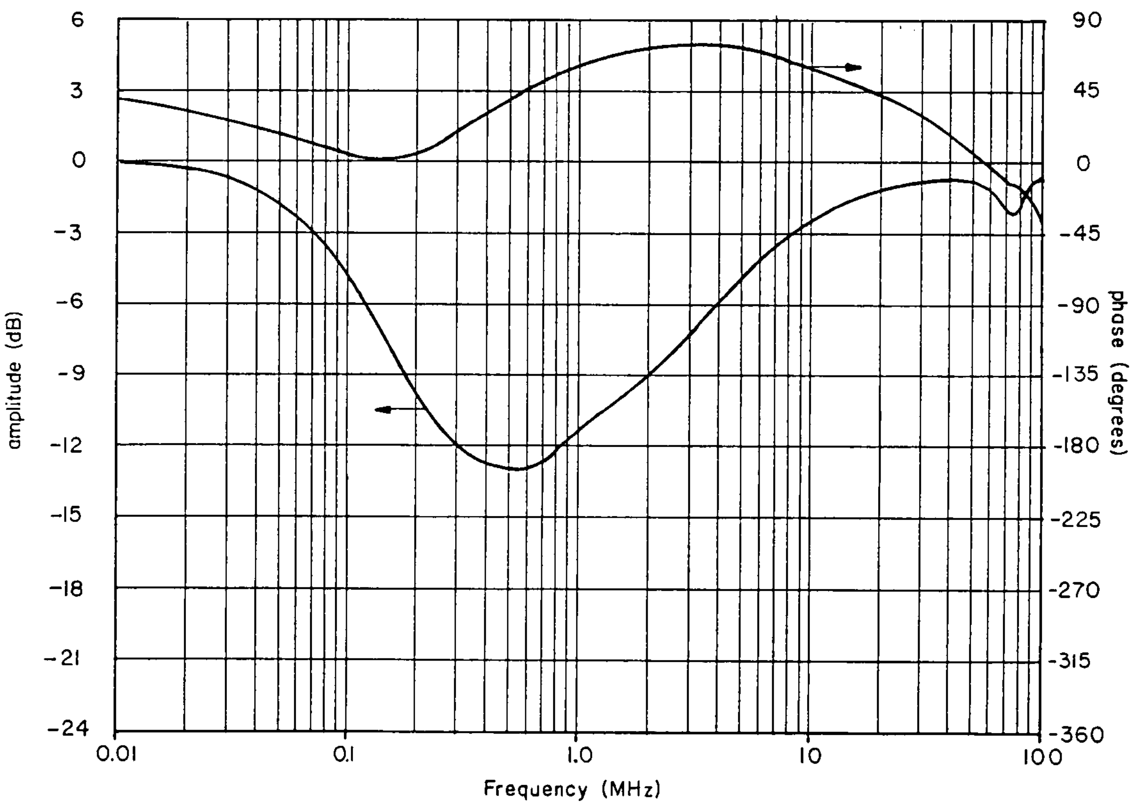

Figure E.4. Reflection coefficient magnitude and phase for two stage transformer with load.

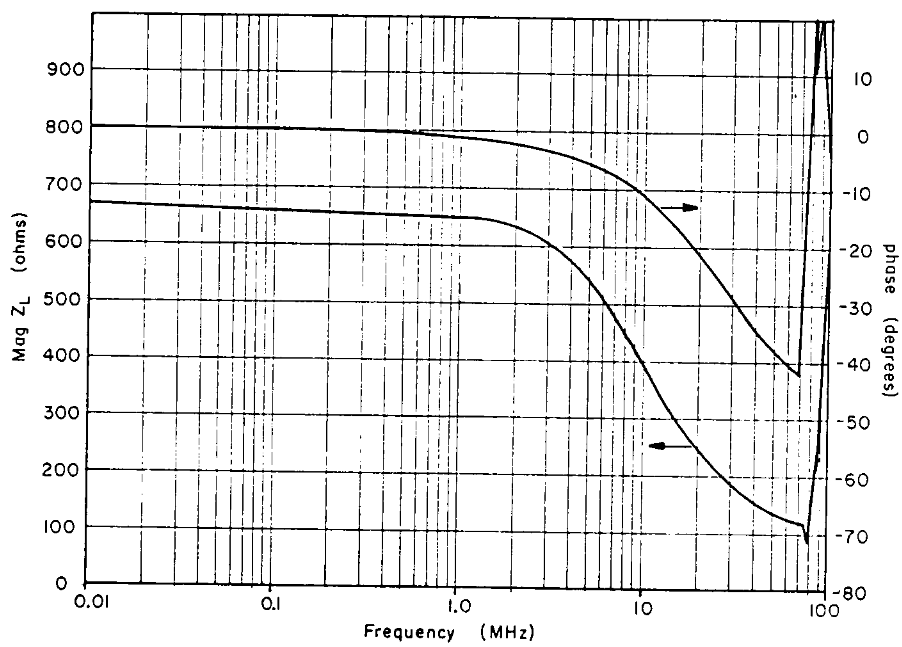

Figure E.5. Load impedance Z_L used with two stage transformer.

and using the value of $\Upsilon\ell_1$ determined by Equation (E.25) the characteristic impedence Z_{o1} is given by,

$$Z_{o1} = \left[2Z_{oc}Z_{sc}\left(1 + \frac{1}{\cosh\Upsilon\ell_1}\right)\right]^{\frac{1}{2}} \quad . \tag{E.27}$$

By measuring the open and short circuit impedances of each stage independently, the characteristic impedances Z_{o1}, Z_{o2} and propagation factors $\Upsilon\ell_1$ and $\Upsilon\ell_2$ can be determined. Using an HP 3577 network analyzer, the measured values of the open circuit impedance Z_{oc1} and short circuit impedence Z_{sc1} of the first stage transformer are shown in Figures E.6 and E.7. The measured values of the open circuit impedance Z_{oc2} and short circuit impedance Z_{sc2} of the second stage transformer are shown in Figures E.8 and E.9. Although measurements are shown down to 10 kHz, considerable loss in dynamic range of the HP 3577 network analyzer occurs below 50 kHz. Measurements of the low frequency portion of the short circuit impedance are the most critical in terms of this loss in dyanamic range. Averaging and graphical smoothing were used with Figures E.7 and E.9 to improve data resolution.

Using a six term series representation for the arc sinh function [Abramowitz and Stegun 1972],

$$\begin{aligned}\operatorname{arc\,sinh}(z) \simeq z - \frac{1}{2\cdot 3}\,z^3 + \frac{1\cdot 3}{2\cdot 4\cdot 5}\,Z^5 - \frac{1\cdot 3\cdot 5}{2\cdot 4\cdot 6\cdot 7}\,z^7 \\ + \frac{1\cdot 3\cdot 5\cdot 7}{2\cdot 4\cdot 6\cdot 8\cdot 9}\,z^9 - \frac{1\cdot 3\cdot 5\cdot 7\cdot 9}{2\cdot 4\cdot 6\cdot 8\cdot 10\cdot 11}\,z^{11} \qquad |z| < 1\,,\end{aligned} \tag{E.28}$$

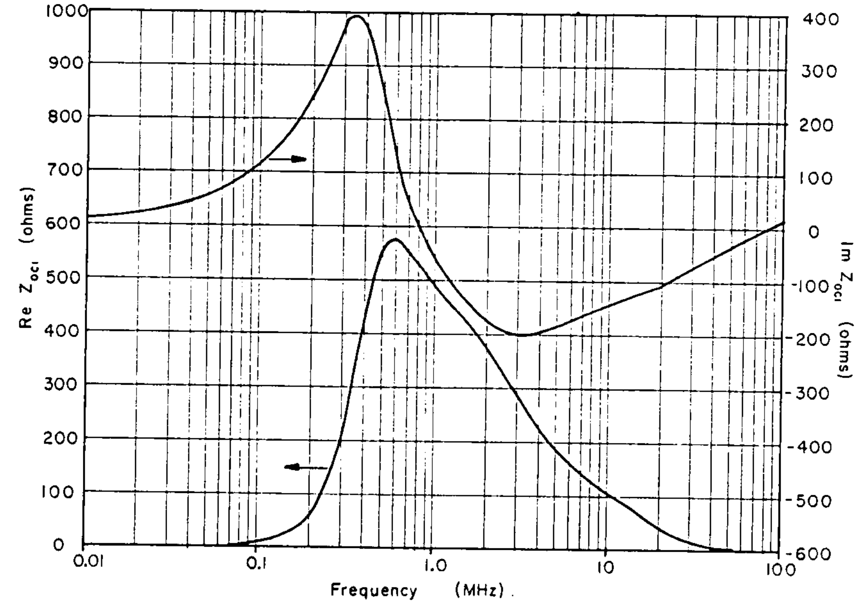

Figure E.6. Open circuit impedance Z_{0c1} for first stage transformer.

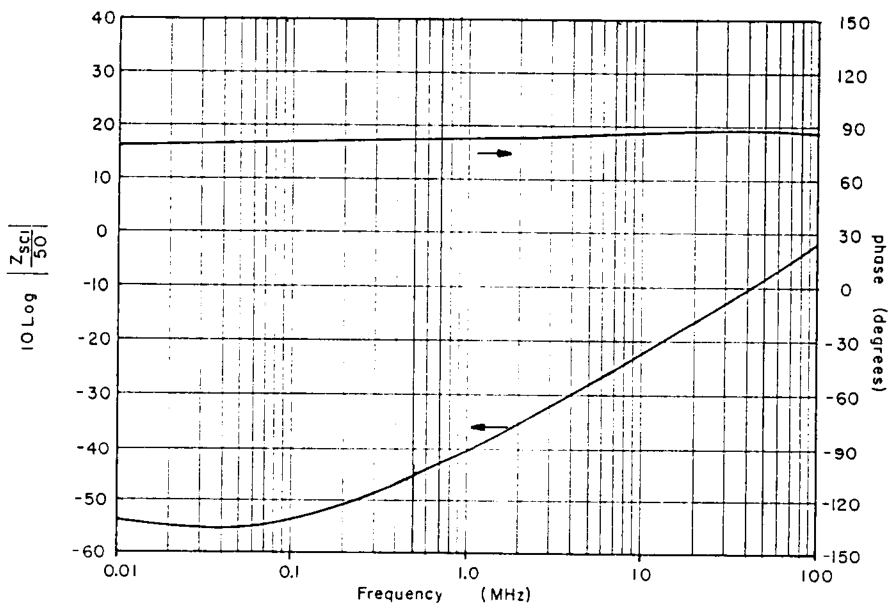

Figure E.7. Short circuit impedance Z_{sc1} for first stage transformer.

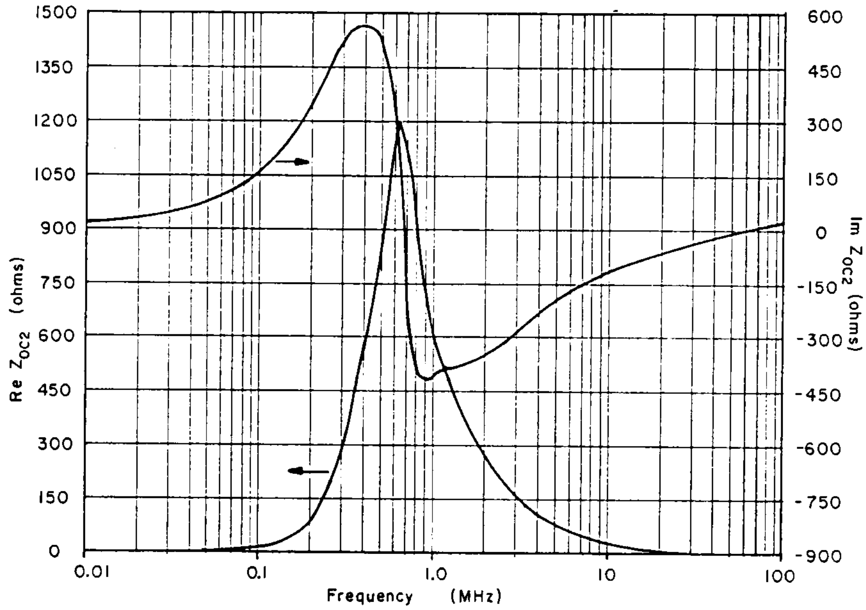

Figure E.8. Open circuit impedance Z_{0c2} of second stage transformer.

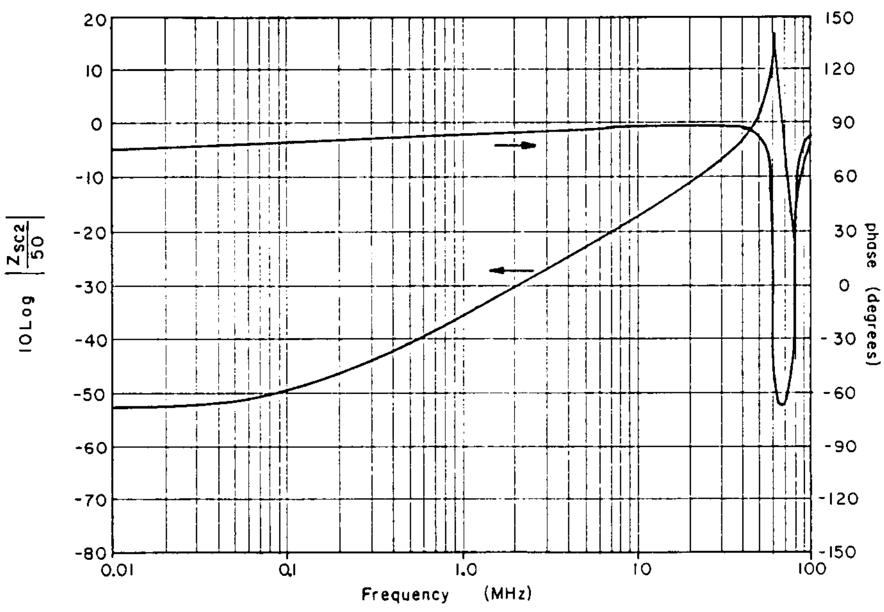

Figure E.9. Short circuit impedance Z_{sc2} of second stage transformer.

and

$$\simeq Ln\ z + \frac{1}{2\cdot 2}\cdot\frac{1}{z^2} - \frac{1\cdot 3}{2\cdot 4\cdot 4}\cdot\frac{1}{z^4} + \frac{1\cdot 3\cdot 5}{2\cdot 4\cdot 6\cdot 6}\cdot\frac{1}{z^6}$$
$$\frac{1\cdot 3\cdot 5\cdot 7}{2\cdot 4\cdot 6\cdot 8\cdot 8}\cdot\frac{1}{z^8} + \frac{1\cdot 3\cdot 5\cdot 7\cdot 9}{2\cdot 4\cdot 6\cdot 8\cdot 10\cdot 10}\cdot\frac{1}{z^{10}} \qquad |z| > 1\ , \tag{E.29}$$

in Equation (E.25), the propagation factors for the two transformer stages were computed using the data in Figures E.6 through E.9. Figures E.10 and E.11 show the calculated values of the propagation constants. Using these values and Equation (E.27), the characteristic line impedance for the two transformer stages are calculated. Figures E.12 and E.13 show the calculated values of Z_{o1} and Z_{o2} respectively.

With the propagation constants $\Upsilon\ell_1$ and $\Upsilon\ell_2$ known, along with the characteristic impedances Z_{o1} and Z_{o2}, the input impedance of the two stage network can be calculated. Using the measured value of the load impedance Z_L (Figure E.5) and the calculated values of Z_{o2} and $\Upsilon\ell_2$ the input impedance Z_{i1} is calculated. Figure E.14 shows the measured value of the input impedance of the network, and Figure E.15 shows the calculated value of the input impedance where $Z_{in} = Z_{i1}$. Visual comparison of Figures E.14 and E.15 show reasonable agreement between the measured behavior of the network and the calculated behavior for frequencies below 20 MHz.

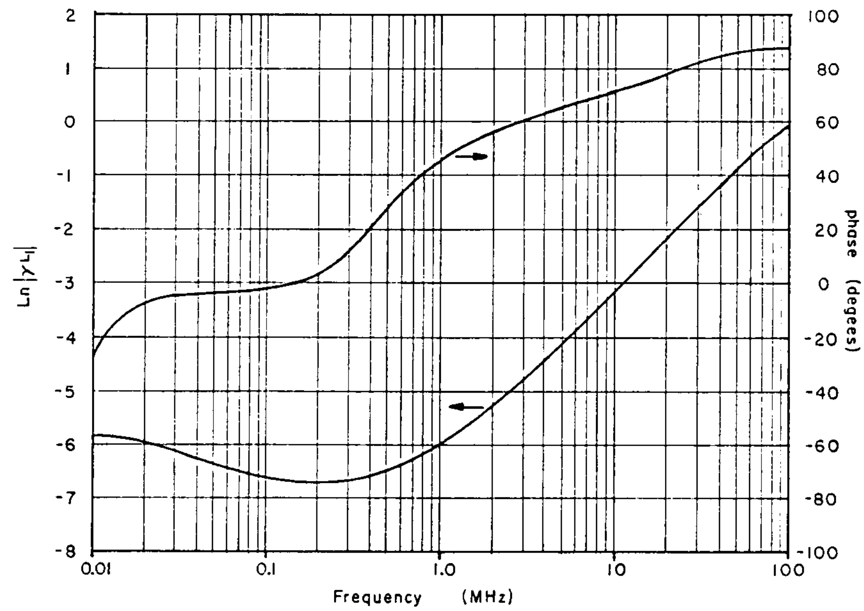

Figure E.10. Calculated value of the propagation factor γL_1 of the first stage transformer.

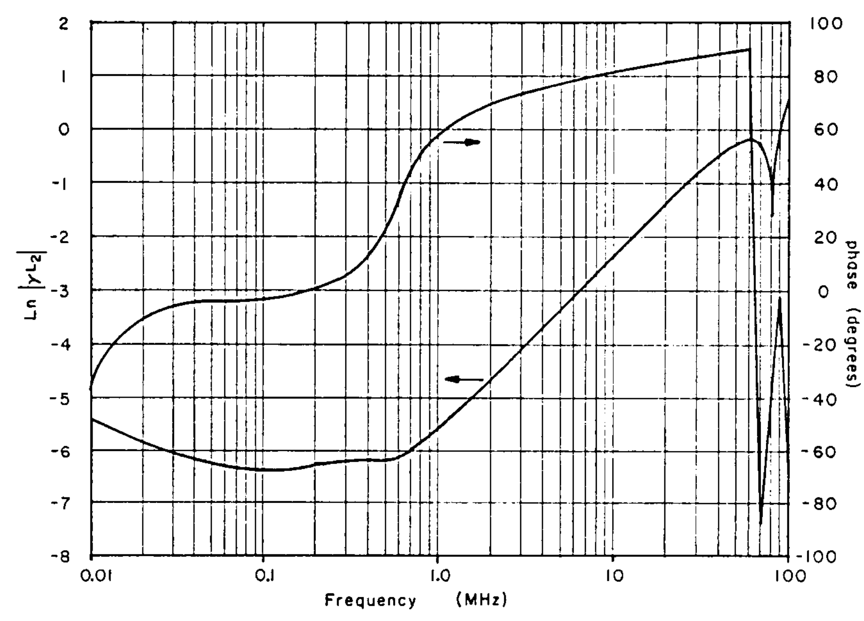

Figure E.11. Calculated value of the propagation factor γL_2 of second stage transformer.

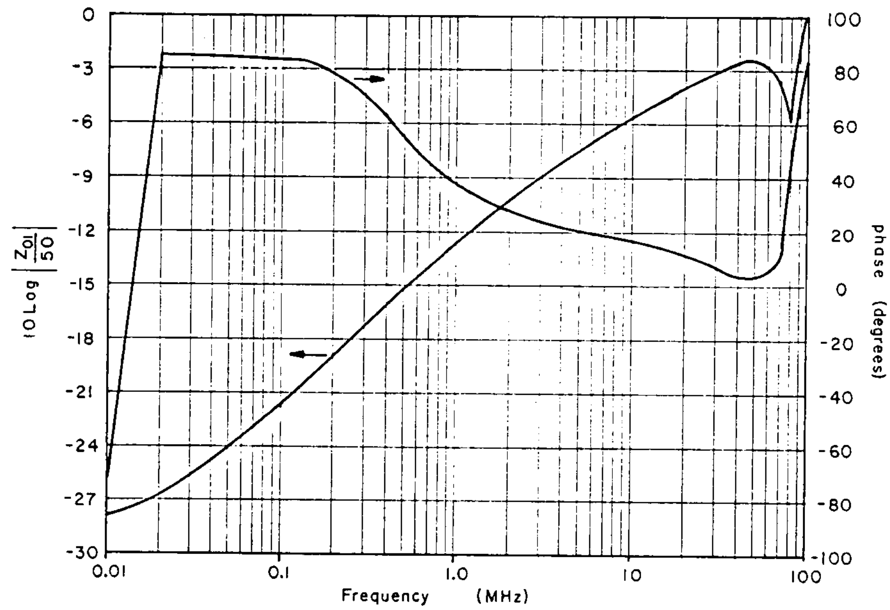

Figure E.12. Calculated value of the characteristic impedance Z_{01} of the first stage transformer.

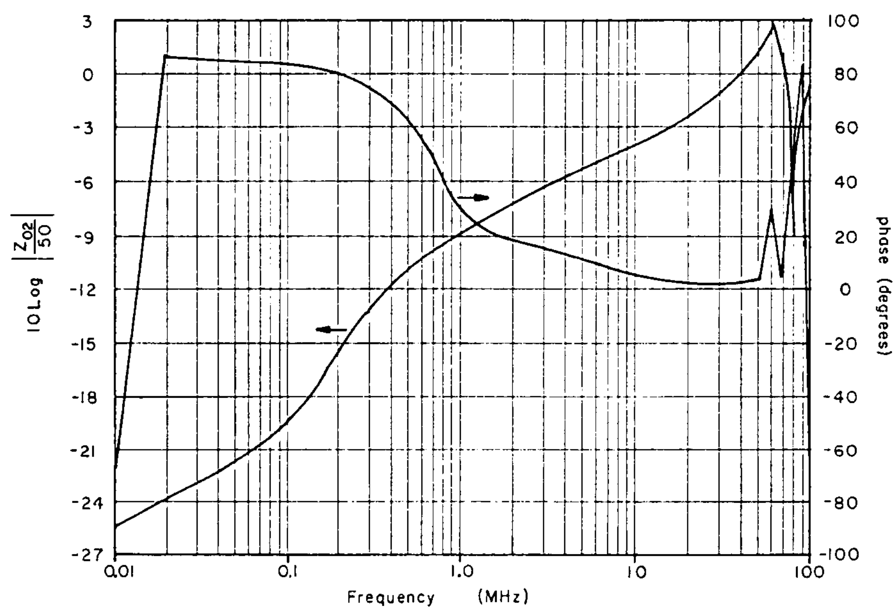

Figure E.13. Calculated value of the characteristic impedance Z_{02} of second stage transformer.

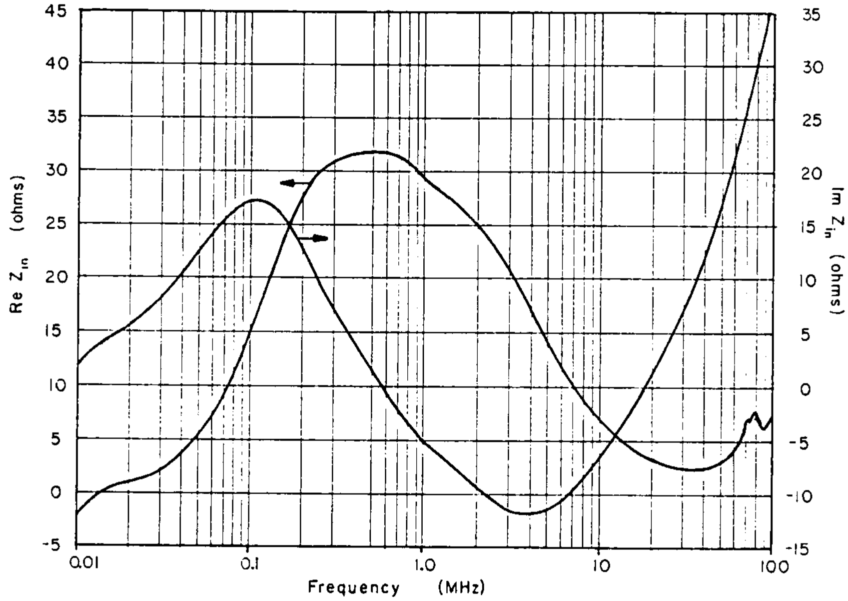

Figure E.14. Input impedance Z_{in} for two stage transformer with load Z_L.

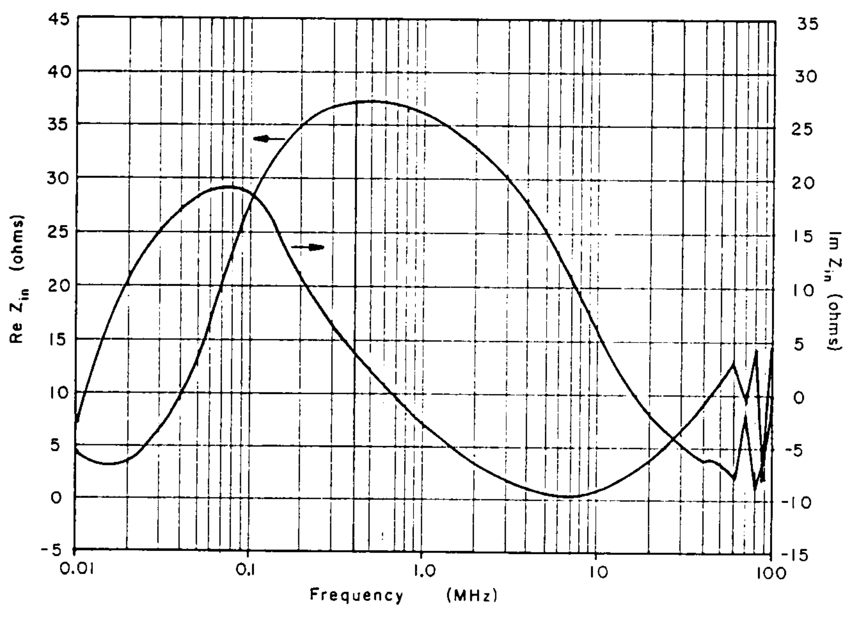

Figure E.15. Calculated value of the input impedance Z_{in}.

APPENDIX F

AXIAL ELECTRON BEAM IN THE PENNING DISCHARGE

The axial potential well illustrated in Figure 2.11 for trapped electrons in the Penning discharge gives rise to the formation of two interpenetrating axial beams of electrons. Electrons emitted by the cathode or generated by an ionization process in the sheath region will be accelerated by the axial electric field of the discharge. If the collision frequency for these electrons is an inverse power of the electron's velocity, electrons above some critical velocity will "run away" and be accelerated to a high velocity (Miyamoto 1980 and Alexandrov et.al. 1984).

In a completely ionized plasma, Coulomb collisions will initially dominate. The collision frequency for Coulomb collisions is proportional to v^{-3} and can result in "run away" electrons at moderate electric fields. For the weakly ionized plasma of the Penning discharge, the electron-neutral collision frequency is typically much larger than the electron-electron Coulomb collision frequency. Although electrons in the weakly ionized Penning discharge will not "run away", a fraction of the background electron population will be accelerated above the thermal velocity by the axial electric field near the cathodes. It is these electrons that tend to generate beam-plasma instabilities such as the two stream instability or ion acoustic turbulence.

Since accelerated electrons will typically lose energy in exciting an instability, an upper limit to the number of electrons accelerated by the axial electric field can be estimated by considering the equation of motion for electrons moving along the magnetic field and damped by electron-neutral collisions,

$$\frac{du}{dt} = \frac{e}{m_e} E(x) - \nu_{en} u \ . \tag{F.1}$$

Here the $\hat{x}$ axis is chosen to lie along the static magnetic field. For the weakly ionized Penning discharge, electron-neutral collisions will initially provide the damping and the electron-neutral collision frequency shown in Figure 2.1 will dominate.

Figure F.1 shows the axial variation of the plasma floating potential, electron number density and electron temperature for Run AGO-2. In order to determine the number density of a beam of electrons produced by the axial electric field, Equation (F.1) must be solved taking into account the axial variation of the electric field, the local number density, the local electron temperature, and the velocity dependence of the electron-neutral collision frequency. Equation (F.1) is solved by curve fitting the parameters in Figure 2.1 and Figure F.1 and then using a fourth order accurate Runge-Kutta scheme (Abramowitz and Stegan 1971).

The electron-neutral collision frequency in Figure 2.1 is fitted to a cubic equation as

$$\nu_{en} = \left[P_0 \times 10^7\right] \ 10^{g(\xi)} \qquad Hz \ , \tag{F.2}$$

where

$$\xi = \text{Log}\left(\mathcal{E}_e \cdot 10^3\right) \ , \tag{F.3}$$

and

$$g(\xi) = -0.028 \ \xi^3 + 0.135 \ \xi^2 + 0.391 \ \xi + 0.5 \ . \tag{F.4}$$

In these expressions, P_0 is the background pressure of the neutral helium gas in Torr, which is taken as constant along the discharge, and $\mathcal{E}_e$ is the axially directed

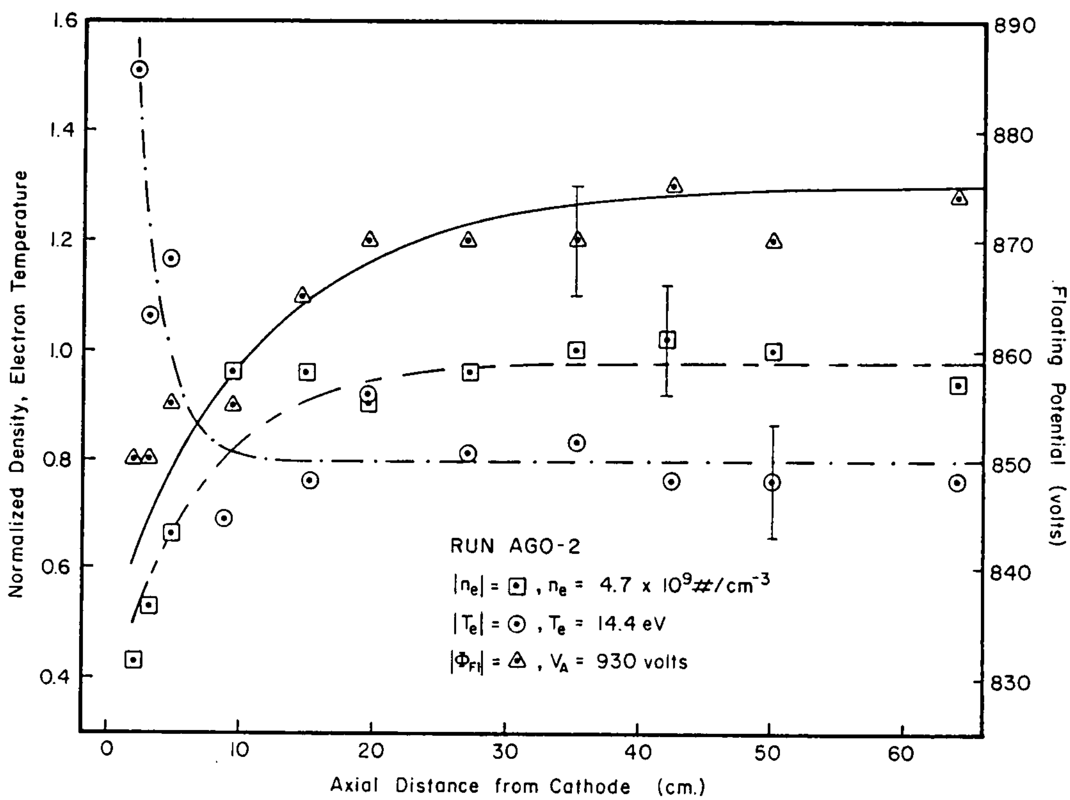

Figure F.1. Axial profiles of plasma floating potential, electron number density and electron temperature with curve fits for Run AGO-2.

energy of accelerated electrons. This energy $\mathcal{E}_e$ in eV is given (for $\dot{x}$ in meters/sec.) by,

$$\mathcal{E}_e = 2.85 \times 10^{-12}\ \dot{x}^2 \qquad \text{eV} \ , \tag{F.5}$$

The discharge parameters shown in Figure F.2 are curve fitted to the following expressions with the first 2 cm from the cathode neglected,

$$\Phi_{F1}(x) = 875 - 40.15\exp(-9.146x) \qquad V \ , \tag{F.6}$$

$$T_e(x) = 14.5[0.8 + 2.215\exp(-52.2\ x)] \ \ \text{eV} \ , \tag{F.7}$$

and

$$n_e(x) = 4.7 \times 10^9[1.03 + 0.642\exp(-14.55\ x)] \qquad \#/cm^3 \ , \tag{F.8}$$

for x in meters. The curves for these equations are shown in Figure F.1.

Figure F.2 shows contour curves of the electron energy for solutions of Equation (F.1) using a Runge-Kutta scheme with the curve fitted parameters described above. Electrons are being accelerated to the right with electrons having low initial energy being rapidly accelerated, and high energy electrons being weakly accelerated. The electron's energy tends to saturate and then drop off as electron motion is continually damped by electron-neutral collisions.

Figure F.3 shows the saturated electron energy as a function of distance. Figure F.3 also shows the initial electron energy on a given contour which equals the final energy at $x = 50$ cm as a function of distance. The local beam density is calculated using this second curve and considers the following. If the beam density is assumed small, and an approximately Maxwellian distribution of background

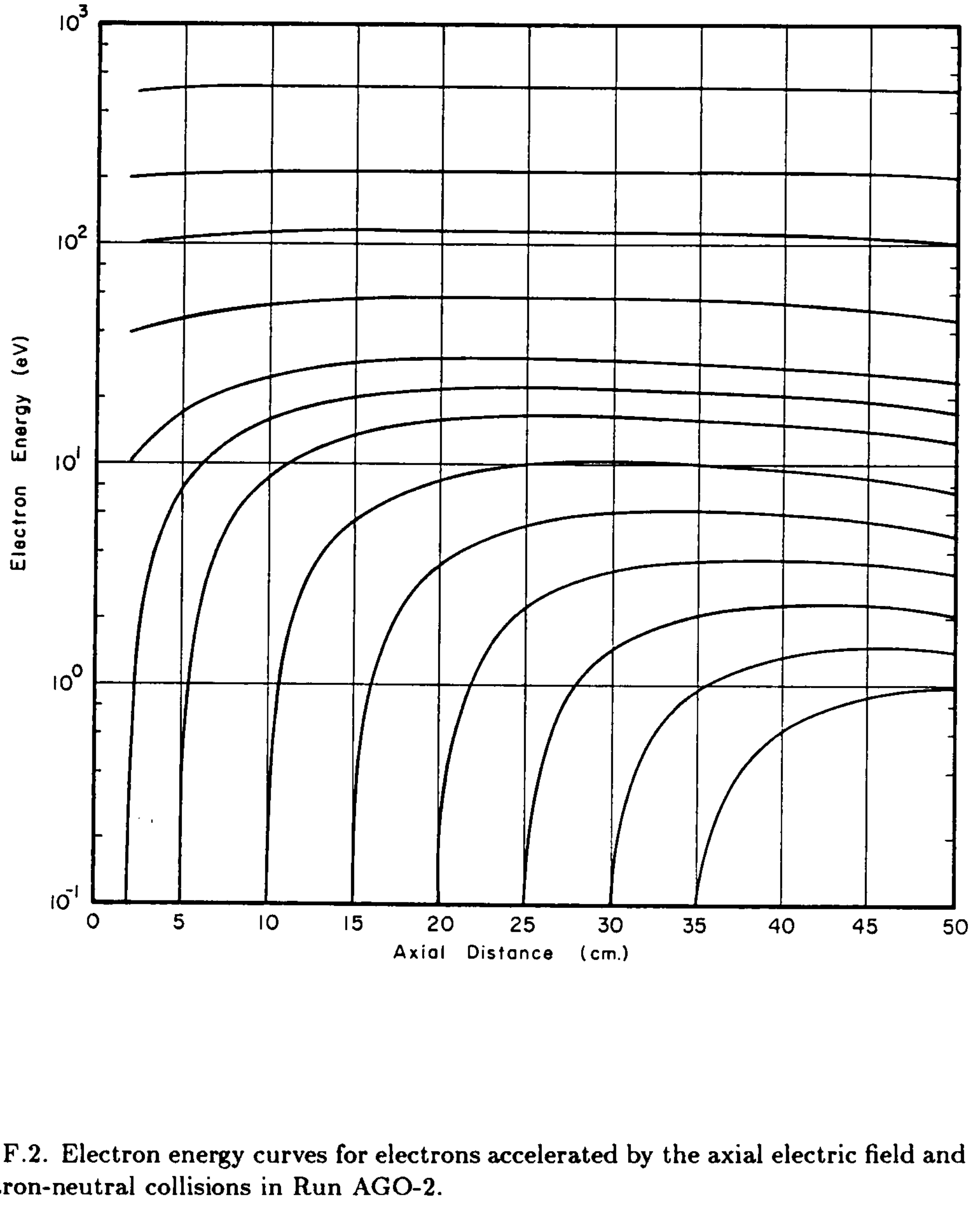

Figure F.2. Electron energy curves for electrons accelerated by the axial electric field and damped by electron-neutral collisions in Run AGO-2.

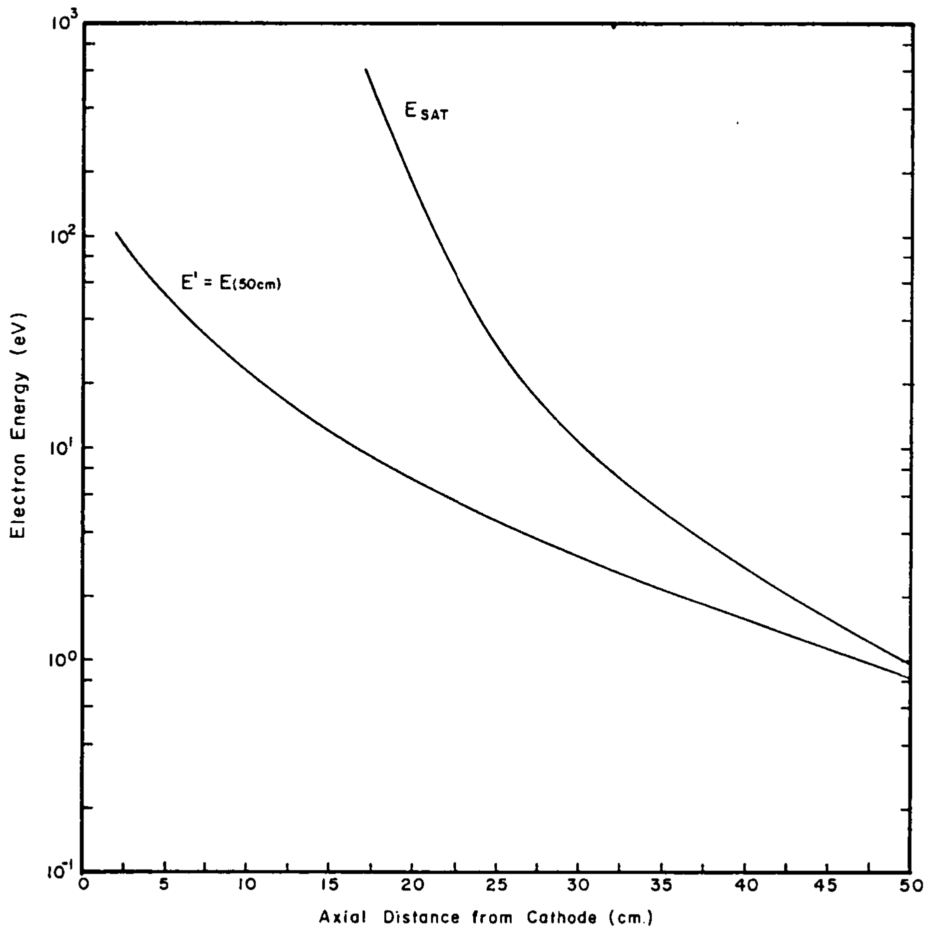

Figure F.3. Curve for the saturated electron energy $\mathcal{E}_{sat}$ versus distance and curve for the initial electron energy that equals the final electron energy at $x = 50$ cm ($\mathcal{E}_i = \mathcal{E}_f$), based on Figure F.2.

electrons exist, the local beam density n_b is given as

$$n_b(x) = n_e(x)\sqrt{\frac{m_e}{2\pi T_e(x)}} \int_0^{u_i} \exp\left(\frac{-v^2}{2v_{th}^2(x)}\right) \, dv \ , \tag{F.9}$$

or

$$n_b(x) = \frac{1}{2} \, n_e(x) \; Erf \, \left(\sqrt{\frac{\mathcal{E}_e(x)}{2T_e(x)}}\,\right) \ , \tag{F.10}$$

where the upper limit u_i is given by

$$u_i = [2.85 \times 10^{-12}]^{-2} \ \ \sqrt{\mathcal{E}_i} \qquad m/\mathrm{sec} \ . \tag{F.11}$$

Figure F.4 shows the solution of Equation (F.10) for Run AGO-2. Using a trapezoidal rule, the result in Figure F.4 is spacially integrated and normalized to give the net beam density at $x = 50$ cm of $n_b = 0.23\ \overline{n}_e$, where $\overline{n}_e = 4.7 \times 10^9/\mathrm{cm}^3$.

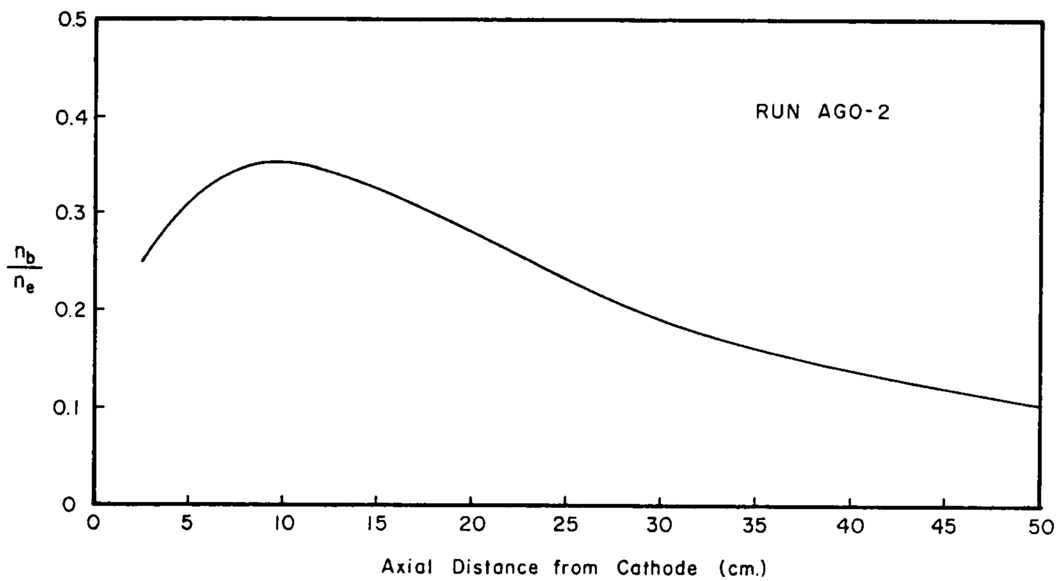

Figure F.4. Curve of the local beam density of axially accelerated electrons based on the $\mathcal{E}_i = \mathcal{E}_f$ curve in Figure F.3.

APPENDIX G

Finite Ion Gyro Radius Effects on the $\mathbf{E} \times \mathbf{B}$ Drift Velocity

The finite gryoradius motion of ions moving through a variable perpendicular electric field gives rise to distinct differences between the ion and electron $\mathbf{E} \times \mathbf{B}$ drift velocities. These differences can enhance the growth of drift and velocity shear instabilities.

Figure G.1 shows the unperturbed orbit of an ion moving in crossed electric and magnetic fields. If the electric and magnetic fields are constant in space, the drift velocity of the ion is given by (Chen, F.F. 1987)

$$\mathbf{V}_{E\times B} = \frac{\mathbf{E} \times \mathbf{B}}{B_0^2} \ . \tag{G.1}$$

If the electric field varies in space, it is clear that the drift velocity will vary as the ion moves through its orbit. Solving the equation of motion,

$$\ddot{\mathbf{V}} = \frac{q}{M} \ [\mathbf{E} + \mathbf{V} \times \mathbf{B}] \ , \tag{G.2}$$

for an electric field that varies as

$$\mathbf{E} = E_0 \ \cos{(kx)} \quad \hat{\mathbf{x}} \ , \tag{G.3}$$

Chen [1987] shows that for $k\rho \ll 1$ the correction to Equation (G.1) is given by

$$\mathbf{V}_{E\times B} = \left(1 + \frac{1}{4}\ \rho^2 \nabla^2\right) \ \frac{\mathbf{E} \times \mathbf{B}}{B_0^2} \ . \tag{G.4}$$

This result agrees with the earlier fluid result of Rosenbluth [1963], except for a factor of $\frac{1}{2}$ instead of the $\frac{1}{4}$ in Equation (G.4).

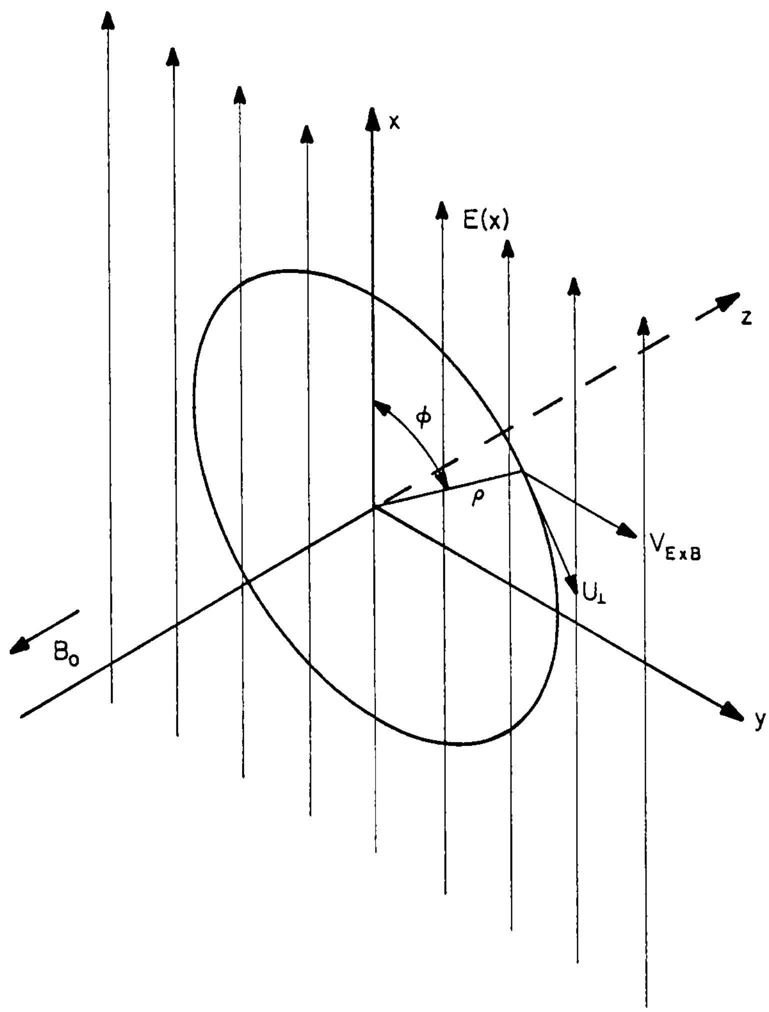

Figure G.1. Geometry used for considering the effect of finite ion gyro radius on the $E \times B$ drift velocity. The $\hat{z}$ component of velocity is neglected here.

Using a slightly different proceedure, Knorr et al. [1987] derives a correction factor of the form

$$\mathbf{V}_{E\times B} = J_0(\rho k)\ \frac{\mathbf{E}\times\mathbf{B}}{B_0}\ , \tag{G.5}$$

where $J_0(\rho k)$ is the zero order Bessel function. When Equation (G.5) is averaged over a Maxwellian velocity distribution, this correction becomes (Knorr et al. [1987])

$$\mathbf{V}_{E\times B} = \exp(-\rho^2 k^2)\ I_0(\rho^2 k^2)\ \frac{\mathbf{E}\times\mathbf{B}}{B_0^2}\ , \tag{G.6}$$

or

$$\mathbf{V}_{E\times B} = \exp(-\ \frac{1}{2}\ \rho^2 k^2)\ \frac{\mathbf{E}\times\mathbf{B}}{B_0^2}\ , \tag{G.7}$$

depending on the form of the particle orbit trajectory used (see Knorr et al. [1987] for details), and $I_0(\rho^2 k^2)$ is the zero order modified Bessel function.

The results in Equations (G.6) and (G.7) differ little for small gyro orbits, $\rho k \ll 1$. However, these results indicate a decrease in the drift velocity due to gyro orbit effects while Equation (G.4) gives an increase in the drift velocity.

For ion motion in a Penning discharge, the previous results are applicable for weak potential gradients in the interior of the plasma, or fields due to a drift wave. However, near the anode of a Penning discharge, strong radial electric fields occur. Consider the orbit shown in Figure G.1 as an ion orbit in a plasma sheath with the orbit center located a distance x_0 from the anode boundary. The sheath potential near the anode is given approximately by (Seshadri 1973)

$$\Phi = \Phi_W\ \exp\left(-\ \frac{x}{\lambda_d}\right)\ , \tag{G.8}$$

where $\Phi_W = V_{\text{anode}}$. The electric field for this potential is given by

$$\mathbf{E}(x) = \frac{\Phi_W}{\lambda_d}\ \exp\left(\frac{-x}{\lambda_d}\right)\ \hat{x}\ . \tag{G.9}$$

The equation of motion for ions with the effects of a velocity independent collision frequency ν_i, can be written

$$\dot{\mathbf{V}} = \frac{q}{M}\ [\mathbf{E} + \mathbf{V} \times \mathbf{B}] - \nu_i\ \mathbf{V}\ . \tag{G.10}$$

For a variable electric field in the $\hat{\mathbf{x}}$ direction and a static magnetic field B_0 in the $\hat{\mathbf{z}}$ direction, the $\hat{\mathbf{x}}$ and $\hat{\mathbf{y}}$ components of Equation (G.10) become

$$\dot{v}_x = -\omega_{bi} v_y + \nu_i v_x + \frac{q}{M}\ E(x) \qquad \hat{\mathbf{x}}\ , \tag{G.11}$$

and

$$\dot{v}_y = \omega_{bi}\ v_y + \nu_i\ v_y \qquad \hat{\mathbf{y}}\ . \tag{G.12}$$

Taking the time derivative of Equations (G.11) and (G.12) and rearranging, yields

$$\ddot{v}_x = \omega_{bi}^2\ v_x + \nu_i \dot{v}_x + \omega_{bi} \nu_i \dot{v}_y \pm \frac{q}{M}\ \frac{\dot{E}(x)}{B_0} \quad \hat{\mathbf{x}}\ , \tag{G.13}$$

and

$$\ddot{v}_y = (\omega_{bi}^2 + \nu_i^2)\ v_y - 2\nu_i \dot{v}_y + \omega_{bi}^2\ \frac{E(x)}{B_0} \quad \hat{\mathbf{y}}\ . \tag{G.14}$$

In order to consider the average drift motion of ions in the $\hat{\mathbf{y}}$ direction, the $\hat{\mathbf{y}}$ component of the ion velocity is written in terms of an oscillatory part and a drift part

$$v_y = \tilde{v}_y + v_d\ . \tag{G.15}$$

If the electric field in Equation (G.14) is constant in space, the correction to the $\mathbf{E} \times \mathbf{B}$ drift velocity due to ion collisions is given by

$$\overline{v}_y = \frac{\omega_{bi}^2}{\omega_{bi}^2 + \nu_i^2}\ \frac{\mathbf{E} \times \mathbf{B}}{B_0^2}\ \hat{\mathbf{y}}\ . \tag{G.16}$$

Hence the presence of collisions tends to decrease the average drift velocity of ions.

For no collisions, but a non uniform electric field of the form given by Equation (G.9), Equation (G.14) becomes

$$\ddot{v}_y + \omega_{bi}^2 \; v_y + \omega_{bi}^2 \; \frac{E_w}{B_0} \; \exp \left(\frac{x}{\lambda_d} \right) = 0 \; , \tag{G.17}$$

where $E_w = \frac{\Phi_w}{\lambda_d}$. If the $\hat{\mathbf{x}}$ position of the ion is taken to be given by the unperturbed ion orbits as:

$$x = x_0 + \rho \; \cos \left(\omega_{bi} t \right) \; , \tag{G.18}$$

then Equation (G.17) becomes

$$\ddot{v}_y + \omega_{bi}^2 \; v_y + \omega_{bi}^2 \; \frac{E_0}{B_0} \; \exp \left(\frac{-\rho}{\lambda_d} \; \cos \; \omega_{bi} t \right) = 0 \; , \tag{G.19}$$

with $E_0 = E_w \; \exp \left(\frac{-x_0}{\lambda_d} \right)$. Averaging Equation (G.14) over a gyro orbit so that $\bar{\ddot{v}}_y = 0$, yields

$$\bar{v}_y = \frac{E_0}{B} \; \frac{1}{2\pi} \int_0^{2\pi} \exp \left(\frac{-\rho}{\lambda_d} \; \cos \; \phi \right) \; d\phi \; . \tag{G.20}$$

Solving the integral in Equation (G.20) yields

$$\bar{v}_y = \frac{E_0}{B} \; I_0 \left(\frac{\rho}{\lambda_d} \right) \; , \tag{G.21}$$

where $I_0(x)$ is the modified Bessel function. This result retains the property that as $\rho \to 0$, the drift velocity reduces to the drift velocity at $x = x_0$.

The result in Equation (G.21) can be averaged over a Maxwellian distribution of gyro radii ρ by considering the Maxwellian velocity distribution,

$$f(v_\perp) \; dv_\perp = \frac{v_\perp}{v_{th}} \; \exp \left(\frac{-v_\perp^2}{2 v_{th}^2} \right) \; dv_\perp \; . \tag{G.22}$$

If the drift velocity is averaged over all gyro radii for all ions with radii at a selected position, then

$$\langle \overline{v}_y \rangle = \frac{E_0}{B} \int_0^\infty I_0 \left(\frac{\rho}{\lambda_d} \right) f(v_\perp)\, dv_\perp \ , \tag{G.23}$$

or

$$\langle \overline{v}_y \rangle = \frac{E_0}{B} \int_0^\infty I_0 \left(\frac{v_\perp}{\omega_{bi}\lambda_d} \right) \frac{v_\perp}{v_{th}} \exp\left(\frac{-v_\perp^2}{2v_{th}^2} \right) dv_\perp \ . \tag{G.24}$$

Making a change in variables allows Equation (G.24) to be written as

$$\langle \overline{v}_y \rangle = \frac{E_0}{B_0} \left(\frac{\lambda_d}{\rho_i} \right)^2 \int_0^n z\, I_0(z) \exp\left(\frac{-1}{2} \left(\frac{\lambda_d}{\rho_i} \right)^2 z^2 \right) dz \ , \tag{G.25}$$

where $\rho_i = \frac{v_{th}^i}{\omega_{bi}}$ and $n = \frac{x_0}{\lambda_d}$. The upper limit is truncated in this manner to accommodate only particles that do not strike the anode boundary.

In order to complete the integral of Equation (G.25), the modified Bessel function $I_0(z)$ is expanded as

$$I_0(z) \sim 1 + \frac{1}{4} z^2 \qquad z < 1 \ , \tag{G.26}$$

and

$$I_0(z) \sim \frac{e^z}{\sqrt{2\pi z}} \qquad z > 1 \ . \tag{G.27}$$

Equation (G.25) can be written as

$$\langle \overline{v}_y \rangle \simeq \frac{E_0}{B_0} \delta^2 \Bigg\{ \int_0^a \left(z + \frac{1}{4} z^3 \right) \exp\left(-\frac{1}{2} \delta^2 z^2 \right) dz + \frac{1}{\sqrt{2\pi}} \int_a^b \sqrt{z} \exp\left(-\frac{1}{2} \delta^2 z^2 + z \right) dz \Bigg\} \ , \tag{G.28}$$

where $\delta = \left(\frac{\lambda_d}{\rho_i}\right)$, and the limits are set as

$$\begin{aligned} a &= n \\ & \qquad\qquad\qquad n \leq z_0 \ , \\ b &= n \end{aligned} \tag{G.29}$$

or

$$\begin{aligned} a &= z_0 \\ & \qquad\qquad\qquad n > z_0 \ , \\ b &= n \end{aligned} \tag{G.30}$$

The factor z_0 is a solution of

$$1 + \frac{1}{4}\ z_0^2 - \frac{e^{z_0}}{\sqrt{2\pi z_0}} = 0 \ , \tag{G.31}$$

which can be solved iteratively by the secant method or Newton's method to yield

$$z_0 = 1.827 \ . \tag{G.32}$$

The first integral of Equation (G.28) can be solved analytically and the second integrated numerically.

The results of Equation (G.28) can be combined with the result in Equation (G.16) for an approximation to the combined effects of ion collisions and a non-uniform radial electric field on the $\mathbf{E} \times \mathbf{B}$ drift motion of ions,

$$\langle \overline{v}_y \rangle \approx \beta_\nu\ \beta_{sh}\ \frac{\mathbf{E} \times \mathbf{B}}{B_0^2} \ , \tag{G.33}$$

with

$$\beta_\nu = \left[1 + \left(\frac{\nu_i}{\omega_{bi}}\right)^2\right]^{-1} , \tag{G.34}$$

and

$$\beta_{sh} = 1 - \exp\left(-\frac{1}{2}\,\delta^2 a^2\right)\left[1 + \frac{1}{2}\,\delta^{-2} + \frac{1}{4}\,a^2\right] + \frac{1}{2}\,\delta^{-2} + \frac{\delta^2}{\sqrt{2\pi}} \int_a^b \sqrt{z}\,\exp\left(-\frac{1}{2}\,\delta^2\,z^2 + z\right)\,dz\ . \tag{G.35}$$

The factor β_{sh} is plotted in Figure G.2 for a range of parameters relavent to the Penning discharge. Figure G.2 shows that the factor β_{sh} can be greater or less than unity, yet the result in Equation (G.35) retains the property:

$$\lim_{\rho \to 0}\ \beta_{sh} = 1$$

Provided that the sheath profile and group velocity of an $\mathbf{E} \times \mathbf{B}$ drift velocity can be measured, these results provide a means for estimating the ion collision frequency in a plasma sheath.

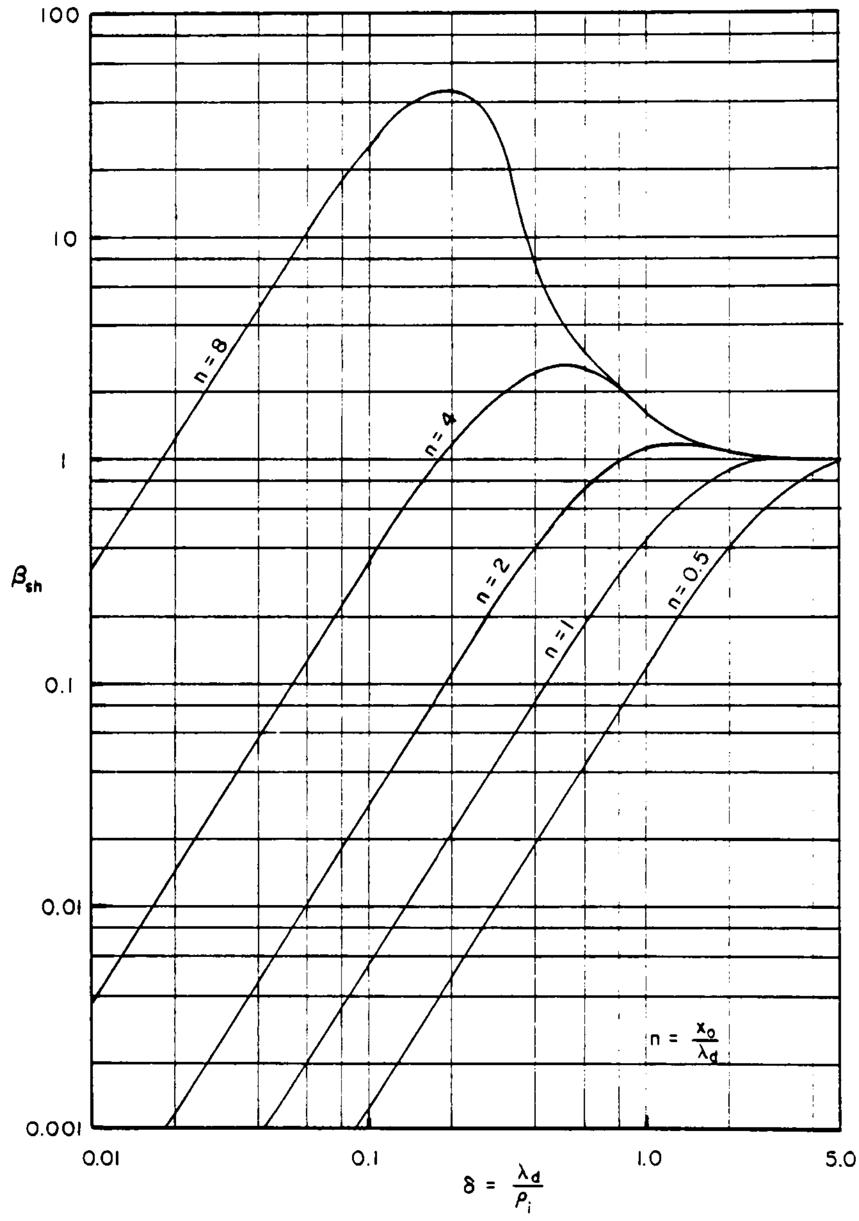

Figure G.2. Finite ion gyro radius correction factor β_{sh} for $E \times B$ drift motion of ions moving in a plasma sheath.

APPENDIX H

EXPERIMENTAL DATA FOR ν_{eff} SCALING

This appendix presents the experimental data used in Chapter V and summarized in Tables 5.2 through 5.6. These data include the following:

1. Radial profiles of the plasma number density, electron temperature and plasma floating potential from Langmuir probe data.
2. Microwave absorption data for the extraordinary mode wave near the upper-hybrid resonance.
3. Calibrated power spectra at two radial positions of electrostatic potential fluctuations sampled by capacitive probes.
4. Calibrated power spectra of electron density fluctuations detected by the microwave scattering system at two scattering angles.
5. Calibrated power spectra of electron and ion density fluctuations detected by a biased Langmuir probe.

For Runs AGN-1 and AGO-2 axial profiles of the plasma number density, electron temperature and floating potential are presented. These runs were made under conditions suitable for an axial probe to produce minimum perturbation of the discharge parameters.

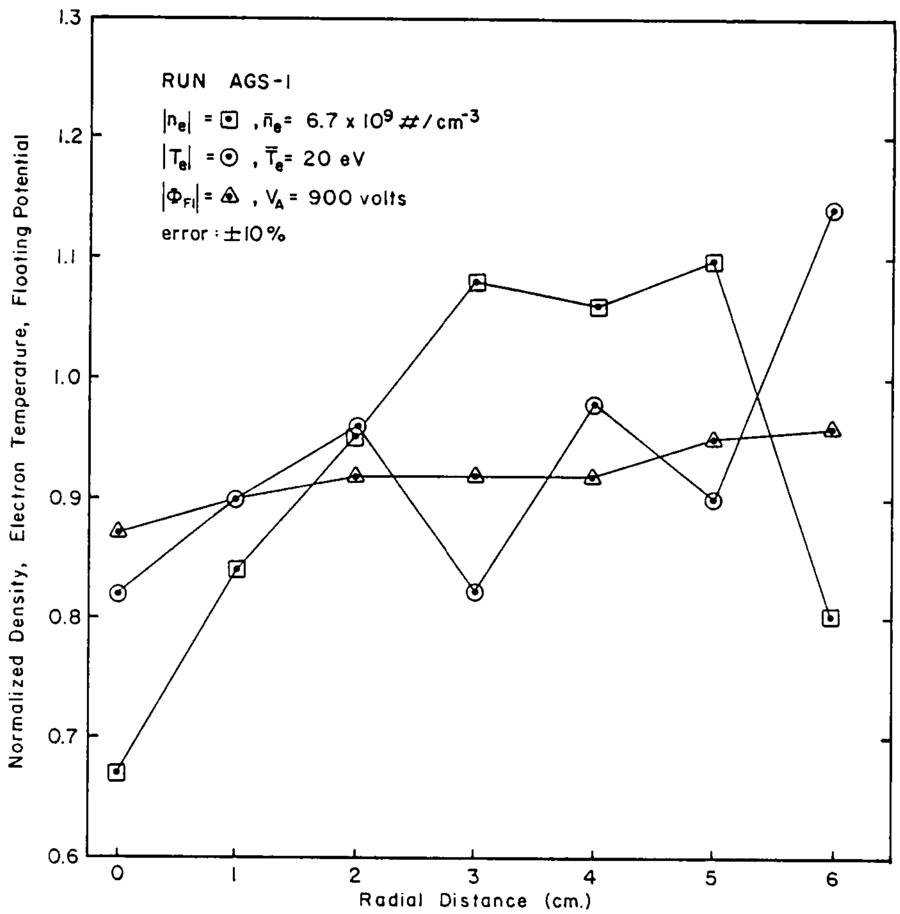

Figure H.1. Radial profile of the electron number density, electron temperature and plasma floating potential for Run AGS-1.

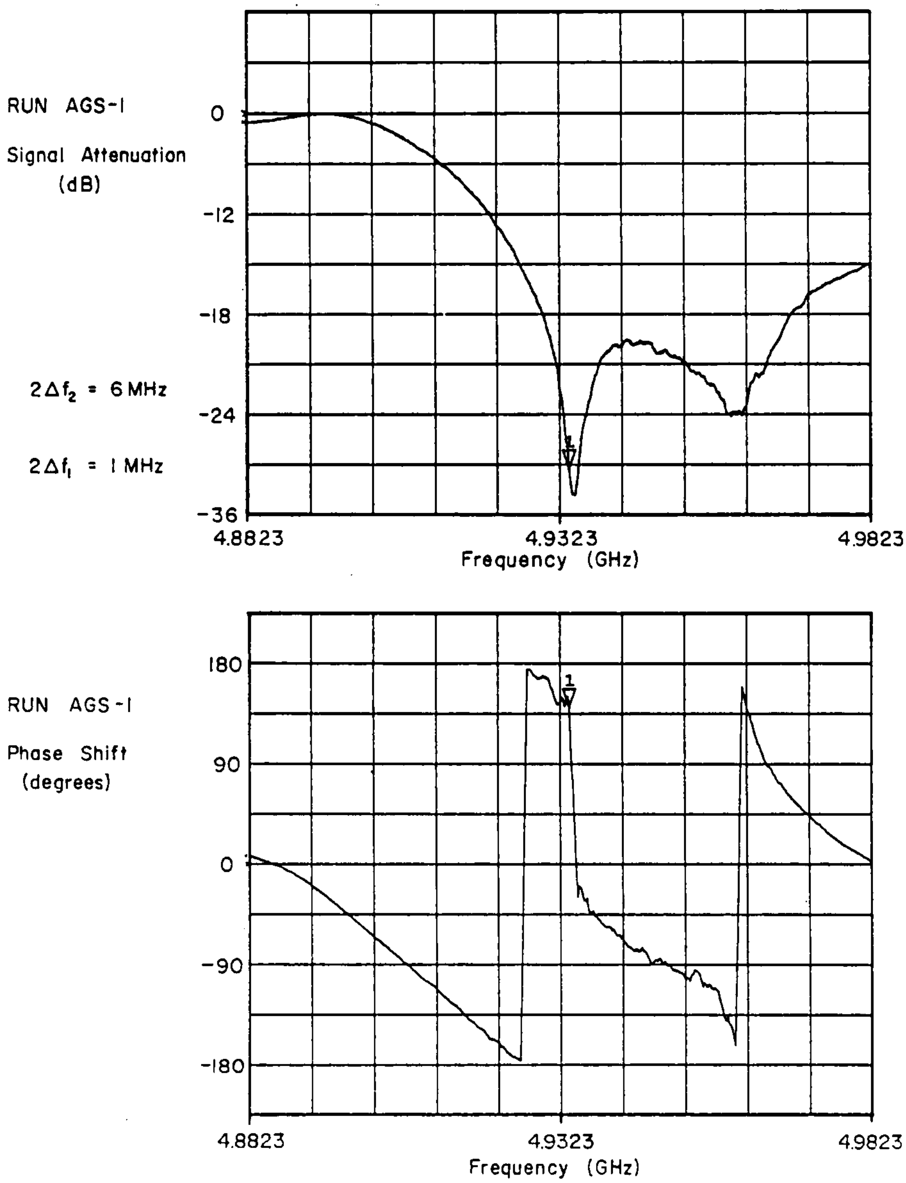

Figure H.2. Microwave absorption data for the extraordinary mode wave at the upper hybrid resonance for Run AGS-1.

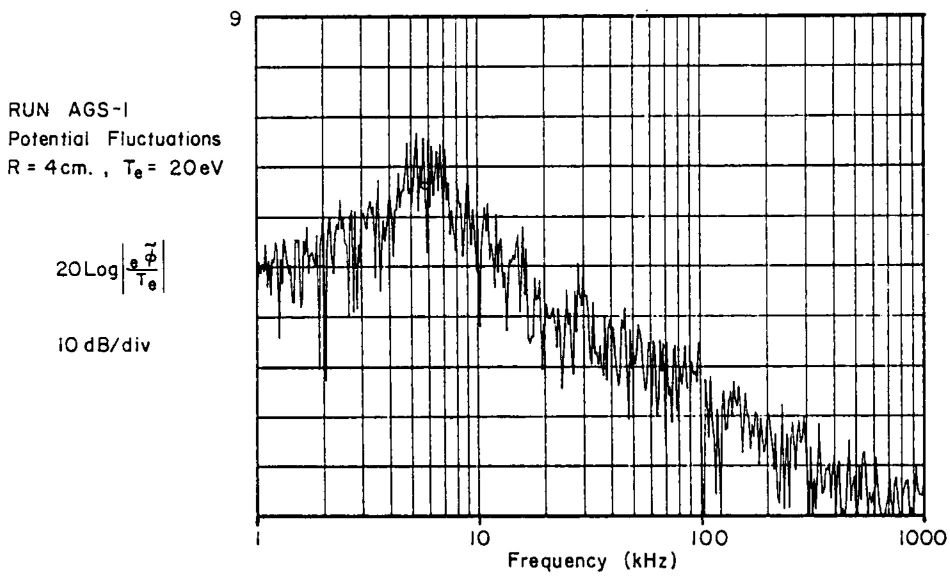

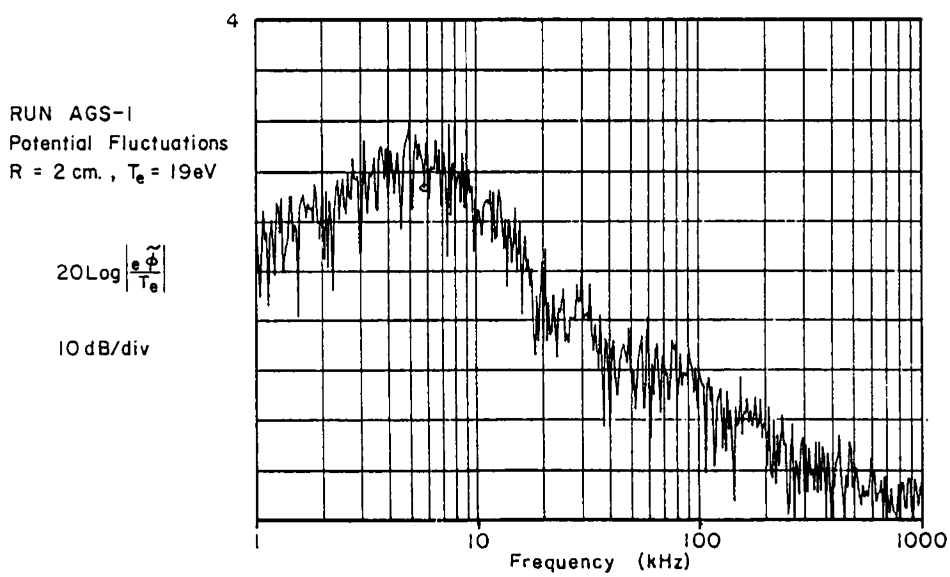

Figure H.3. Calibrated power spectra of electrostatic potential fluctuations normalized to the local electron temperature for Run AGS-1.

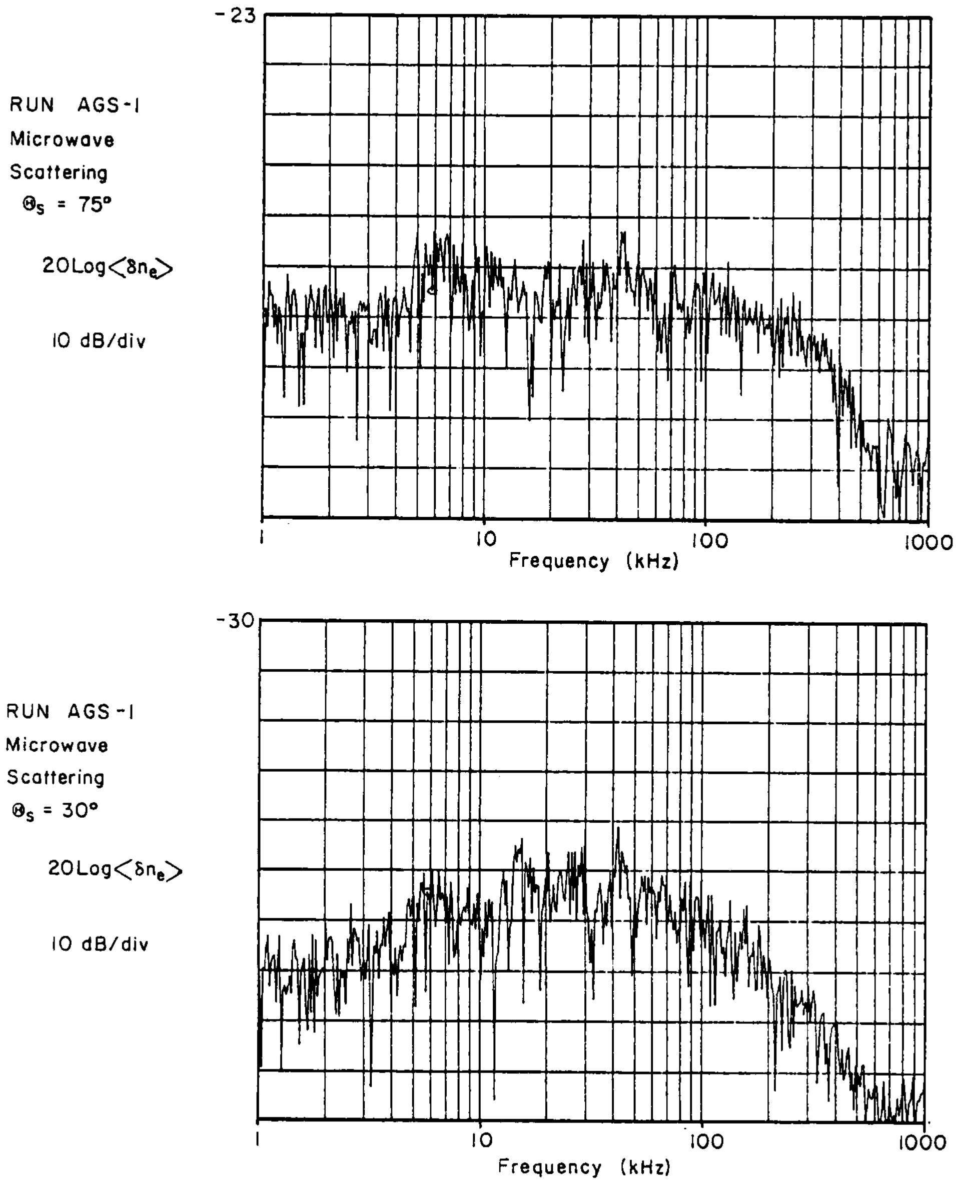

Figure H.4. Calibrated power spectra of electron density fluctuations detected by the microwave scattering system for Run AGS-1.

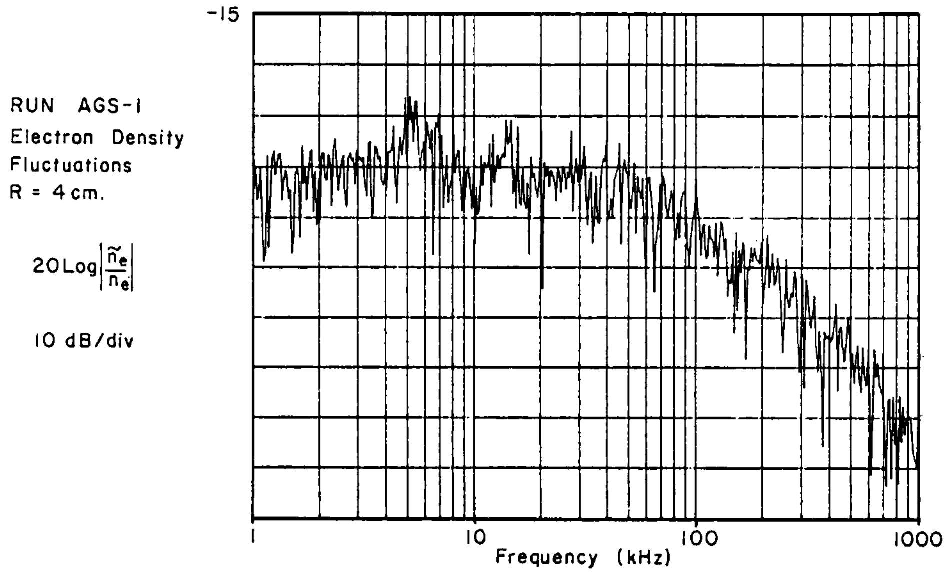

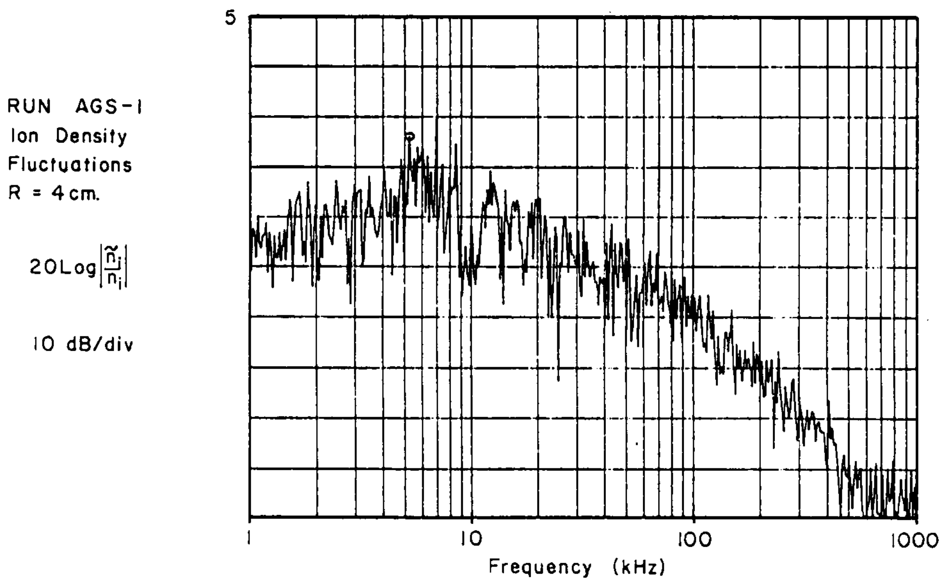

Figure H.5. Calibrated power spectra of electron and ion density fluctuations detected by a biased Langmuir probe for Run AGS-1.

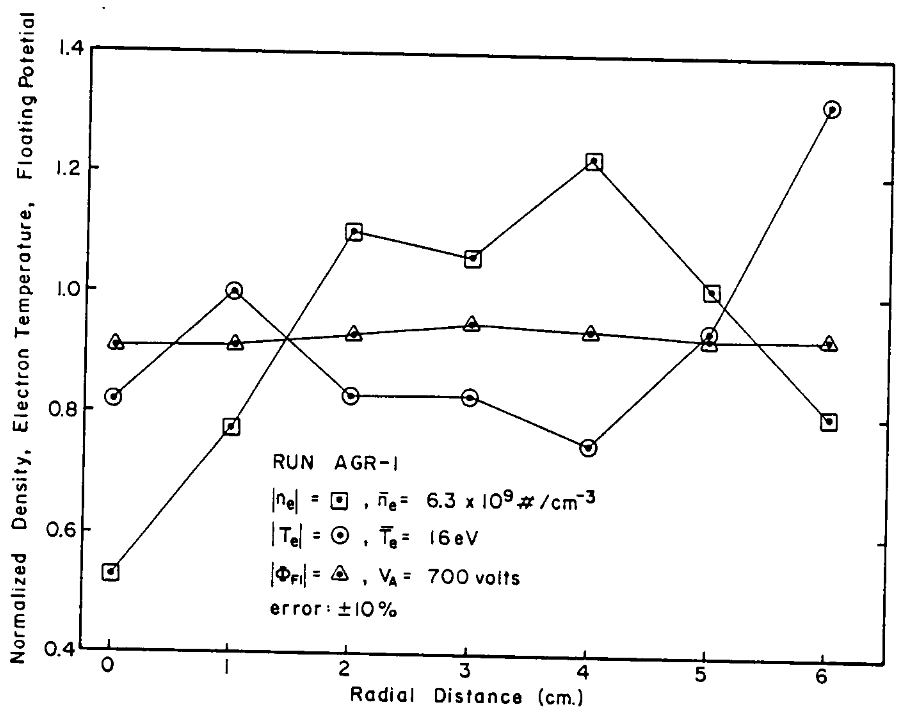

Figure H.6. Radial profile of the electron number density, electron temperature and plasma floating potential for Run AGR-1.

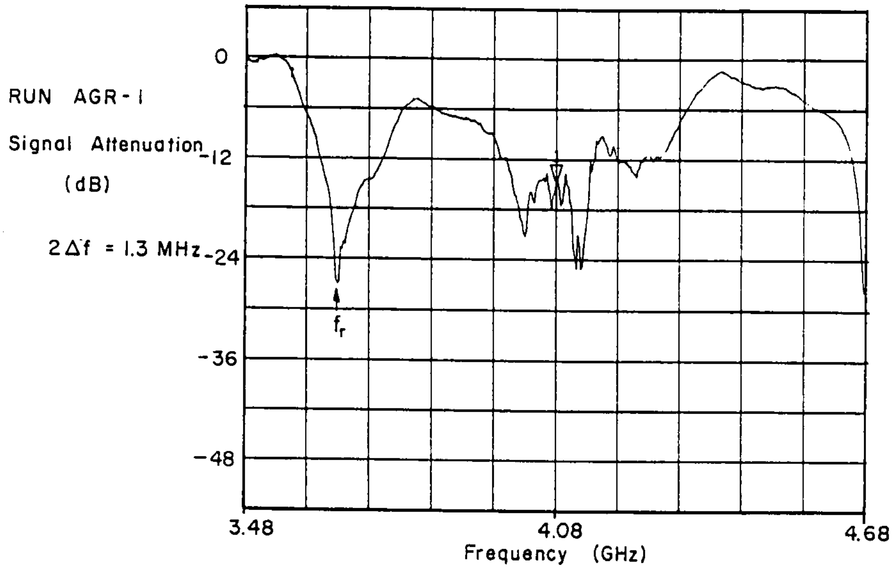

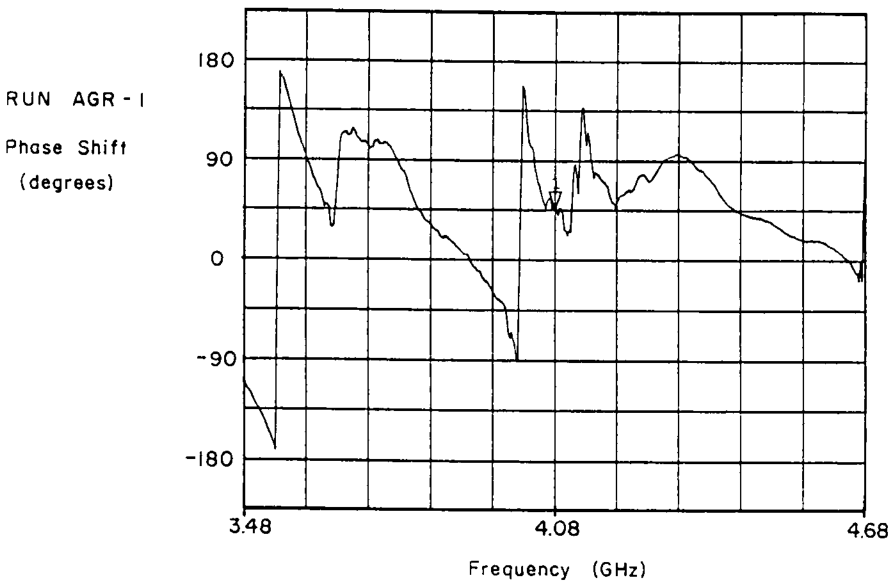

Figure H.7. Microwave absorption data for the extraordinary mode wave at the upper hybrid resonance for Run AGR-1.

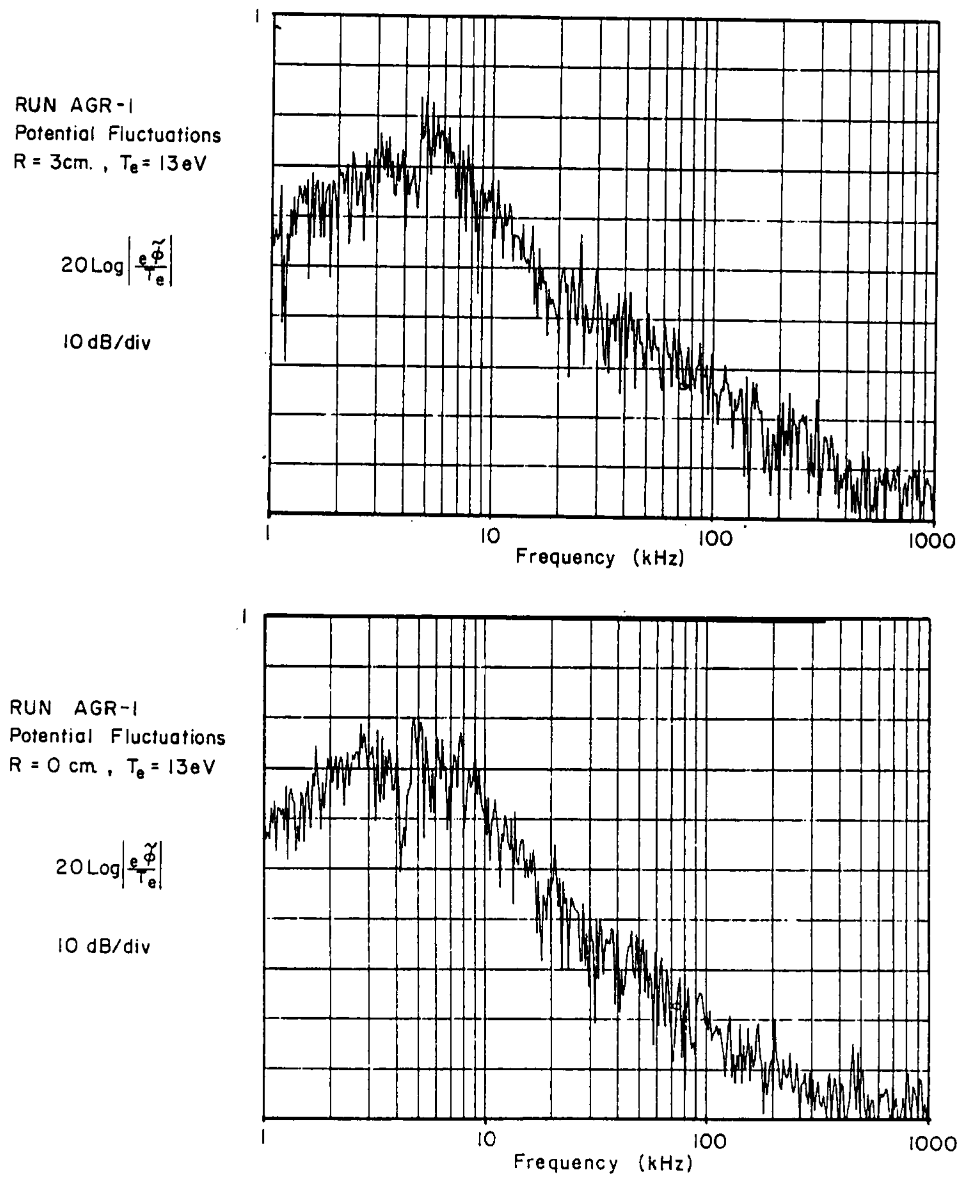

Figure H.8. Calibrated power spectra of electrostatic potential fluctuations normalized to the local electron temperature for Run AGR-1.

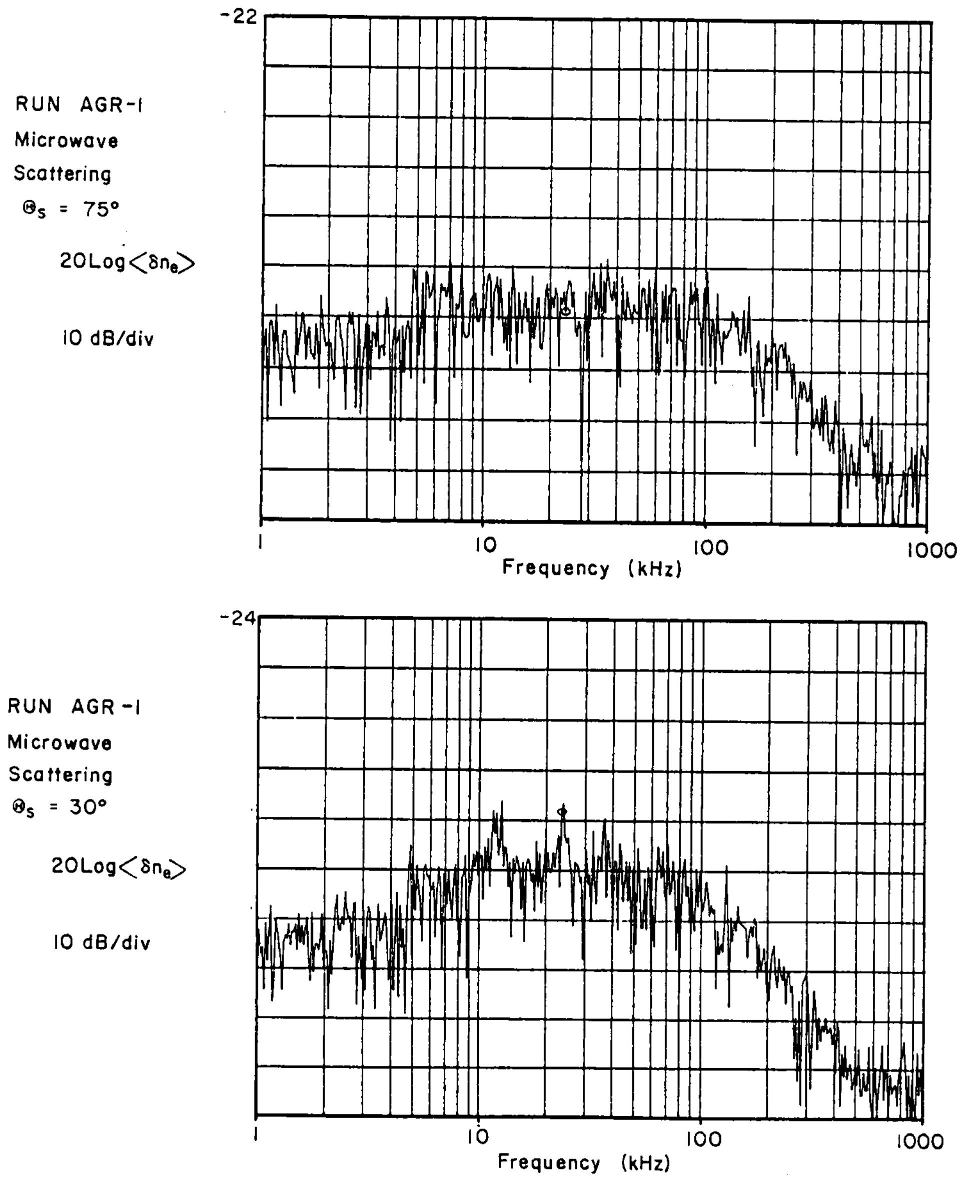

Figure H.9. Calibrated power spectra of electron density fluctuations detected by the microwave scattering system for Run AGR-1.

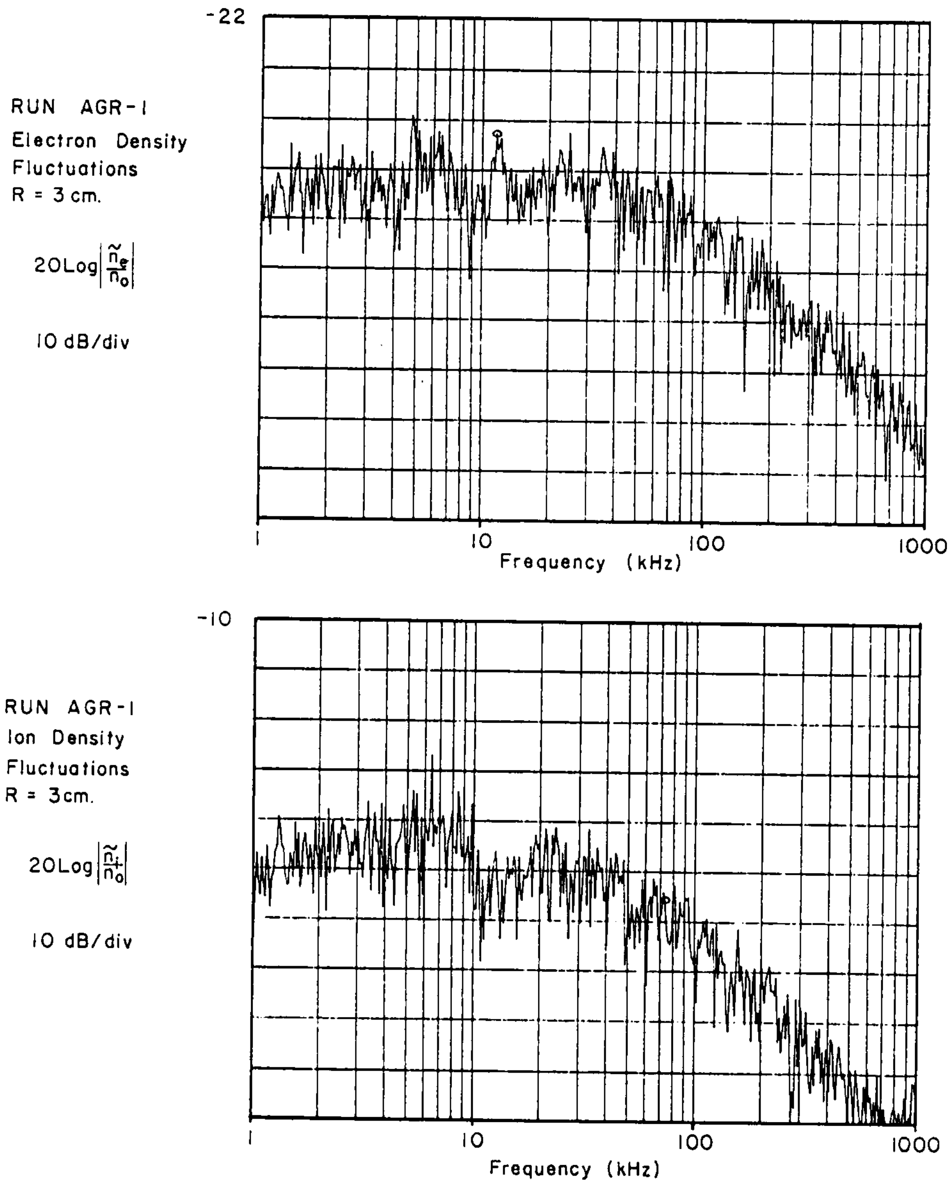

Figure H.10. Calibrated power spectra of electron and ion density fluctuations detected by a biased Langmuir probe for Run AGR-1.

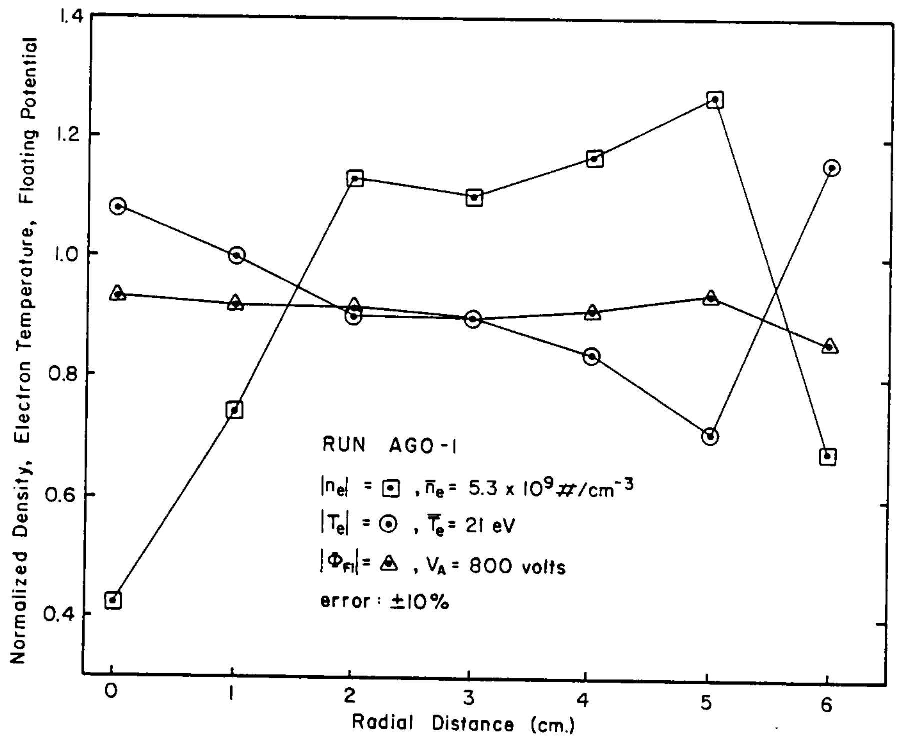

Figure H.11. Radial profile of the electron number density, electron temperature and plasma floating potential for Run AGO-1.

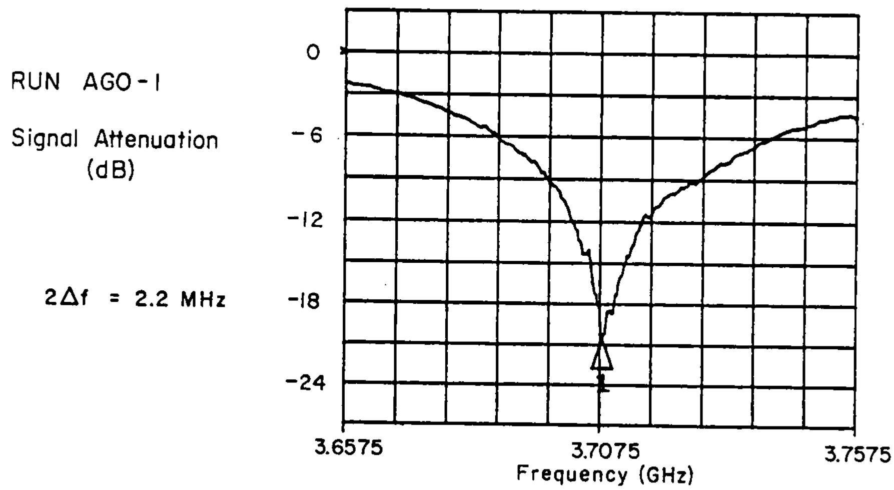

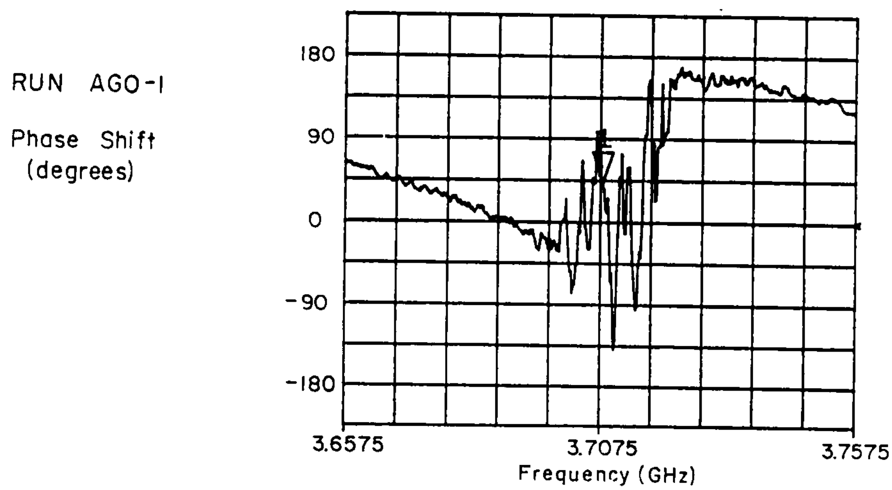

Figure H.12. Microwave absorption data for the extraordinary mode wave at the upper hybrid resonance for Run AGO-1.

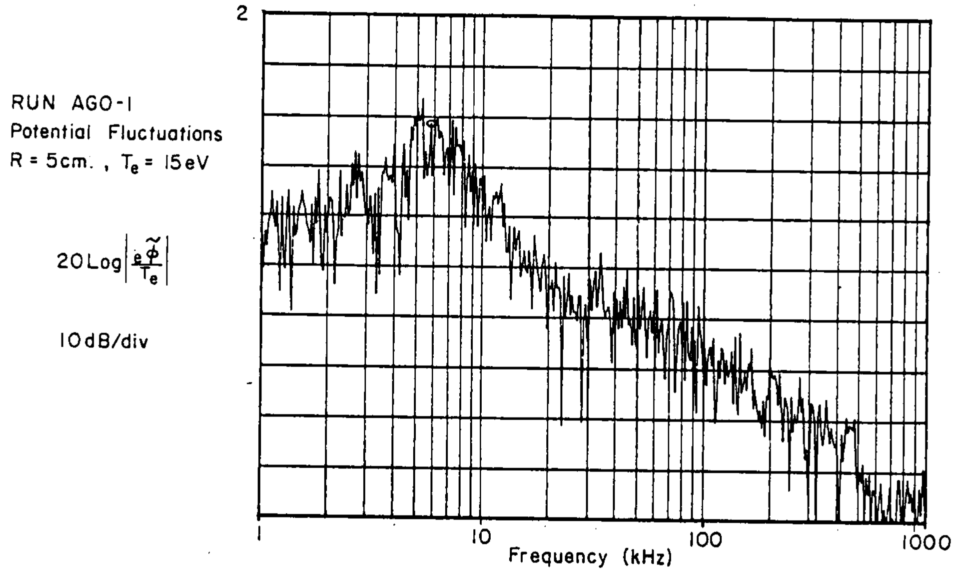

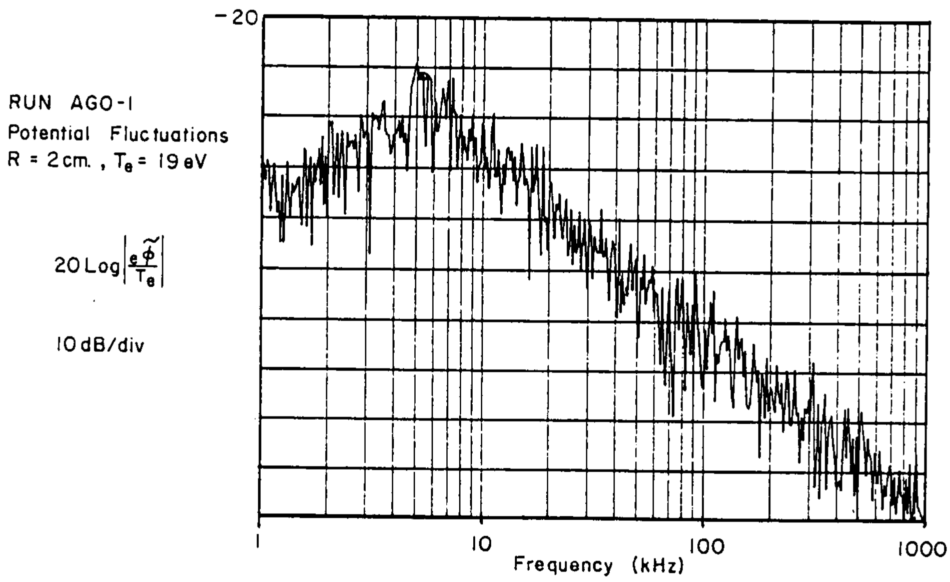

Figure H.13. Calibrated power spectra of electrostatic potential fluctuations normalized to the local electron temperature for Run AGO-1.

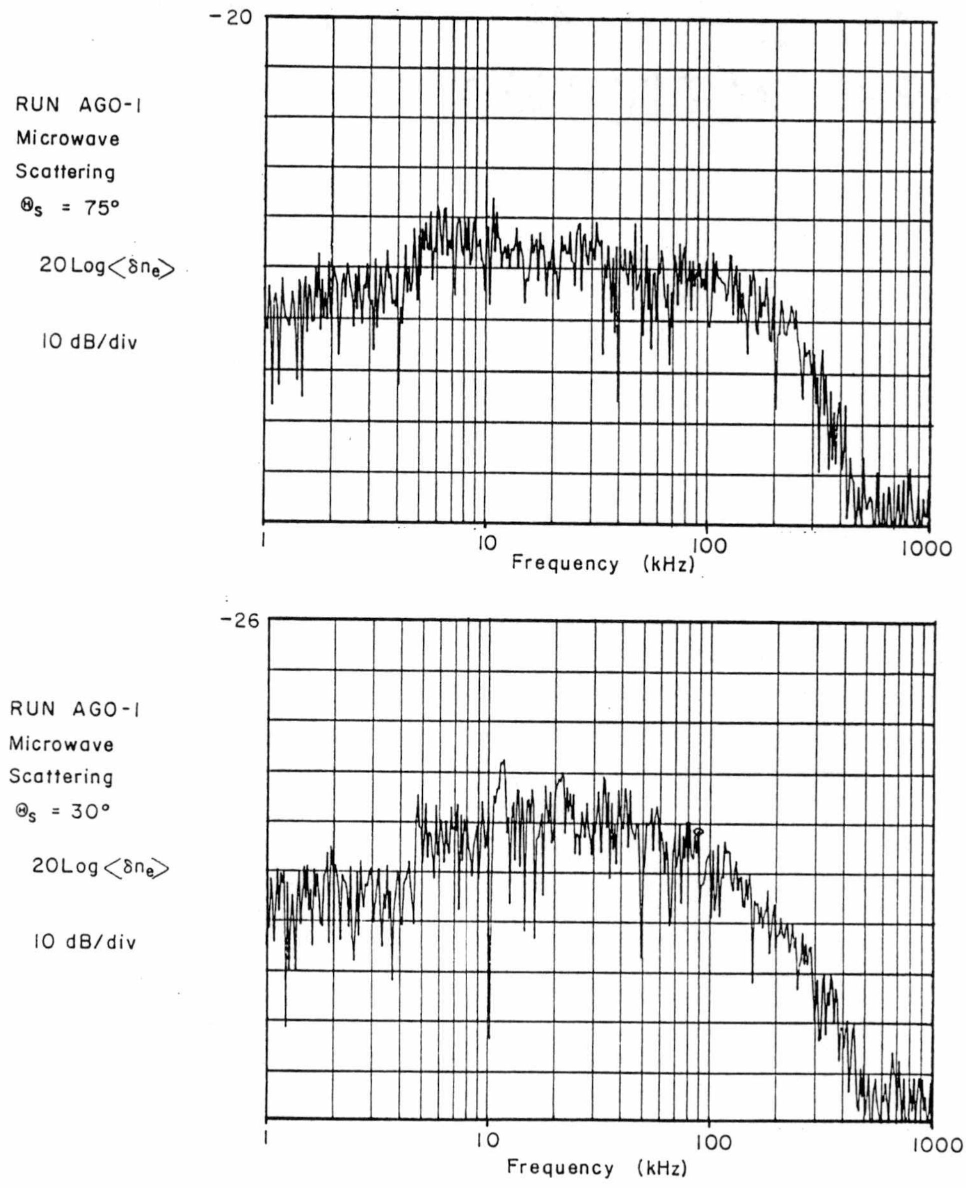

Figure H.14. Calibrated power spectra of electron density fluctuations detected by the microwave scattering system for Run AGO-1.

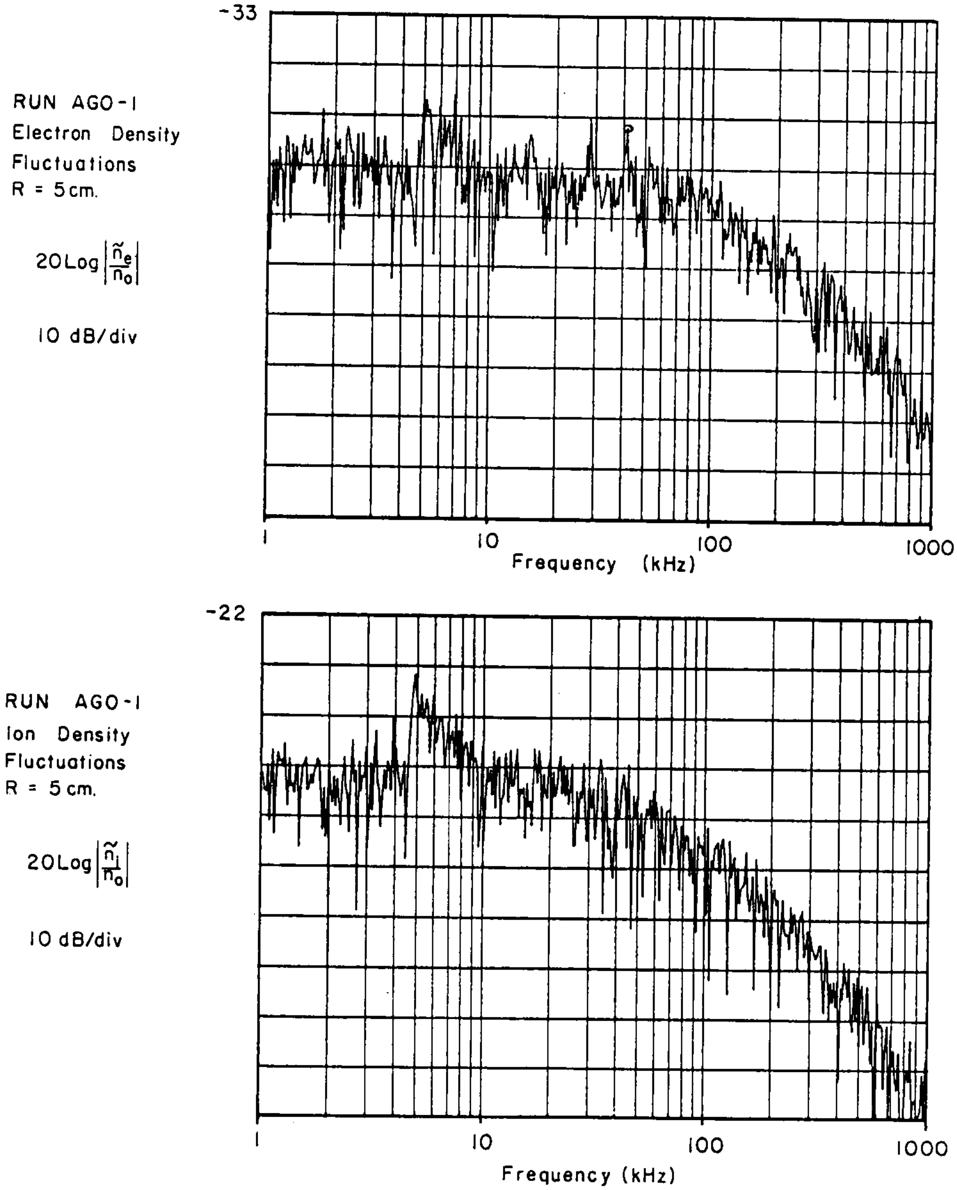

Figure H.15. Calibrated power spectra of electron and ion density fluctuations detected by a biased Langmuir probe for Run AGO-1.

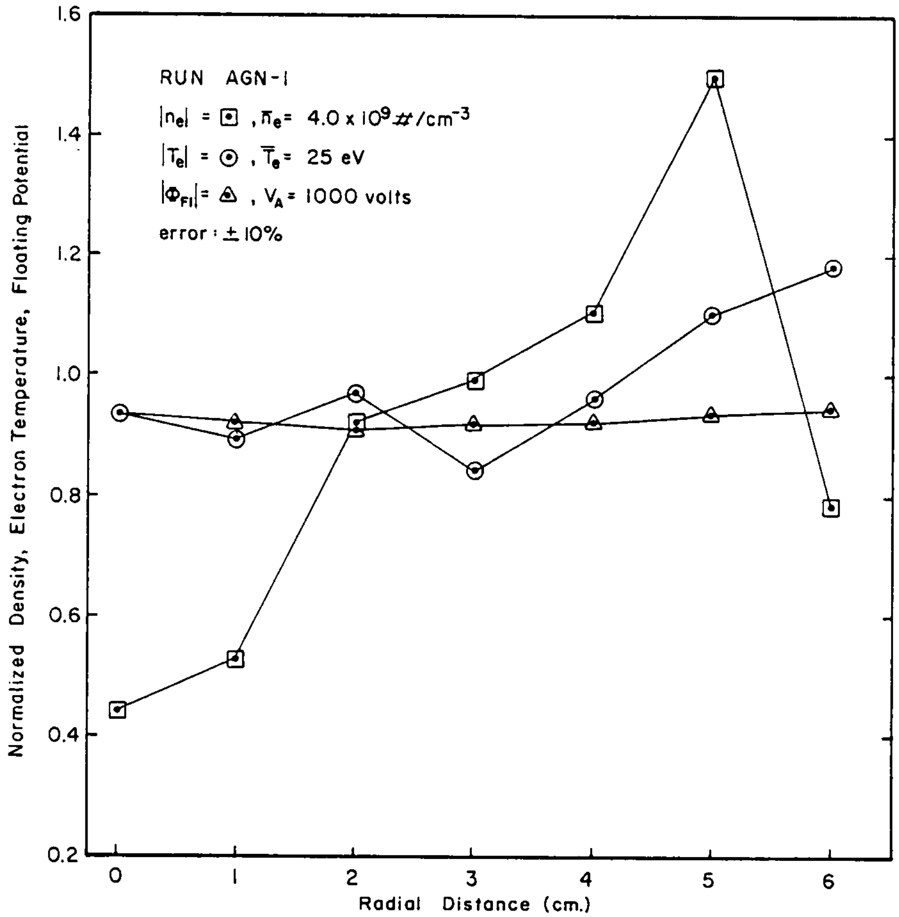

Figure H.16. Radial profile of the electron number density, electron temperature and plasma floating potential for Run AGN-1.

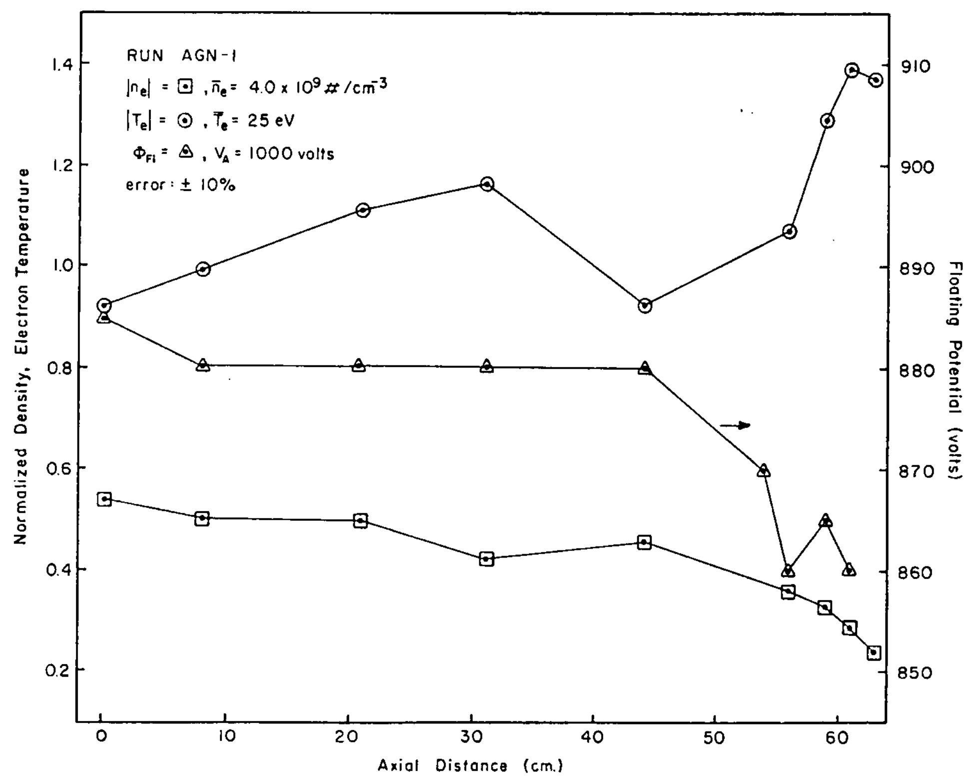

Figure H.17. Axial profile of the electron number density, electron temperature and plasma floating potential for Run AGN-1.

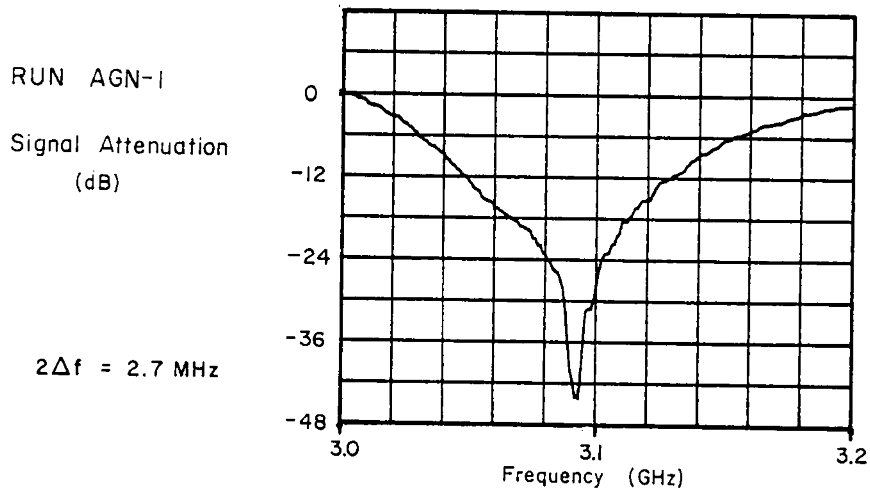

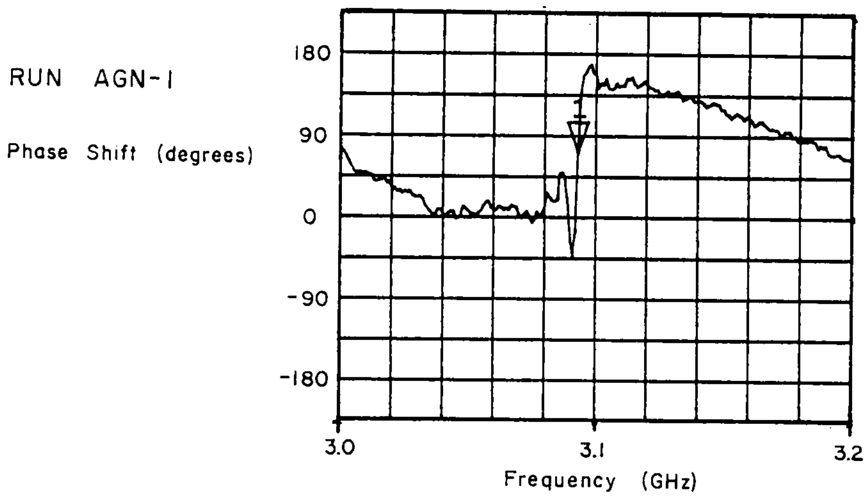

Figure H.18. Microwave absorption data for the extraordinary mode wave at the upper hybrid resonance for Run AGN-1.

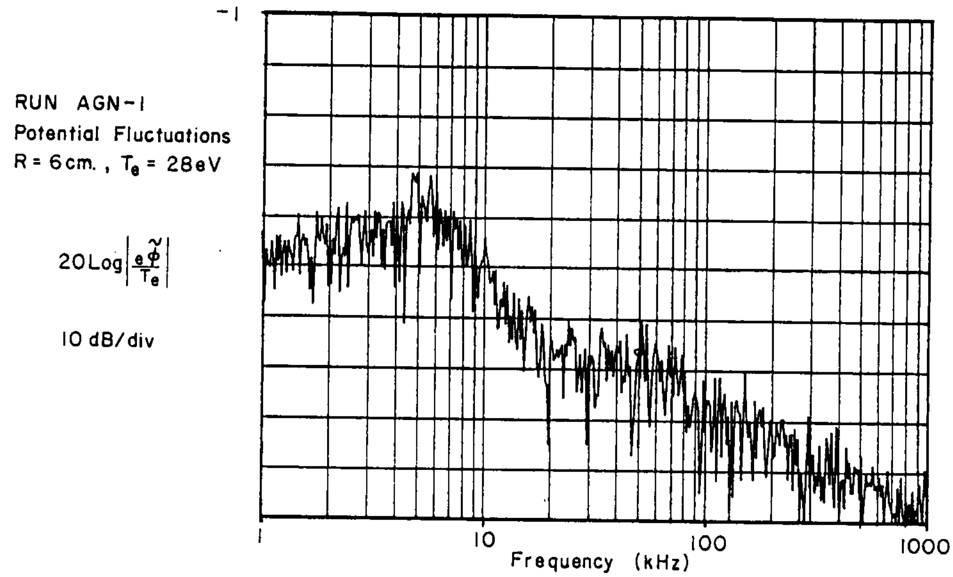

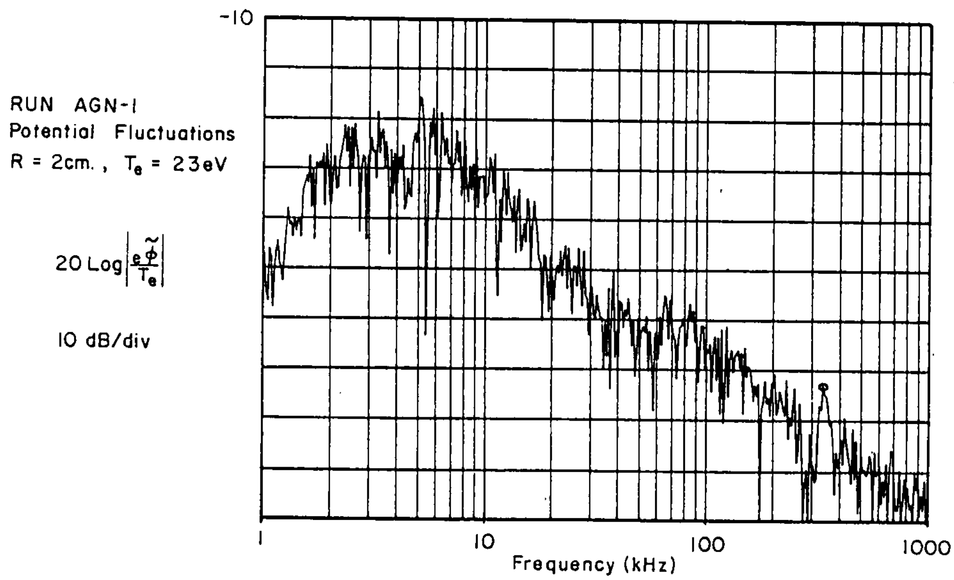

Figure H.19. Calibrated power spectra of electrostatic potential fluctuations normalized to the local electron temperature for Run AGN-1.

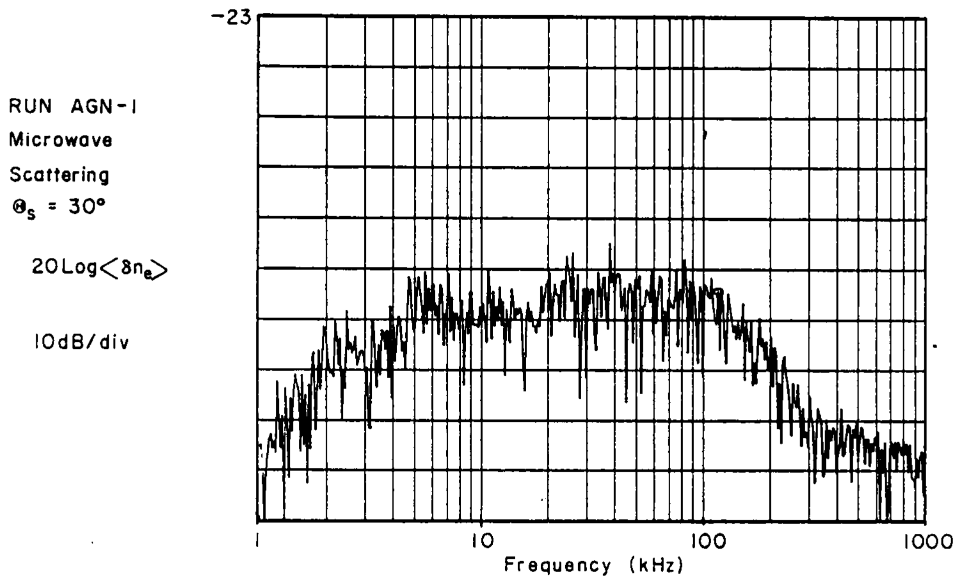

Figure H.20. Calibrated power spectra of electron density fluctuations detected by the microwave scattering system for Run AGN-1.

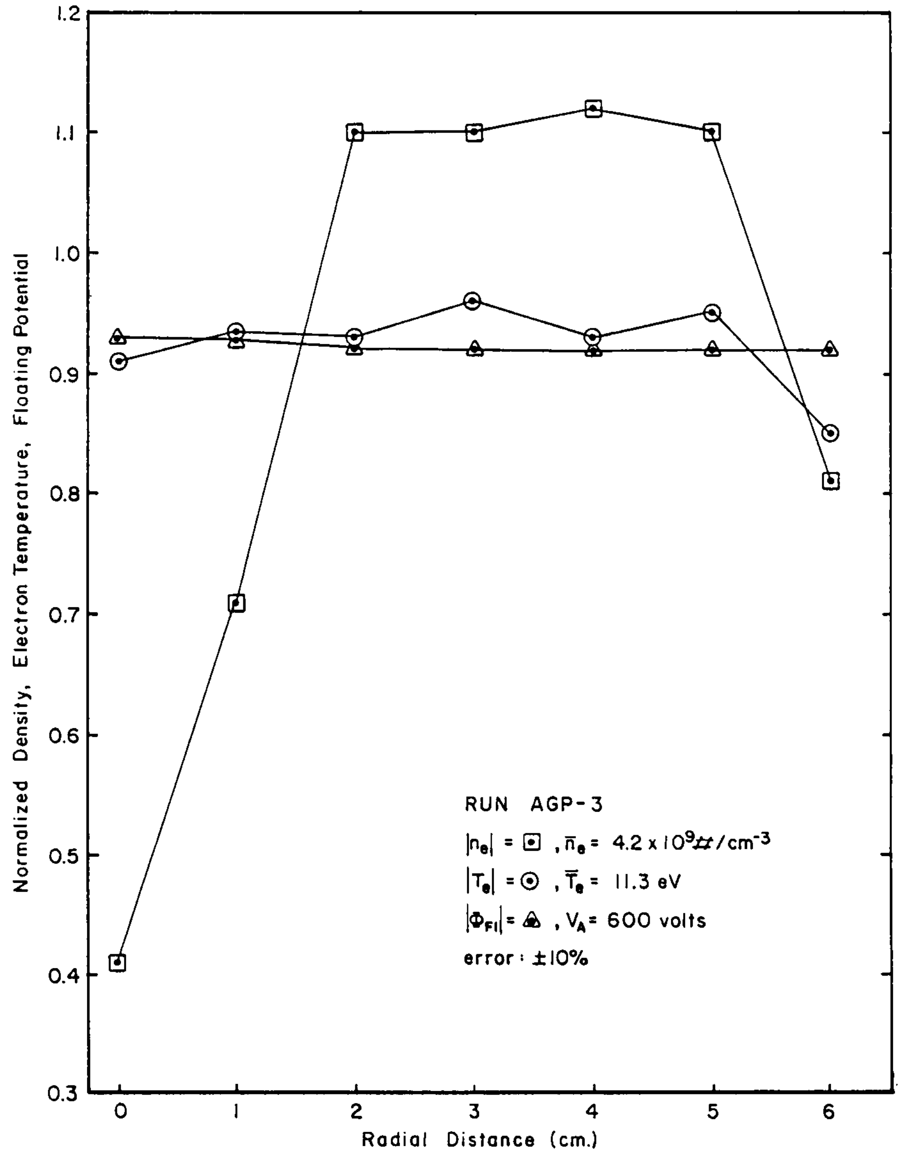

Figure H.21. Radial profile of the electron number density, electron temperature and plasma floating potential for Run AGP-3.

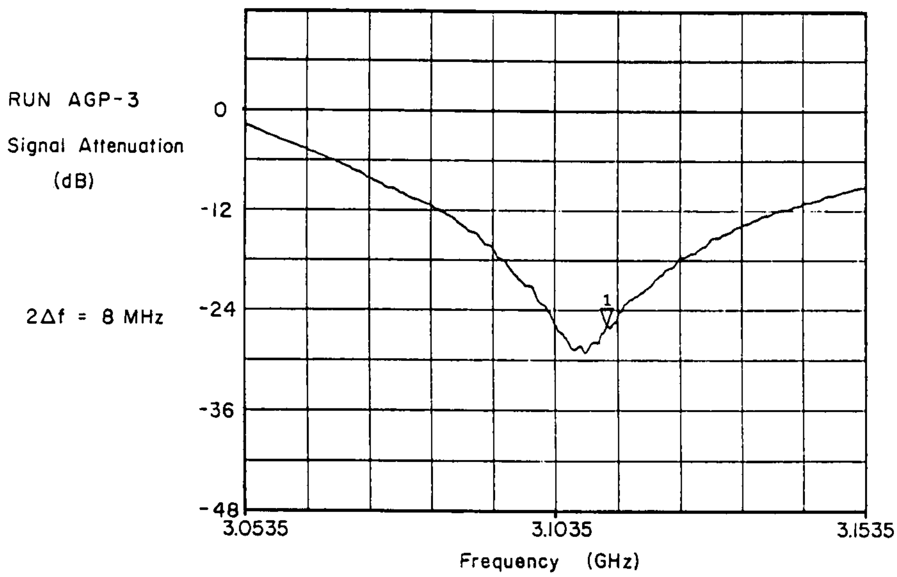

Figure H.22. Microwave absorption data for the extraordinary mode wave at the upper hybrid resonance for Run AGP-3.

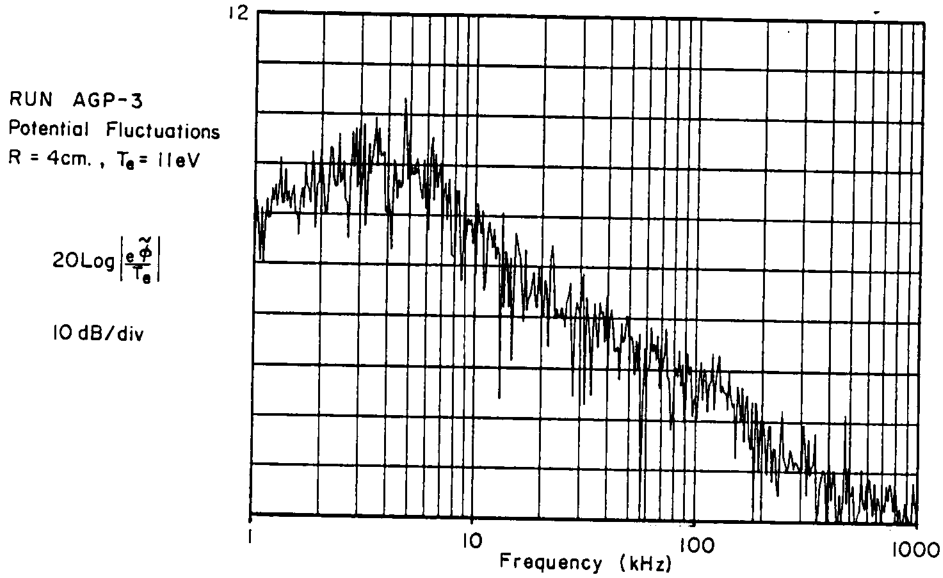

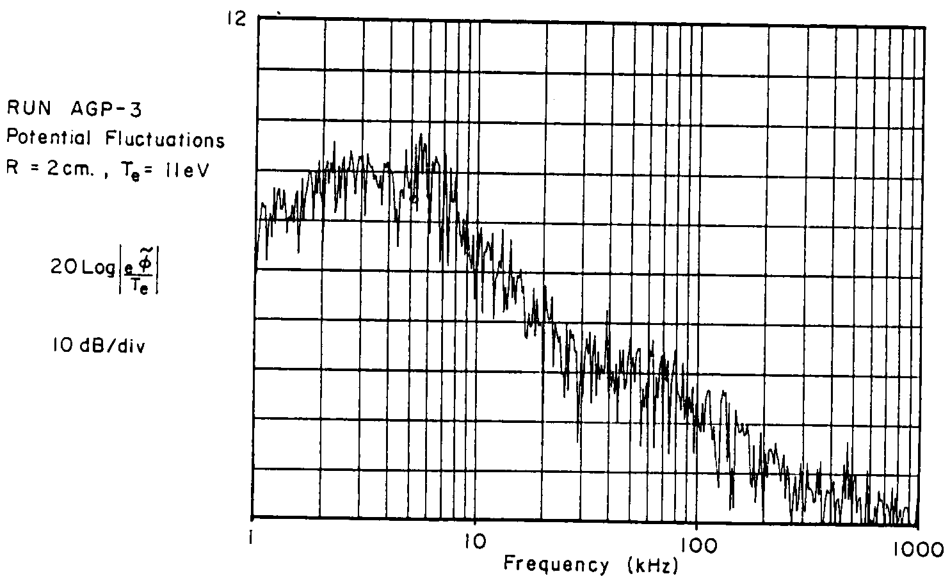

Figure H.23. Calibrated power spectra of electrostatic potential fluctuations normalized to the local electron temperature for Run AGP-3.

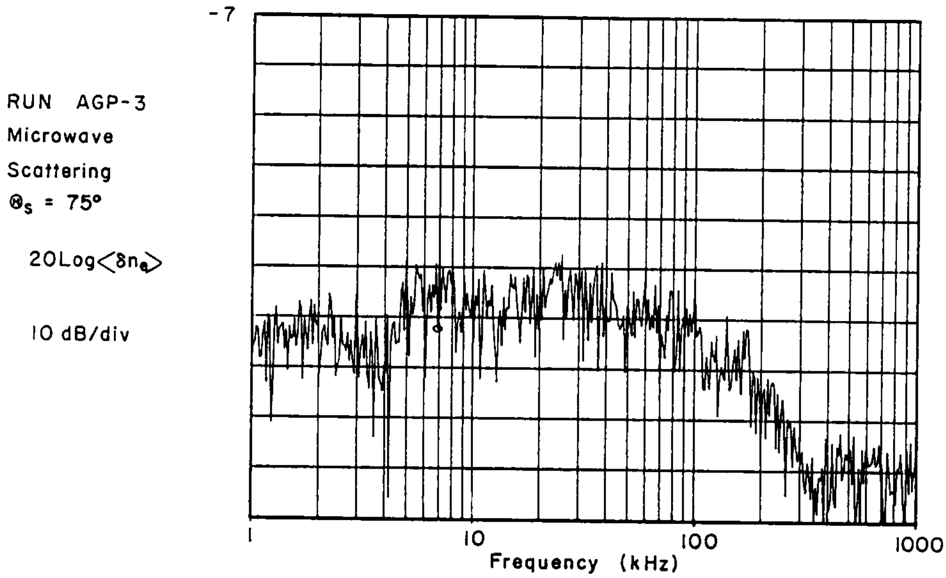

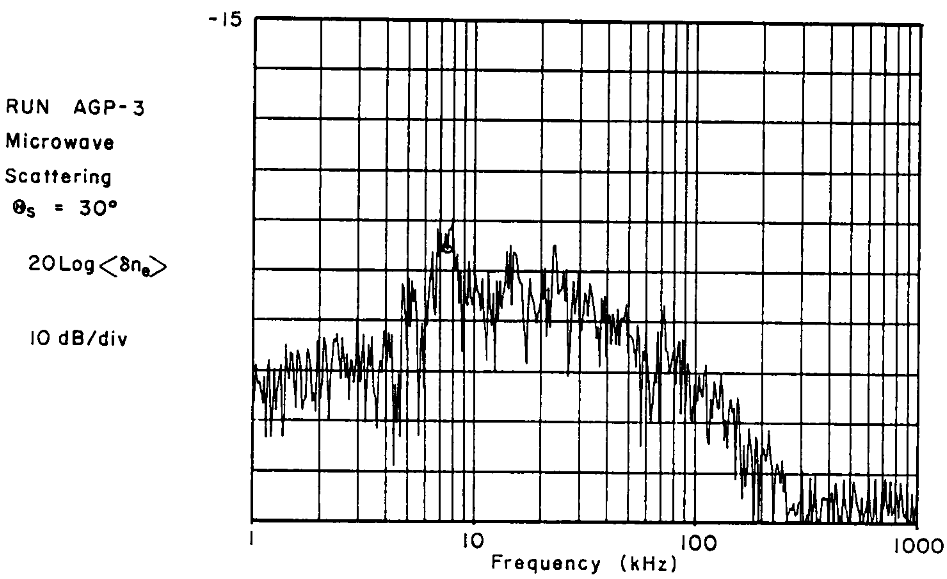

Figure H.24. Calibrated power spectra of electron density fluctuations detected by the microwave scattering system for Run AGP-3.

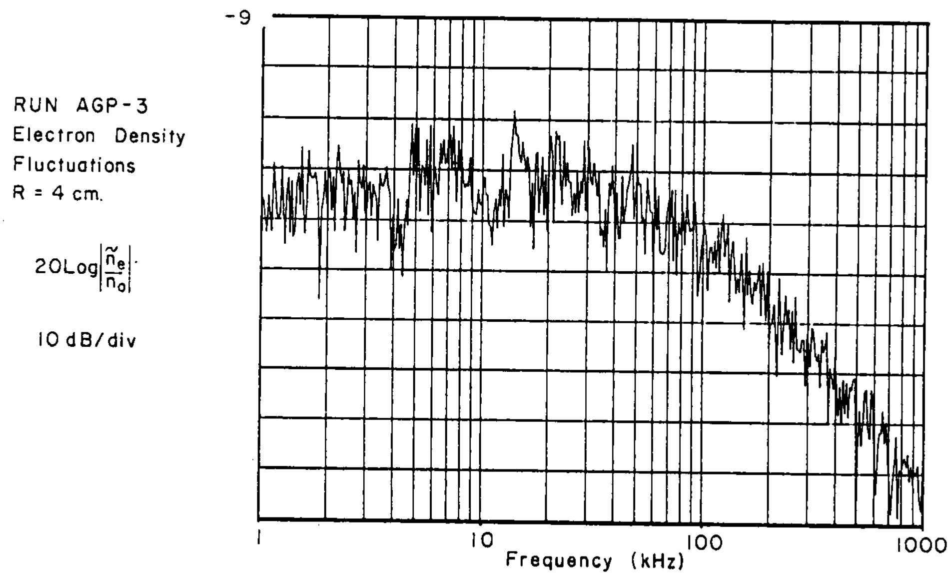

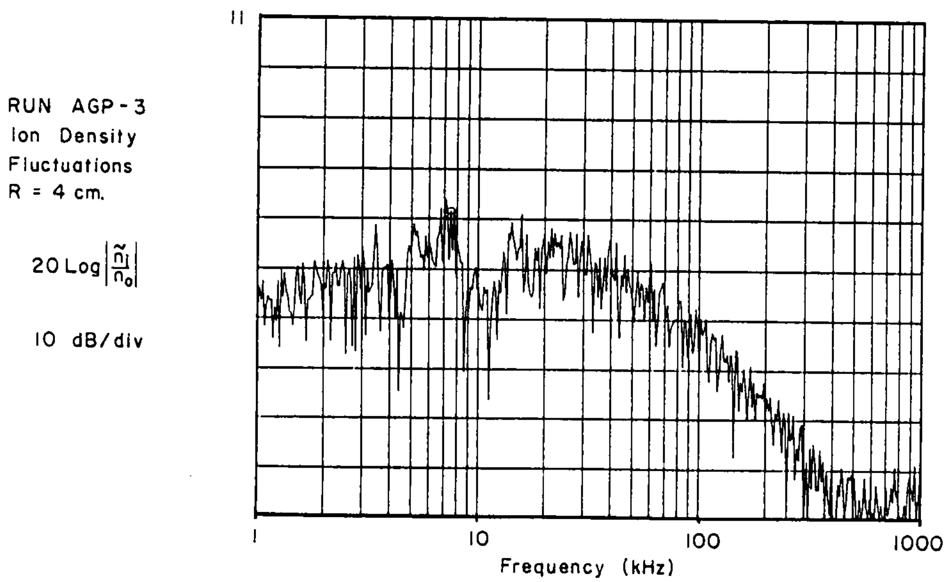

Figure H.25. Calibrated power spectra of electron and ion density fluctuations detected by a biased Langmuir probe for Run AGP-3.

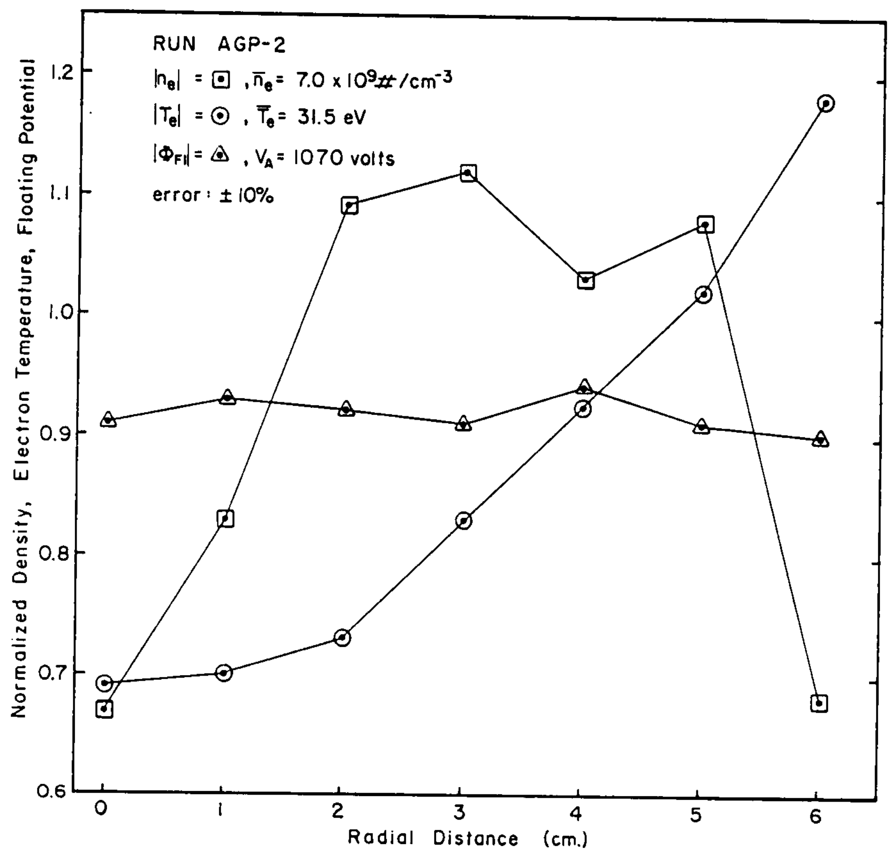

Figure H.26. Radial profile of the electron number density, electron temperature and plasma floating potential for Run AGP-2.

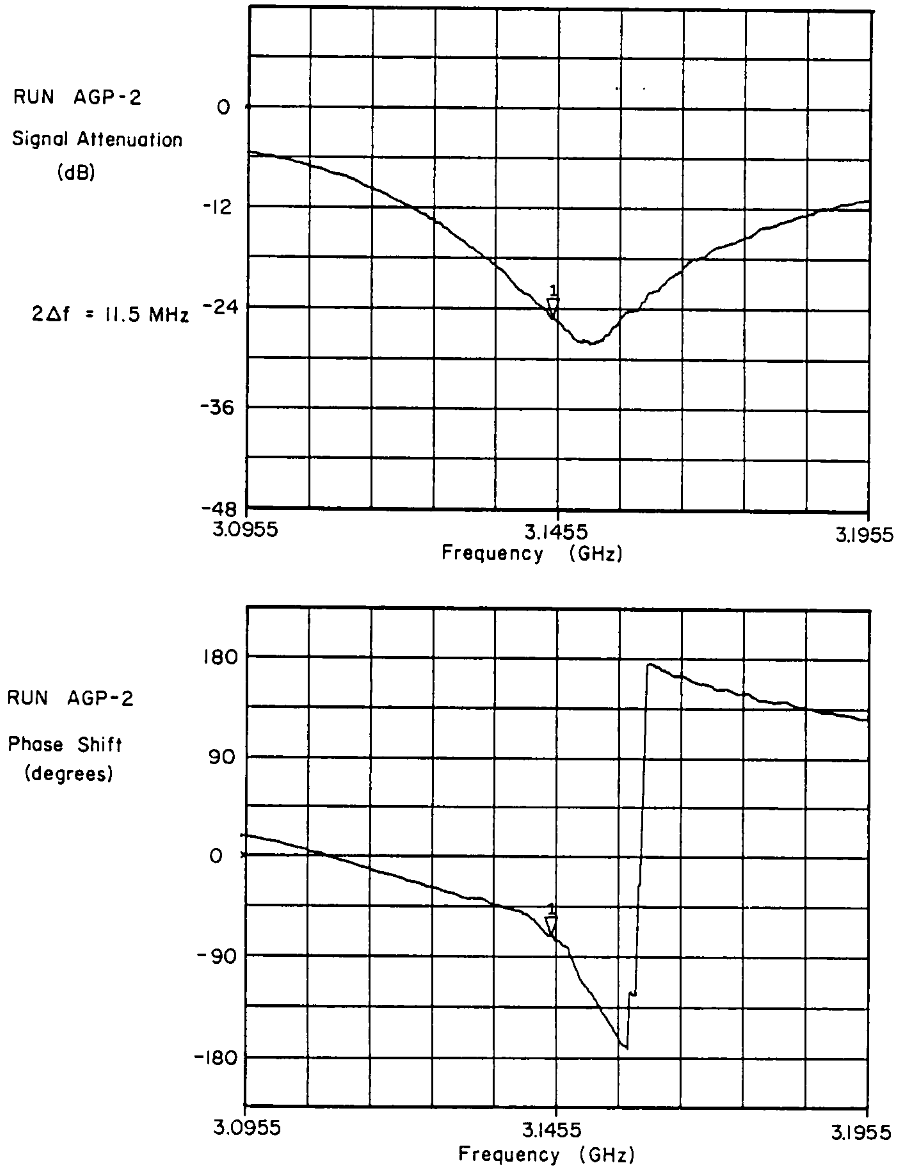

Figure H.27. Microwave absorption data for the extraordinary mode wave at the upper hybrid resonance for Run AGP-2.

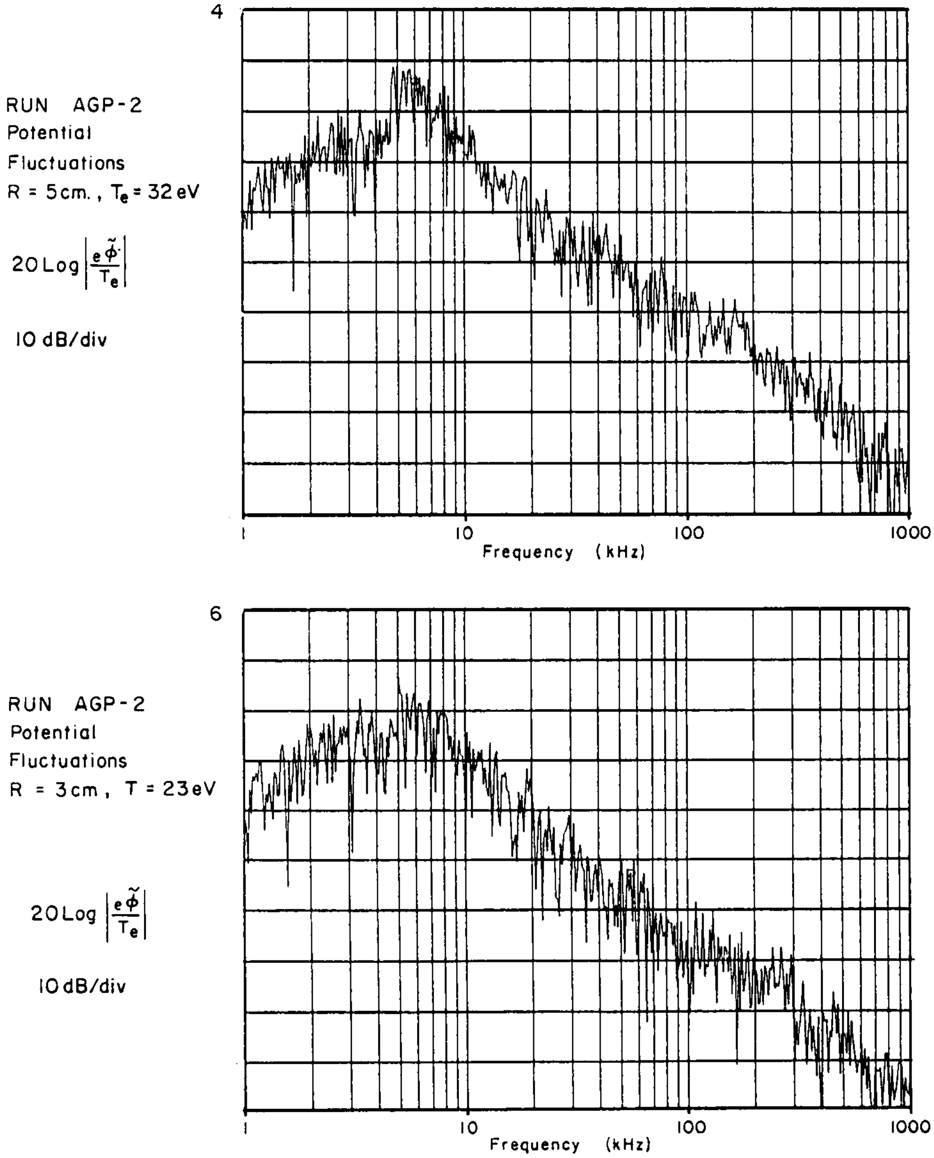

Figure H.28. Calibrated power spectra of electrostatic potential fluctuations normalized to the local electron temperature for Run AGP-2.

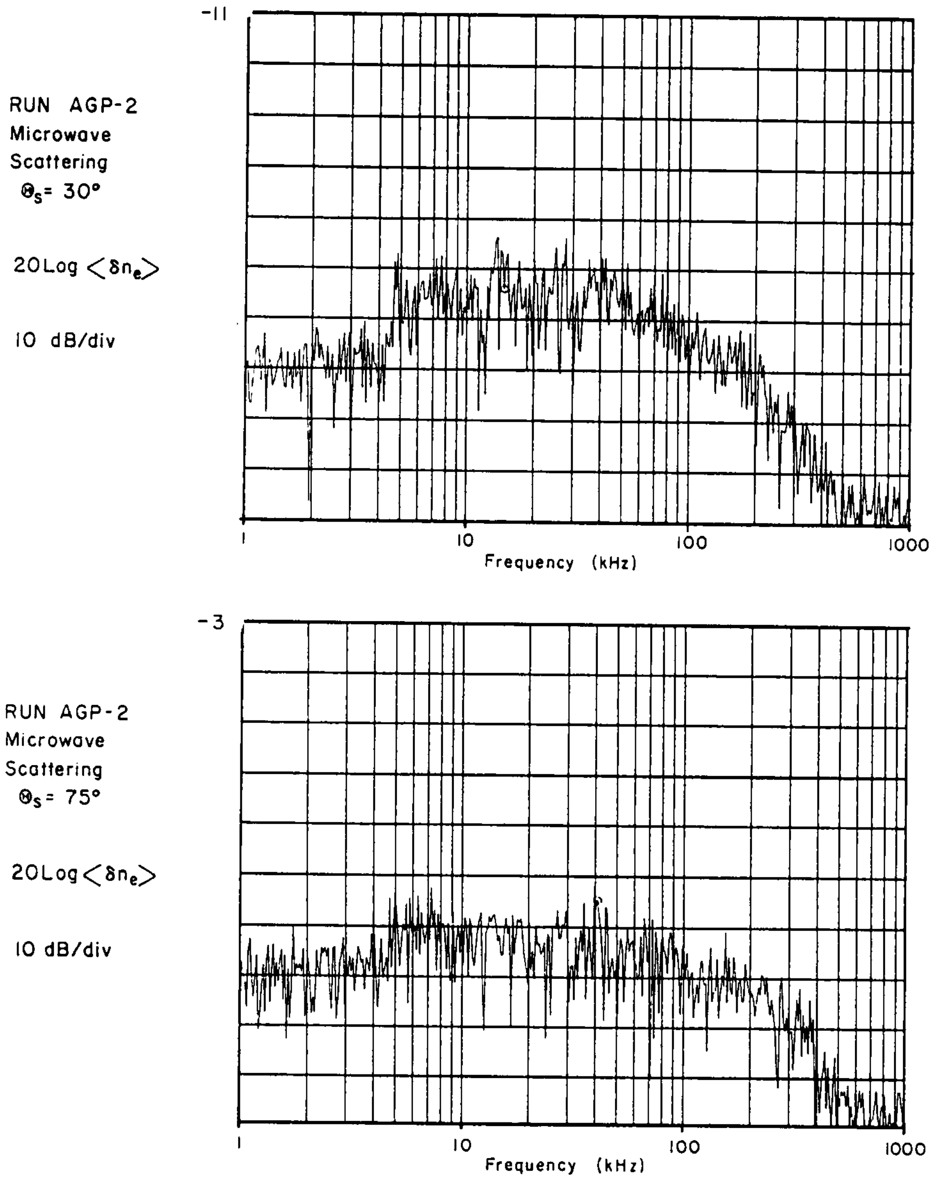

Figure H.29. Calibrated power spectra of electron density fluctuations detected by the microwave scattering system for Run AGP-2.

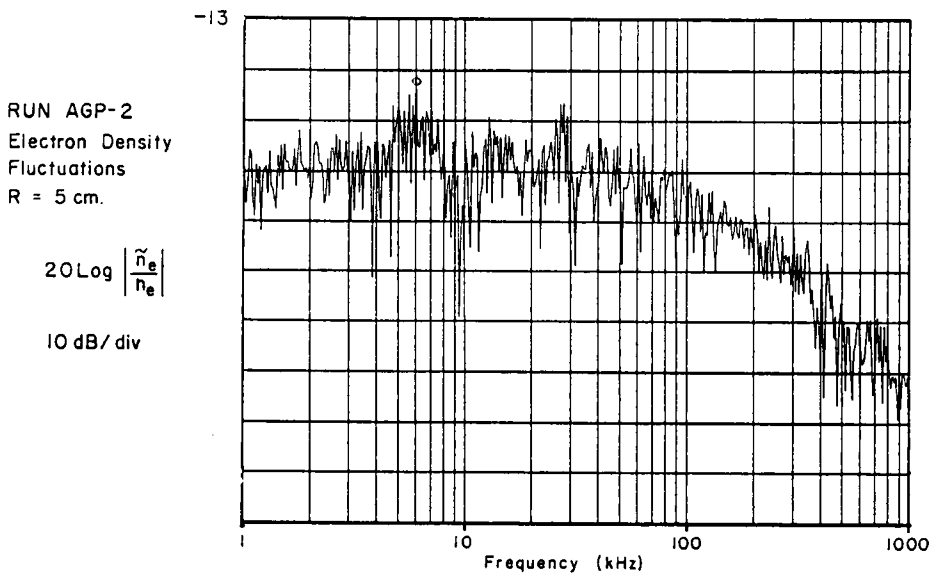

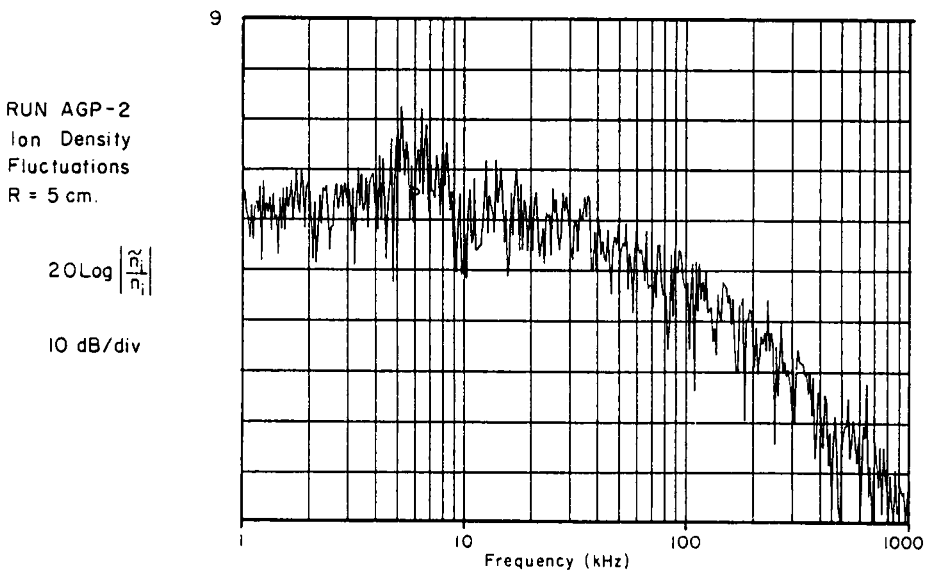

Figure H.30. Calibrated power spectra of electron and ion density fluctuations detected by a biased Langmuir probe for Run AGP-2.

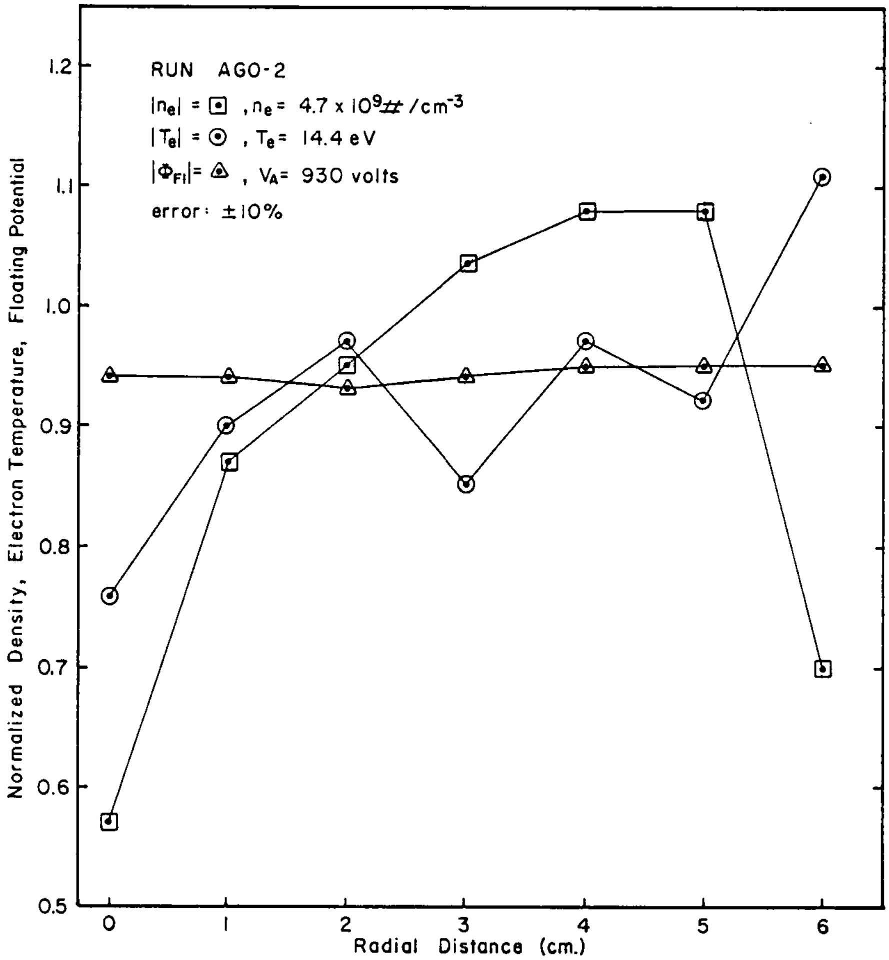

Figure H.31. Radial profile of the electron number density, electron temperature and plasma floating potential for Run AGO-2.

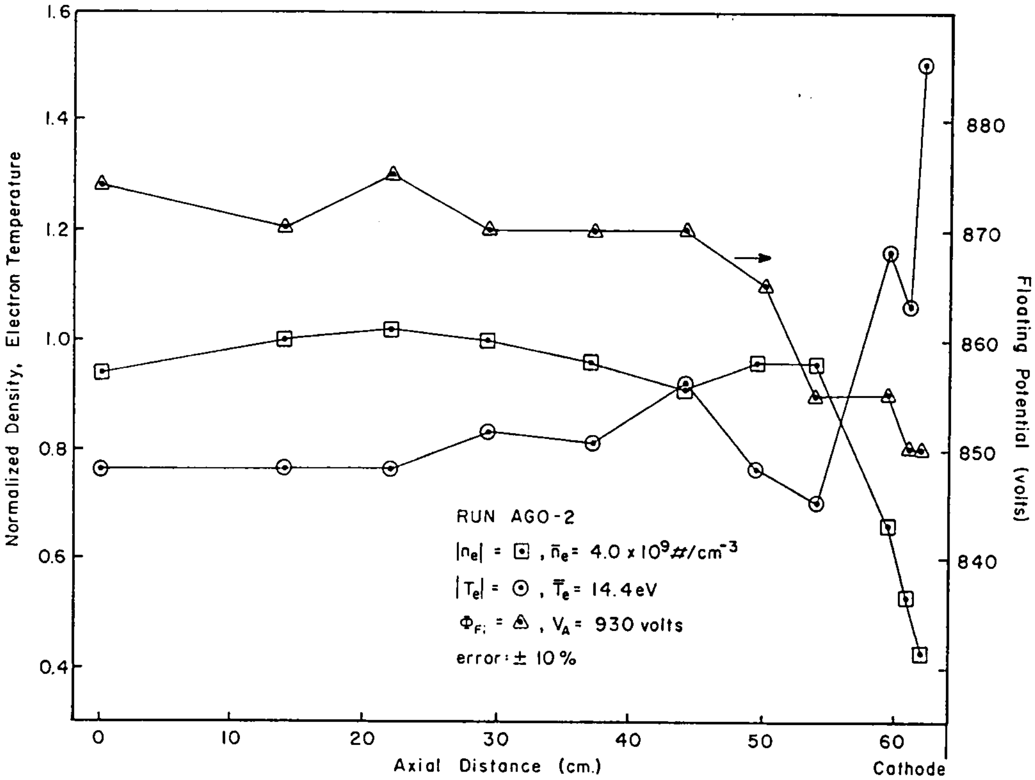

Figure H.32. Axial profile of the electron number density, electron temperature and plasma floating potential for Run AGO-2.

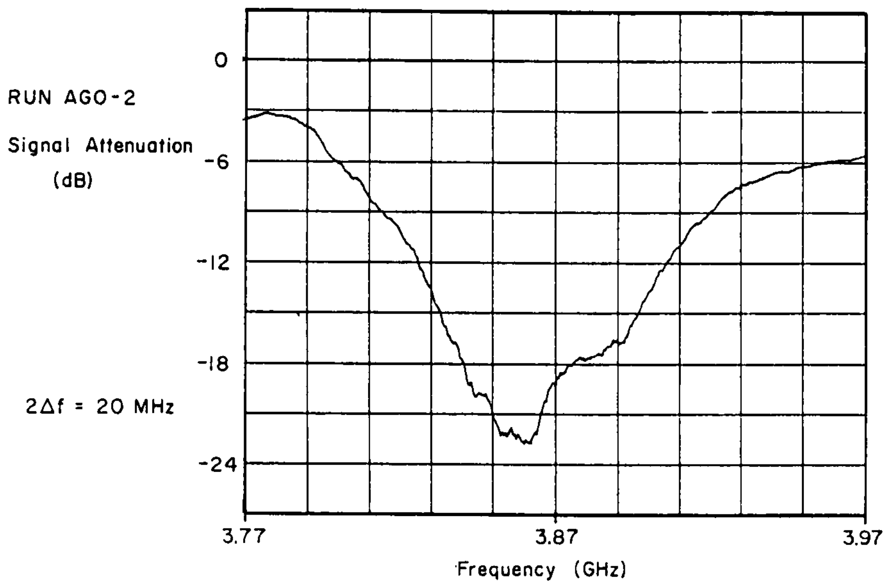

Figure H.33. Microwave absorption data for the extraordinary mode wave at the upper hybrid resonance for Run AGO-2.

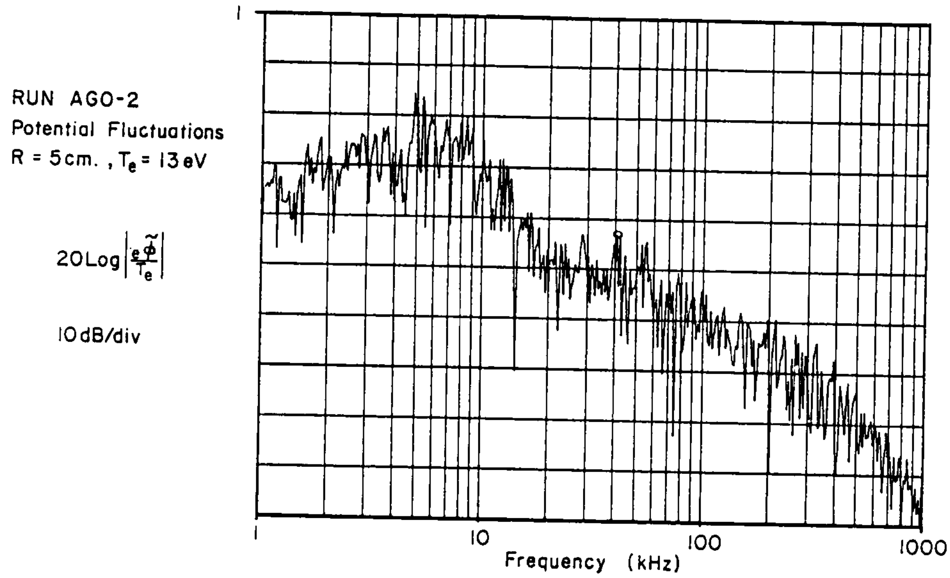

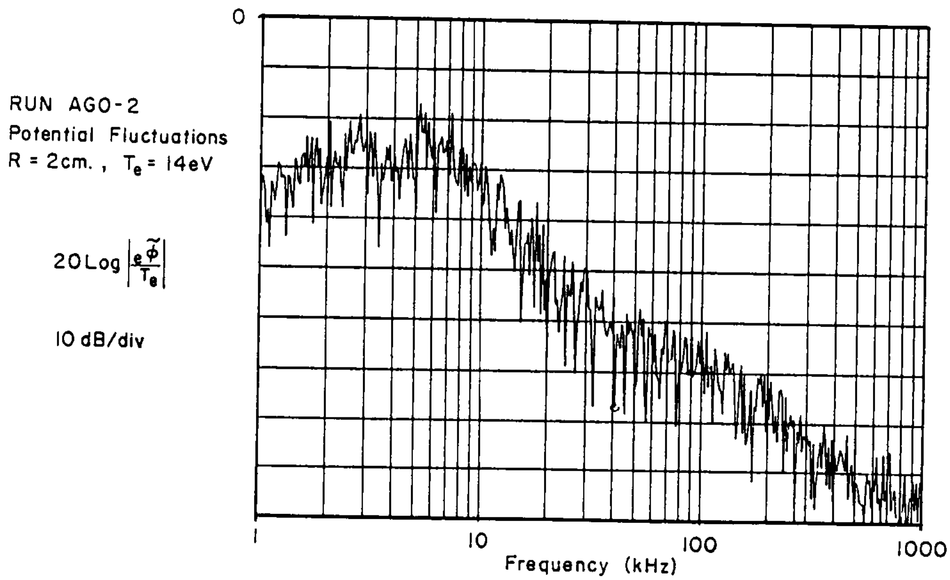

Figure H.34. Calibrated power spectra of electrostatic potential fluctuations normalized to the local electron temperature for Run AGO-2.

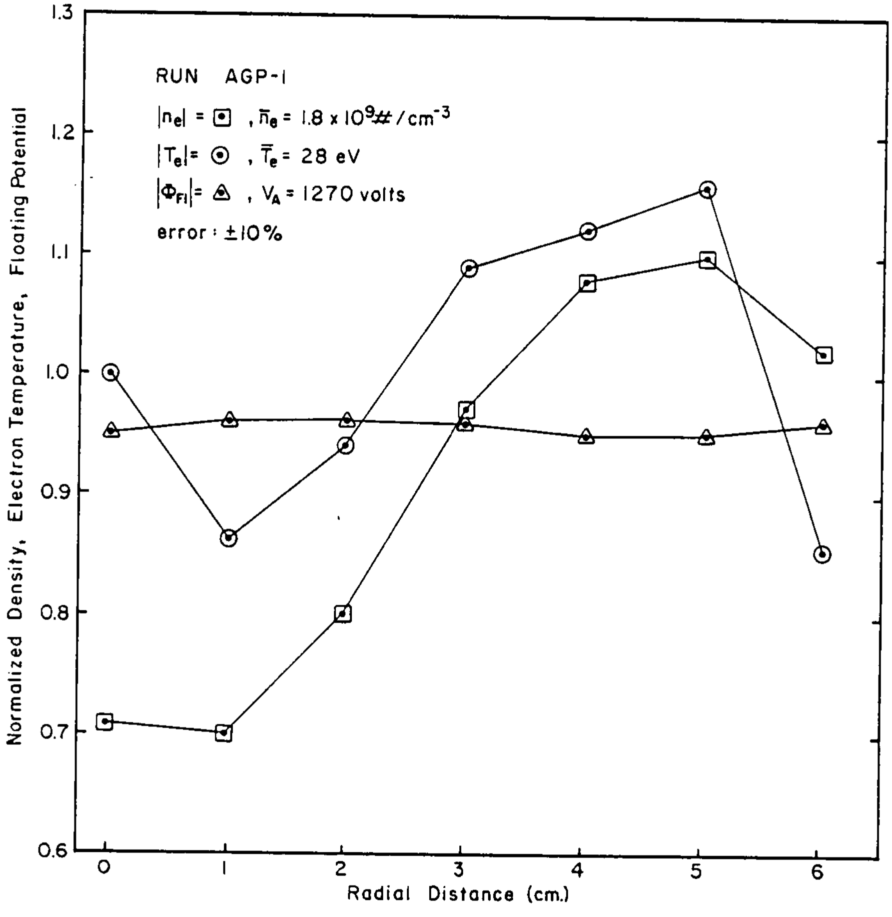

Figure H.35. Radial profile of the electron number density, electron temperature and plasma floating potential for Run AGP-1.

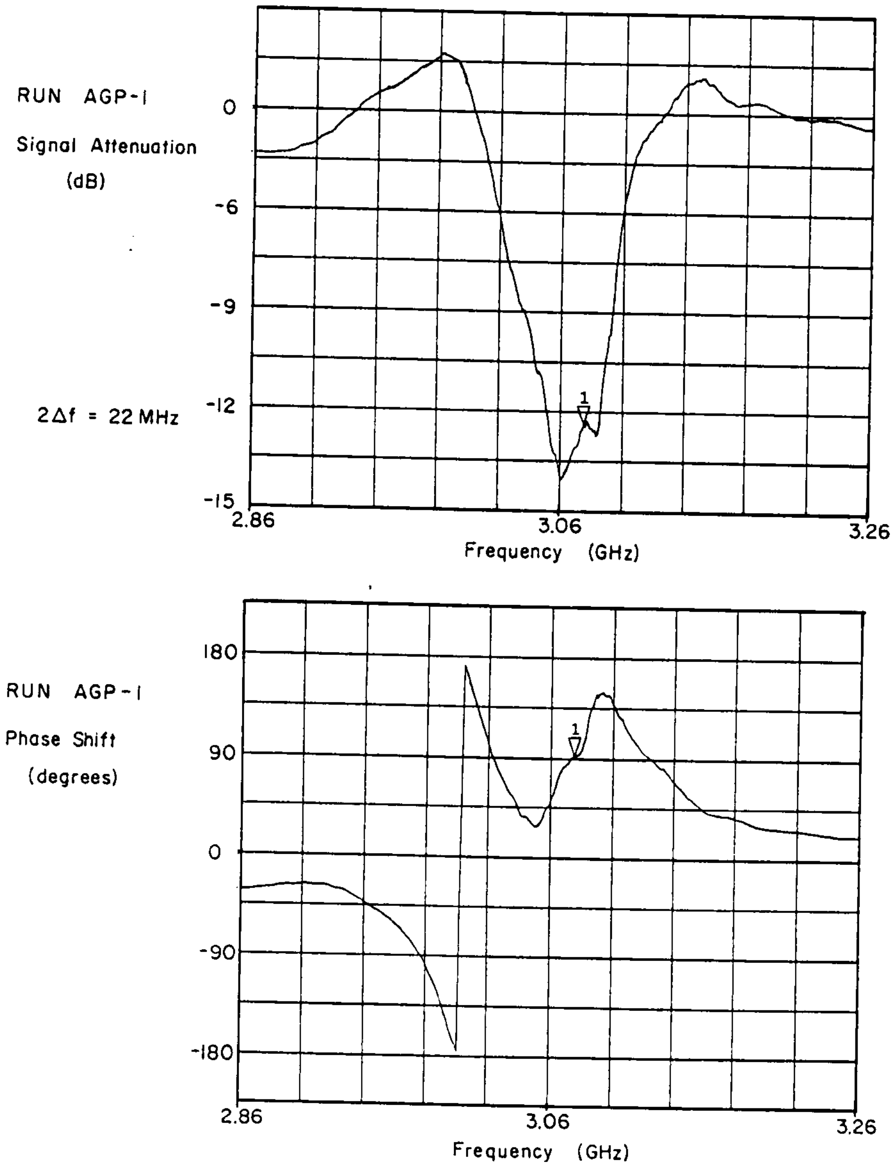

Figure H.36. Microwave absorption data for the extraordinary mode wave at the upper hybrid resonance for Run AGP-1.

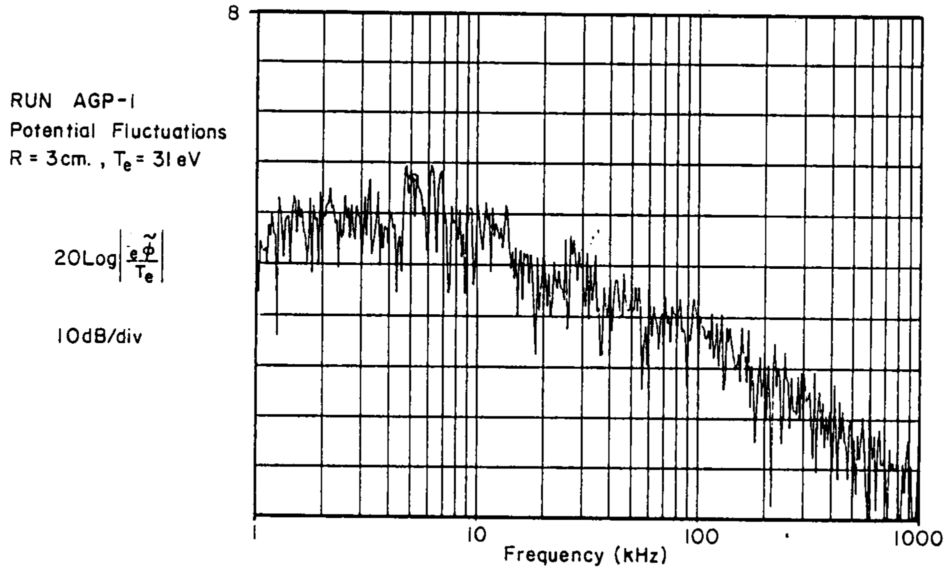

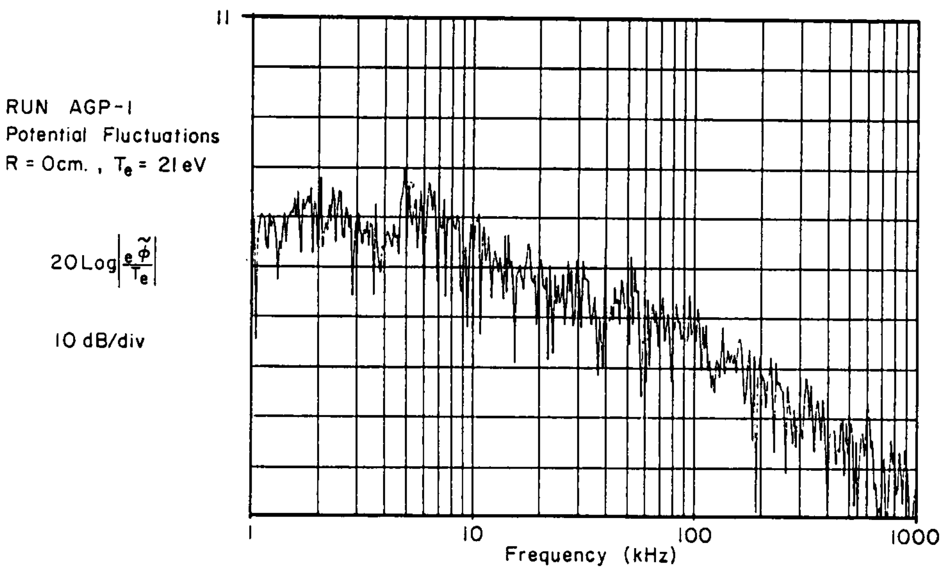

Figure H.37. Calibrated power spectra of electrostatic potential fluctuations normalized to the local electron temperature for Run AGP-1.

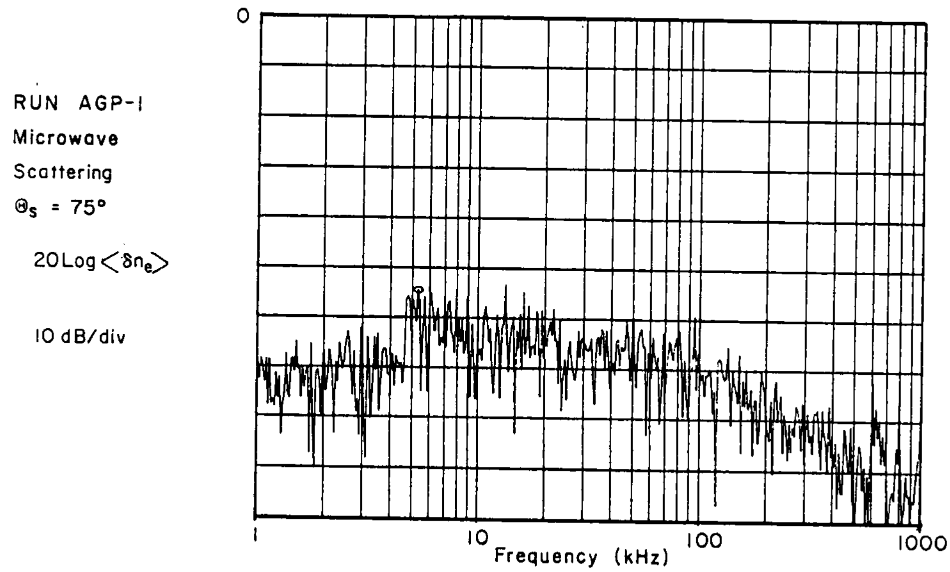

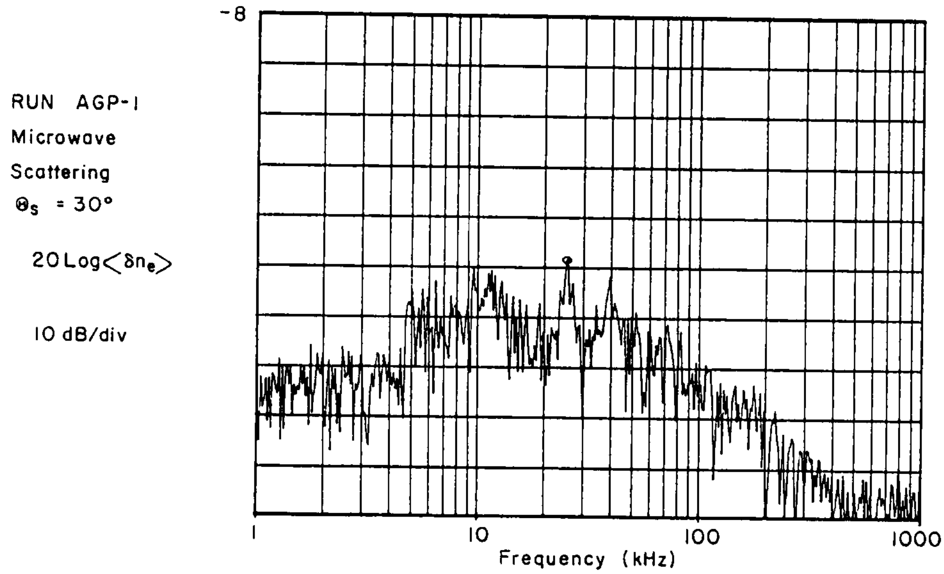

Figure H.38. Calibrated power spectra of electron density fluctuations detected by the microwave scattering system for Run AGP-1.

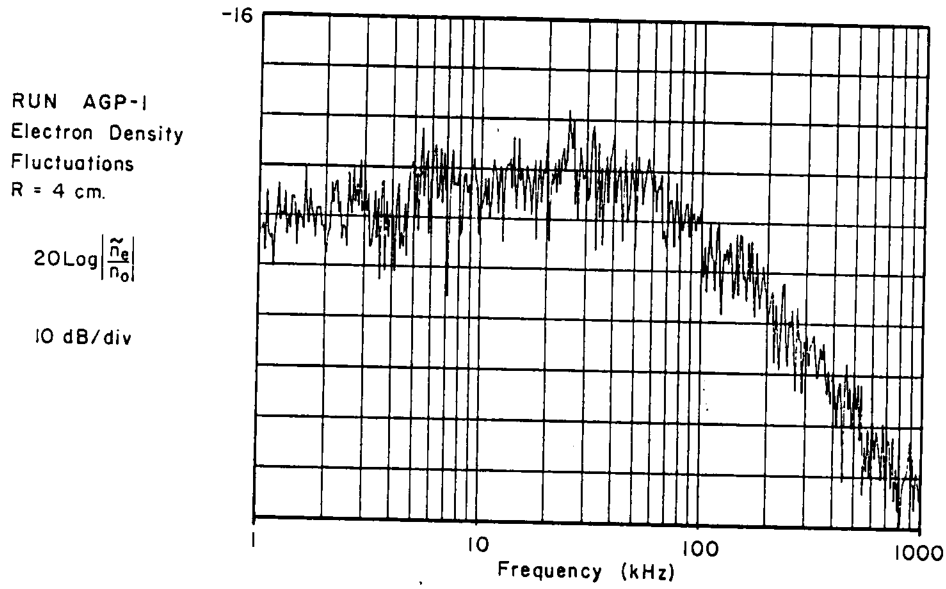

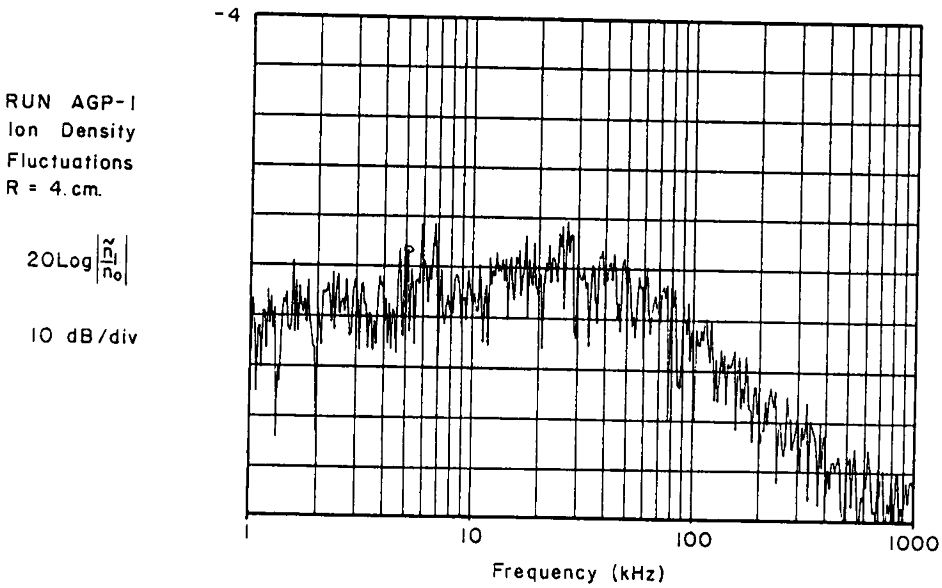

Figure H.39. Calibrated power spectra of electron and ion density fluctuations detected by a biased Langmuir probe for Run AGP-1.

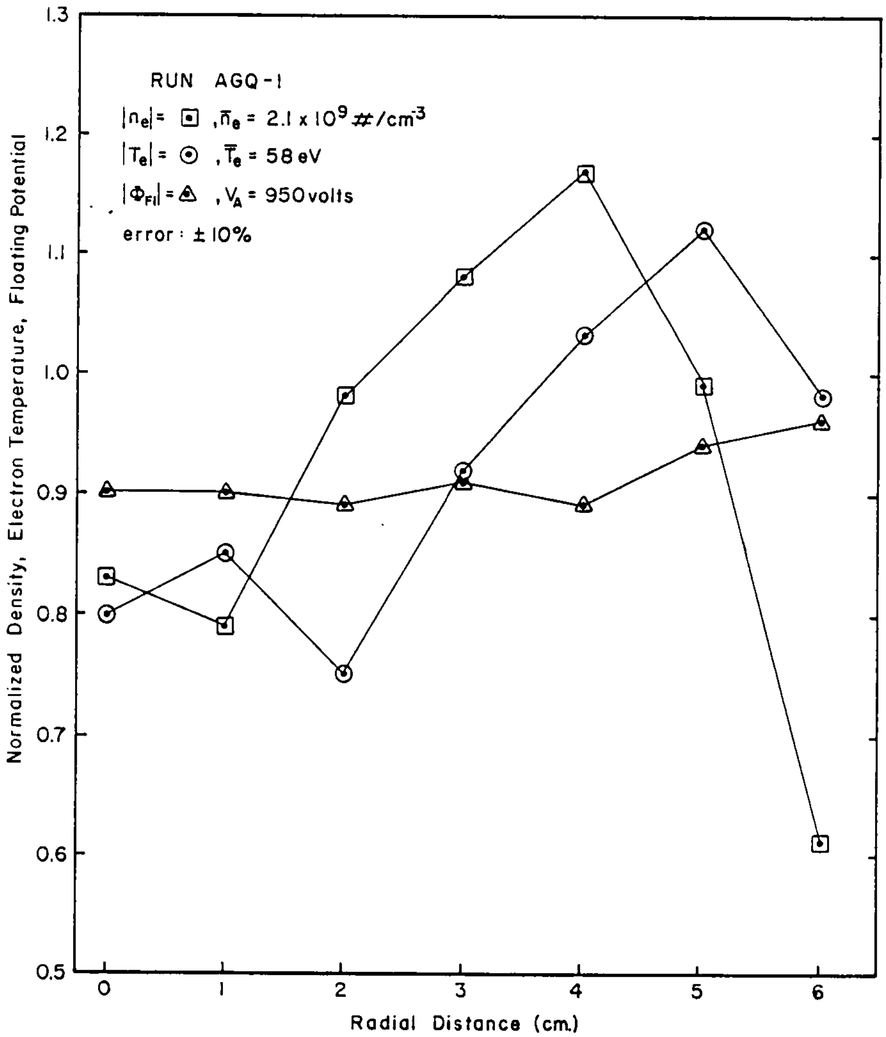

Figure H.40. Radial profile of the electron number density, electron temperature and plasma floating potential for Run AGQ-1.

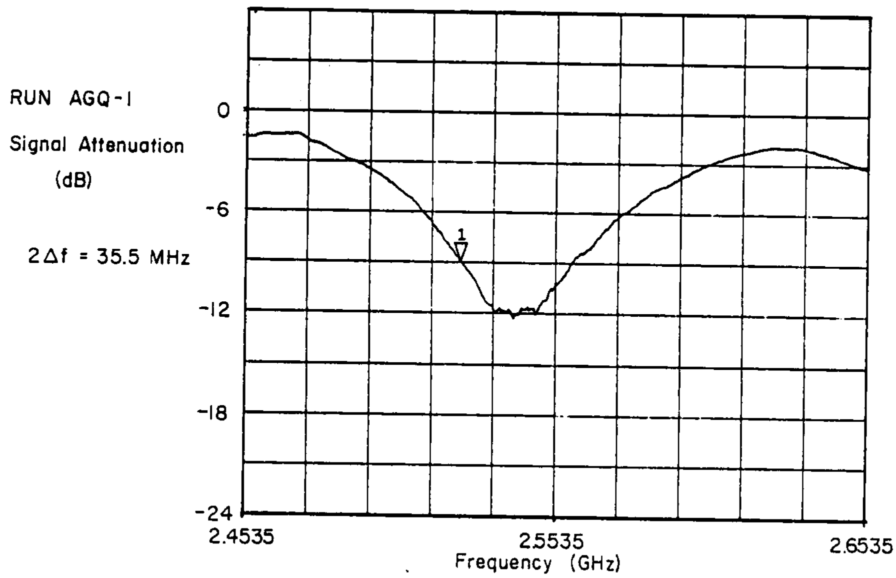

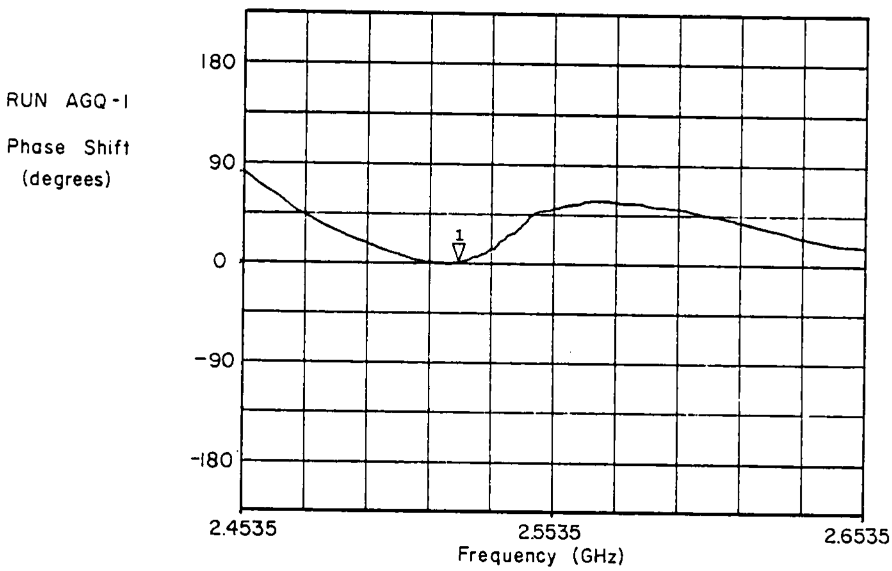

Figure H.41. Microwave absorption data for the extraordinary mode wave at the upper hybrid resonance for Run AGQ-1.

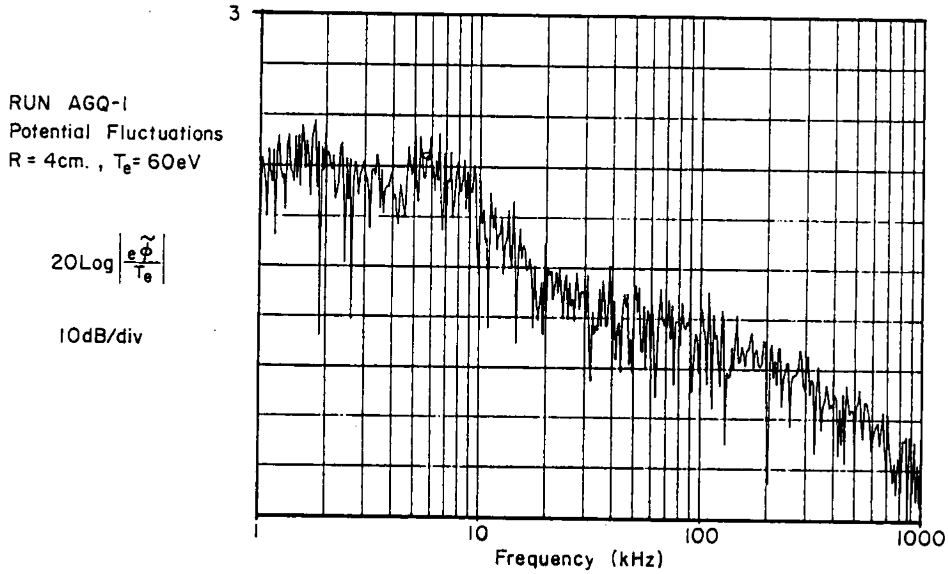

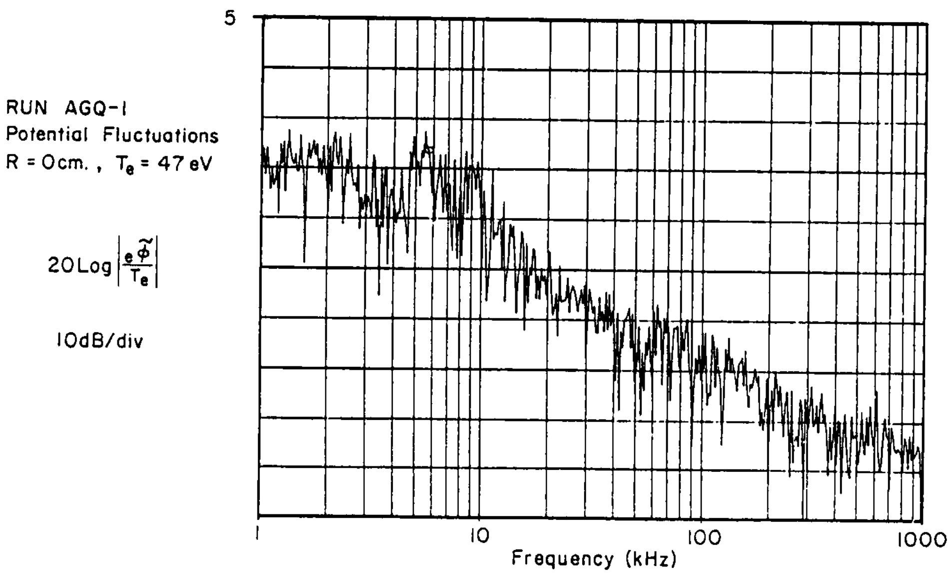

Figure H.42. Calibrated power spectra of electrostatic potential fluctuations normalized to the local electron temperature for Run AGQ-1.

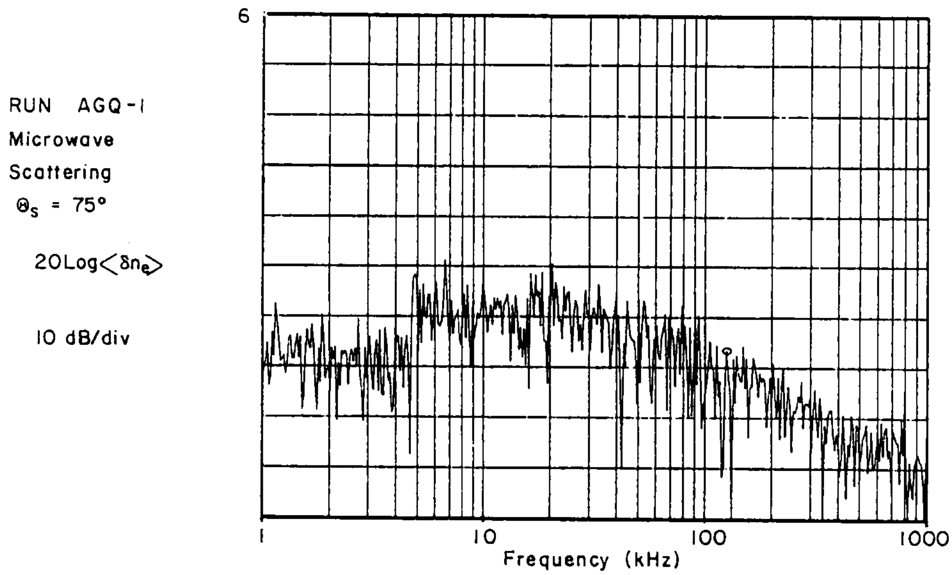

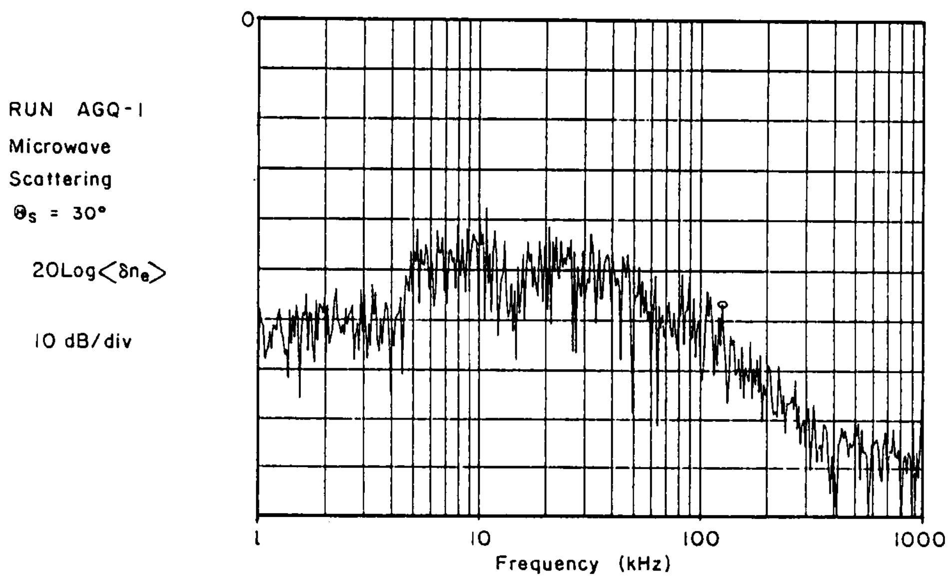

Figure H.43. Calibrated power spectra of electron density fluctuations detected by the microwave scattering system for Run AGQ-1.

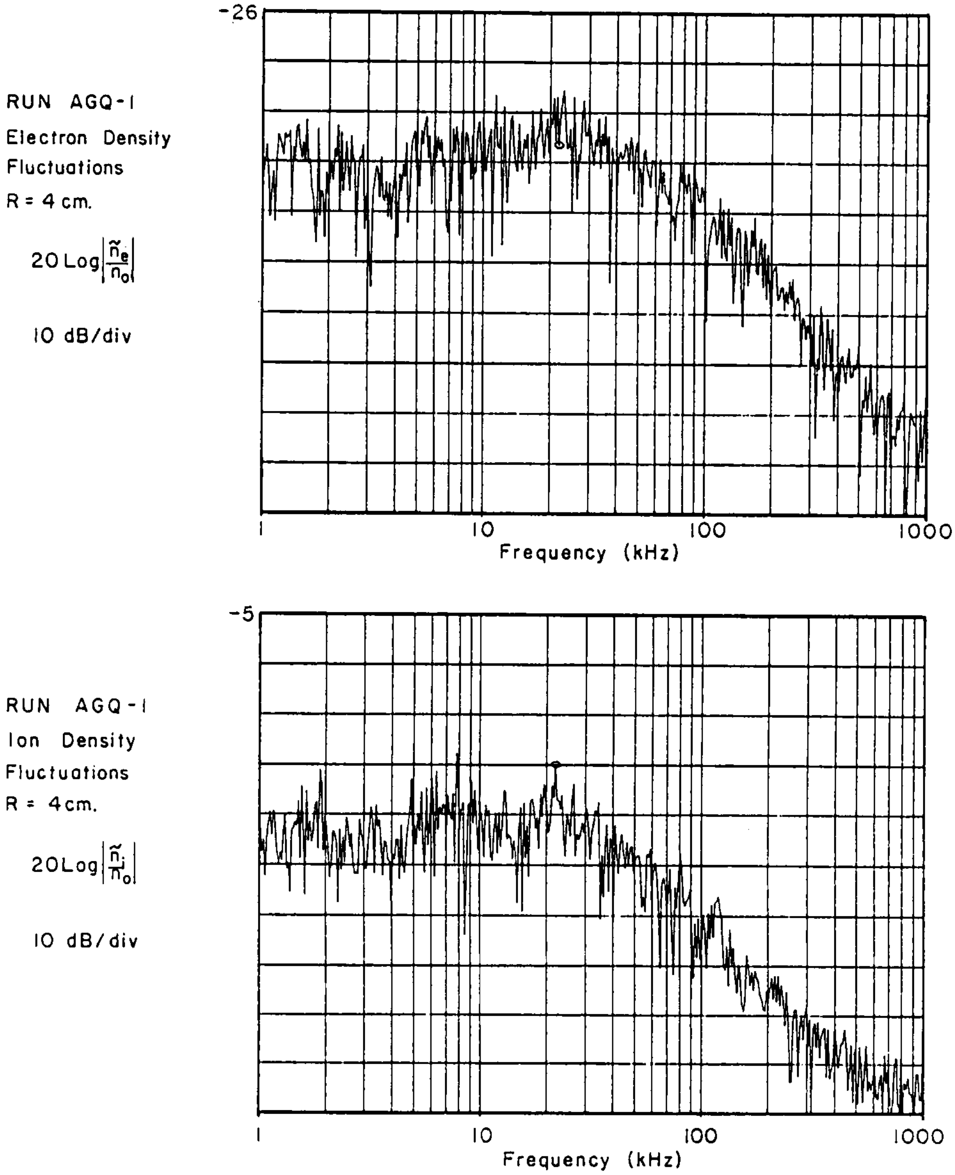

Figure H.44. Calibrated power spectra of electron and ion density fluctuations detected by a biased Langmuir probe for Run AGQ-1.

APPENDIX I

EXPERIMENTAL DATA ILLUSTRATING THE ENHANCEMENT OF ν_{eff}

The following appendix lists the data discussed in Chapter V for the collisional drift instability. These data include radial profiles of the electron number density, electron temperature and plasma floating potential; and electrostatic potential fluctuation spectra for Runs AGU-1, AGU-2, AGV-1, and AGV-2. These data runs were taken on the experimental system shown in Figure 2.3 with the elongated anode cylinder. Except for the microwave absorption data, these data were taken in the same manner as the data presented in Appendix H.

The microwave absorption data for these runs were taken using two capacitive probes located at the midplane and displaced azimuthally 180°. These probes were each inserted one centimeter into the plasma. The source probe was coupled to the HP 8510 Network Analyzer through a 40dB gain amplifier for isolation and to accommodate the large reflection coefficient of the small probes. The receiving probe was D.C. isolated from the network analyzer with a high voltage dual capacitor D.C. block. When used in this manner with a high frequency signal, the capacitive probes behaved as small monopole antennae (Balanis 1982a). The electric field detected by two antennae oriented in this manner will still be perpendicular to the static magnetic field and subject to collisional broadening at the upper hybrid resonance.

The run numbers with a -2 had the level of electrostatic potential fluctuations enhanced by the application of a high voltage R.F. signal applied to the anode cylinder. Using the transformer network discussed in Appendix E and an Amplifier Research 100L broadband R.F. amplifier, a sine wave perturbation at 12 MHz was coupled to the anode cylinder. For Run AGU-2 a 75 volt, 0.6 ampere signal with a 41° current-voltage phase lag was applied, and for Run AGV-2 a 70 volt, 0.18 ampere signal with a 58° current-voltage phase lag was applied.

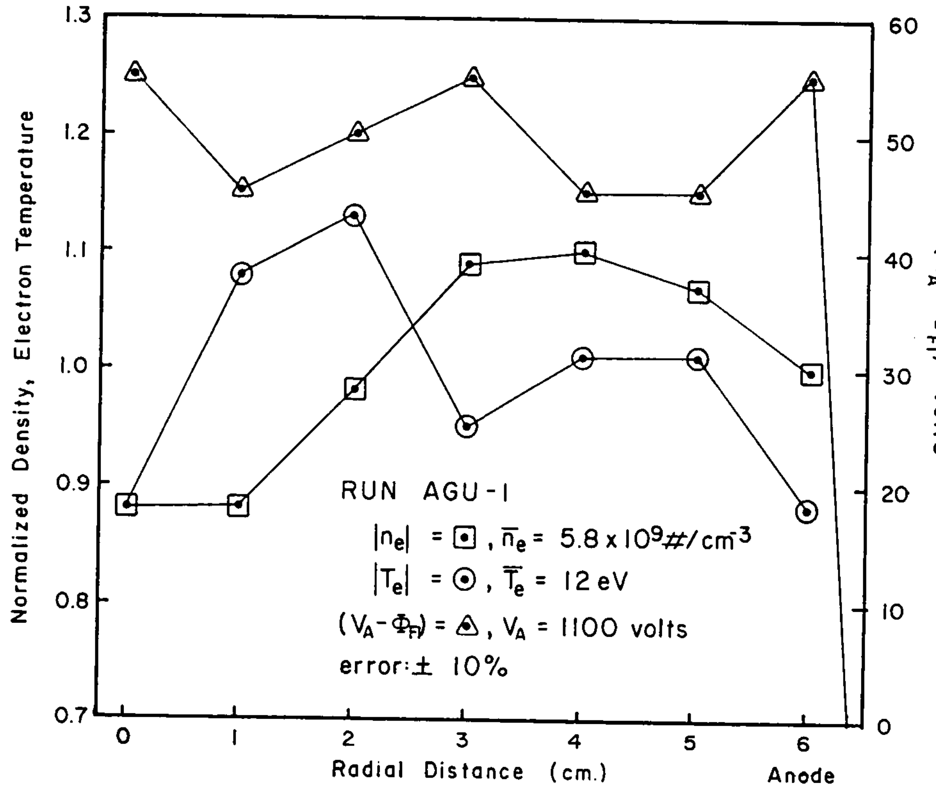

Figure I.1. Radial profile of electron number density, electron temperature and anode voltage-floating voltage difference for Run AGU-1.

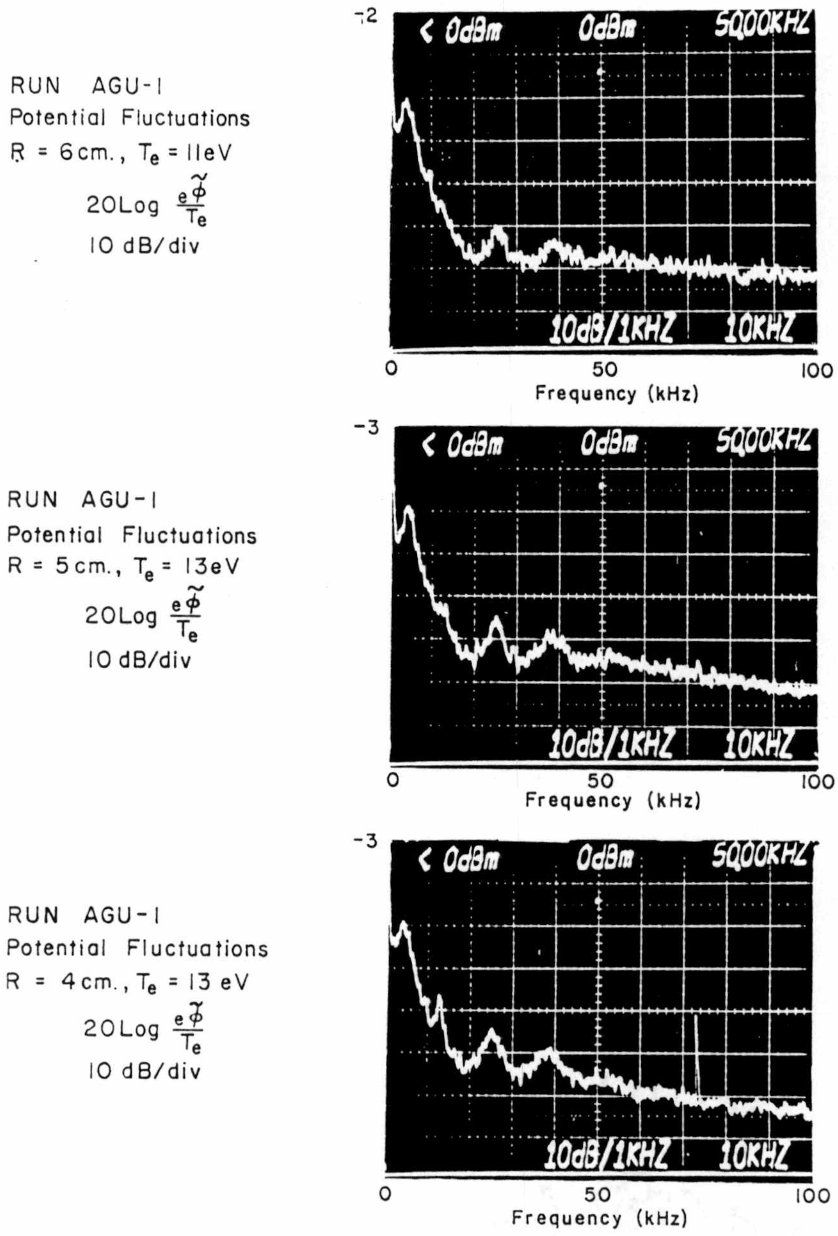

Figure I.2. Calibrated electrotastic potential fluctuation spectra at R =6cm., 5cm. and 4cm. for Run AGU-1.

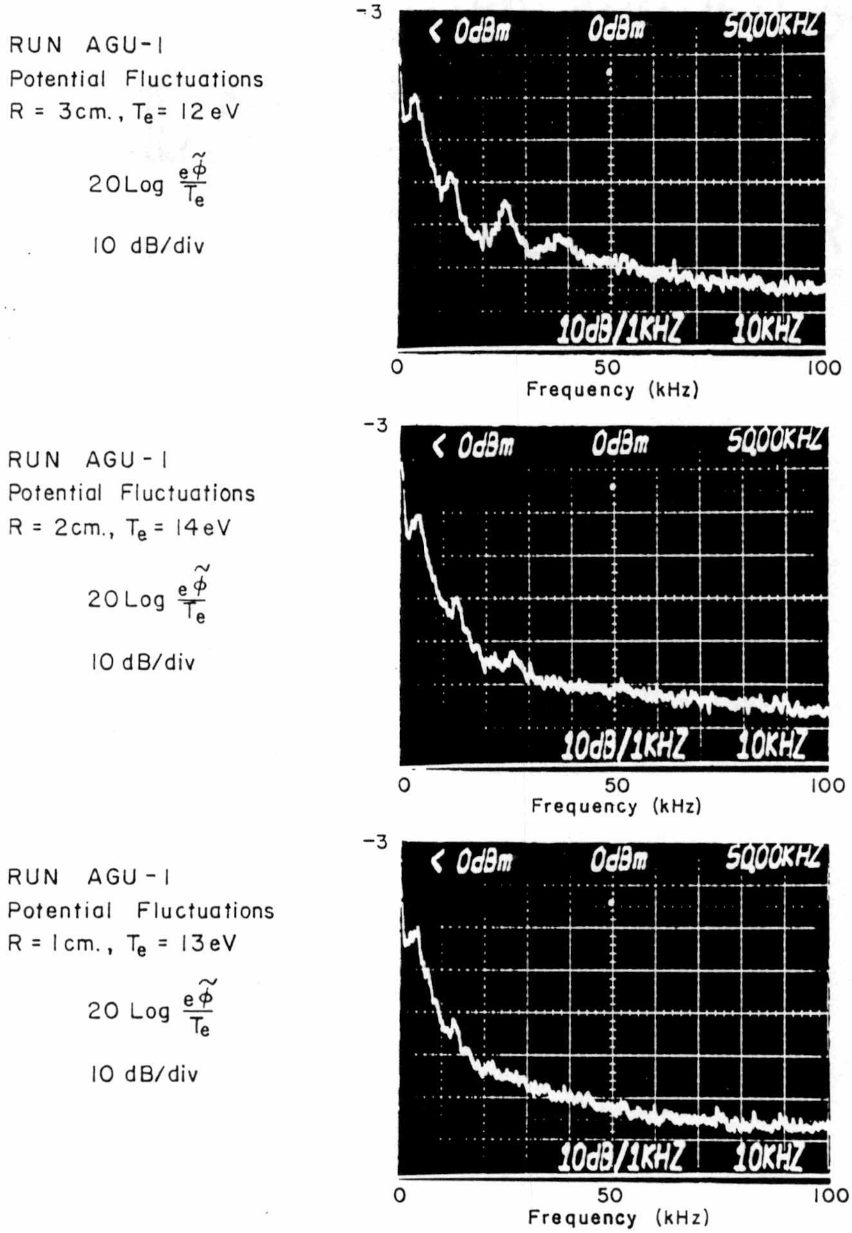

Figure I.3. Calibrated electrostatic potential fluctuation spectra at R =3cm., 2cm. and 1cm. for Run AGU-1.

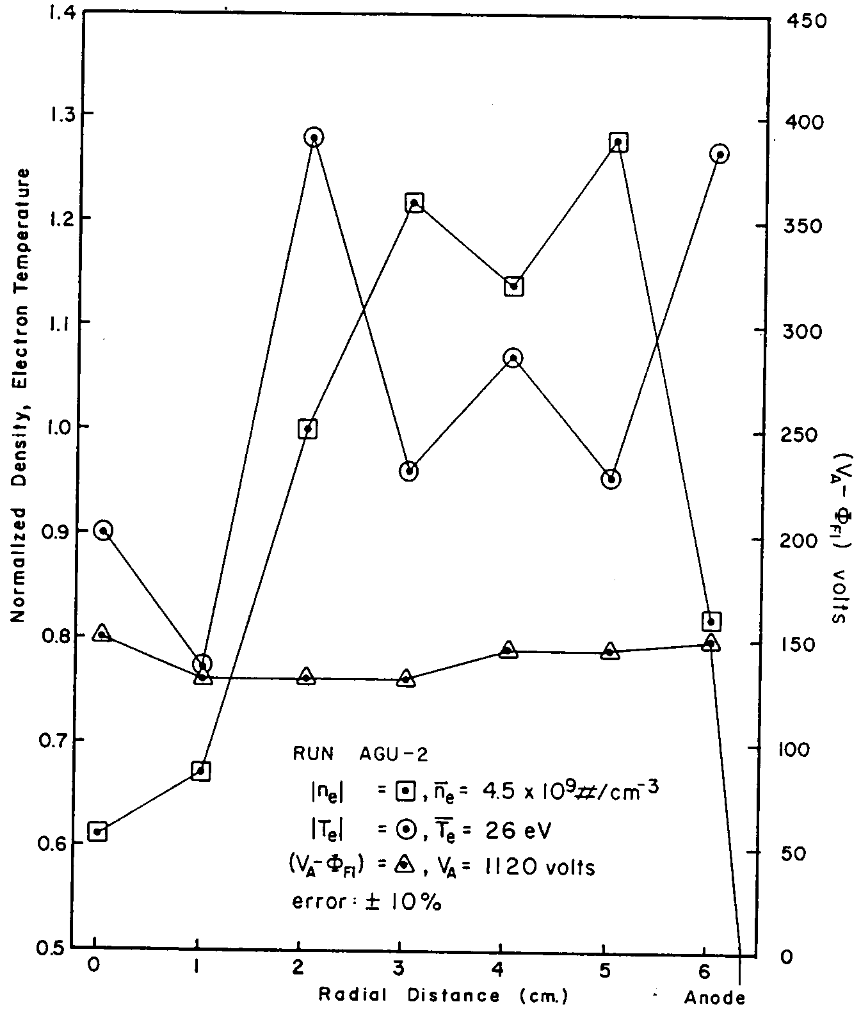

Figure I.4. Radial profile of electron number density, electron temperature, and anode voltage-floating voltage difference for Run AGU-2.

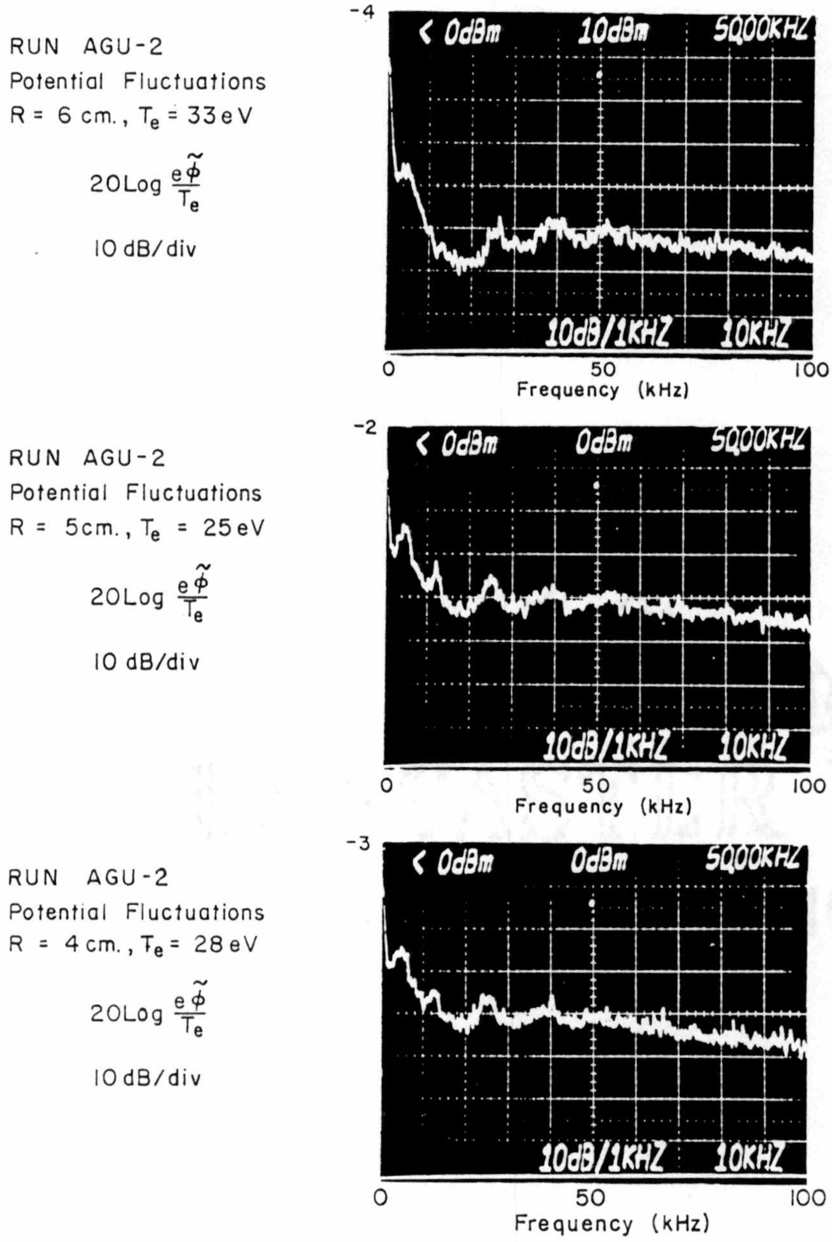

Figure I.5. Calibrated electrotastic potential fluctuation spectra at R =6cm., 5cm. and 4cm. for Run AGU-2.

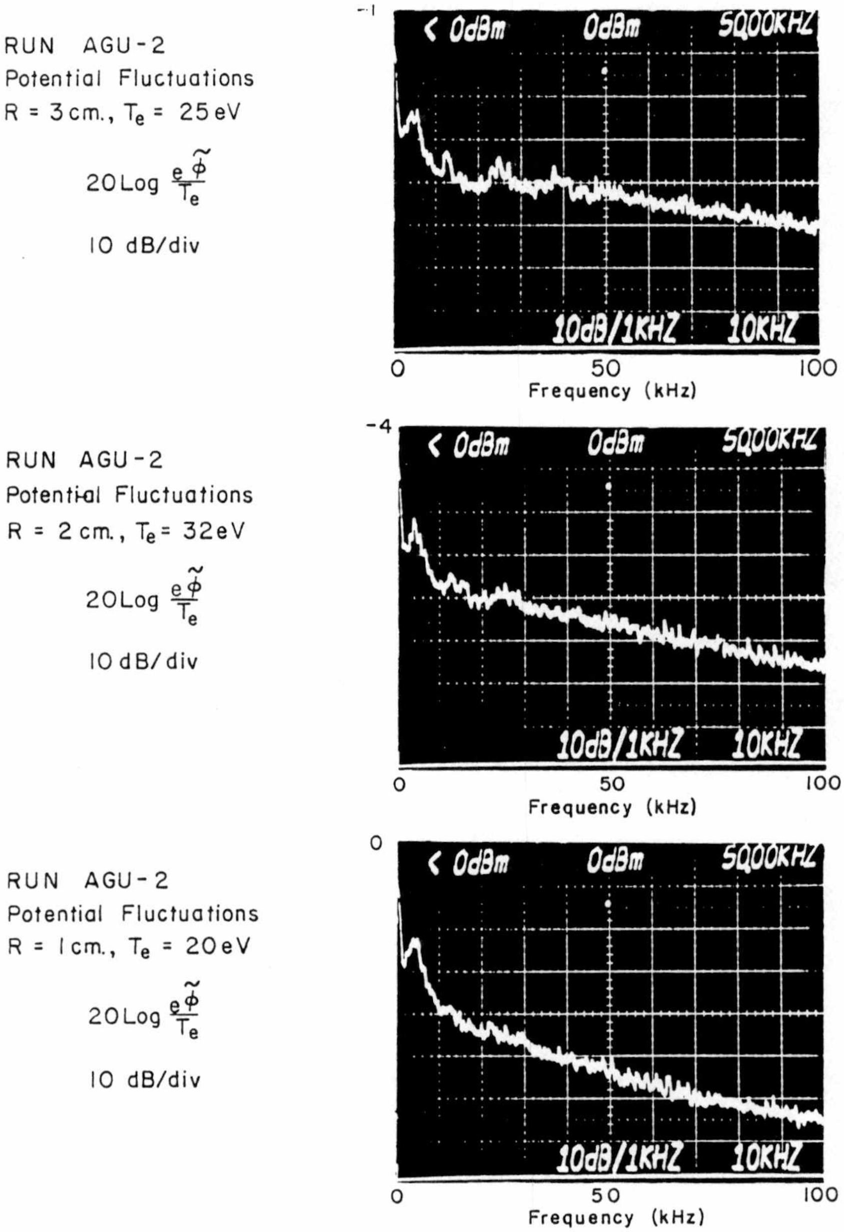

Figure I.6. Calibrated electrostatic potential fluctuation spectra at R =3cm., 2cm. and 1cm. for Run AGU-2.

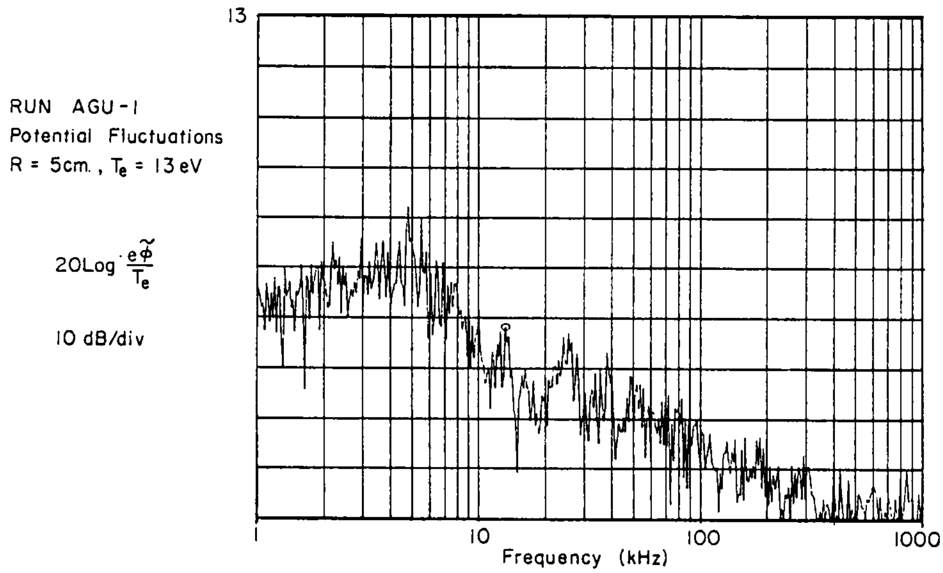

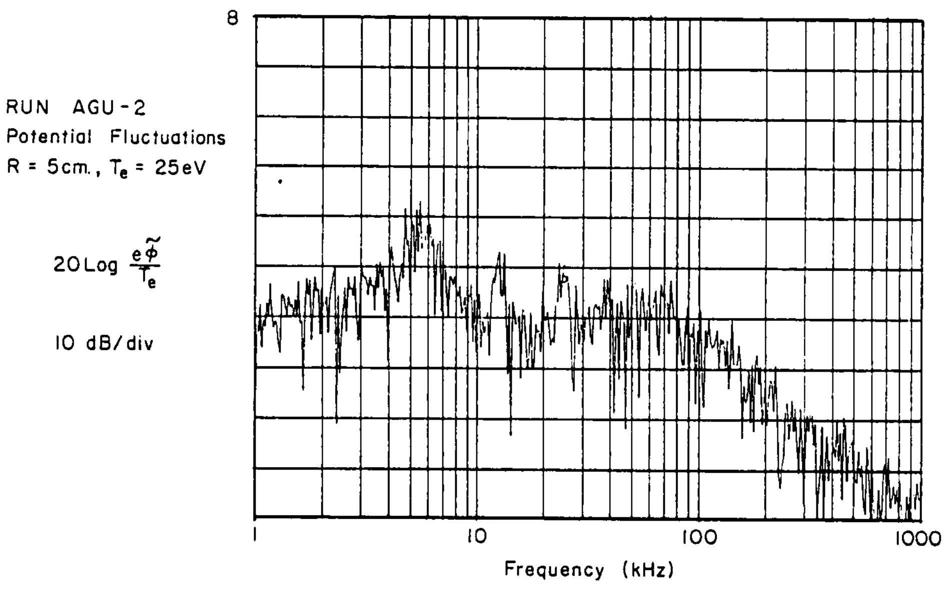

Figure I.7. Comparison of calibrated electrostatic potential fluctuation spectra for Runs AGU-1 and AGU-2 at R =5cm. on log frequency axis.

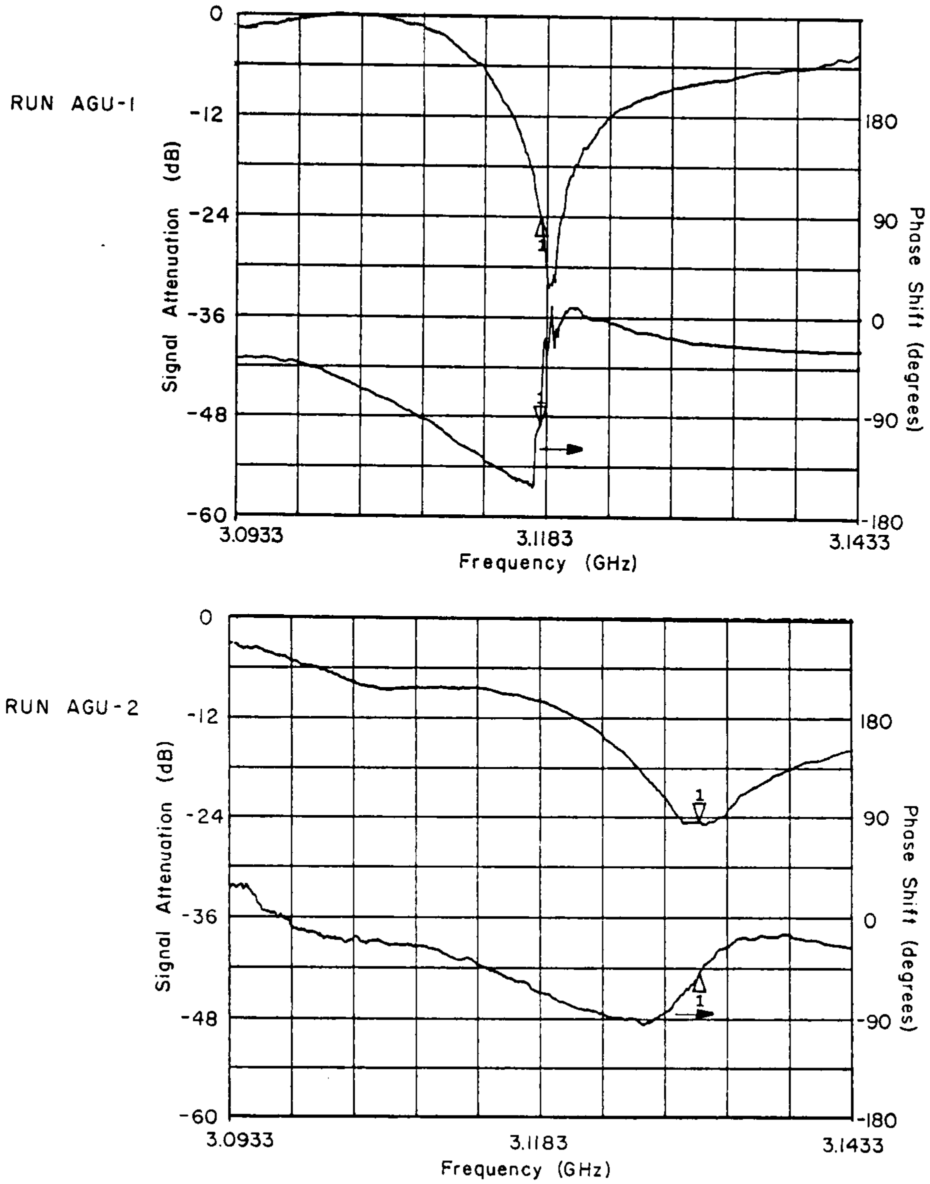

Figure I.8. Microwave absorption data for the extraordinary mode wave launched and received by small monopole antennae for Runs AGU-1 and AGU-2.

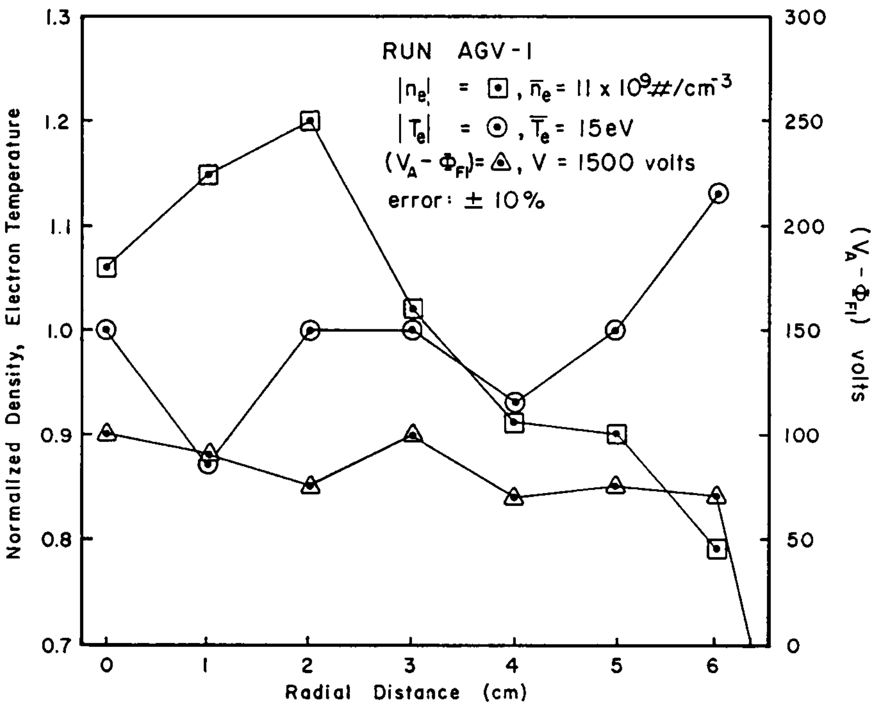

Figure I.9. Radial profile of electron number density, electron temperature and anode voltage-floating voltage difference for Run AGV-1.

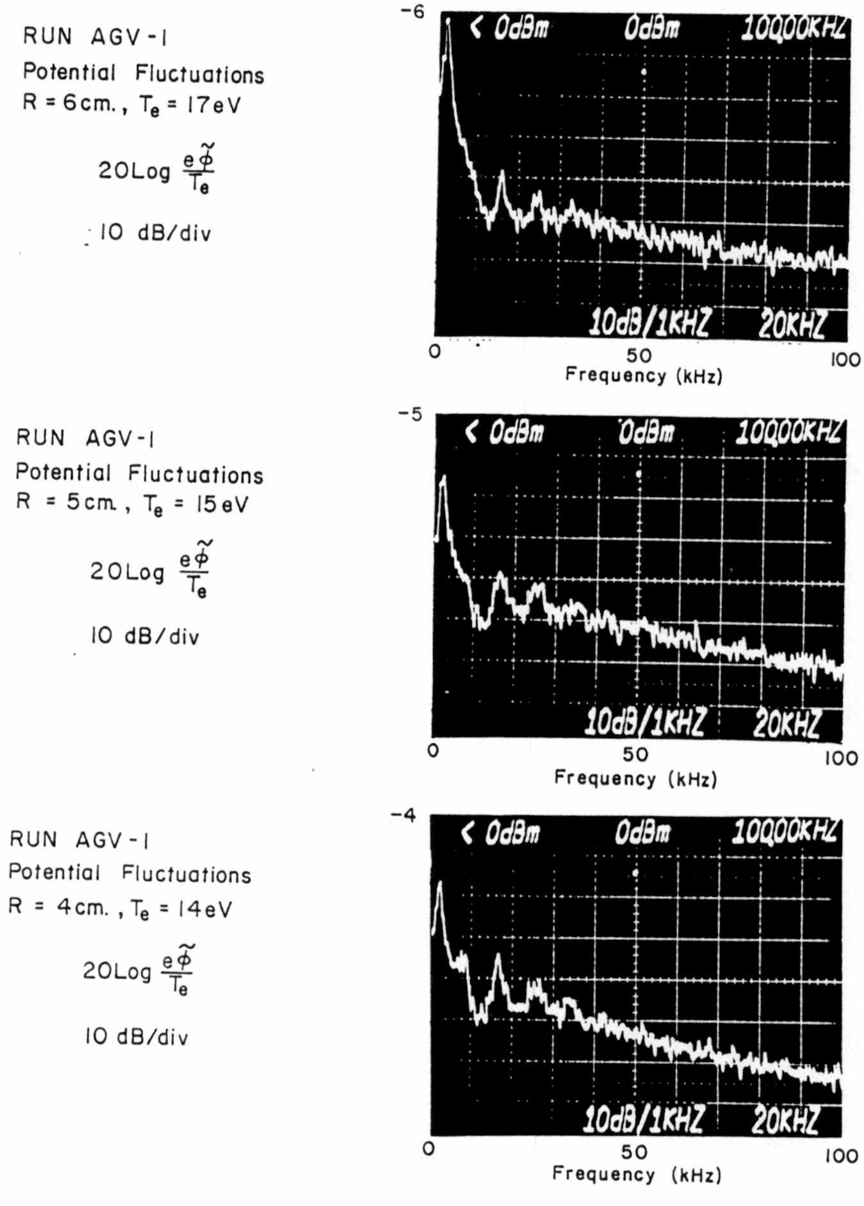

Figure I.10. Calibrated electrostatic potential fluctuation spectra at R =6cm., 5cm. and 4cm. for Run AGV-1.

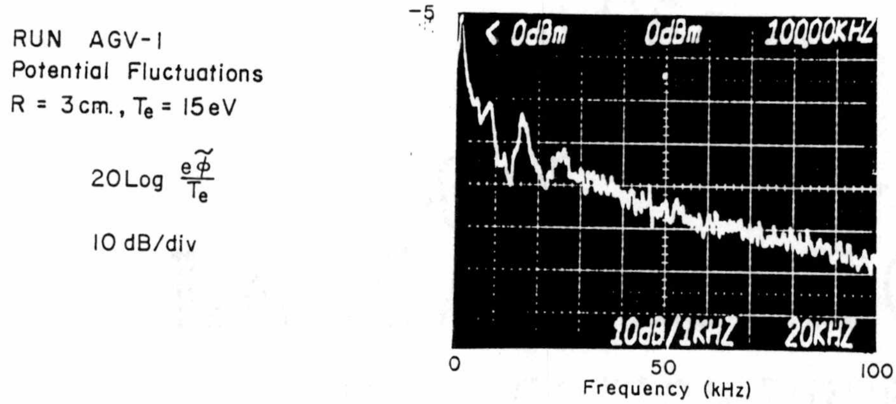

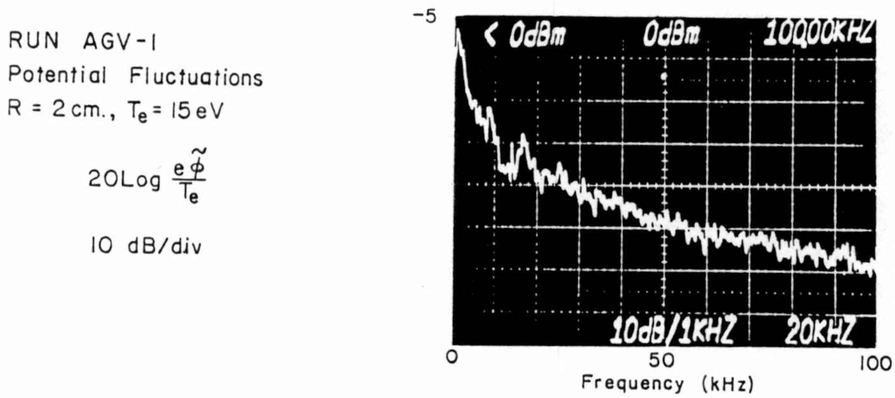

Figure I.11. Calibrated electrostatic potential fluctuation spectra at R =3cm. and 2cm. for Run AGV-1.

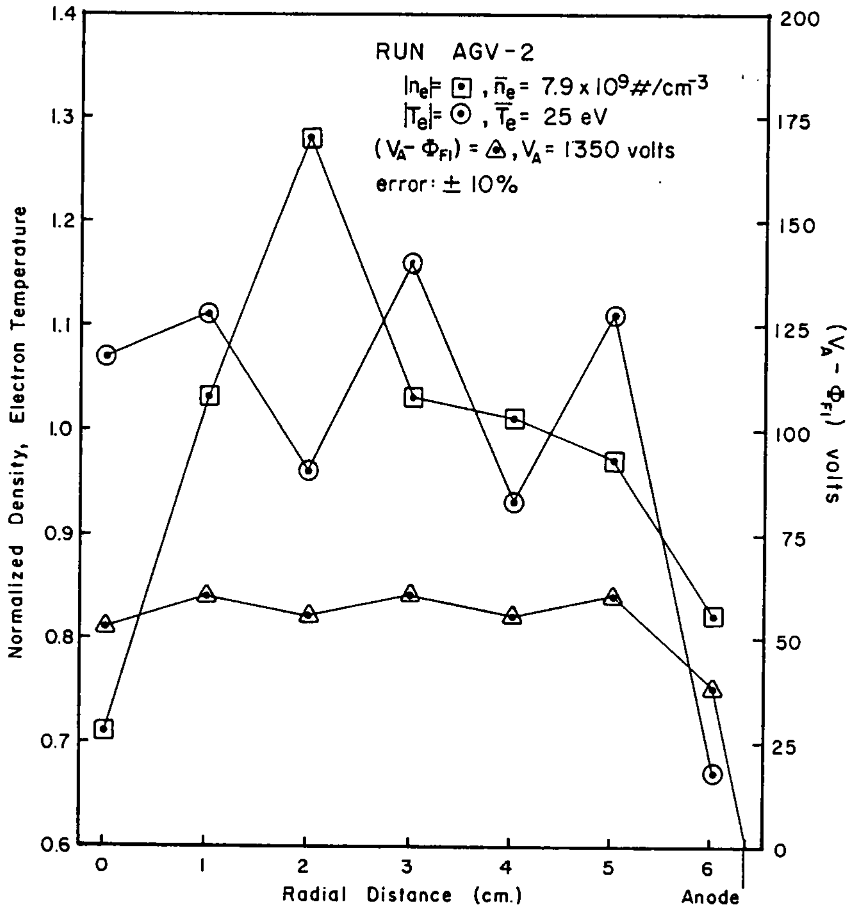

Figure I.12. Radial profile of electron number density, electron temperature and anode voltage-floating voltage difference for Run AGV-2.

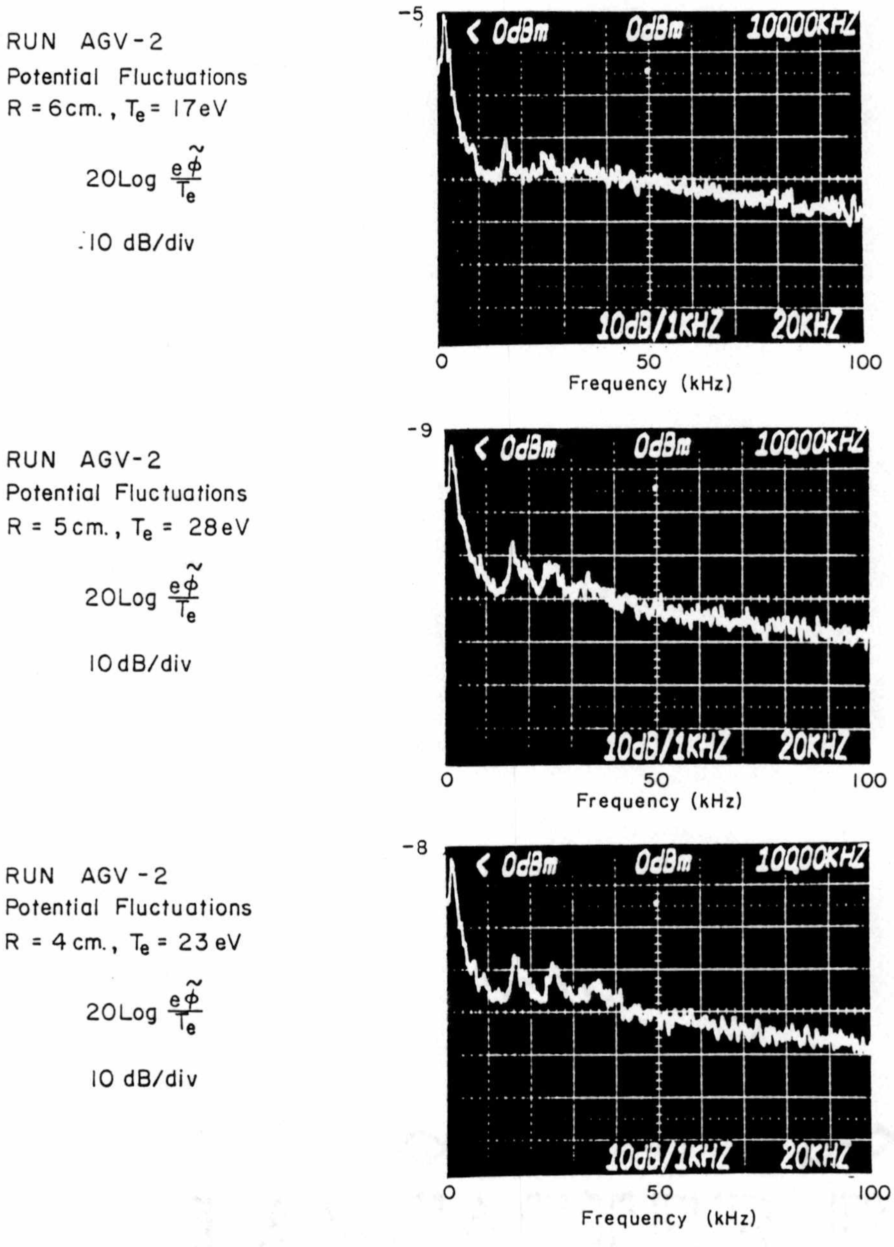

Figure I.13. Calibrated electrostatic potential fluctuation spectra at R =6cm., 5cm. and 4cm. for Run AGV-2.

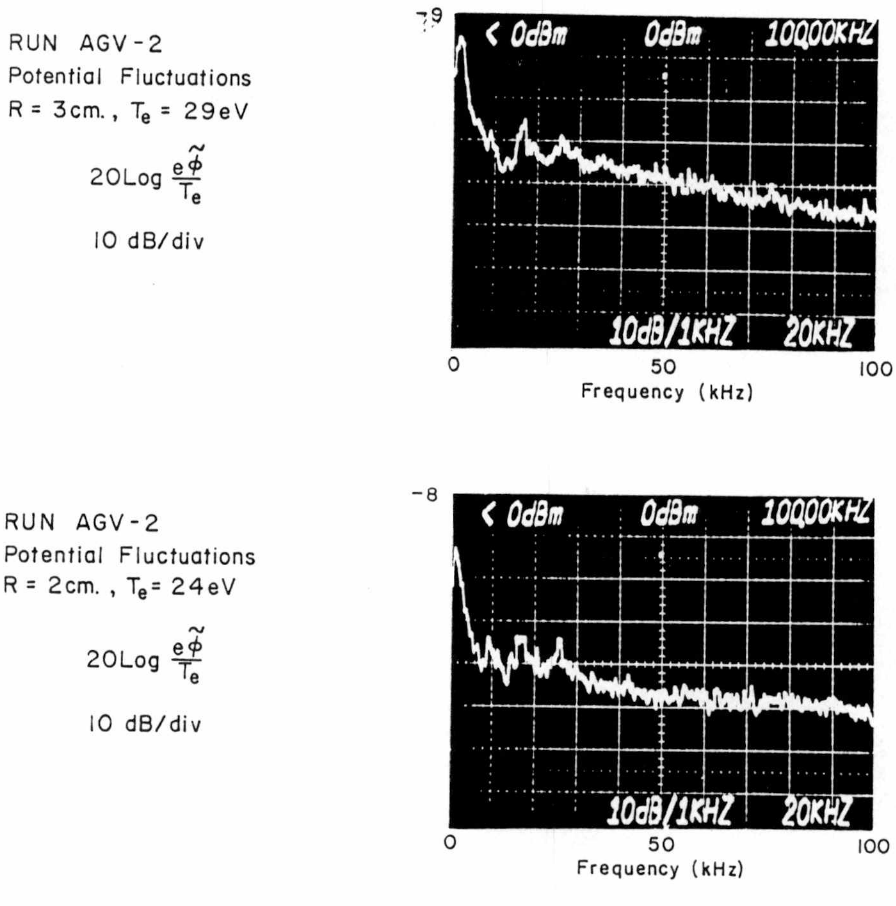

Figure I.14. Calibrated electrostatic potential fluctuation spectra at R =3cm. and 2cm. for Run AGV-2.

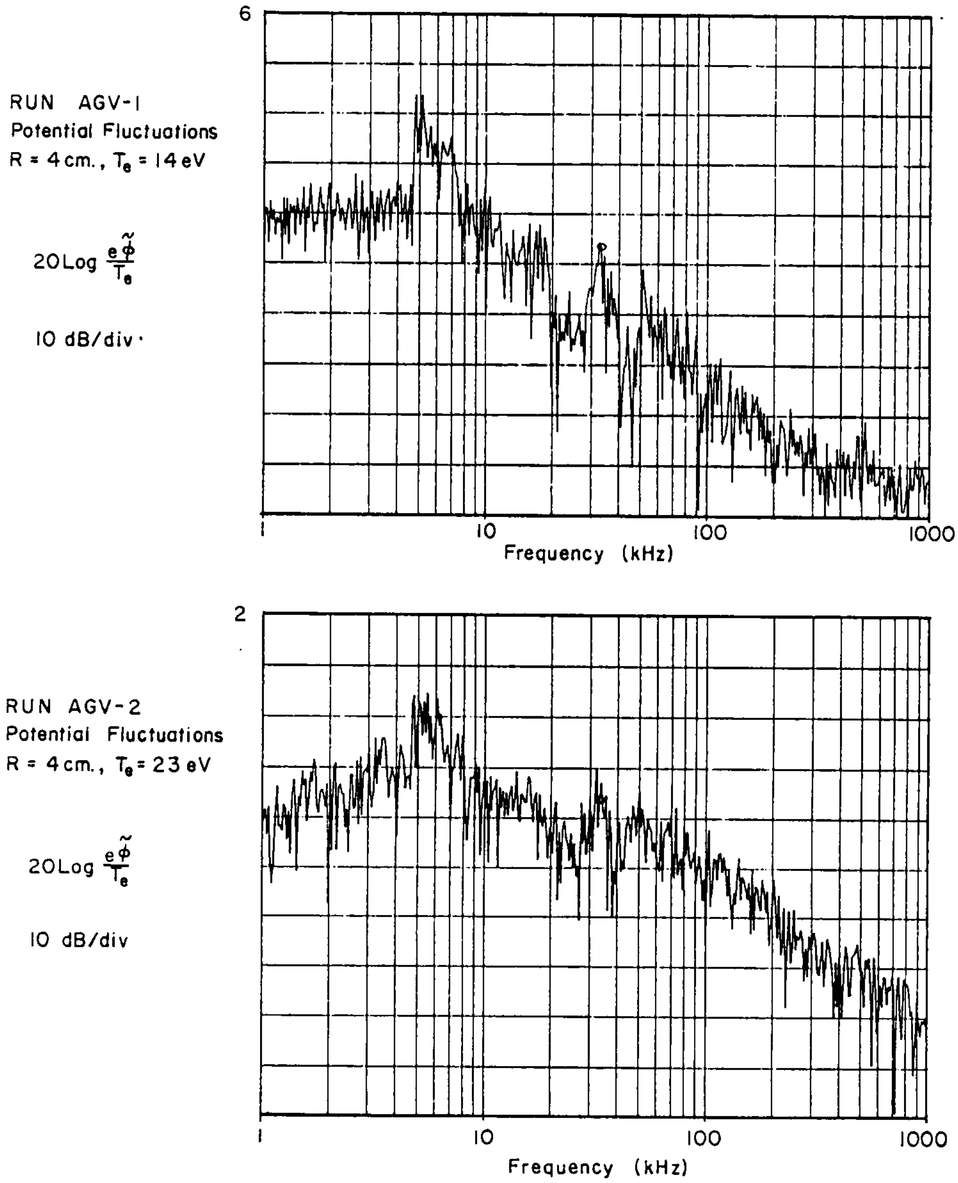

Figure I.15. Comparison of calibrated electrostatic potential fluctuation spectra for Runs AGV-1 and AGV-2 at R =4cm. on log frequency axis.

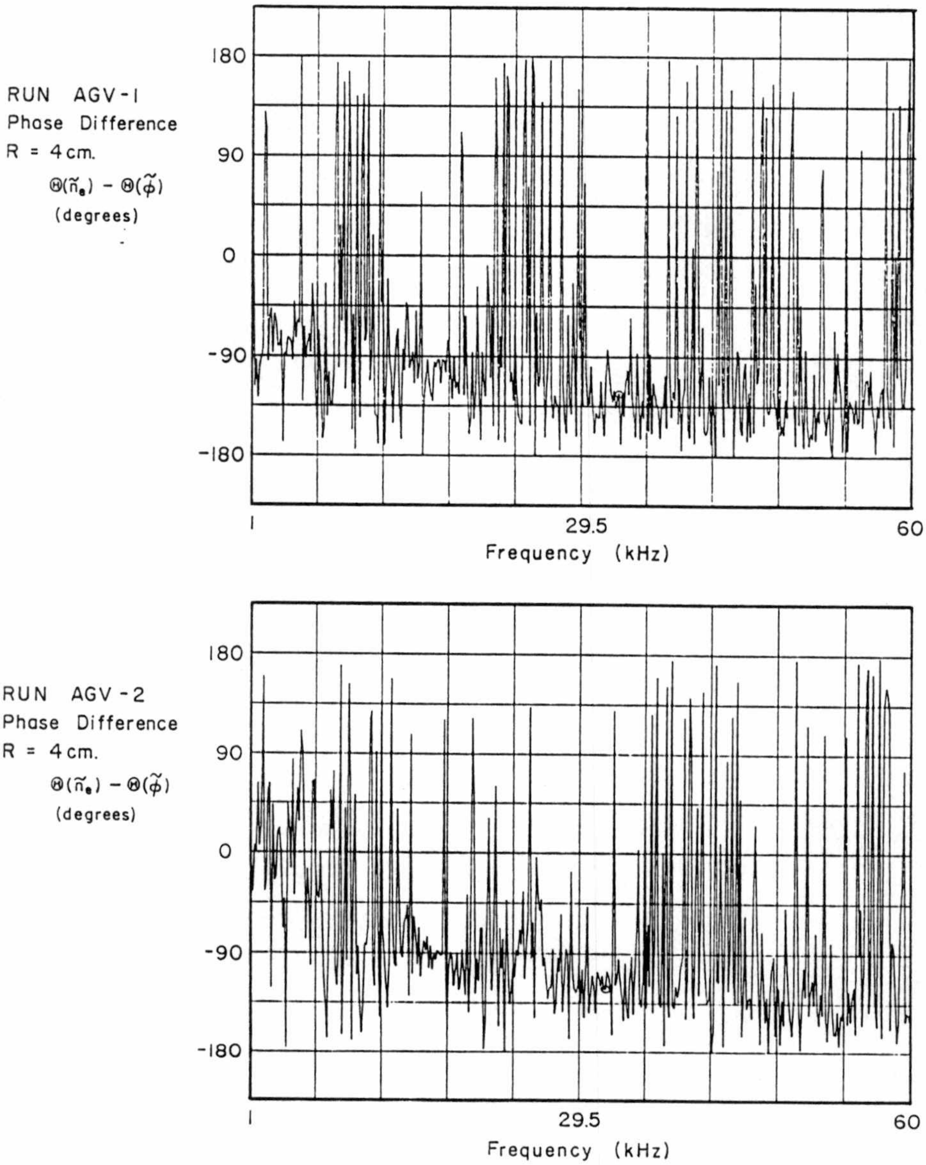

Figure I.16. Phase spectra of the difference in phase between electron density fluctuations and electrostatic potential fluctuations for Runs AGV-1 and AGV-2 at R =4cm.

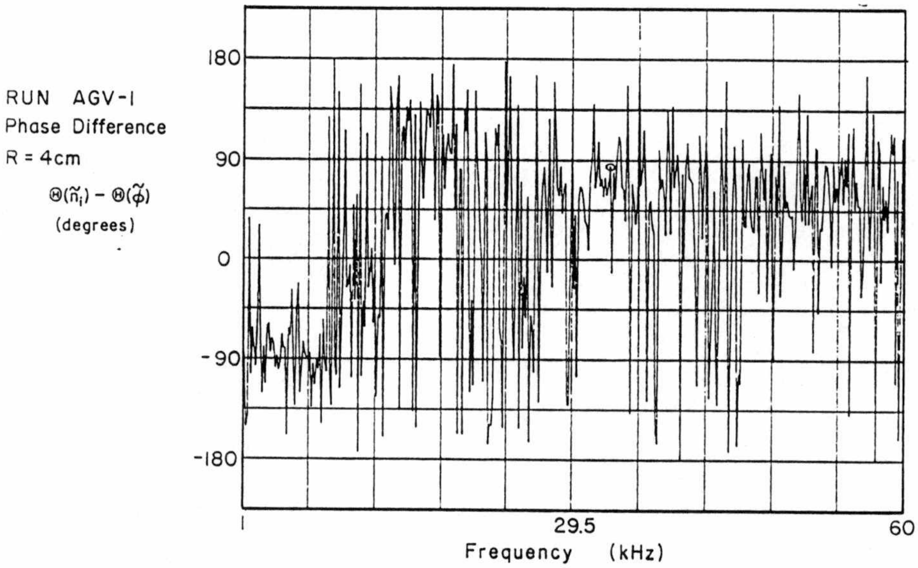

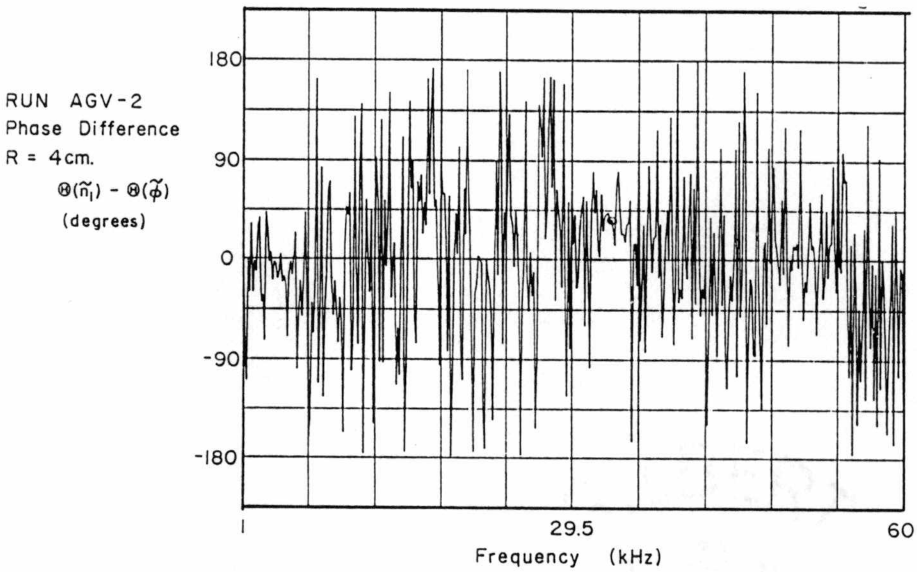

Figure I.17. Phase spectra of the difference in phase between ion density fluctuations and electrostatic potential fluctuations for Runs AGV-1 and AGV-2 at R =4cm.

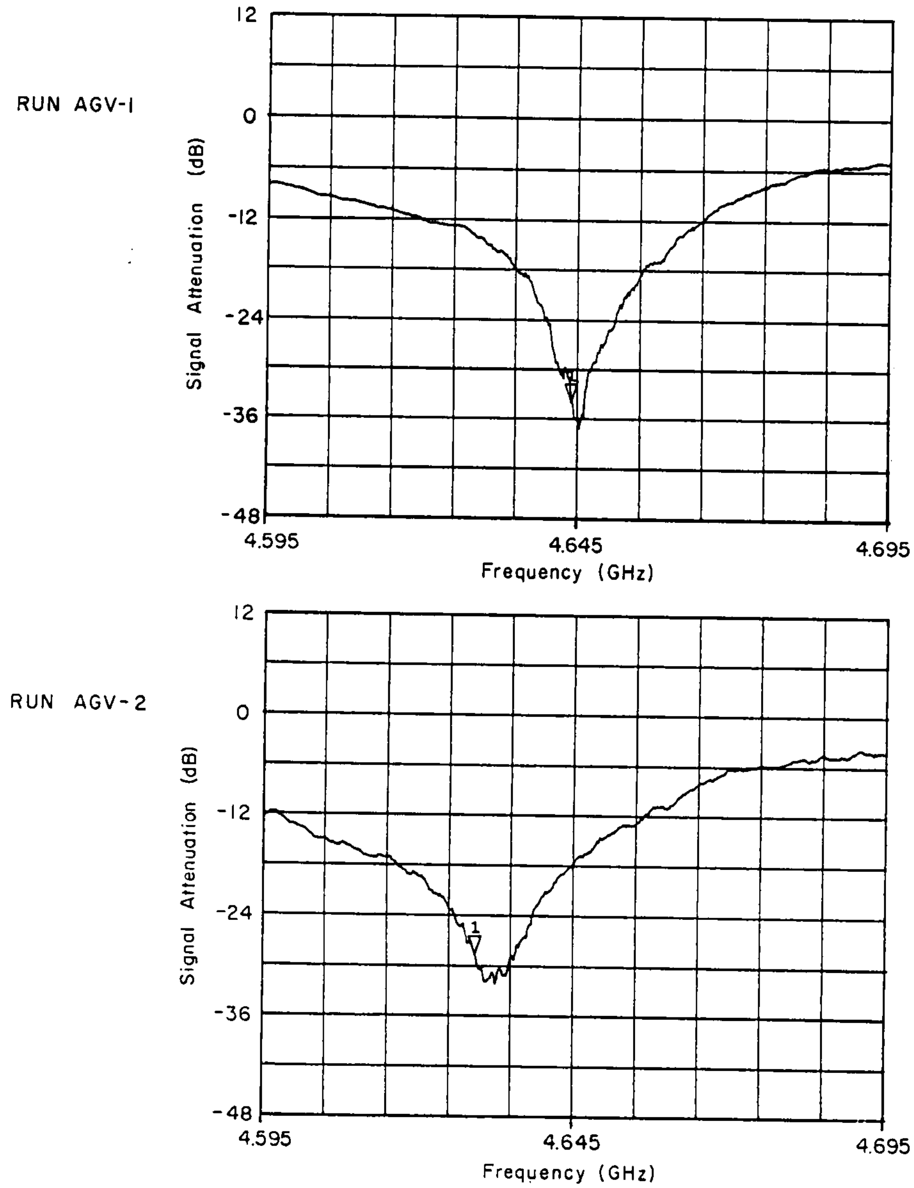

Figure I.18. Microwave absorption data for the extraordinary mode wave launched and received by small monopole antennae for Runs AGV-1 and AGV-2.

VITA

The author was born in Jacksonville, Florida on January 13, 1957. He was raised in Gainsville, Florida and attended Gainsville High School. In August of 1980 he received Bachelor's degrees in Mechanical Engineering and Physics from the Georgia Institute of Technology, Atlanta Georgia. During his undergraduate education he was employed part time as a machinist and welder.

The author attended the University of Tennessee Space Institute in Tullahoma Tennessee from September 1980 to June 1981. He transferred to the University of Tennessee, Knoxville, in September 1981 and was employed as a graduate research assistant. In June 1982 he received a Master of Science degree in Engineering Science from the University of Tennessee, Knoxville.

From July 1982 to September 1988 the author was employed as a graduate research assistant in the University of Tennessee's Department of Electrical Engineering Plasma Lab under Dr. J. Reece Roth. During this time he continued his studies as a graduate student and performed experimental studies on a Penning discharge plasma. He received his Ph.D. in Engineering Science from the University of Tennessee Knoxville in August 1990.